ABSTRACT

Title of Document: Understanding Actuation Mechanisms of Conjugated Polymer Actuators: Ion Transport

Xuezheng Wang, Doctor of Philosophy, 2007

Directed By: Dr. Elisabeth Smela

Department of Mechanical Engineering

Conjugated polymer actuators have demonstrated their promising applications in several fields ranging from BioMEMS to microrobotics, biomimetics, and medical devices. However, actuators' performance (strain, stress, speed, and lifetime) still can not be correctly predicted by theoretical models, mainly because actuation mechanisms of these actuators are not well-understood yet. The lack of knowledge on actuation mechanisms also makes it difficult to improve these actuators. Therefore, decoding actuation mechanisms is critical for successful applications of conjugated polymer actuators.

This dissertation explored ion transport in conjugated polymers. Ions are known to give major contributions to volume change of conjugated polymer films that directly drive actuators. Study in this dissertation focused on following subjects: 1. Driving mechanisms (migration and diffusion) for ion transport. 2. Correlation among ions,

charge, and volume change. 3. Effects of experimental situations (voltage, swelling of polymers, film thickness, ion barrier thickness, electrolyte, and temperature) on ion transport. 4. Developing a physics-based model and conducting numerical simulations for ion transport in conjugated polymers. A good understanding of these fundamental topics related with ion transport will build up a concrete knowledge base for predicting behavior of conjugated polymer actuators. The research results of this dissertation were summarized mainly in 3 articles and presented in Chapter 3, Chapter 4, and Chapter 5 respectively.

Chapter 3, *Visualizing Ion Currents in Conjugated Polymers*, is a published journal paper in *Advanced Materials*. It reported preliminary experimental and modeling results of cation ingress in polypyrrole doped with dodecylbenzenesulfonate, PPy(DBS), a cation-transporting conjugated polymer. Cation ingress in the polymer was displayed through phase front propagations that were formed by electrochromism. Migration was found to dominate ion ingress evidenced by a linear relationship between phase front velocity and reduction potentials. The preliminary modeling results also confirmed the significant effect of migration, whose role during ion transport has been under debate in the literature for years.

Chapter 4, *Ion Transport in Conjugated Polymers: Part 1. Experimental Studies on PPy(DBS)*, is a full-scale experimental study of ion transport in PPy(DBS). Besides phase front propagation velocity and broadening, current data and actuation strains of PPy(DBS) were also collected. Comparisons among these data gave more insights of cation transport in PPy(DBS). Diffusion of ions in PPy(DBS) was found to be non-Fickian diffusion, which has not been included in models in the literature. Cation

egress was found to be independent with applied potentials, suggesting a diffusion controlled process, while cation ingress was found to be dominated by migration. This difference between cation ingress and cation egress has not been realized before this dissertation. The effect of polymer swelling on cation ingress was characterized for the first time, which suggested an exponential relationship between ion mobility and ion concentration.

Chapter 5, *Ion Transport in Conjugated Polymers: Part 2. Modeling and Simulation Results,* reported more advanced theoretical modeling and simulation results. Nernst-Planck-Poisson's equations were used to model hole transport, ion transport, and potential profiles in conjugated polymers. The model was able to explore ion transport with various experimental situations including changing of voltage, ion diffusivity, hole mobility, Einstein relation, electrolyte concentration, and film geometry. The model successfully predicted both ion ingress and ion egress features for PPy(DBS), which had not been achieved before in the literature. In this article, predictions of anion transport conjugated polymers such as PPy(ClO_4) were also reported.

Understanding Actuation Mechanisms of Conjugated Polymer Actuators:

Ion Transport

By

Xuezheng Wang

Dissertation submitted to the Faculty of the Graduate School of the
University of Maryland, College Park, in partial fulfillment
of the requirements for the degree of
Doctor of Philosophy
2007

Advisory Committee:

Professor Elisabeth Smela, Chair
Professor Amr Baz
Professor Hugh Bruck
Professor Peter Kofinas
Professor Miao Yu

Forward

This dissertation includes one published paper and two paper drafts co-authored by Xuezheng Wang, Dr. Elisabeth Smela, and Dr. Benjamin Shapiro. These papers are included with the permission of the dissertation advisor, Dr. Elisabeth Smela, and the graduate director, Dr. Balakumar Balachandran. The examining committee has determined that the author of this dissertation, Xuezheng Wang, has made substantial contributions to these papers and agrees that these papers should be included in the dissertation.

Acknowledgements

I would like to send my most sincere thanks to my wife and my families for their invaluable support and encouragement. I want to give special thanks to Dr. Smela for her mentorship during my Ph.D. study and to Dr. Shapiro for collaborations on modeling work. I also want to thank Dr. Peomelli, Dr. Balachandran, and Elyse Beulieu-Lucey for helping me to complete the required procedures. I also feel grateful to all my friends in Dr. Smela's group: Lance Oh, Yingkai Liu, Marc Christophersen, Pei-Schuan Jian, Mario Urdaneta, Steve Fanning, Remi Delille, Marc Dandin, and Samuel Moseley.

Table of Contents

List of Figures

List of Tables

Chapter 1 Introduction

1.1 Conjugated Polymer Actuators

Inspired by biological muscles, researchers are highly interested in developing muscle-like actuators, which can produce similar performance with biological muscles. As we know, cheetahs can run as fast as 70 mph [1]. Spittlebugs can jump over 100 times higher than their body length [2]. Hummingbirds can flap their wings as quick as 200 beats per second [3]. Red kangaroos can leap as far as 30 feet [4]. Giant octopuses can squeeze through a tiny hole or crack to escape [5]. Biological muscles are also known to be light weight, compact, compliant, self-healing, self-contained, efficient, and tailored to applications. Compared with biological muscles, current actuators, such as motors, engines, and hydraulic actuators, are bulky, heavy, and noisy. Although current actuators can be superior to biological muscles in one or two areas, it is very difficult for current actuators to achieve a combination of merits demonstrated by biological muscles. However, it is very difficulty to use biological muscles outside their grow-up environment. Therefore, developing artificial muscles becomes a logical approach.

Conjugated polymer actuators have attracted special interests because of their performance. As polymers, they are light weight (approximately 1 g/cm3) and compliant. They produce mechanical work with low applied voltages (1 V) [6-8]. Conjugated polymers respond in seconds. They can produce strains (along the film length direction) as large as 12% [10] and stress 1000 times higher than skeleton muscles [11]. Reported modulus of conjugated polymers is approximately between

0.01 GPa to 100 GPa [12-15]. A special feature of conjugated polymer actuators is that they work well in liquid electrolytes and several biofluids [9]. More interesting, conjugated polymer actuators can also be microfabricated [16-22].

Conjugated polymer actuators have attracted special interests in biomedical applications ranging from blood vessel connectors to drug delivery devices[9, 18, 23-26]. Conjugated polymer actuators, as macroactuators, have been used in applications of camber foils [27], integrated oxygen control system [28], and biorobotic pectoral fin [29]. However, all the above applications are still in their prototype stages and have not reached commercial stages yet.

Reported conjugate polymer actuators have very simple configurations. They are either free standing conjugated polymer films [30, 31], fibers [32, 33], bilayer structures [21, 34], or multilayer structures [35-37]. The bilayer structure is the most commonly reported and studied and is made of conjugated polymer films attached to a substrate (such as a gold film), which is typically not electroactive. Bending motion is typically achieved with bilayer structures, while linear motion is typically achieved with free standing films.

In all reported conjugated polymer actuators, conjugated polymers are the only active component. During actuation, they undergo volume change (either expand or contract) once electrical stimulations are applied. As a result, in a free standing film, the volume change causes the film to either elongate or contract. In a bilayer actuator, since the substrate does not undergo geometry change, the bilayer structure will bend due to the elongation or contraction of conjugated polymer films.

Apparently, to design, improve, predict, or control conjugated polymer actuators, volume change of conjugated polymers must be thoroughly understood.

So far, available models [14, 36, 38-41] of conjugated polymer actuators address only the relationship between actuator geometry and actuators' deformation, leaving physics of volume change untouched. However, volume change of conjugated polymers varies with experimental situations such as synthesis condition, driving voltage, surrounding ions & fluids, cycle history, and film thickness. In practical applications, conjugated polymer actuators will be operated in various environments and with different work requirements. Certainly, models that only relate the geometry with actuation strain are not able to predict the actuation performance (strain, speed, stress, bending angle, and etc.) of conjugated polymer actuators in these environments. A clear understanding of the fundamental process that determines the volume change and mechanical properties of conjugated polymers must be achieved in order to successfully predict actuators' performance in a wide range.

Unfortunately, the fundamental process during actuation has not been well-understood in the literature. Numerous issues regarding ion transport, electron transport, film volume change, film anisotropy, and modulus change have not been well answered. An important is that these issues are inherently related with a complicate electrochemical doping/dedoping process (also called electrochemical oxidation/reduction respectively.) triggered by electrical stimulations. Therefore, before discussing ion transport and volume change in conjugated polymers, I will first

review the basic knowledge of the electrochemical doping/dedoping of conjugated polymers in the next section.

1.2 Doping of Conjugated Polymers

Doping of conjugated polymers is determined by their unique polymer backbones, which will be first introduced in this section. Following the introduction of the polymer backbone, events during doping will be explained.

1.2.1 Conjugated Polymer Backbones

Conjugated polymers have a unique polymer backbone characterized by alternating single and double bonds, as shown in Figure 1 [42]. Polyacetylene has the simplest polymer chain by repeating CH_2 except at the two ends, which are CH_3. In the sketch, every turn-point is a carton atom. Hydrogen atoms connected with carbon atoms are not shown in the sketch. Polypyrrole has a repeated unit of (C_4H_4NH) that forms a pentagon shape. The alternating single and double bonds go through carbon atoms. A review of carbon's atomic orbitals is necessary to understand single and double bonds and is given in the next paragraph.

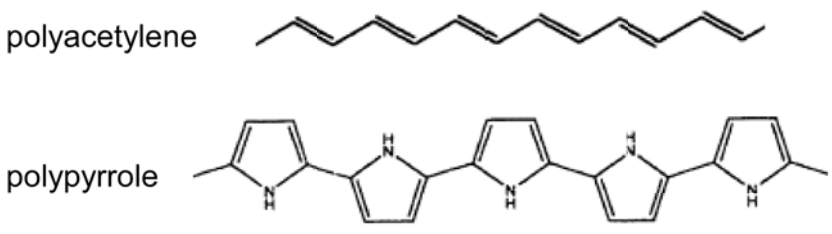

Figure 1. Polymer backbones of polyacetylene and polypyrrole.

Carbon is the No. 6 element in the periodical table. Each carbon atom has 6 electrons: 2 electrons in the 1s orbital, 2 electrons in the 2s orbital, and 2 electrons in 2 of the p_x, p_y, and p_z orbitals. When carbon atoms form bonds with other atoms, either sp, sp^2, or sp^3 hybridization can occur depending on how many atoms are connected [43]. In conjugated polymers, sp^2 hybridization occurs since a carton atom is connected with three other atoms. For example, in polpyrrole, a carbon atom is connected with one hydrogen atom and two carbon atoms. The sp^2 hybridization rearranges 2 electrons in 2s orbitals and 1 electron in the 2p orbital into 3 sp^2 orbitals whose energy levels are between 2s and 2p and leaves 1 electron in the 2p orbital untouched. The three hybridized orbitals are identical and distributed evenly in a single plane, forming a 120^{o} angel between bonds as shown in Figure 2. The left p orbital is perpendicular to the plane [43]. When carbon atoms are connected to form conjugated polymer backbones, these angles will be maintained or slightly altered.

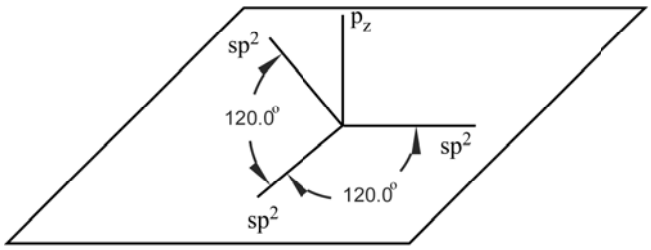

sp^2 hybridization

Figure 2. Atomic orbitals of a carbon atom during sp^2 hybridization

In conjugated polymers, two types of bonds are formed when carbons atoms are connected to form polymer backbones: σ bonds and π bonds. σ bonds are formed by the end overlap of sp^2 orbitals, while π bonds are formed by side overlapping of p

orbitals. Electrons in σ bonds and π bond behave quite differently. Electrons in the σ bonds are confined between the two carbon atoms and require more energy to excite, while electrons in the π bonds are less bonded to carbon atoms. An important feature for electrons in π bonds is that they are shared by all the carbon atoms as long as they are connected with π bonds. Since conjugated polymers have alternating single and double bonds, each carbon atom is connected with a π bond. Therefore, electrons in π bonds are shared by the whole polymer backbone. These delocalized electrons in the π bonds create a "highway" for electrons to move along polymer backbones [42-45].

When forming bonds, both π bonds (bonding orbitals) and π^* bonds (antibonding orbitals) are created, since orbitals need to be conserved [43]. The π bonds (bonding orbitals) are fully filled with electrons, while the π^* bonds are empty. In analogy with silicon band structures, π bonds are comparable with valence band, which is filled with electrons, and π^* bonds are comparable with conduction band [45-47]. π bonds are called the highest occupied molecular orbitals (HOMO), and the π^* bonds are called the lowest unoccupied molecular orbitals (LUMO). The energy difference between HOMO and LUMO are different for different types of conjugated polymers. For example, the energy difference between HOMO and LUMO is reported to be approximate 1.5 eV [48, 49], similar with the band gap energy of 1.1 eV for silicon [50]. The band gap of polypyrrole is larger with reported values of approximate 3.0 eV [51, 52].

As reviewed before, it is the π bonds that make conjugated polymers organic semiconductors. Doping of conjugated polymers can alter material properties greatly, which will be reviewed in next sections.

1.2.2 Doping of Conjugated Polymers

Doping of conjugated polymers generates net charges in polymer chains. Without doping, chains of conjugated polymers are neutral. N-doping refers to creation of negative charges in polymer chains, while p-doping refers to creation of positive charges. Since p-doping are commonly used in conjugated polymer actuators, I will limit the review to p-doping.

P-doping can be achieved either chemically or electrochemically. Chemical doping is done by exposing conjugated polymers to oxidants, while the electrochemical doping is done by applying electrical potential and providing compensation ions to conjugated polymers. Both chemical doping and electrochemical doping remove electrons from polymer chains (oxidation). Since electrochemical doping is widely used in conjugated polymer actuators, I will further focus the following review on electrochemical p-doping of conjugated polymers.

Upon electrochemical p-doping, voltage is applied to conjugated polymers to remove electrons from polymer chains. Several parameters affect the ability of voltage to remove electrons from polymer backbone. Type of polymers, conjugated length, solvents, compensation ions, and temperature all affect the doping process.

A positive charge is created in polymer chains due to removal of one electron. Because of π bonds, the generated positive charge is delocalized along polymer

chains, which makes conjugated polymers electrically conductive [46]. Unlike charge carriers in silicon semiconductors, charge carriers created in polymer chains induce lattice distortion [49, 53, 54]. When they move along the polymer chains, they induce the lattice distortion along with them. Number of charge carriers that can be removed from conjugated polymers is limited. Experimental data suggest that one electron can be removed from approximately 20 carbon atoms [55, 56].

Since charge carriers in conjugated polymers induce lattice distortion, they have different names other than electrons and holes. Solitons, polarons (single charged), and bipolarons (double charged) [48, 55, 57, 58] are named for charge carriers in conjugated polymers. Solitons are the charge carriers in trans-polyacetylene because polymer chains of trans-polyacetylene is symmetrical, while polarons and bipolarons are charge carriers for the rest conjugated polymers [48, 49, 53]. When charge carrier concentration is low, only polarons present in conjugated polymer chains. When charge carrier concentration becomes high, two polarons will combine to form a bipolaron [59].

Dedoping of conjugated polymers is the reverse process of doping. It lowers the net charge concentration of polymer chains. If conjugated polymers are p-doped, dedoping will put electrons back to polymer chains.

1.2.3 Doping Induced Property Change of Conjugated Polymers

An important result of doping is the introduction of compensation ions, which come from external electrolytes and enter conjugated polymer films to maintain charge neutrality. The addition of ions makes conjugated polymers to increase volume,

which is used to make conjugated polymer actuators. The measured volume change along conjugated polymer films ranges from 3% to as high as 12%, while the measured out-of-plane strain reaches as high as 35% [6, 8, 10, 12, 13, 60-69].

Besides ions, solvent insertion also occurs due to the high osmotic pressure in conjugated polymers built up by accumulation of ions. Solvent insertion causes conjugated polymers to expand more [63, 70].

Due to the formation of charge carries of polymer backbones and addition of ions and solvents, chain conformation relaxation also occurs, which also give contribution to volume change [71, 72].

As a result of doping, conjugated polymers change from an insulator to an electronic conductor. For example, polypyrrole doped with dodecylbenzenesulfonate (PPy/DBS) has a conductivity of 10^{-4} S/cm when the polymer chain is neutral [73]. Its conductivity reaches as high as 10 S/cm when it is highly doped [73]. A highly doped polyacetylene with well-aligned polymer chains can reach 10^5 S/cm, which is comparable with copper (10^6 S/cm) [47].

Doping also introduces additional energy levels between the HOMO and LUMO by creating charge carriers in polymer chains. As shown in Figure 3, before doping, no energy levels exist between LUMO and HOMO. For polyacetylene, a soliton level is introduced between the LUMO and HOMO [42]. The soliton energy level is thought to be at the middle of the band gap. For conjugated polymers other than polyacetylene, levels of polaron and bipolaron are added between LUMO and HOMO depending on doping levels [57]. Solitons, polarons, and bipolarons have different

energy levels. Note: the dash lines for polaron/bipolaron energy levels in the figure are not representing the actual values.

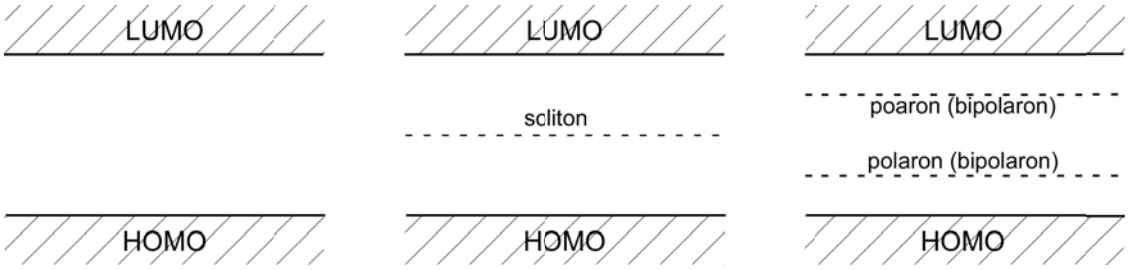

Figure 3. Addition of soliton, polaron, and bipolaron energy levels between LUMO and HOMO.

A direct consequence of addition of new energy levels between HOMO and LUMO is that the optical absorption of conjugated polymers films is altered. Figure 4 shows absorption data of PPy(DBS) upon doping [74]. At +0.5 V vs. Ag/AgCl, the polymer is highly doped. At -0.9 V, the polymer chain is neutral. When the film is highly doped at +0.5 V, red light (around 800 nm) absorbance substantially increased, because the addition of bipolaron energy levels allows more red lights, which has lower energy level, to be absorbed. In experiments, the absorption change causes color change of conjugated polymers, which is a known fact in the scientific community. Since the color change is directly related with doping levels of conjugated polymer, this dissertation uses it to display ion transport.

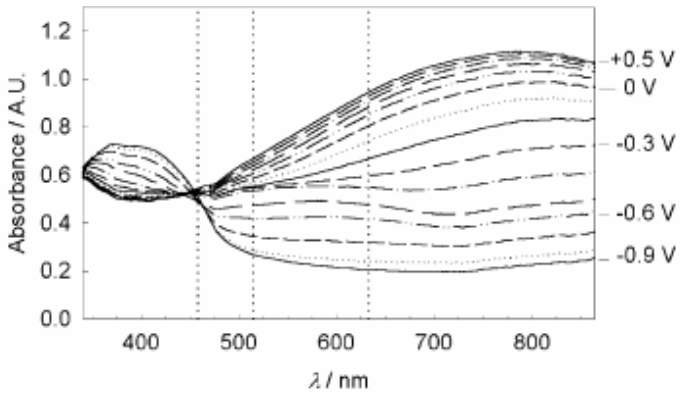

Figure 4. Absorbance of PPy(DBS) upon electrochemical doping. Reference: Ag/AgCl. Electrolyte: 0.1 M NaClO4. The plot is taken from [74].

Modulus of conjugated polymers is also found to change upon doping. For example, modulus of PPy(DBS) increases from 0.1 GPa, when no charge is on the polymer chain, to 1 GPa, when it is highly doped [12, 14].

1.3 Contributors to Volume Change of Conjugated Polymers

As pointed out, volume change of conjugated polymers includes contributions of ions, solvents, and polymer chain conformation relaxation. This section reviews current understandings of how ion transport, solvent transport, and chain conformation relaxation affect volume change and how experimental parameters affect these processes.

1.3.1 Ion Transport

As introduced in the prior chapter, ions egress/ingress occurs upon doping to maintain charge neutrality in the film. These ions come from external source such as an electrolyte. They travel through electrolytes, cross the polymer/electrolyte interface, and move among polymer chains to reach every area of polymer films. Ions are found to be mainly responsible for volume change of conjugated polymers [15, 61,

75]. Ion ingress causes conjugated polymers to increase volume, while ion egress causes volume to decrease.

For actuation directions it is important to know whether anions move into or cations leave the polymer upon doping. Since ions enter the film to maintain charge neutrality, anion egress and cation ingress have the same effect in term of maintaining charge neutrality. For actuators, however, anion egress and cation ingress cause different motions of actuators. If anions move into the polymer, films expand. But if cations leave the polymer, films shrink.

In the literature, which ion is mobile can be determined through experiment techniques such as bending beam method [75], AFM [61], EQCM (electrochemical quartz crystal microbalance) [76, 77]. Experimental data suggest that size of ions plays an important role to determine mobile ions during dedoping/doping cycles [78-82]. Typically, when small anions and large cations are used, anion transport will be dominant.

(1) $$P^0 + A^- - e^- \leftrightarrow P^+(A^-)$$

where P^+ represents the oxidized (charged) state of the polymer chain, P° represents the reduced (neutral) state, e^- represents the electrons, and A^- represents the anions. However, when both anions and cations are small, anion egress and cation egress can occur simultaneously, which poses great difficulties in controlling motion of actuators. When large anions, such as DBS and PSS (poly(styrenesulfonate)), and small cations are used, ion transport is found to be dominated by cations [77-79, 81,

83, 84], as shown in equation (2). Note: DBS or PSS enter conjugated polymer film are incorporated in the polymer matrix during synthesis.

(2) $$P^{+}(A^{-}) + C^{+} \leftrightarrow P^{0}(A^{-}C^{+}) - e^{-}$$

where C^{+} represents cations.

It is also important to determine ion concentrations in polymer films since they are responsible for the volume change. An in-situ measurement will be the best, because it allows us to predict speed of conjugated polymer actuators. But in the literature, no experimental data are available that report a direct count of ions in conjugated polymers. Number of ions in polymers is estimated based on indirect experimental data. For example, number of ions is assumed to equal to the number of electronic charges passing through conjugated polymer films by ignoring currents from other reactions and capacitive currents[85, 86]. Number of ions is also obtained through color change by monitoring transmitted light intensity [87].

Another important question is how to control ion concentrations in conjugated polymers, which determine actuation strains. In the literature, voltage is an important parameter to control doping of polymer chains, which determines ion concentrations [22].

In aqueous electrolytes, ions enter conjugated polymers with their hydration shells [77, 83, 88, 89]. As known, ions in aqueous electrolytes are surrounded by water molecules, which have strong electrostatic interaction with ions. As a result, ions attract a number of water molecules, which move along with ions. When ions enter

conjugated polymers, they also bring certain number of water molecules with them. However, number of water molecules that ions bring into conjugated polymers is not consistent among published results [82, 83, 88, 90].

For actuation speed, it is important to understand how fast ions move in and out of polymers. This brings up an important question: what are the driving mechanisms for ion transport in conjugated polymers. Unfortunately, this question is still not answered in the literature.

An on-going discussion of driving mechanisms in the literature is that whether migration plays a role in ion transport[40, 71, 77, 91-96]. Migration, known as the movement of charged particle in electrical field, determines the velocity of charged particle by $v = \mu E$, where v is the velocity (m/sec), μ is the mobility (cm/secV), and E is the electrical field (V/m). Researchers hold different views of how to treat the ion-polaron/bipolaron interaction in the polymer. A group of researchers think that ion transport in the polymer is not driven by electrical field because polaron/bipolaron will have strong electrostatic interactions with ions once ions present in the polymer [97]. The new entity formed by ion and polaron/bipolaron has no net charge and diffuse together in the film. On the other hand, Pickup and Lacroix pointed out that diffusion is not enough to explain experimental results especially when large potential is applied [94, 96].

Other than migration, ion diffusion in conjugated polymers is not been well understood either. Fickian diffusion, which is the ion motion caused by concentration gradient, has been widely adopted in models that predict ion transport in conjugated

polymers [93, 96-102], ignoring the fact that diffusion in polymers is likely to be under the influence of polymer relaxation process [103, 104]. Although conjugated polymers are known to undergo conformation relaxation changes especially in the first cycle [78, 101, 107-109], non-Fickian diffusion has not been properly handled in reported models. In the literature, non-Fickain diffusion can cause completely different transport phenomena from Fickian diffusion. For example, when polymer relaxation process is the rate limiting step, Case II diffusion occurs, which creates a linearly relationship between absorbed solvents and time [105, 106].

In summary, ion transport in conjugated polymers is a very complicate topic. Assuming the listed on-going discussions or issues have been solved successfully, the society still has more questions that need to be answered. Ion transport in conjugated polymers has been found to depend on both material properties and experimental situations. For example, ion diffusivity is found to increase with film thickness [110]. Using organic solvents, such as propylene carbonate, can cause anion transport even when DBS anions are used [111]. Electrolyte pH is also found to lower the volume change [112]. Other parameters that affect ion transport include conjugated polymer type [113] , synthesis condition [114], temperature [115], electrolyte concentrations [63, 70], and ion type[77, 79, 116]. We certainly can not answer all the questions simultaneously. It is a logical strategy to start and clarify driving mechanisms first and then study the rest issues.

1.3.2 Solvent Transport

A widely used solvent for conjugated polymer actuators is water [18, 22, 34, 63]. Organic solvents are also used in actuator demonstrations [85, 117-119]. Since water is the only solvent used in the dissertation, the introduction will focus on current understandings of aqueous electrolytes.

Water contributes to volume change by two means: water molecules in the hydration shell enter the polymer simultaneously with ions [82, 83, 88, 90], and the others are driven by osmotic pressure [63, 70]. The first way has been discussed in the section of ion transport. Bay is the first researcher who discovered the second way [63]. By increasing the electrolyte concentration from 0.1 M to 5 M, the elongation of a free standing conjugated polymer film decreased by approximately 50%. Since number of ions in conjugated polymers did not change, the decrease of elongation was thought to be caused by solvent transport. The explanation was that increase of electrolyte concentrations lowered the osmotic pressure between polymers and electrolytes. As a result, less solvent molecules entered conjugated polymers that caused films to expand less.

In the literature, few efforts have been made to separate contributions of water transport from ion transport. The speed difference between water transport and ion transport has not been isolated yet.

1.3.3 Chain Conformation Relaxation

Chain conformation relaxation refers to the 3D shape change of polymer chains [43]. In conjugated polymers, polymer chain conformation relaxation is thought to be caused by three reasons: creation of net charges alters carbon-carbon bond length

[49, 120]; repulsion of net charges stretches polymer chains [101]; insertion of ions and solvents stretch chains further [101]. Otero developed a charge transport model that takes chain conformation relaxation into account [71, 72, 121, 122].

Although the contribution of chain conformation relaxation to volume change of conjugated polymers is still under debate, chain conformation relaxation is very likely to be the rate limiting step during volume change of conjugated polymers that may determine the actuation speed. Chain conformation relaxation is also likely to affect the modulus, creep, and hysterysis of conjugated polymers.

1.4 PPy(DBS): a Model System Used in this Dissertation

Since properties of conjugated polymers are sensitive to many parameters such as type of polymers , length of polymer chains, compensation ions, and synthesis conditions, it is necessary to start with a known system to explore the main actuation mechanisms. PPy(DBS) is the model material system selected in this dissertation. It has been widely used in research[61, 63, 74, 78, 83, 111, 112, 114, 123-126]. An important reason why PPy(DBS) is widely researched is because cations are ensured to be the mobile ions when conjugated polymers are cycled in aqueous electrolyte with DBS as anions [78]. This gives a very good control on actuation direction using applied voltage. PPy(DBS) also has good stability in air. Its conductivity can reach as high as 100 S/cm [73]. Approximately 1 electron out of 3~4 rings is removed from polymer chains, resulting charge density along polymers chains as high as 3 M [55,

56]. The weight fraction of DBS right after deposition is approximately 0.56[1] (Calculation is based on 1 DBS anion out of 4 pyrrole rings.). Assuming absolute charge neutrality is maintained in polymer films, both DBS anions and mobile cations in polymer films can reach approximately the same concentration (3 M). For actuators, it produces approximately 35% reversible out-of-plane strain [61] and 3% reversible in-plane strain [39, 100], and can be operated in various biofluids [9].

The dopant of PPy(DBS) is the DBS anion, which is a large anion as shown in Figure 5[20]. It is a surfactant that has a benzene ring, a SO_3^- anion and an alky tail with 12-13 carbon atoms. DBS anions are incorporated into the conjugated polymer during polymerization of pyrrole monomers to form polymer chains. Since a positive voltage is applied during polymerization, doping of conjugated polymers occurs simultaneously, which attracts DBS anions into the polymer matrix. After polymerization, DBS anions become immobile in the polymer. In the following doping/dedoping cycles, since DBS anions can not move, cations move in and out of conjugated polymer films to maintain charge neutrality.

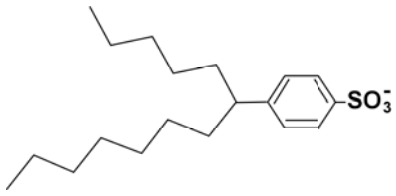

Figure 5. DBS ions[20].

DBS anions also tend to form lamella structure in conjugated polymers [127] [128]. X-ray diffraction results of PPy(DBS) suggested that lamellar structures were formed

[1] Formula of DBS is $C_{19}H_{31}SO_3$, which has a molecular weight of 339. Molecular weight of 4 PPy repeating units ($C_{16}N_4H_{12}$) is 260. Assuming 1 DBS every 4 PPy repeating units, the weight fraction is 339/(339+260)=0.56.

in polymer films [127] The layer structures in PPy(DBS) may cause anisotropic property in diffusion, modulus, and volume change. For example, reported in-plane strain of PPy(DBS) was approximately 3%, while reported out-of-plane strain can reach 30% [60] . Such large difference between in-plane and out-of-plane strain can not be explained by the fact that in-plane deformation of PPy(DBS) is constrained by the substrate. The reason is that even assuming a large Poisson's ration such as 0.5, out-of-plane strain due to in-plane deformation is only 1.5% (3%*0.5=1.5%), which is far less than the out-of-plane strain (30%). Therefore, the large deference between in-plane and out-of-plane strains is most likely caused by material anisotropy.

1.5 Operation of Conjugated Polymer Actuators

This section explains the setup of operating conjugated polymer actuators. The setup is where the electrochemical doping of conjugated polymers occurs. Functions of each component of the setup will be explained. Two methods used in this dissertation for electrochemical doping of conjugated polymers are explained. The knowledge of this section is necessary to understand the experimental setup in Chapter 4 and the potential modeling in Chapter 5.

1.5.1 Operation Setup

A three-electrode electrochemical cell is used to control conjugated polymer actuators, as shown in Figure 6. The setup includes a power source (potentiostat), a working electrode (conjugated polymers), a reference electrode, and a counter electrode. The working electrode, reference electrode, and counter electrode are

submerged in electrolytes that provide compensation ions. A container made of Teflon is used to physically hold electrolytes and the three electrodes.

Each component of the setup serves a different function. The potentiostat applies and monitors the electrical signals (voltage and current) of the working electrode. Either voltage or current are carefully controlled. The reference electrode provides a constant potential reference in the setup, because the electrochemical reaction at the reference electrode is always at equilibrium [129]. A commonly used reference electrode is Ag/AgCl in a saturated NaCl (3 M) electrolyte. The working electrode is the conjugated polymer actuator, which undergoes electrochemical doping/dedoping. No interests will be put on reactions at the counter electrode, whose purpose is to complete the circuits. Without the counter electrode, doping of conjugated polymers at the working electrode will not occur continuously, since the electrolyte will be charged after ions enter conjugated polymers. The counter electrode is preferably to have large surface area so that it will not limit the current flow in the setup. The electrolyte in the setup is to provide compensation ions during electrochemical doping. The electrolytes used in this dissertation are aqueous NaDBS.

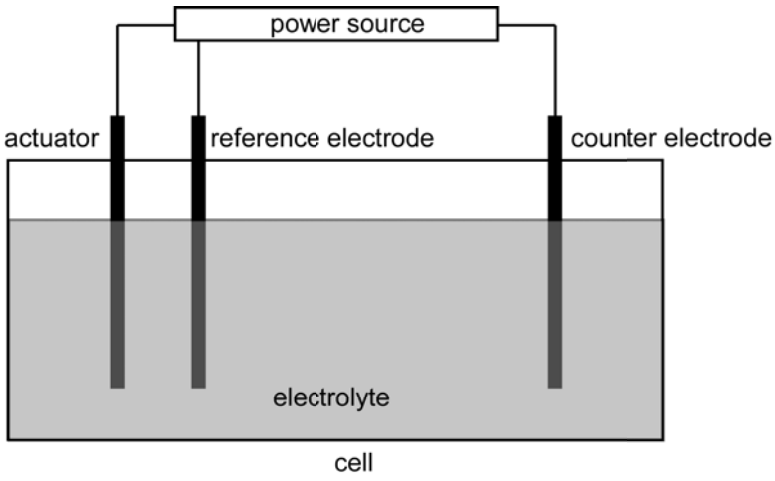

Figure 6. A three-electrode electrochemical cell to operate conjugated polymer actuators.

1.5.2 Voltage and Current of the Working Electrode

Voltage and current are two types of data commonly collected by a potentiostat during the electrochemical doping of conjugated polymers. They can provide important information of the doping process such as doping levels, minimum voltage required to initiate doping, and charge transport rate. But both voltage and current data contain information more than the electrochemical doping process and need to be carefully analysis for each experiment.

Voltage at the working electrode is controlled based on the voltage of the reference electrode, because reactions at the reference electrode are always at equilibrium. Potential drop in the electrochemical system occurs in several locations including the electronic connections, the polymer, and the electrolyte, as shown in Figure 7 (The counter electrode is removed because it plays no role to determine the voltage of the working electrode.). The potential between the working and the reference electrode is expressed as:

(3) $$V = V_{circuit} + V_{actuator} + V_{cell}$$

where V is the voltage between the working and the reference; $V_{circuit}$ is the voltage drop of the electrical wire; $V_{actuator}$ is the voltage drop between the actuator and the electrolyte; V_{cell} is the voltage drop of the electrolyte between the actuator/electrolyte interface and the reference electrode. Due to the low resistance of the electrical wire, $V_{circuit}$ is negligible. V_{cell} is determined by the electrolyte resistance and the current, following ohm's law. V_{cell} can be lowered by using highly concentrated electrolytes and reduce the distance between the working electrode and the reference electrode. $V_{actuator}$ is the voltage that controls the doping level, which can be further divided in to two components: an equilibrium potential, $V_{equilibrium,}$ and an over potential, $V_{overpotential}$. The equilibrium potential is the minimum potential that initiates the doping process. For example, if $V_{actuator}$ is less positive than $V_{equilibrium}$, no doping process will occur.

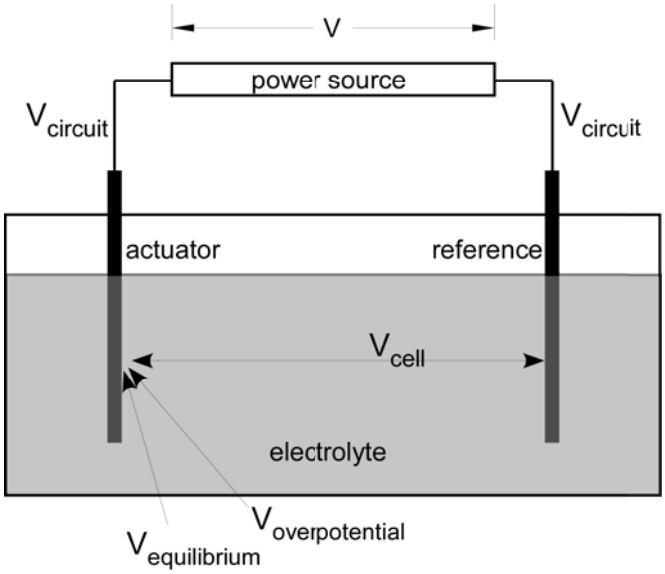

Figure 7. A schematic illustration of potential drop between the actuator and the reference electrode.

Currents running through the working electrode are collected. Figure 8 shows the possible components of currents (The reference electrode is not shown because it passes zero current.). Three components may form the total current: Faraday current, parasitic current, and capacitive current. The Faraday current counts the electrons that are removed or donated to the polymer chain. It provides the exact count of charge carrier concentration and ion concentration in conjugated polymers. The parasitic currents are the electrons from electrochemical reactions other than the doping of conjugated polymers. For example, when negative potential is applied to conjugated polymers that are operated in aqueous electrolytes, water molecules decompose to hydrogen and OH^- at approximately 0.67 V vs. Ag/AgCl [130]. If several parasitic reactions are actuated by applied voltage, currents from these parasitic reactions can dominate the current response of the system, which makes it difficult to obtain charge carrier concentration in the film. The last component of the current is the capacitive current that is generated by the capacitance of the cell and the polymer. A major contributor to the capacitive current is the double layer formed at the electrode/electrolyte interface [129]. Also, any separation of dipoles in conjugated polymers can generate additional capacitive current [131].

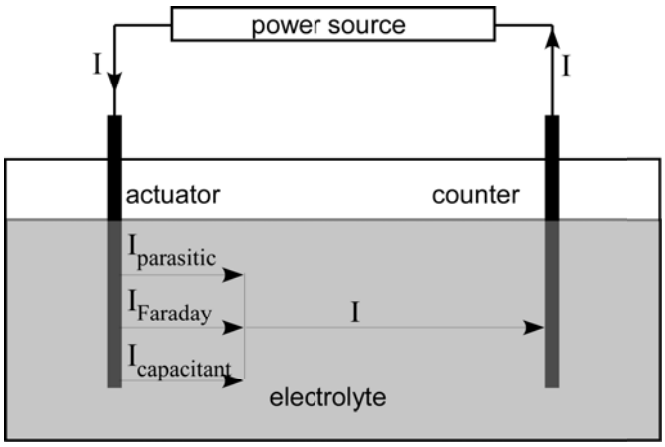

Figure 8. A schematic illustration of current components running through conjugated polymers.

1.5.3 Control Methods

This dissertation uses two control methods during electrochemical doping: constant potentials and linearly-ramped potentials. In this section, basic procedures of the two methods are introduced, and representative results of PPy(DBS), the model system in this dissertation, are explained.

The constant potential control method is also called chronoamperometry [129]. In this method, the potentiostat steps the potentials from one value to another, while the current response is monitored. Figure 9 shows representative current data of a PPy(DBS) film cycled in 0.1 M NaDBS electrolyte. (Reminder: PPy(DBS) is a cation-transporting conjugated polymers. Na ions in the electrolyte will move in and out of polymer films to maintain charge neutrality.) Two potentials are used. At the beginning, a 0 V (vs. Ag/AgCl) is applied that keeps PPy(DBS) at the fully doped (oxidized) state for 5 seconds. No current is flowing through the system since no additional charges are created. Then, the voltage is stepped to a -1 V for 10 seconds to dedope (reduce) PPy(DBS). Right after the voltage is stepped to -1 V, current data

show an immediate spike most likely due to capacitive current, and then the current will decay to a value close to zero indicating completion of the dedoping process. A small residue current will still present due to parasitic reactions. At the end of 10 seconds, the voltage is stepped back to 0 V to dope the polymer. Current data again show a spike and decay due to similar reasons with the dedoping process. At -1 V Volt, Na ions enter conjugated polymer films since electrons are donated to polymer chains. As a result of Na insertion, polymer films expand. When 0 V is applied, Na ions leave conjugated polymer films, and films contract.

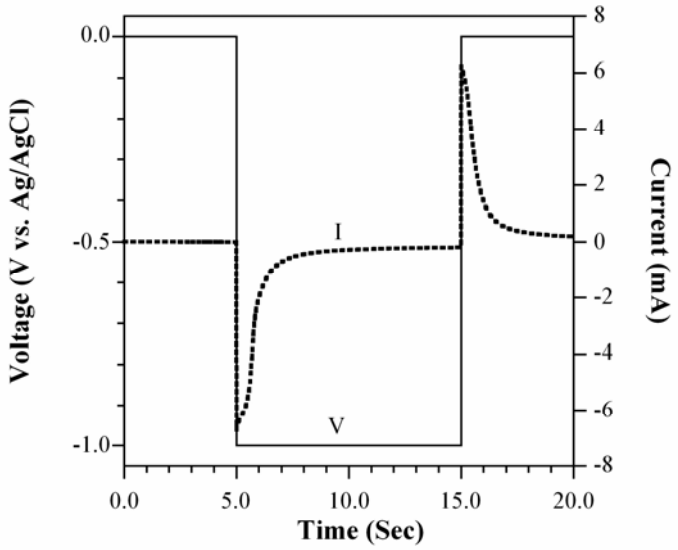

Figure 9. Chronoamperometry of PPy(DBS). Film thickness: 300 nm. Electrolyte: 0.1 M NaDBS.

The second control method used in this dissertation is to linearly ramp voltage between two different values. In this method, a triangle waveform of potential is applied to the actuator as shown in Figure 10a (solid line). The potential is linearly ramped between 0 and -1V. Current responses are monitored (Figure 10a, dash line).

The current is typically plotted with voltage as shown in Figure 10b. Such a plot is called cyclic voltammogram [129].

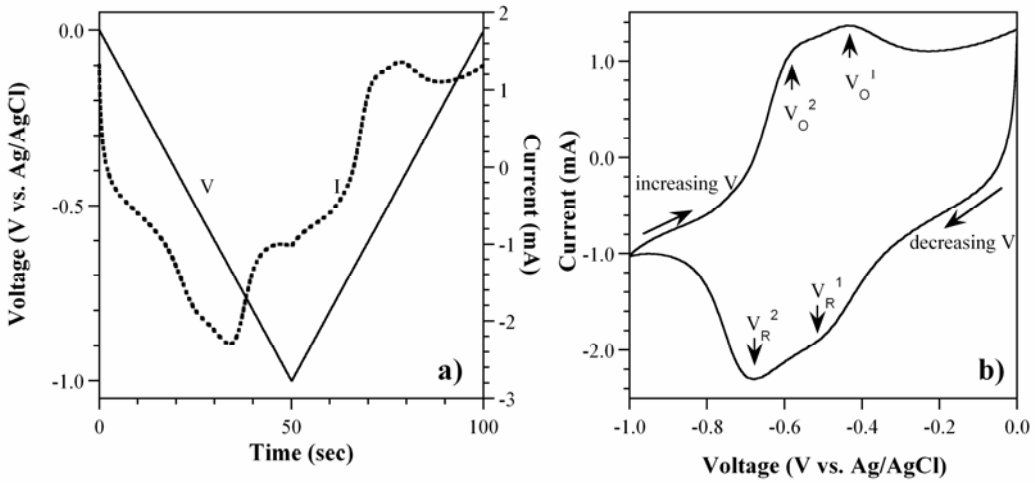

Figure 10. A typical CV of PPy(DBS). Film thickness: 300 nm. Electrolyte: 0.1 M NaDBS. Scan rate: 20 mV/sec. Voltage: 0 V to -1 V vs. Ag/AgCl.

In this dissertation, the main purpose of obtaining a cyclic voltammogram is to find out the doping potential and dedoping potentials of PPy(DBS). Examining Figure 10, four current peaks, indicated by arrows, are identified. The corresponding potentials are V_R^1, V_R^2, V_O^1, and V_O^2. The V_R^2 and V_O^2 are the reduction potential (dedoping potential) and oxidation potential (doping potential), which cause Na ingress/egress. The V_R^2 and V_O^2 potentials are thought to be caused by OH^- insertion/dissertion [112]. The reduction potential of PPy(DBS) gives an approximate estimation on the least negative potential that is required to put electrons back to conjugated polymers. The oxidation potential of PPy(DBS) gives estimation on the least positive potential that is required to take electrons off the polymer.

1.6 References

[1] C. speed, http://www.factmonster.com/ipka/A0004737.html.

[2] Spittlebugs, http://www.newscientist.com/article.ns?id=dn4008.

[3] Hummingbirds, http://hypertextbook.com/facts/2000/MarkLevin.shtml.

[4] Red_Kangaroo, http://en.wikipedia.org/wiki/Red_Kangaroo.

[5] Octopuse, http://nationalzoo.si.edu/support/adoptspecies/animalinfo/giantoctopus/default.cfm.

[6] R. Baughman, "Conducting polymer artificial muscles," *Synth. Met.*, vol. 78 (3), pp. 339-353, 1996.

[7] Q. B. Pei and O. Inganas, "Electrochemical Muscles - Bending Strips Built from Conjugated Polymers," *Synth. Met.*, vol. 57 (1), pp. 3718-3723, 1993.

[8] T. F. Otero and J. M. Sansinena, "Artificial Muscles Based on Conducting Polymers," *Bioelectrochem. Bioenerg.* , vol. 38 (2), pp. 411-414, 1995.

[9] C. Immerstrand, K. Holmgren-Peterson, K. E. Magnusson, E. Jager, M. Krogh, M. Skoglund, A. Selbing, and O. Inganas, "Conjugated-polymer micro- and milliactuators for biological applications," *MRS Bulletin*, vol. 27 (6), pp. 461-464, 2002.

[10] L. Bay, K. West, P. Sommer-Larsen, S. Skaarup, and M. Benslimane, "A conducting polymer artificial muscle with 12% linear strain," *Adv. Mat.*, vol. 15 (4), pp. 310-313, 2003.

[11] L. Hunter, "A comparison of muscle with artificial actuators," Proc. IEEE Solid-State Sensor and Actuator Workshop, Hilton Head Island, SC, USA, 1992, pp. 178-185.

[12] L. Bay, N. Mogensen, S. Skaarup, P. Sommer-Larsen, M. Jorgensen, and K. West, "Polypyrrole doped with alkyl benzenesulfonates," *Macromol.*, vol. 35 (25), pp. 9345-9351, 2002.

[13] P. Murray, G. M. Spinks, G. G. Wallace, and R. P. Burford, "In-situ mechanical properties of tosylate doped (pTS) polypyrrole," *Synth. Met.*, vol. 84 (1-3), pp. 847-848, 1997.

[14] G. M. Spinks, L. Liu, G. G. Wallace, and D. Z. Zhou, "Strain response from polypyrrole actuators under load," *Adv. Funct. Mater.* , vol. 12 (6-7), pp. 437-440, 2002.

[15] P. Chiarelli, D. Derossi, A. Della Santa, and A. Mazzoldi, "Doping-Induced Volume Change in a Pi-Conjugated Conducting Polymer," *Polym. Gels Networks* vol. 2 (3-4), pp. 289-297, 1994.

[16] E. Jager, "On-chip microelectrodes for electrochemistry with moveable PPy bilayer actuators as working electrodes," *Sensors and Actuators B*, vol. 56 (1-2), pp. 73-78, 1999.

[17] E. Jager, "Microfabricating conjugated polymer actuators," *Science*, vol. 290 (24), pp. No1540-1545., 2000.

[18] E. W. H. Jager, O. Inganas, and I. Lundstrom, "Microrobots for micrometer-size objects in aqueous media: Potential tools for single-cell manipulation," *Science*, vol. 288 (5475), pp. 2335-2338, 2000.

[19] E. W. H. Jager, E. Smela, O. Inganas, and I. Lundstrom, "Polypyrrole microactuators," *Synth. Met.*, vol. 102 (1-3), pp. 1309-1310, 1999.

[20] E. Smela, "Microfabrication of ppy microactuators and other conjugated polymer devices," *J. Micromech. Microeng.*, vol. 9, pp. 1-18, 1999.

[21] E. Smela, "controlled folding of micrometer-sized structures," *Science*, vol. 268 (5218), pp. 1735-1738, 1995.

[22] E. Smela, M. Kallenbach, and J. Holdenried, "Electrochemically driven polypyrrole bilayers for moving and positioning bulk micromachined silicon plates," *J. Microelectromech. Syst.*, vol. 8 (4), pp. 373-383, 1999.

[23] E. Smela, "Conjugated polymer actuators for biomedical applications," *Adv. Mat.*, vol. 15 (6), pp. 481, 2003.

[24] J. M. Pernaut and J. R. Reynolds, "Use of conducting electroactive polymers for drug delivery and sensing of bioactive molecules. A redox chemistry approach," *J. Phys. Chem. B*, vol. 104 (17), pp. 4080-4090, 2000.

[25] S. Skaarup, N. Mogensen, L. Bay, and K. West, "Polypyrrole actuators for tremor suppression," Proc. SPIE 11th Annual International Symposium: Smart Structures and Materials, vol. 5051, San Diego, CA, USA, 2003, pp. 423-428.

[26] H. Xu, C. Wang, C. L. Wang, J. Zoval, and M. Madou, "Polymer actuator valves toward controlled drug delivery application," *Biosens. Bioelectron.* , vol. 21 (11), pp. 2094-2099, 2006.

[27] J. D. W. Madden, B. Schmid, M. Hechinger, S. R. Lafontaine, P. G. A. Madden, F. S. Hover, R. Kimball, and I. W. Hunter, "Application of polypyrrole actuators: Feasibility of variable camber foils," *IEEE Journal of Oceanic Engineering*, vol. 29 (3), pp. 738-749, 2004.

[28] M. K. Andrews, M. L. Jansen, G. Spinks, D. Zhou, and G. G. Wallace, "An integrated electrochemical sensor-actuator system," *Sensors and Actuators a-Physical*, vol. 114 (1), pp. 65-72, 2004.

[29] I. W. Hunter, http://bioinstrumentation.mit.edu/Projects/CP/AUV.aspx.

[30] Rajesh, S. S. Pandey, D. Kumar, W. Takashima, and K. Kaneto, "Electrochemomechanical deformation studies of [Fe(CN)6]3- ion doped conducting polypyrrole film," *Thin Solid Films*, vol. 467 (1-2), pp. 227-230, 2004.

[31] G. M. Spinks, D. Z. Zhou, L. Liu, and G. G. Wallace, "The amounts per cycle of polypyrrole electromechanical actuators," *Smart Mater. Struct.*, vol. 12 (3), pp. 468-472, 2003.

[32] A. Mazzoldi, "Actuative properties of polyaniline fibers under electrochemical stimulation," *Materials Science and Engineering C*, vol. 6 (1), pp. 65-72, 1998.

[33] B. H. Qi, W. Lu, and B. R. Mattes, "Strain and energy efficiency of polyaniline fiber electrochemical actuators in aqueous electrolytes," *J. Phys. Chem. B*, vol. 108 (20), pp. 6222-6227, 2004.

[34] Q. B. Pei and O. Inganas, "Conjugated Polymers and the Bending Cantilever Method - Electrical Muscles and Smart Devices," *Adv. Mat.*, vol. 4 (4), pp. 277-278, 1992.

[35] T. Otero, "Characterization of triple layers," Proc. Smart Structures and Materials, 2001, vol. 4329, San Diego, California USA, 2001, pp. 93-100.

[36] G. Alici, B. Mui, and C. Cook, "Bending modeling and its experimental verification for conducting polymer actuators dedicated to manipulation applications," *Sensors and Actuators a-Physical*, vol. 126 (2), pp. 396-404, 2006.

[37] G. Han and G. Shi, "High-response tri-layer electrochemical actuators based on conducting polymer films," *J. Electroanal. Chem.*, vol. 569 (2), pp. 169-174, 2004.

[38] A. Della Santa, A. Mazzoldi, C. Tonci, and D. De Rossi, "Passive mechanical properties of polypyrrole films: a continuum, poroelastic model," *Materials Science & Engineering C-Biomimetic Materials Sensors and Systems*, vol. 5 (2), pp. 101-109, 1997.

[39] M. Christophersen, B. Shapiro, and E. Smela, "Characterization and modeling of PPy bilayer microactuators - Part 1. Curvature," *Sens. Actuators, B*, vol. 115 (2), pp. 596-609, 2006.

[40] J. Madden, P. G. A. Madden, and I. W. Hunter, "Polypyrrole actuators: modeling and performance," Proc. Smart Mater. Struct. , vol. 4329, San Diego, CA, 2001, pp. 72-83.

[41] A. Della Santa, "Characterization and modeling of a conducting polymer muscle-like linear actuator," *Smart Mater. Struct.* , vol. 6 (1), pp. 23-34, 1997.

[42] J. L. Bredas and R. Silbey, *Conjugated Polymers*, MA, USA, Kluwer Academic Publishers, 1991.

[43] P. Y. Bruice, *Organic Chemistry*, New Jersey, USA, Prentice-Hall Inc., 1998.
[44] R. Kaner, "Plastics that conduct electricity," *Sci. Amer.*, Feb, pp. 60-65, 1988.

[45] A. J. Heeger, "Semiconducting and metallic polymers: The fourth generation of polymeric materials," *J. Phys. Chem. B*, vol. 105 (36), pp. 8475-8491, 2001.

[46] W. Barford, *The International Series of Monographs on Physics*, New York, USA, Oxford University Press Inc., 2005.

[47] A. Pron, "Processible conjugated polymers: from organic semiconductors to organic metals and superconductors," *Prog. Polm. Sci.*, vol. 27 (1), pp. 135-190, 2002.

[48] W. P. Su, J. R. Schrieffer, and A. J. Heeger, "Soliton Excitations in Polyacetylene," *Phys. Rev. B*, vol. 22 (4), pp. 2099-2111, 1980.

[49] A. J. Heeger, S. Kivelson, J. R. Schrieffer, and W. P. Su, "Solitons in Conducting Polymers," *Reviews of Modern Physics*, vol. 60 (3), pp. 781-850, 1988.
[50] B. G. Streetman and S. Banerjee, *Solid State Electronic Devices*, 5th ed, Upper Saddle River, Prentice-Hall, 2000.

[51] D. Blackwood and M. Josowicz, "Work Function and Spectroscopic Studies of Interactions between Conducting Polymers and Organic Vapors," *J. Phys. Chem.* , vol. 95 (1), pp. 493-502, 1991.

[52] R. Yang, W. H. Smyrl, D. F. Evans, and W. A. Hendrickson, "Evolution of Polypyrrole Band-Structure - a Scanning Tunneling Spectroscopy Study," *J. Phys. Chem.* , vol. 96 (3), pp. 1428-1430, 1992.

[53] W. P. Su, J. R. Schrieffer, and A. J. Heeger, "Solitons in Polyacetylene," *Phys. Rev. Lett.*, vol. 42 (25), pp. 1698-1701, 1979.

[54] R. G. Davidson and T. G. Turner, "An Ir Spectroscopic Study of the Electrochemical Reduction of Polypyrrole Doped with Dodecyl-Sulfate Anion," *Synth. Met.*, vol. 72 (2), pp. 121-128, 1995.

[55] J. C. Scott, P. Pfluger, M. Krounbi, and G. B. Street, "Electron-spin-resonance studies of pyrrole polymers: Evidence for bipolarons," *Phys. Rev. Lett.*, vol. 28 (4), pp. 2140-2145, 1983.

[56] G. Zotti and G. Schiavon, "Spin and Spinless Conductivity in Polypyrrole. Evidence for Mixed-Valence Conduction," *Chem. Mater.*, vol. 3 (1), pp. 62-65, 1991.

[57] J. L. Bredas, J. C. Scott, K. Yakushi, and G. B. Street, "Polarons and bipolarons in polypyrrole: Evolution of the band structure and optical spectrum upon doping," *Phys. Rev. B*, vol. 30 (2), pp. 1023-1025, 1984.

[58] J. F. Kaufman and N. Colaneri, "Evolution of polaron states into bipolarons in polypyrrole," *Phys. Rev. Lett.*, vol. 53 (10), pp. 1005-1008, 1984.

[59] T. A. Skotheim, *Handbook of Conducting Polymers*, vol. 2, New York, USA, Marcel Dekker Inc., 1986.

[60] E. Smela and N. Gadegaard, "Volume changes in polypyrrole studied by atomic force microscopy," *J. Phys. Chem. B*, vol. 105 (39), pp. 9395-9405, 2001.

[61] E. Smela, "Surprising volume change in PPy(DBS): an atomic force microscopy study," *Adv. Mat.*, vol. 11 (11), pp. 953-957, 1999.

[62] Q. B. Pei and O. Inganas, "Conjugated Polymers as Smart Materials, Gas Sensors and Actuators Using Bending Beams," *Synth. Met.*, vol. 57 (1), pp. 3730-3735, 1993.

[63] L. Bay, T. Jacobsen, S. Skaarup, and K. West, "Mechanism of actuation in conducting polymers: Osmotic expansion," *J. Phys. Chem. B*, vol. 105 (36), pp. 8492-8497, 2001.

[64] X. W. Chen and O. Inganas, "Doping-Induced Volume Changes in Poly(3-Octylthiophene) Solids and Gels," *Synth. Met.*, vol. 74 (2), pp. 159-164, 1995.

[65] M. R. Gandhi, P. Murray, G. M. Spinks, and G. G. Wallace, "Mechanism of Electromechanical Actuation in Polypyrrole," *Synth. Met.*, vol. 73 (3), pp. 247-256, 1995.

[66] L. Lizarraga, E. M. Andrade, and F. V. Molina, "Swelling and volume changes of polyaniline upon redox switching," *J. Electroanal. Chem.*, vol. 561 (1-2), pp. 127-135, 2004.

[67] M. Pyo and C. H. Kwak, "In situ scanning tunneling microscopy study on volume change of polypyrrole/poly (styrene sulfonate)," *Synth. Met.*, vol. 150 (2), pp. 133-137, 2005.

[68] K. Kaneto, "Soft actuators based on conducting polymers," *Electrochemistry*, vol. 71 (9), pp. 804-808, 2003.

[69] K. Kaneto, "Artificial muscle: electromechanical actuators using polyaniline films," *Synth. Met.*, vol. 71 (1-3), pp. 2211-2212, 1995.

[70] Y. Velmurugu and S. Skaarup, "Ion and solvent transport in polypyrrole: Experimental test of osmotic model," *Ionics*, vol. 11 (5-6), pp. 370-374, 2005.

[71] T. Otero, H. Grande, and J. Rodriguez, "A new model for electrochemical oxidation of polypyrrole under conformation relaxation control," *J. Electroanal. Chem.*, vol. 394 (pp. 211-216, 1995.

[72] T. Otero, H. Grande, and J. Rodriguez, "Reinterpretation of polypyrrole electrochemistry after consideration of conformational relaxation processes," *J. Phys. Chem. B*, vol. 101 (19), pp. 3688-3697, 1997.

[73] K. West, L. Bay, M. M. Nielsen, Y. Velmurugu, and S. Skaarup, "Electronic Conductivity of Polypyrrole-Dodecyl Benzene Sulfonate Complexes," *J. Phys. Chem.* , vol. 108 (39), pp. 15001-15008, 2004.

[74] K. Crowley and J. Cassidy, "In situ resonance Raman spectroelectrochemistry of polypyrrole doped with dodecylbenzenesulfonate," *J. Electroanal. Chem.*, vol. 547 (1), pp. 75-82, 2003.

[75] Q. Pei and O. Inganas, "Electrochemical applications of the bending beam method: a novel way to study ion transport in electroactive polymers," *Solid State Ionics*, vol. 60 (1-3), pp. 161-166, 1993.

[76] Y. J. Qiu and J. R. Reynolds, "Dopant Anion Controlled Ion-Transport Behavior of Polypyrrole," *Polym. Eng. Sci.*, vol. 31 (6), pp. 417-421, 1991.

[77] C. Baker, Y. J. Qiu, and J. Reynolds, "Electrochemically induced charge and mass transport in polypyrrole/poly(styrenesulfonate) molecular composites," *J. Phys. Chem.*, vol. 95, pp. 4446-4452, 1991.

[78] Q. B. Pei and O. Inganas, "Electrochemical Applications of the Bending Beam Method .2. Electroshrinking and Slow Relaxation in Polypyrrole," *J. Phys. Chem.* , vol. 97 (22), pp. 6034-6041, 1993.

[79] S. Skaarup, L. Bay, K. Vidanapathirana, S. Thybo, P. Tofte, and K. West, "Simultaneous anion and cation mobility in polypyrrole," *Solid State Ionics*, vol. 159 (1-2), pp. 143-147, 2003.

[80] H. Ge and G. G. Wallace, "Ion-Exchange Properties of Polypyrrole," *Reactive Polymers*, vol. 18 (2), pp. 133-140, 1992.

[81] X. M. Ren and P. G. Pickup, "Ion-Transport in Polypyrrole and a Polypyrrole Polyanion Composite," *J. Phys. Chem.* , vol. 97 (20), pp. 5356-5362, 1993.

[82] R. A. Khalkhali, W. E. Price, and G. G. Wallace, "Quartz crystal microbalance studies of the effect of solution temperature on the ion-exchange properties of polypyrrole conducting electroactive polymers," *React. Funct. Polym.* , vol. 56 (3), pp. 141-146, 2003.

[83] Q. J. Xie, S. Kuwabata, and H. Yoneyama, "EQCM studies on polypyrrole in aqueous solutions," *J. Electroanal. Chem.*, vol. 420 (1-2), pp. 219-225, 1997.

[84] K. M. Mangold, C. Weidlich, J. Schuster, and K. Juttner, "Ion exchange properties and selectivity of PSS in an electrochemically switchable PPy matrix," *J. Appl. Electrochem.* , vol. 35 (12), pp. 1293-1301, 2005.

[85] T. Otero, C. Santamaria, and R. K. Bunting, "Kinetic studies of polypyrrole electrogeneration in three solvents," *J. Electroanal. Chem.*, vol. 380 (1-2), pp. 291-294, 1995.

[86] X. W. Chen and O. Inganas, "Three-step redox in polythiophenes: Evidence from electrochemistry at an ultramicroelectrode," *J. Phys. Chem.* , vol. 100 (37), pp. 15202-15206, 1996.

[87] Y. Tezuka and K. Aoki, "Concentration profiles of conducting species in polypyrrole films in cyclic voltammetry by means of a diode array detector," *J. Electroanal. Chem.*, vol. 425 (1-2), pp. 167-172, 1997.

[88] H. Yang and J. Kwak, "Mass transport investigated with the electrochemical and electrogravimetric impedance techniques .1. Water transport in PPy/CuPTS films," *J. Phys. Chem. B*, vol. 101 (5), pp. 774-781, 1997.

[89] H. Yang and J. Kwak, "Mass transport investigated with the electrochemical and electrogravimetric impedance techniques .2. Anion and water transport in PMPy and PPy films," *J. Phys. Chem. B*, vol. 101 (23), pp. 4656-4661, 1997.

[90] J. J. L. Cascales and T. F. Otero, "Molecular dynamics simulations of the orientation and reorientational dynamics of water and polypyrrole rings as a function of the oxidation state of the polymer," *Macromol. Theory Simul.* , vol. 14 (1), pp. 40-48, 2005.

[91] W. T. Yap, R. A. Durst, E. A. Blubaugh, and D. D. Blubaugh, "Chronoamperometry of polymer-modified electrodes charge transport by diffusion and migration," *J. Electroanal. Chem.*, vol. 144 (1-2), pp. 69-75, 1983.

[92] R. Lange and K. Doblhofer, "The transient response of electrodes coated with membrane-type polymer films under conditions of diffusion and migration of the redox ions," *J. Electroanal. Chem.*, vol. 237 (1-2), pp. 13-26, 1987.

[93] C. D. Paulse and P. G. Pickup, "Chronoamperometry of polypyrrole: migration of counterions and effect of uncompensated solution resistance," *J. Phys. Chem.*, vol. 92 (1), pp. 7002-7006, 1988.

[94] P. G. Pickup and R. A. Osteryoung, "Charging and discharging rate studies of polypyrrole films in AlCl3: 1-methyl-(3-ethyl)-imidazolium chloride molten salts and in CH3CN," *J. Electroanal. Chem.*, vol. 195 (2), pp. 271-88, 1985.

[95] F. Miomandre, M. N. Bussac, E. Vieil, and L. Zuppiroli, "Monte-Carlo simulation of linear sweep voltammograms during redox switching of conducting polymers," *Electrochim. Acta*, vol. 44 (12), pp. 2019-2024, 1999.

[96] J. C. Lacroix, K. Fraoua, and P. C. Lacaze, "Moving front phenomena in the switching of conductive polymers," *J. Electroanal. Chem.*, vol. 444 (1), pp. 83-93, 1998.

[97] P. G. A. Madden, J. D. W. Madden, P. A. Anquetil, N. A. Vandesteeg, and I. W. Hunter, "The relation of conducting polymer actuator material properties to performance," *IEEE Journal of Oceanic Engineering*, vol. 29 (3), pp. 696-705, 2004.

[98] Y. Osada and D. De Rossi, *Polymer Sensors and Actuators*, New York, Springer, 2000.

[99] X. Z. Wang, E. Smela, and B. Shapiro, "Visualizing ion currents in conjugated polymers," *Adv. Mat.*, vol. 16 (18), pp. 1605-1609, 2004.

[100] Q. B. Pei and O. Inganas, "Electrochemical Applications of the Bending Beam Method .1. Mass-Transport and Volume Changes in Polypyrrole During Redox," *J. Phys. Chem.* , vol. 96 (25), pp. 10507-10514, 1992.

[101] T. Otero, H. Grande, and J. Rodriguez, "Role of conformational relaxation on the voltammetric behavior of polypyrrole. Experiments and mathematical model," *J. Phys. Chem. B*, vol. 101 (42), pp. 8525-8533, 1997.

[102] P. J. S. Foot, F. Mohammed, P. D. Calvert, and N. C. Billingham, "Diffusion in conducting polymers," *J. Phys. D: Appl. Phys.*, vol. 20 (11), pp. 1354-1360, 1987.

[103] D. A. Edwards, "Non-Fickian diffusion in thin polymer films," *Journal of Polymer Science Part B-Polymer Physics*, vol. 34 (5), pp. 981-997, 1996.

[104] N. E. Schlotter and P. Y. Furlan, "A Review of Small Molecule Diffusion in Polyolefins," *Polymer*, vol. 33 (16), pp. 3323-3342, 1992.

[105] N. L. Thomas, "A theory of case II diffusion," *Polymer*, vol. 23 (4), pp. 529-542, 1982.

[106] M. Ilg, B. Pfleiderer, K. Albert, W. Rapp, and E. Bayer, "Investigation of the Diffusion Process in Cross-Linked Polystyrenes by Means of NMR Imaging and Solid-State NMR-Spectroscopy," *Macromol.*, vol. 27 (10), pp. 2778-2783, 1994.

[107] M. Kalaji, L. Nyholm, and L. M. Peter, "A microelectrode study of the influence of pH and solution composition on the electrochemical behavior of polyaniline films," *J. Electroanal. Chem.*, vol. 313 (1-2), pp. 271-289, 1991.

[108] X. Wang, E. Smela, and B. Shapiro, "Understanding Ion Transport in Conjugated Polymers," Proc. SPIE 12th Annual International Symposium: Smart Structures and Materials, San Diego, California USA, 2005.

[109] C. Odin and M. Nechtschein, "Slow relaxation in conducting polymers," *Phys. Rev. Lett.*, vol. 67 (9), pp. 1114-1117, 1991.

[110] H. Mao and P. G. Pickup, "In situ measurement of the conductivity of polypyrrole and poly(1-methyl-3-(pyrrole-1-ylmethyl)pyridinium)+ as a function of potential by mediated voltammetry. Redox conduction or electronic conduction," *Journal of American Chemical Society*, vol. 112 (5), pp. 1776-1782, 1990.

[111] K. P. Vidanapathirana, M. A. Careem, S. Skaarup, and K. West, "Ion movement in polypyrrole/dodecylbenzenesulphonate films in aqueous and non-aqueous electrolytes," *Solid State Ionics*, vol. 154 (Sp. Iss), pp. 331-335, 2002.

[112] S. Shimoda and E. Smela, "The effect of ph on polymerization and volume change in ppy(DBS)," *Electrochim. Acta*, vol. 44 (2-3), pp. 219-238, 1998.

[113] H. Mao and P. G. Pickup, "Ion-Transport in a Polypyrrole-Based Ion-Exchange Polymer," *J. Phys. Chem.* , vol. 93 (17), pp. 6480-6485, 1989.

[114] S. Maw, E. Smela, K. Yoshida, P. Sommer-Larsen, and R. B. Stein, "The effects of varying deposition current density on bending behavior in PPy(DBS)-actuated bending beams," *Sensors and Actuators A-Physical*, vol. 89 (3), pp. 175-184, 2001.

[115] M. Christophersen and E. Smela, "Polypyrrole/gold bilayer microactuators: response time and temperature effects," Proc. SPIE 13th Annual Int'l. Symposium on Smart Structures and Materials, EAPAD, vol. 6168, San Diego, CA, 2006.

[116] K. Neoh, "Structure and degradation behavior of polypyrrole doped with sulfonate anions of different sizes subjected to undoping -redoping cycles," *Chem. Mat.*, vol. 8 (1), pp. 167-172, 1996.

[117] S. Skaarup, K. West, L. Gunaratne, K. P. Vidanapathirana, and M. A. Careem, "Determination of ionic carriers in polypyrrole," *Solid State Ionics*, vol. 136 (Sp. Iss), pp. 577-582, 2000.

[118] W. Lu, "Use of ionic liquids for pi-conjugated polymer electrochemical devices," *Science*, vol. 297 (5583), pp. 983-987, 2002.

[119] A. Della Santa, D. DeRossi, and A. Mazzoldi, "Characterization and modeling of a conducting polymer muscle-like linear actuator," *Smart Materials & Structures*, vol. 6 (1), pp. 23-34, 1997.

[120] X. Lin, J. Li, E. Smela, and S. Yip, "Polaron-induced conformation change in single polypyrrole chain: an intrinsic actuation mechanism," *Int. J. Quant. Chem.*, vol. 102 (5), pp. 980-985, 2005.

[121] T. F. Otero and I. Boyano, "Comparative study of conducting polymers by the ESCR model," *J. Phys. Chem. B*, vol. 107 (28), pp. 6730-6738, 2003.

[122] T. F. Otero, H. Grande, and J. Rodriguez, "A conformational relaxation approach to polypyrrole voltammetry," *Synth. Met.*, vol. 85 (1-3), pp. 1077-1078, 1997.

[123] K. Naoi, Y. Oura, M. Maeda, and S. Nakamura, "Electrochemistry of surfactant-doped polypyrrole film (I): formation of columnar structure by electropolymerization," *J. Electrochem. Soc.* , vol. 142 (2), pp. 417-22, 1995.

[124] E. W. H. Jager, E. Smela, and O. Inganas, "Microfabricating conjugated polymer actuators," *Science*, vol. 290 (5496), pp. 1540-1545, 2000.

[125] H. Xu, V. V. Konovalov, C. I. Contescu, S. A. Jaffe, and M. Madou, "Water trans port in a non-aqueous, polypyrrole electrochemical cell," *Sens. Actuators, B*, vol. 114 (1), pp. 248-253, 2006.

[126] V. Syritski, K. Idla, and A. Opik, "Synthesis and redox behavior of PEDOT/PSS and PPy/DBS structures," *Synth. Met.*, vol. 144 (3), pp. 235-239, 2004.

[127] W. Wernet, M. Monkenbusch, and G. Wegner, "A new series of conducting polymers with layered structure: Polypyrrole n-alkylsulfates and n-alkylsulfonates," *Makromol. Chem., Rapid Commun.*, vol. 5 (1), pp. 157, 1984.

[128] D. M. Collard and M. S. Stoakes, "Lamellar Conjugated Polymers by Electrochemical Polymerization of Heteroarene-Containing Surfactants - Potassium 3-(3-Alkylpyrrol-1-Yl)Propanesulfonates," *Chem. Mat.*, vol. 6 (6), pp. 850-857, 1994.

[129] K. Oldham and J. C. Myland, *Fundamentals of electrochemical science*, Academic Press, 1994.

[130] D. R. Lide, *CRC Handbook of Chemistry and Physics*, 85th ed, CRC press, 2004.

[131] Z. H. Cai and C. R. Martin, "Electrochemical investigations of electronically conductive polymers .6. Mechanism of the redox reactions for the electronically conductive form of polypyrrole," *J. Electroanal. Chem.*, vol. 300 (1-2), pp. 35-50, 1991.

[132] S. Govindjee and J. C. Simo, "Coupled Stress Diffusion - Case-II," *Journal of the Mechanics and Physics of Solids*, vol. 41 (5), pp. 863-887, 1993.

[133] A. S. Argon, R. E. Cohen, and A. C. Patel, "A mechanistic model of case II diffusion of a diluent into a glassy polymer," *Polymer*, vol. 40 (25), pp. 6991-7012, 1999.

[134] N. L. Thomas and A. H. Windle, "A Deformation Model for Case-II Diffusion," *Polymer*, vol. 21 (6), pp. 613-619, 1980.

Chapter 2 Aim of Current Study and Organization of this Dissertation

2.1 Aim of Current Study

As reviewed in the introduction, ion transport, which gives major contributions to volume change of conjugated polymer, is still far from well-understood yet. Without thorough knowledge of ion transport, it is very difficult to develop a model that can be used to predict performance of conjugated polymer actuators for various operational situations. Therefore, this dissertation focuses on ion transport in conjugated polymers.

A central question this dissertation aims to answer is whether migration is or is not a driving mechanism for ion transport in conjugated polymers. Without answering this question, it is impossible to give correct predictions on ion transport speed and ion concentration profiles in conjugated polymers, which also makes it impossible to predict dynamic behavior of conjugated polymer actuators. Another topic of this dissertation is to explore diffusion process of ion transport in conjugated polymers. Whether diffusion is Fickian or non-Fickian need to be clarified. The third topic of this dissertation is to find out whether ions ingress is identical to ions egress. This is an important question because actuators use both ion egress and ion ingress to complete a work cycle. Therefore, both moving directions of conjugated polymer actuators need to be predicted. The fourth topic of this dissertation is to correlate ion concentration with electronic charge and volume change, which will help choosing a

good control parameter for actuation. The last topic of the dissertation is to develop a model that can correctly predict ion concentration in conjugated polymers for a various experimental situations.

2.2 Organization

Chapter 1 of the dissertation reviews the necessary background information to understand the rest of the dissertation. Chapter 2, the current chapter, explains the scope and organization of this dissertation. The main body of this dissertation, Chapter 3, Chapter 4, and Chapter 5, consists of three articles, summarizing important research results. The three articles include:

- X. Z. Wang, E. Smela, and B. Shapiro, "Visualizing ion currents in conjugated polymers," *Adv. Mat.*, vol. 16 (18), pp. 1605-1609, 2004. This article reports the preliminary experimental results and modeling work of this dissertation. I designed the experiments, collected all the experimental data, conducted all the simulation results, and prepared the preliminary draft.

- X. Z. Wang and E. Smela, "Ion Transport in Conjugated Polymers: Part 1. Experimental Studies on PPy(DBS)". This article is a detailed report of experimental work of this dissertation. Experimental exploration on migration, diffusion, break-in phenomena, ion ingress/egress, and volume change of conjugated polymers are reported. I collected all the experimental data and finished the draft together with Dr. Smela. Before submission, the text in the supplementary materials needs to be finalized.

- X. Z. Wang, B. Shapiro, and E. Smela, "Ion Transport in Conjugated Polymers: Part 2. Modeling and Simulation Results". The last paper reports the more advanced modeling work and simulation results for ion transport in conjugated polymers. Both 1D and 2D models are presented as well as simulation results. The 1D model is also used to give predictions on various experimental situations including electrolyte concentration, polymer anisotropy, and anion transport. I worked on model development from the very beginning of this project, solved several modeling issues, initiated a large part of the simulation cases, collected all the simulation results and took a major role in writing the draft with Dr. Smela and Dr. Shapiro. The paper has been drafted except the supplementary materials. Another on-going effort is to improve the interpretation of results of certain cases.

Chapter 6 summarizes the scientific contributions of this dissertation. Chapter 7 lists further development of this project. The last part of this dissertation is a section of supplementary materials, listing additional experimental results and simulation results that are not included in the body of these three articles.

Chapter 3 Visualizing Ion Currents in Conjugated Polymers[1]

3.1 Introduction

In numerous technologically important materials, electrochemical reactions are accompanied by mass transport of charged particles. For example, ion ingress and egress during electrochemical oxidation and reduction of conjugated polymers is the basis of a broad range of devices from electrochromic displays to batteries, chemical sensors, and actuators.[1] The direct measurement and visualization of ion transport would therefore be instrumental in formulating and validating physics-based models of such electrochemical reactions.

In this paper we report a new technique for the study of ion transport in materials that are electrochromic, and show initial results obtained by applying the method to polypyrrole doped with dodecylbenzenesulfonate, PPy(DBS), a conjugated polymer that is starting to find commercial applications in biomedical micro-actuators.[2] We introduce an experiment that makes electron transport fast compared with ion transport, allowing the ionic current to be characterized independently of the electronic current, and we present a first-cut model. These experimental and modeling results are the first from an ongoing research effort; the aim of this particular study was to elucidate the roles played by ion drift and diffusion in the reduction reaction.

---

[1] Originally published as:

X. Z. Wang, E. Smela, and B. Shapiro, "Visualizing ion currents in conjugated polymers," *Adv. Mat.*, vol. 16 (18), pp. 1605-1609, 2004.

Previous studies have shed enough light on the oxidation and reduction (redox) processes and the associated volume change in conjugated polymers that we understand the basic mechanisms.[3-6] Yet despite the numerous laboratory demonstration actuators that have been reported,[7,8] we do not yet have predictive models for actuator behavior. Without determining the constitutive equations governing the volume change, it will be impossible to design materials with non-incrementally increased speed, strain, and other performance metrics as required for particular applications.

When a sufficiently reducing potential is applied to PPy(DBS), electrons are transferred to the polymer backbone and cations enter the material in response to the electric field.[9] The ions, which are typically solvated, move between the chains through a combination of drift and diffusion. This mass insertion is responsible for the volume increase that is exploited in actuators. Space between the polymer chains must be created in order for the ions to enter, so the ion current depends on chain movements,[10] as well as on the degree of polymer solvation, the ion size, ion-polymer interactions, etc. Diffusion in conjugated polymers is therefore not Fickian.[11,12]

The discussion in the literature has focused on whether a diffusion model or a migration (drift) model is more appropriate to describe charge transport in conjugated polymers, and different authors have seen evidence for each. This is because in actual fact, electron and ion currents have *both* diffusion and migration terms. Which one is dominant depends on the magnitude of the applied potential.

Results from a first-cut model that includes both diffusion and drift are presented below. The first equation in the model is standard and describes the conservation of species:

$$\frac{\partial C_i}{\partial t} = -\nabla \bullet \vec{J}_i \qquad (4)$$

where C_i is the concentration of *i* (mol/cm^3) and J_i is the flux of species *i* (mol/sec-cm^2). This equation is exact: it just counts molecules. The flux J_i must next be quantified in terms of the physical conditions. Accepted models are given by $\vec{J}_i^{\,diff} = -D_i \nabla C_i$ for the diffusion component, where D_i is the diffusion coefficient (cm^2/sec), and $\vec{J}_i^{\,drift} = z_i \mu_i C_i \vec{E}$ for the drift component, where z_i is the charge, μ_i is the mobility (cm^2/V-sec), and $\vec{E}$ is the electric field.[13,14] Note that these two equations contain a number of assumptions[14,15]. We ignore convection since this is not present in the polymer and is negligible in an unstirred solution. This results in:

$$\frac{\partial C_i}{\partial t} = -\nabla \bullet \vec{J}_i = -\nabla \bullet \left(- D_i \nabla C_i - z_i \mu_i C_i \nabla \phi \right), \qquad (5)$$

where we have expressed the electric field as the gradient of the electric potential, ϕ: $\vec{E} = -\nabla \phi$. If the Einstein relation,[14] $D/\mu = kT/q = RT/F$, is employed, which may or may not be true for conjugated polymers, then equation (5) reduces to the familiar Nernst-Planck equation.[13] Equation (5) can be used for both ions and electrons. Finally, Maxwell's equations give the potential in terms of the net charge density Q:

$$\varepsilon_0 \nabla (\varepsilon \nabla \phi) = Q = C_i - n \,. \qquad (6)$$

Here n is the electronic charge, ε_o is the permittivity of a vacuum, and ε is the dielectric constant of the conjugated polymer.

There has also been a discussion in the literature about whether the speed of the redox reaction is limited by electron transport or ion transport. However, the rate limiting step depends on the experiment. Unfortunately, the electronic and ionic components of the current are difficult to disentangle in most experiments. As a result, the literature reports values for an "apparent diffusion coefficient" whose meaning is not clearly defined, but that seems to include both diffusion and drift components of both electron and ion transport. Reported apparent diffusion coefficients vary over 13 orders of magnitude.[11]

Below we describe an experiment that allows ion transport parallel to the surface of the film to be characterized independently of the electronic current during redox. This work was inspired by that of Tezuka et al.[16,17] These authors established electrical contact to a polypyrrole (PPy) film along only one of its edges, and when an oxidizing potential was applied, they observed a phase front that traveled outward from the electrode. The phase front was detected by changes in the optical absorption of the PPy, which is electrochromic. (Oxidation introduces new electronic states into the band gap, causing the color of the polymer to change.) In that experiment, however, electron and ion transport rate limitations could not be definitively separated.

Lacroix et al. [18] presented a theoretical analysis of mass transport during redox that assumed ion transport could be described as a migration phenomenon, rather than a

diffusion phenomenon. This resulted in a moving front that separated the conducting and insulating states during switching. These authors also found that a moving front could result from an oxidation-level-dependent electron diffusion constant.

3.2 Experimental

The fabrication process for the devices was as follows. Over an oxidized silicon wafer, an adhesion layer of Cr (100 Å thick) was deposited by either electron beam evaporation or sputtering, followed immediately by a layer of Au (3000 Å thick) that served as the working electrode. A layer of PPy(DBS) was electrochemically deposited from an aqueous solution of 0.1 M NaDBS and 0.1 M pyrrole (pH 7) at a constant potential of 0.47 V (vs. Ag/AgCl) with an EcoChemie pgstat30 to a thickness of 0.3 μm, at which the color changes are very apparent. All thicknesses were measured by profilometery (Tencor Alphastep 500). A 2 μm thick layer of a photosensitive polymer (SU8-2000[1], MicroChem Corp.) was photolithographically patterned over the PPy into the shape of a rectangular stripe following the manufacturer's directions. The PPy that was not covered by SU8 was removed by dry etching in an oxygen plasma,[22] leaving a stripe of PPy covered by SU8 on the electrode surface.

All cycling experiments were performed under a nitrogen atmosphere to prevent oxygen doping. The electrochromic response was recorded with a digital camera (Nikon Coolpix 4500) connected to a camcorder (Sony DCR-TRV 330) from directly overhead through a microscope (Leica MZ125) onto digital tape. The images were

[1] SU8-2000 is an epoxy. The CAS number of its epoxy resin is 28906-96-9.

later processed using Studio DV to reduce the number of frames and Matlab to analyze the images.

3.3 Results

3.3.1 Experimental Results

Our experimental configuration is illustrated in Figure 11. (The figure is not to scale: the vertical axis is exaggerated for clarity.) A thin conjugated polymer film 0.3 μm thick, 300 μm wide, and 8 mm long is covered by a transparent ion-blocking layer that prevents ions from entering or exiting the film through the top surface, allowing ion transport only from the sides. This makes the path for ions to and from the center of this stripe (150 μm) 500 times longer than the path for electrons (0.3 μm), since electrons are able to enter and leave along the entire bottom surface. This configuration ensures that ion transport is the rate-limiting step in the reaction. (In addition, the mobility of electrons is believed to be orders of magnitude higher than that of ions.) Since the ion-blocking layer is transparent, the color change of the electrochromic film during redox can be visualized.

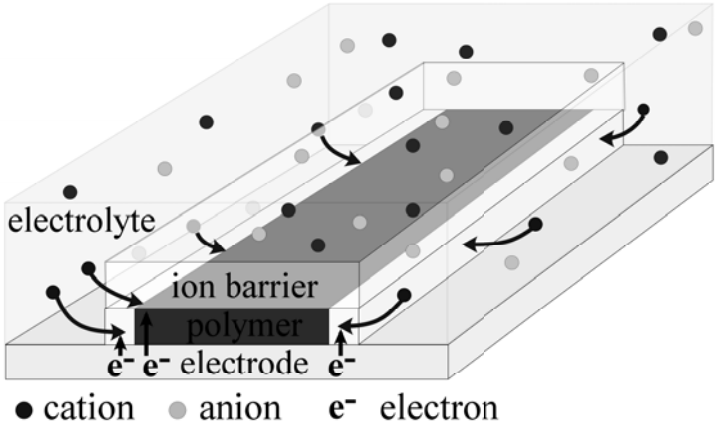

Figure 11. An experimental configuration that makes ion transport the rate-limiting step in PPy(DBS) (vertical dimensions exaggerated). A thin stripe of the electrochromic material is in contact with an electrode on its bottom side, and its top side is covered by an ion-blocking layer. During electrochemical reduction, cations are transported into the film, but they can only enter from the edges. Electrons therefore have a short path, ions a long one. The polymer cannot significantly change its oxidation level until charge compensating cations arrive. The change in oxidation level results in a color change.

In this paper, we focus only on the reduction reaction in PPy(DBS), which is a cation-transporting material since DBS is immobile in the polymer.[19-21] (To describe the behavior during oxidation, we must take into account conformational relaxation of the polymer chains,[10] which is beyond the scope of our first-cut model.) During reduction of PPy(DBS), the polymer starts in the fully oxidized, conducting state in which one DBS^- anion compensates each positive charge on the backbone.

The PPy was electrochemically cycled in deoxygenated aqueous 0.1 M NaDBS by stepping the voltage between 0 and various negative potentials. For potentials more negative than -0.8 V vs. Ag/AgCl, we observed phase fronts that travelled from the outer edges of the stripe to the center. Figure 12a shows an overhead image of a film part-way through the reduction process under an applied potential of -1 V vs. Ag/AgCl. The center of the stripe is oxidized (dark red), and the outer edges are

reduced (transparent yellow). Between them is a broad phase boundary. Red, blue, and green channel intensities were measured along a cross-section of the stripe, schematically indicated by the dashed line in Figure 12a; all three channels gave essentially the same signal, with red having the largest intensity variation, so the red channel was used for tracking the color change (Figure 12b). Thresholds were set, with intensities below the lower threshold marking the "inner boundary," inside which all the material was still fully oxidized, and intensities above the upper threshold marking the "outer boundary," outside which all of the material had been completely reduced. The positions of the boundaries were traced over time (Figure 12d) to give the phase front velocities.

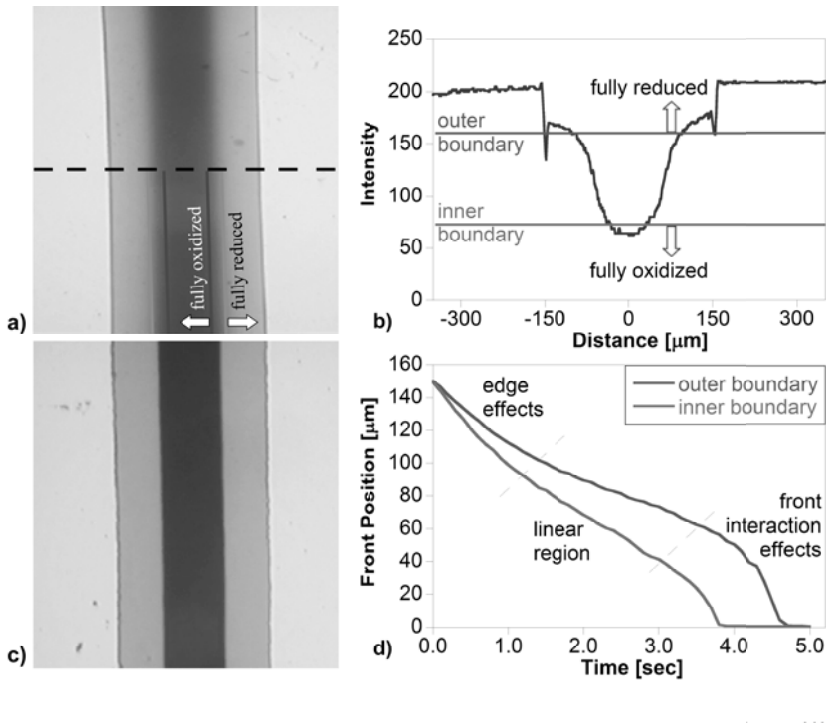

Figure 12. a) Overhead view of a film in the process of being reduced. The oxidized material is dark red, and reduced material is nearly transparent; there is a broad phase front between them. Inner and outer boundaries of the front are indicated schematically. b) The intensity of the red channel at the cross-section indicated by the dashed line in a). Thresholds for fully oxidized and reduced states are indicated schematically. The negative intensity spikes arise from the shadows at the edges of the polymer strip. c) During the first-ever reduction cycle, the phase boundary is very sharp, and the front velocity very slow. d) The position of the phase boundaries vs. time, 0 μm being the center of the stripe and 150 μm the edge. The slopes used to calculate the phase front velocities of the inner and outer boundaries were taken from the linear regions.

For reduction potentials smaller than approximately –0.8 V, there were no clearly visible phase boundaries (after the first reduction scan); instead, the film gradually lightened (see cross-section intensity profiles in Figure 14a). This is consistent with an interpretation that the diffusion component of the ion current is larger than the drift component in this regime.

For larger reduction potentials, we always observed phase fronts. After the front had progressed some distance into the film, both inner and outer boundaries moved with constant velocity (Figure 12d). The velocities of the boundaries are plotted as a function of applied potential in Figure 13. Between -0.8 and –1.6 V vs. Ag/AgCl the velocity was proportional to the voltage, as would be expected for migration: $v = \mu E$.[14] In this voltage range, therefore, migration plays the dominant role in ion transport.

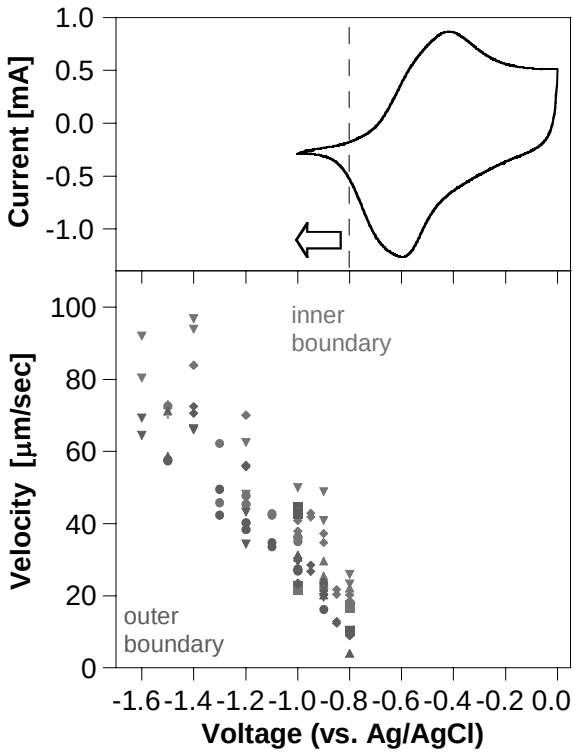

Figure 13. (Upper) The cyclic voltammogram of an *uncovered* PPy(DBS) film shows, approximately, the applied potentials relative to the redox peaks. (Lower) Velocity vs. applied potential. Different symbol shapes correspond to different samples, and repeated symbols indicate duplicate runs on the same sample. Above –0.8 V, no phase boundaries were observed, and below –1.6 V, the velocity saturated at ~70 μm/sec.

The transition region between oxidized and reduced states (the distance between inner and outer boundaries, or the front width) broadened over time (Figure 12d). Our hypothesis is that the broadening is due to diffusion, but additional experiments are required to confirm this. As the fronts from either side of the stripe approached each other, they started to interact and move faster.

At potentials more negative than –1.6 V, the velocity did not increase any further, but remained constant at approximately 70 μm/sec. The speed may be limited by diffusion in the electrolyte, or possibly by electron transport; further work is necessary to determine the cause.

During the first-ever reduction of the film, the phase boundary was very sharp (Figure 12c), and it stayed sharp from the outer edge right to the center. Moving fronts were seen for reducing potentials as small as –0.7 V, at which ion transport is primarily diffusion-driven. This is a clear demonstration that the diffusion process is not Fickian, since in the film's as-deposited state, the polymer chains are exceptionally compactly packed,[9,10] so the ion diffusion coefficient and mobility are very low. This is a clear validation of the finding in the Lacroix model [18] that an oxidation-level dependent diffusion coefficient can give rise to a phase front. The velocity of the front was 20-30 times slower during the first scan than during subsequent reductions.

3.3.2 Simulation Results

Our simulations of the ion transport were based on equations (5) and (6). The equations were solved in only a single spatial dimension (left-right in Figure 12). Ion

transport was assumed to be much slower than electron transport due to the design of the experiment, so equation (5) for electrons was discarded. Instead, we assumed a fixed electron density, $n(x,t) = n_o$. The ion diffusion coefficient was assumed to be constant. The resulting nonlinear partial differential equations were solved using the software FEMLAB. The simulation results are compared with experimental red-channel intensity data in Figure 14.

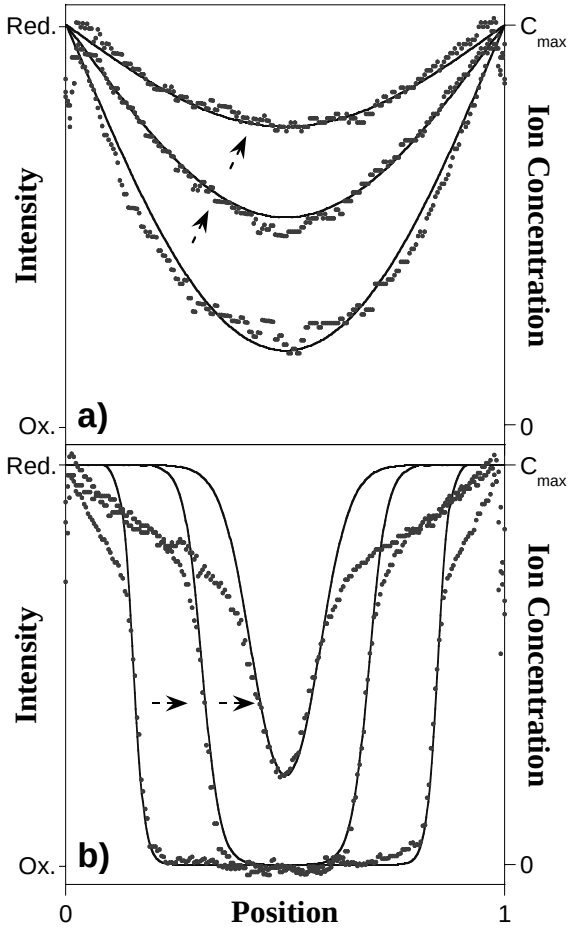

Figure 14. Experimental data (red points) vs. modeling results for ion concentration (blue line). The edges of the film are positions 0 and 1. The intensity minimum is for the fully oxidized state, and the maximum is for the fully reduced state. a) Applied potential = –0.7 V (vs. Ag/AgCl); data at 30, 60, and 90 seconds. Modeling curves are *not* equally spaced in time. b) Applied potential = –1.5 V; data at 0.6, 1.5, and 2.4 seconds (0.9 seconds apart). The modeling curves are again not equally spaced in time.

This simple simulation predicted the existence of phase fronts when drift dominates the ion current, and it did a remarkably good job of capturing the shapes of the intensity profiles for both low and high diffusion. However, it did not correctly predict the front velocities. In addition, the diffusion-like behavior behind the leading edge of the phase front was not captured. The assumption of a fixed electron density did not take into account the important fact that additional electrons are transferred to

the polymer once charge neutrality is re-established locally by the arrival of the cation front. Also, the assumption that the diffusion constant is fixed, rather than a function of the oxidation level, is not valid, as shown by the striking differences in shape and velocity during the first-ever reduction. The next stage in our modeling will take these effects into account.

While the experimental and modeling curves in Figure 14 are strikingly similar, it is important to keep in mind that the experimental curves are color intensity profiles. In order to convert the intensities in the images into ion concentrations (the quantity in our model), the Faradic charge consumed by the PPy needs to be determined, and these measurements are under way. Once we know $\vec{E}$ in the film, we will extract the mobility from the data in Figure 13. Future studies will also more closely examine the diffusion terms in the model.

3.4 Conclusions

In conclusion, we have introduced a simple experimental tool that directly measures ion transport in electrochromic materials and have presented preliminary results on the reduction process in PPy(DBS). We have shown that there are different rate-limiting processes at different potentials, that migration plays a critical role in ion transport, and that a simple model can account for much of the behavior. Initial physics-based modeling has correctly predicted the existence of the phase fronts and captured much of their shapes. Future experimental work will include quantification of the coefficients in the equations as well as studies of the oxidation process and

correlations between ion transport and volume change. The next stages in modeling will take additional physics into account.

3.5 Acknowledgements

This material is based upon work supported in part by the U. S. Army Research Laboratory and the U. S. Army Research Office under contract number DAAD190310085. We would also like to acknowledge the U. S. Army Research Laboratory for use of equipment while completing this research and funding through DuPont's Educational Aid Program (Young Professor Grant).

3.6 References

[1] P. Yam, *Sci. Amer.*, **1995**, (July), 74.

[2] E. Smela, *Adv. Mat.*, **2003**, *15 (6)*, 481.

[3] Q. Pei, O. Inganäs, *Sol. State Ion.*, **1993**, *60*, 161.

[4] M. R. Gandhi, P. Murray, G. M. Spinks, G. G. Wallace, *Synth. Met.*, **1995**, *73*, 247.

[5] P. Chiarelli, A. Della Santa, D. De Rossi, A. Mazzoldi, *J. Intell. Mater. Syst. Struct.*, **1995**, *6*, 32.

[6] T. F. Otero, H. Grande, J. Rodriguez, *J. Phys. Org. Chem.*, **1996**, *9*, 381.

[7] J.-M. Sansiñena, V. Olazábal, in *Electroactive Polymer (EAP) Actuators as Artificial Muscles: Reality, Potential, and Challenges* (Ed: Y. Bar-Cohen) SPIE Press, Bellingham, **2001**, p. 193.

[8] R. H. Baughman, *Synth. Met.*, **1996**, *78*, 339.

[9] E. Smela, N. Gadegaard, *Adv. Mat.*, **1999**, *11 (11)*, 953.

[10] T. F. Otero, I. Boyano, *J. Phys. Chem. B*, **2003**, *107 (28)*, 6730

[11] P. J. S. Foot, F. Mohammed, P. D. Calvert, N. C. Billingham, *J. Phys. D: Appl. Phys.*, **1987**, *20 (11)*, 1354.

[12] T. J. Alfrey, E. F. Gurnee, W. G. Lloyd, *J. Polym. Sci.*, **1966**, *C12***,** 249–61.

[13] A. J. Bard, L. R. Faulkner, *Electrochemical Methods: Fundamentals and Applications*, 2nd ed., John Wiley & Sons, Inc., New York, **2001**.

[14] B. G. Streetman, S. Banerjee, *Solid State Electronic Devices*, 5th ed., (Ed: N. J. Holonyak) Prentice-Hall, Upper Saddle River, **2000**.

[15] R. P. Feynman, R. B. Leighton, M. Sands, *The Feynman Lectures on Physics*, Addison-Wesley Publishing Company, **1964**.

[16] Y. Tezuka, S. Ohyama, T. Ishii, K. Aoki, *Bull. Chem. Soc. Jpn.*, **1991**, *64***,** 2045.

[17] Y. Tezuka, K. Aoki, H. Yajima, T. Ishii, *Journal of Electroanalytical Chemistry*, **1997**, *425***,** 167.

[18] J. C. Lacroix, K. Fraoua, P. C. Lacaze, *J. Electroanal. Chem.*, **1998**, *444 (1)***,** 83.

[19] M. A. De Paoli, R. C. D. Peres, S. Panero, B. Scrosati, *Electrochim. Acta*, **1992**, *37 (7)***,** 1173.

[20] T. Matencio, M.-A. De Paoli, R. C. D. Peres, R. M. Torresi, S. I. Cordoba de Torresi, *Synth. Met.*, **1995**, *72***,** 59.

[21] E. Smela, N. Gadegaard, *J. Phys. Chem. B*, **2001**, *105 (39)***,** 9395.

[22] E. Smela, *J. Micromech. Microeng.*, **1999**, *9***,** 1.

Chapter 4 Charge Transport in Conjugated Polymers: Part 1. Experimental Research of PPy(DBS)[1]

4.1 Introduction

Since conjugated polymer actuators were first demonstrated [1-4], a large variety of "proof of concept" devices have been fabricated. (For reviews, see [5-9].) However, improvement in device performance has been hampered by a lack of fundamental understanding of the underlying physics that occurs during electrochemical switching. Mathematical models to describe material behavior during actuation, i.e. the constitutive equations, have not yet been formulated and validated. As a result, rate-limiting processes have not been clearly identified and trade-offs between strain, stress, and speed have not been mapped.

The work presented in this series of papers is part of a longer-term effort to develop physics-based models of the coupled chemical, electrical, and mechanical processes that occur during reduction and oxidation (redox) of conjugated polymers (Figure 15). These models should ideally have no adjustable parameters and should account for the dominant physical effects, if not all the details. Such "white box" modeling [10] is not the same as curve-fitting (black-box modeling of phenomena).

[1] To be submitted as:
X. Z. Wang and E. Smela, "Charge Transport in Conjugated Polymers: Part 1. Experimental Research of PPy(DBS)".

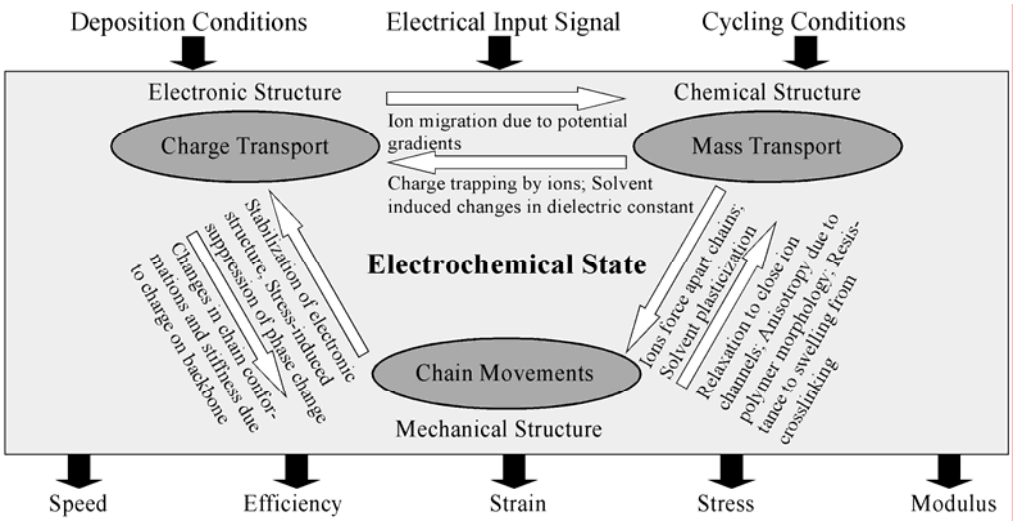

Figure 15. A given electrical input signal results in an electrochemical state with particular mechanical, chemical, and electrical properties, which in turn result in particular actuator metrics. Changing the oxidation level requires inter-related charge and mass transport, as well as polymer chain conformational changes; several of these interrelations are indicated. The final state also depends on the deposition and cycling conditions.

To build such models, experiments need to be designed in which only a single effect is dominant, so that it can be isolated and characterized without confounding and unknown contributions from the other effects. We chose to begin by characterizing charge transport, since that drives the other effects, and to focus particularly on ion transport, since that is directly responsible for actuation strain [11]. In our previous communication [12] we presented a device that ensured that ion transport was the rate-limiting step in the electrochemical reaction and which allowed us to track ion transport inside the film through electrochromic color changes. In this Part 1, complete experimental studies are presented on ion transport in polypyrrole doped with dodecylbenzenesulfonate, PPy(DBS). We report results from an extensive analysis of the reduction process, present new data on the oxidation process, and

supplement the electrochromic studies with film thickness profiles recorded during redox that reveal the relationship between charge transport and volume change.

We do not yet include studies of chain movement or solvent transport. These play very important roles during switching (Figure 15), as shown by Otero et al. [6, 13-25] and West et al. [26]. Otero et al. have contributed a large body of knowledge on chain conformational changes during redox, and combining the models for a more complete understanding of the switching behavior will be the focus of future work.

As noted above, in order to develop the constitutive equation for ion transport during redox, each of the terms needs to be identified and the form of the coefficients determined, without confounding influence from other processes that occur simultaneously. We have previously introduced a device configuration that ensures that ion transport is the rate-limiting step by making electron/hole transport comparatively fast, chain conformational changes constant, and solvent transport invisible[12, 27, 28]. The schematic diagram in Figure 16 illustrates this experimental approach. A long, narrow strip of a thin conjugated polymer film is sandwiched between an electrode on the bottom and a transparent ion-blocking layer on the top. When the polymer is switched, ions cannot enter or leave the polymer through the top or bottom, but only from the long edges. Holes (polarons and bipolarons), on the other hand, are able to enter and leave anywhere through the bottom electrode area. The distance that the ions must travel to get to the center of the strip is 500 times longer than the path for holes to reach the top surface. The

higher mobility of holes (orders of magnitude higher than that of ions), increases their speed relative to the ions even further.

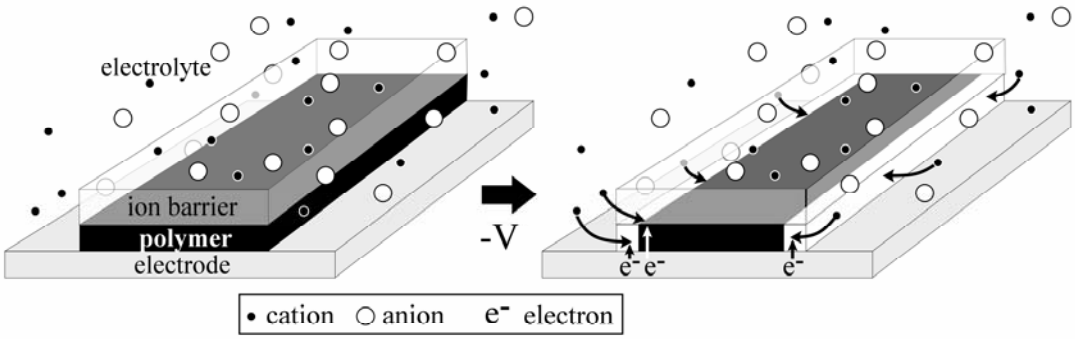

Figure 16. Device configuration to make ion transport the rate-limiting step during electrochemical switching of a conjugated polymer. The polymer is patterned into a long, narrow stripe over an electrode and covered on the top side with a transparent ion-blocking layer (vertical dimensions exaggerated for clarity). Ions enter and exit the polymer from the long edges. The color of the film varies with its oxidation level, which cannot change until charge-compensating ions arrive or leave.

Conjugated polymers are electrochromic, meaning that they change color with applied potential. (Oxidation introduces additional electronic states into the band gap, allowing absorption of light at lower energy [29, 30].) The ion barrier was made transparent to enable visualization of the colors underneath. The polymer film was kept thin so that changes in oxidation level could easily be observed (when PPy films on Au are thicker than approximately 1 μm, they appear black even in the reduced state). PPy changes from brown to light yellow upon reduction, but for a thin film on Au, the film appears red in the oxidized state and transparent in the reduced state.

This experiment was inspired by those of Tezuka et al.[31,32], who made electrical connection to one end of a strip of PPy(ClO_4), the face of which was exposed to the electrolyte. In that configuration, the path of the holes was long compared to that for

the ions. When the film, an anion-conductor, was switched from the reduced to the oxidized state, the oxidized state grew outward from the electrical connection at constant velocity [31]. There was a clear boundary between the two states, which could be observed by the color and was tracked using an array of photodiodes. Speeds were on the order of 1 mm/sec and increased exponentially with potential. Upon reduction, the film changed color simultaneously over the whole area [32], stopping at a doping level of ~13%, when the percolation threshold was crossed, leaving electrically disconnected islands of charge in the film. In these experiments, the speeds of hole and ion transport may have been comparable, so it is not clear which was the rate-limiting step. Similar experiments have also been reported by Inganäs et al. with poly(3,4-ethylenedioxythiophene), PEDOT [33], and poly(3-hexylthiophene), P3HT [34].

The polymer studied in this paper is PPy(DBS), a cation-transporting material in which DBS is immobile. This polymer was chosen as our model system because of our extensive prior work with it, and our view that it is important to understand one system well in order to build a good, predictive model based on the dominant physical effects. The PPy(DBS) films were cycled in a solution of NaDBS to ensure that charge compensation was essentially only by Na^+. (In NaDBS a small amount of OH^- may also be transported, but it does not contribute to volume change [35]. In solutions of NaCl, however, Cl^- transport also takes place [36] which *does* contribute to actuation strain.) When a sufficiently negative potential is applied to the polymer, electrons are added to the polymer backbones from the electrode. Since the negatively charged DBS is immobile, hydrated Na^+ co-ions enter the polymer to

maintain charge neutrality. (This process is described in more detail in the Discussion section below.)

The oxidation and reduction processes are not symmetric, since the oxidized state is electronically conducting while the reduced state is resistive; this affects the electric fields within the polymer. In addition, in the oxidized state the polymer matrix is more compact and contains less water, and the chain segments are straighter and stiffer, so ion mobility is significantly lower than in the reduced state (Figure 17) [37]. The reduced state matrix is swollen with ions and solvent, which disrupt hydrogen bonding and pi-pi stacking between chains.

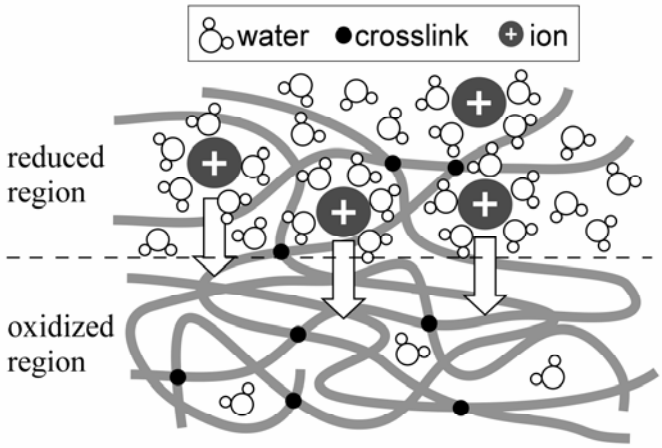

Figure 17. The polymer structure in the oxidized state of PPy(DBS) is more compact and contains less water.

4.2 Experimental Methods

4.2.1 Device Fabrication

The device used for in-plane ion transport studies is illustrated in Figure 16 and was fabricated using standard microfabrication techniques. The Au electrode was

deposited by either sputtering (ATC 1800, AJA International, 200 W, $5x10^{-3}$ Torr, 5 Å/sec) or thermal evaporation (Cooke, 80 A, $5x10^{-6}$ Torr, 5 Å/sec) to a thickness of 3000 Å over an adhesion layer of Cr 150 Å thick (3 Å/sec) onto 4" diameter oxidized silicon wafers. Film thicknesses were measured by mechanical profilometry (Dektak 3ST or Alphastep 500). The wafers were cleaved into pieces 1 cm x 3 cm.

PPy was deposited potentiostatically at 0.47 V (0.1 mA/cm^2) (Echochemie pgstat30) onto the Au-coated Si working electrode (WE) to a thickness of 300-400 nm. The deposition electrolyte contained 0.1 M pyrrole and 0.1 M NaDBS (Aldrich) in deionized (DI) water. Pyrrole (Aldrich) was stored at -40 °C and filtered through alumina (Aldrich) before use. A three-electrode cell was used with Ag/AgCl (BAS) as the reference electrode (RE) and porous carbon (VWR) as the counter electrode (CE) (3 x 2 x 0.5 cm^3). The WE and CE were parallel and separated by 3 cm.

The ion barrier material, SU8-2002 (MicroChem), a negative photoresist that is mainly made of epoxy, was spin-coated over the PPy to a thickness of 2 μm (1000 rpm, 30 sec). (Note that SU8 cannot be applied to PPy(DBS) films that have already been electrochemically cycled in NaDBS, since the resist dewets in this case.) The SU8 was pre-baked (65 ^oC for 1 min, then ramped at 300 °C/hr to 95 ^oC and baked for a further 1 min) and exposed under ultraviolet light (365 nm, 24 seconds) through a mask to form 300 μm wide, 8 mm long stripes. The SU8 was then post-baked (conditions the same as during prebake) and developed (MicroChem SU8 developer) for 2 min.

To pattern the PPy, it was etched by reactive ion etching (RIE) in an oxygen plasma (March Jupiter, 0.2 mTorr, 200 W, etch rate 300 nm/min). The SU8 served as a mask, and PPy was removed in the uncovered areas, leaving the PPy that remained under the SU8 with perpendicular edges. Etching usually produced a few star-shaped cracks in the SU8 at isolated points, particularly if high power and oxygen flow rates were used.

Cyclic voltammetry was also performed on PPy(DBS) films deposited on identical substrates after coating with SU8 and rinsing it off, without UV exposure, in SU8 developer to determine whether the redox reactions had been adversely affected by exposure to these substances. The cyclic voltamogramms were unaltered.

4.2.2 Electrochemical Cycling

Samples were placed horizontally in a flat-bottomed electrochemical cell (12.0 mm x 8.5 mm, similar to the one shown in [38]). Gold-plated screws, nuts, and washers were used to make electrical contact. Leads from the potentiostat were attached outside the electrolyte to the heads of the screws using alligator clips. The electrolyte was 8 mm deep over the sample.

Experiments were carried out in a glove box filled with argon gas to provide an oxygen-free environment (oxygen chemically dopes PPy and therefore interferes with the electrochemical reduction process). To reduce the amount of oxygen in the NaDBS electrolyte (0.1 M in DI water), argon gas was bubbled through it (1-2 psi) for 15 minutes. The RE and CE were the same as for PPy deposition.

Samples that delaminated during the experiment were discarded. There were two modes of delamination. In one, the PPy came off the substrate suddenly and entirely. In the other, the film delaminated in spots but adhered well elsewhere. The cause of the second mode appears to be accumulation of hydrogen gas in the film, which forms what appear to be bubbles. These circular areas remain dark red (oxidized) when a reducing potential is applied, while the rest of the film turns transparent. In thin PPy films, bubbles were observed only after many cycles, but in films > 1 μm thick, bubbles formed after only a few cycles. Bubbles first appeared during oxidation, typically at the center of the film but later spreading [28]. This hydrogen generation complicated data analysis, requiring a careful choice of a region of the image that avoided the bubbles.

4.2.3 Out-of-Plane Strain Measurement

Sample thickness was measured in situ with a Dektak 3ST mechanical profilometer using a 65 μm vertical range, a 1 mm horizontal scan length at 20 μm/sec, and a 5 mg stylus force. A sketch of the measurement is showed in Figure 18. Scans were performed before immersion in the electrolyte, after immersion, and during the first reduction scan. Thereafter, scans were taken in the oxidized state and in the reduced state for several cycles. Each steady-state height profile reported below represents an average of at least 6 repeated scans at the same nominal position. When bubbles showed up in the film under the stylus, the stylus was repositioned to an adjacent location where no bubbles were observed.

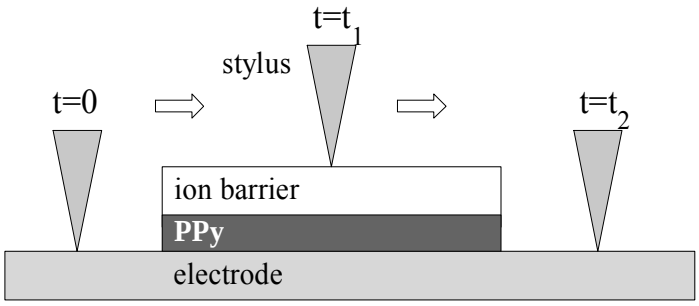

Figure 18. Thickness measurements by mechanical profilometry, performed immersed in electrolyte. The time t_2 to complete each trace was 50 seconds.

4.2.4 Phase Front Analysis

4.2.4.1 Data Collection

The samples were observed from overhead through a stereomicroscope (Leica MZ12.5) with a halogen light source (ACE1, Schott-Fostec LLC). Because of the mirror surface of the substrate, coaxial illumination was used. A digital camera (Nikon Coolpix 4500) mounted to the microscope transmitted a video signal to a digital camcorder (Sony DCR-TRV330) via an analog video cable to the video input port. Video was recorded on Hi8 digital tape at 30 fps.

The video was downloaded to a PC in DV format using video editing software (Studio, Ver. 8). Slower frame rates (down to 5 fps) were used for large files to reduce analysis time. The video was read using Matlab, and every frame saved to the hard disk in bitmap format.

4.2.4.2 Intensity Correction

The video signal taken from the digital camera was the one sent to its LCD screen. The camera therefore adjusted the intensity of the image in response to changing brightness of the scene, such as when the PPy changed from red to yellow. This shift

could not be prevented and had to be corrected. This was done based on the two Au regions on either side of the PPy stripe (Figure 19), the color of which did not change with applied potential (confirmed on substrates without PPy). The images were read into Matlab with RGB format with 8 bit depth (256 intensity levels). The images were corrected to bring the Au to a constant level by multiplying the intensity of each pixel by the normalized gold film intensity on the red channel: $I_{corrected} = I \times (I_{Au}/I_{Au\ final})$. An offset was not used.

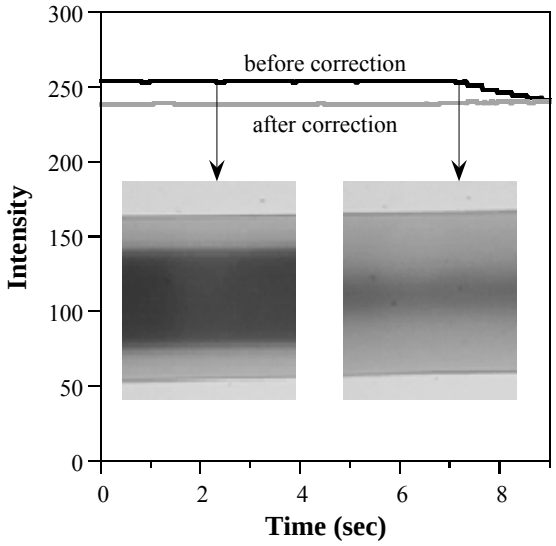

Figure 19. Red color intensity of the Au in the image as a function of time before and after correction. The inserted overhead-view photographs indicate the image at the times corresponding to the arrows.

4.2.4.3 Data Analysis

As reported previously [12] and as shown in Figure 20a, when the PPy was reduced, a phase front moved from the edges of the PPy strip to the center, broadening with time. The intensity of a line across this image in the red, green, and blue channels is shown in Figure 20b. The intensity increased on all three channels upon reduction,

but the change was largest on the red channel. Therefore, in later analysis only the red channel signal was used in order to reduce computation time. (This method of image analysis did not take into account the shift in the wavelength of the peaks associated with the polaron and bipolaron bands as a function of oxidation level [22]. We examine the correlation of charge and red channel intensity below. It should be noted that the camera represents the color of each pixel as a combination of red, green, and blue intensities, but this is not the same as what would be recorded at those frequencies in a spectrophotometer.) The difference in intensity between the fully reduced and oxidized states was approximately 100 levels on the red channel. The downward intensity spikes at either edge of the stripe were due to shadows.

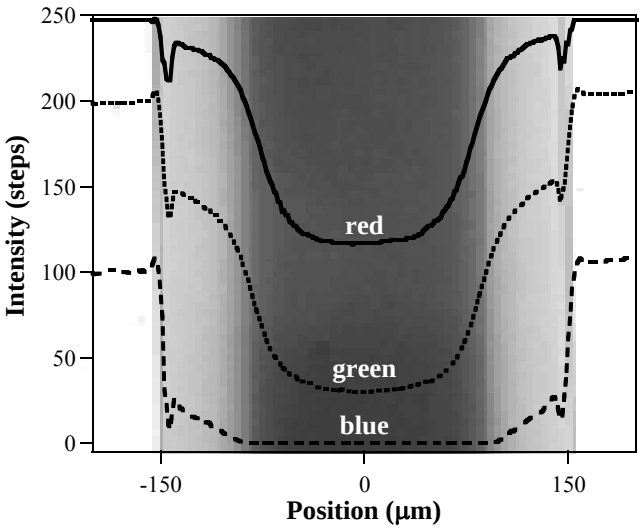

Figure 20. Overlay of an image of a partially reduced PPy(DBS) film under an SU8 ion barrier (-1 V vs. Ag/AgCl, 300 nm thick, t = 1.5 sec) and cross-section intensity profiles on the red, green, and blue channels.

Phase front positions were obtained by tracking intensity changes over the film width vs. time. The intensity of the oxidized state was used as a baseline. The intensity difference between fully oxidized and reduced states was arbitrarily divided into 20

levels, and the position of three of these levels was tracked, as shown in Figure 21a. In the analysis presented below, the 10^{th} level was tracked versus time to obtain phase front positions. Once phase front positions were obtained, two parameters, velocity and front width, were further extracted from the phase front positions. The velocity was determined by taking a linear fit to the center portion of the position-vs.-time curve (Figure 21b). To obtain the center portion, we disregarded data before phase fronts were formed, such as the data between 0 and 0.4 second in Figure 21b. A portion of the data at the beginning of reduction (typically 1**0%** of the reduction time) was discarded, such as between 0.5 second and 1 second. Also, data when phase fronts reached the center of the film (For example, data between 3.5 seconds and 4 seconds) were also disregarded, because two phase fronts started to interact. The left data were fitted by a straight line using least-square regression. Slope of this line was used for the velocity of the phase front. The width of the phase front was arbitrarily defined as the distance between the 5^{th} and 15^{th} levels.

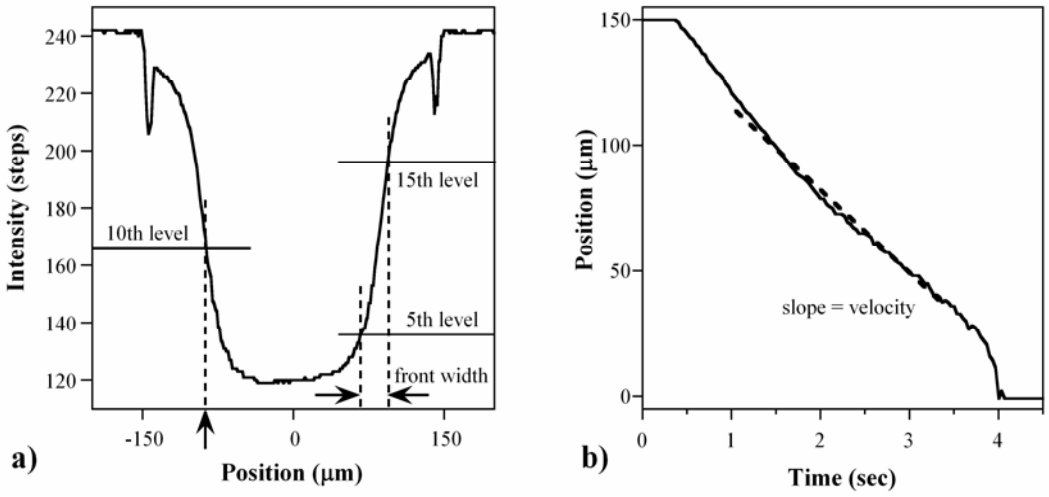

Figure 21. a) Illustration of the 10th normalized intensity level, used to determine the front velocity, and the 5th and 15th levels, used to determine the front width. b) Front position vs. time. The slope of the linear part of the curve was used to determine the velocity.

Two factors limit the spatial resolution of the data analysis: the number of pixels in the images and the resolution of the data read into Matlab, which determines the number of intensity levels. The camcorder created video with a resolution of 640x480 pixels. The phase fronts propagated along the direction of 480 pixels, and the sample covered approximately half of the picture, so approximately 200 pixels are used in tracking the front positions. Considering the sample width is 300 μm, the minimum spatial resolution is 1.5 μm. The second factor is the 256 intensity levels. If two pixels have the same intensity, the tracking program chooses one of them, but the real position could be the average of the two. Such cases occur when the phase front is close to the fully reduced area, where the intensity plateaus. Also, when the pixel does not have exactly the same intensity as the threshold, the program chooses the pixel with the closest intensity, and this occurs frequently. Therefore, the tracking method is only accurate to $\pm$ 1 pixel ($\pm$3 μm).

Errors of this magnitude are acceptable for tracking front position, since that changes from 0 to 150 μm, creating an uncertainty of 2%. However, these errors are large in front broadening analysis. For a front broadening rate of 5 pixels/sec, an increase by a factor of 1.5 from 4 to 6 pixels is within the noise.

4.2.5 Current Correction during Chronoamperometry

When using chronoamperometric currents (shown in Figure 22) to obtain consumed charges, the background current needs to be removed. The data in this figure were collected during reduction at -1.5 V, and the phase fronts reached the center at t = 2 seconds. The original current (dashed line) had a large residual component (indicated by the gray line) even after 10 seconds. This was subtracted to obtain a corrected current (heavy dashed line) and integrated to obtain an estimate of the charge consumed by the PPy (solid line). This method removed only parasitic currents, though, and not capacitive currents. (It should be noted that the propagating phase fronts complicated the data analysis because of the continuously changing potential profile over the film.)

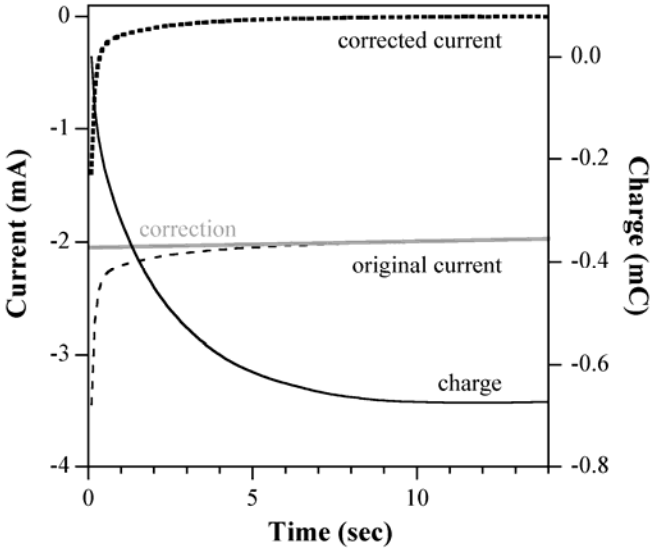

Figure 22. Method for correcting the current and integrating the charge.

4.3 Results

Section 4.3.1 begins with the phase front behavior during reduction, starting with the first reduction cycle and then describing the steady-state reduction behavior, focusing on the front velocity. The broadening of the front is examined next, followed by the effect of the initial oxidation potential. Section 4.3.2 describes the color changes that occur during the oxidation reaction. In section 4.3.3, the color changes are correlated with the charge consumed and the actuation strain.

4.3.1 Electrochemical Reduction

In these experiments, the potential was stepped from 0 V, unless otherwise noted, to various reducing potentials. The oxidizing potential had been held for at least 30 seconds, so the Na^+ cations encountered the same compacted matrix, in which the chains had undergone conformational relaxation to eliminate free volume. The work required to open the matrix was therefore essentially the same in every case,

eliminating the conformational state as a variable. Likewise, hole transport was not a factor in these experiments because of the relatively short hole path and high hole mobility compared to the cations. Referring to Figure 15, the experiments allowed us to probe mass transport into the polymer with minimal confounding effects from electron transport and chain movement. As is shown in section 4.3.1.4, when the initial state of the matrix is changed, the effects of chain movement are substantial.

4.3.1.1 First Reduction Step

It is well known that the first reduction scan of a conjugated polymer is anomalous, and that it can take several cycles to "break in" the polymer before it starts to show steady state behavior. This is due to a high degree of compaction of the chains (see e.g. [25] and references therein) and because a considerable amount of water enters the polymer during the first reduction scan that does not readily leave in subsequent scans [39, 40].

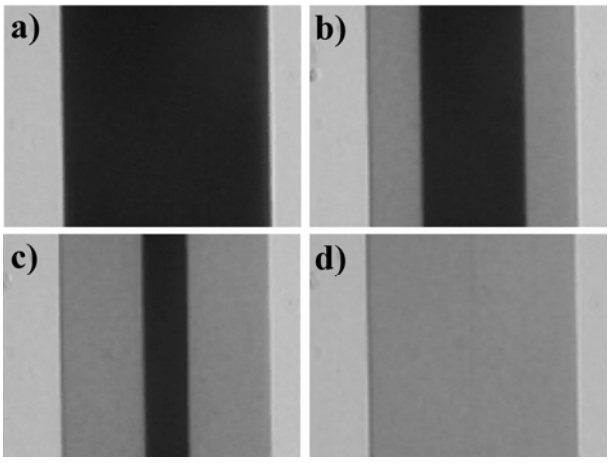

Figure 23. Phase front during the first reduction potential step from 0 to -1 V vs. Ag/AgCl at a) 0 seconds, b) 60 seconds, c) 120 seconds, and d) 180 seconds.

Overhead images of the PPy(DBS) stripes during the first reduction scan are shown at different times in Figure 23. Phase fronts traveled from both edges of the stripe to the center. The fronts stayed sharp and parallel to the edges, and the intensity profile showed nearly vertical steps (Figure 24). Phase front velocities were on the order of 1 μm/sec. This velocity was independent of the amount of time that the sample spent immersed in the electrolyte prior to electrochemical reduction: velocities were the same for samples immersed for 10 minutes and 24 hours.

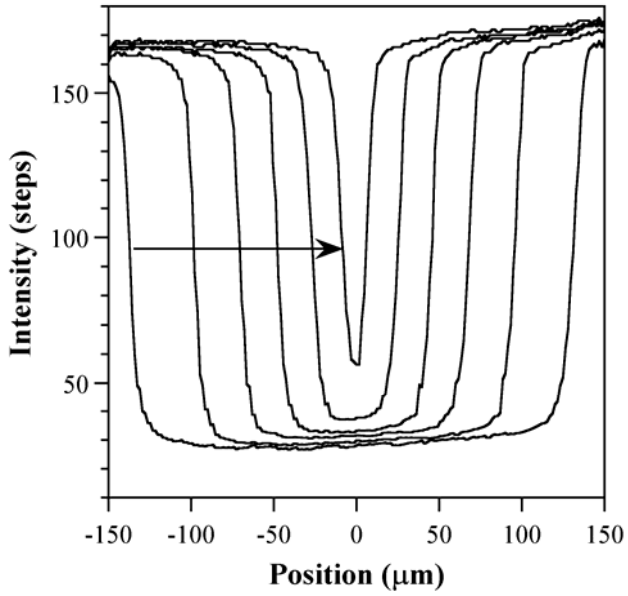

Figure 24. Intensity profiles at 30 second time intervals during the first-ever reduction at -1 V vs. Ag/AgCl. The arrow indicates the direction of front movement.

The position of the front at the 10th intensity level (approximately 50% doping) is shown in Figure 25 versus time. The position goes from 150 (at the edge) to 0 (the center). The slope of these curves (i.e., the front velocity, v) varied, as shown in the Supplementary Materials, for reasons that are not yet entirely clear. The velocities varied in their time dependence from $v \sim t$ to $v \sim \sqrt{t}$, with Figure 25 illustrating a

typical case intermediate between the two limits. As we show in Part 2, if the electric field in the reduced area decreases linearly with the length of the reduced area, then the front should move as $v \sim \sqrt{t}$. (This is the case even if the cations move only by migration; the $\sqrt{t}$ dependence, as seen in classical Fickian diffusion, is coincidental.[*]). Also shown in Part 2, several situations could lead to a phase front propagating linearly with *t*. For example, when hole mobility equals ion mobility, potential profiles in the film keep constant, which creates a phase front moving linearly with time. Although hole mobility is typically regarded to be much higher than ion mobility at oxidized states, hole mobility could be close to ion mobility at reduced states. Simulations in Part 2 also show that when ion transport in electrolyte is the rate limiting step, the phase front moves linearly with *t*. However, such situation may not occur in our experiments since a concentrated NaDBS electrolyte (0.1 M) was used. Another reason needs to be taken into account is the polymer relaxation process, which can be the rate limiting step and creates a front moving linearly with *t*.

[*] Diffusion is movement of species down a concentration gradient, whereas drift (also known as migration) is movement under a force, such as that of a charged particle in an electric field. This is discussed further in Part 2.

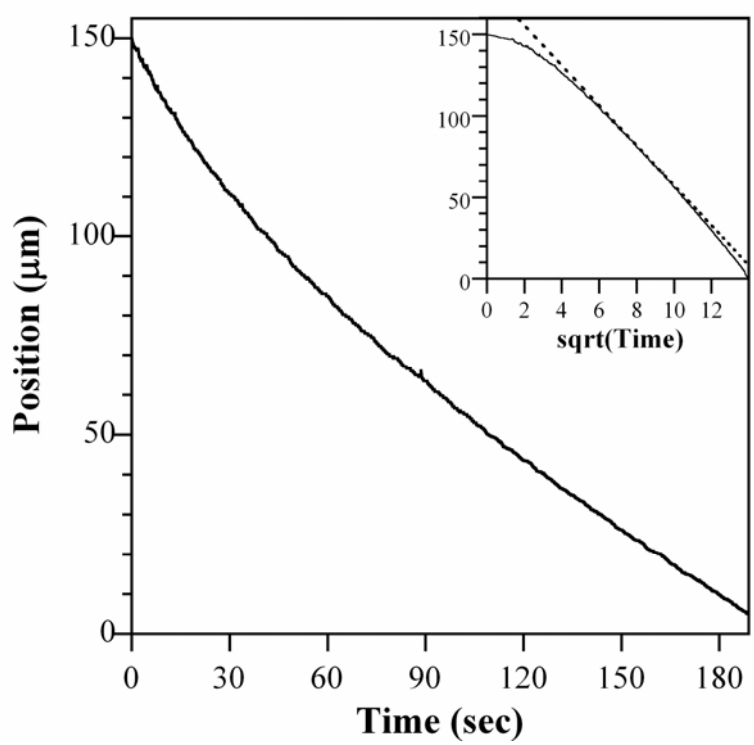

Figure 25. Front position (at the 10th level, ~50% doped) vs. time during the first reduction step (-1.0 V). The insert shows the position vs. the square root of time and a linear fit to the data after 17 seconds.

If the ions were moving under only classical Fickian diffusion there would be no phase front [41]** and, in addition, the velocity would not depend on applied potential, as discussed in Part 2. The dependence of front velocity *v* on reduction potential is shown in Figure 26. Each point represents a separate sample (since the first cycle can only be run once). The PPy(DBS) did not reduce at all at potentials less negative than -0.6 V. Upon switching to potentials of -0.7 V or more negative, a phase front was launched. Between -0.6 V and -0.7 V, only sample edges slightly changed from brown to dark red after 0.5 hour. No phase front was observed either. The minimum potential to have a phase front is -0.7 V. There was a linear

** A phase front can, however, result during diffusion if the diffusion coefficient is concentration-dependent; this is one form of Case II diffusion.

relationship between the velocity of the front and the applied voltage, $v \sim V$ (Figure 26). This is as would be expected if the ions were moving under drift (migration) with a field-independent mobility μ: $v = \mu E$, where E is the electric field, which increases linearly with the applied potential. The cyclic voltammogram of an uncovered film of the same thickness during the first-ever reduction scan is shown in Figure 26 for reference. The intercept to zero velocity occurred near the potential V_0 corresponding to the onset of the reduction current in the cyclic voltammogram, which is reasonable and consistent.

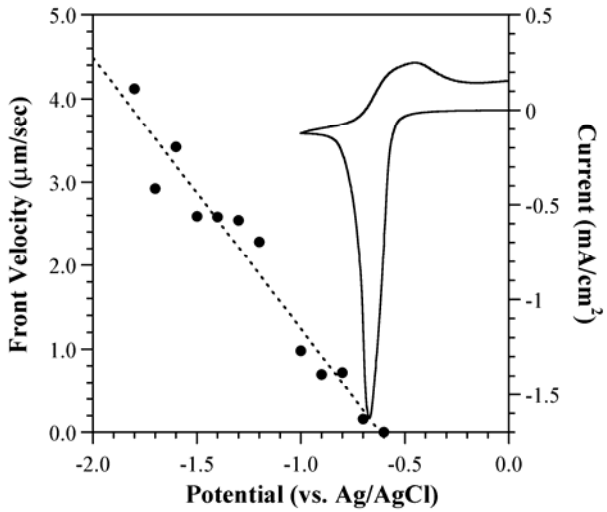

Figure 26. Effect of applied potential on velocity (points) in the first reduction cycle. The dashed line is a linear fit to the data (R = 0.975). A cyclic voltammogram (line) from the first cycle of a film without an ion barrier is shown for reference (20 mV/sec).

4.3.1.2 Later Reduction Steps

In later reduction steps, recorded after at least 3 cycles to ensure steady-state behavior, the phase fronts moved much more rapidly. They remained parallel to the film edges, but were no longer sharp, broadening over time (Figure 27c and d). At

potentials between -0.6 and -0.75 V, no phase fronts were discernible to the eye; instead the films gradually lightened from the edges inward (Figure 27a and b).

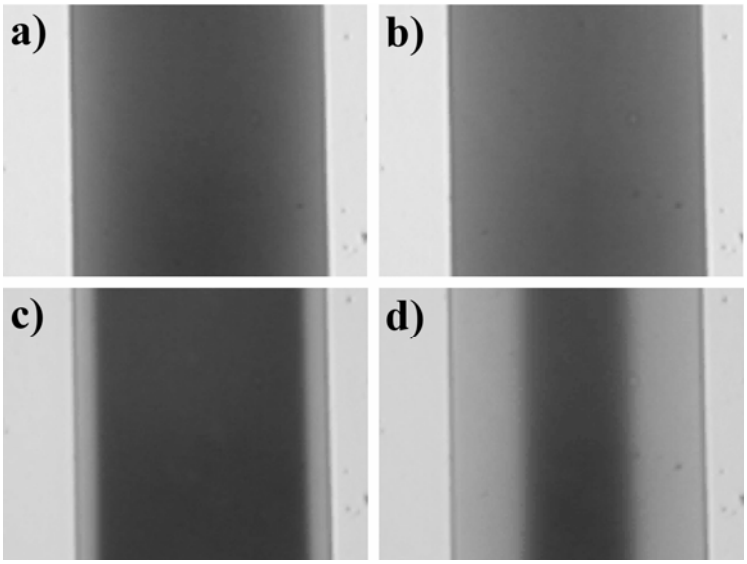

Figure 27. Phase fronts during later reduction steps to -0.7 V (vs. Ag/AgCl) at a) 10 seconds and b) 22 seconds and to -1.5 V at c) 0.3 seconds, and d) 1.3 seconds.

The higher mobility in the film in later cycles, compared to the first cycle, has consistently been observed; see for example [39, 42-45]. This has been attributed to the uptake of solvent that remains in the film. Volume change measurements have also revealed irreversible swelling during the first cycle [38] (see also section 4.3.3.1).

Intensity profiles at several time intervals are shown in Figure 28 for the two cases in Figure 27. The curves at low overpotential η (i.e. the difference between the applied voltage and the onset of the peak in the cyclic voltammogram, $\eta = V\text{-}V_0$) were smooth and u-shaped (Figure 28a), lifting up from the center of the stripe. Profiles at potentials more negative than -0.8 V (Figure 28b) were stepped, although the step walls were slanted because the fronts were not perfectly sharp. Over time the slopes

of the steps decreased as the fronts became increasingly diffuse. Behind the phase fronts were regions with lower slope extending right to the edges of the film.

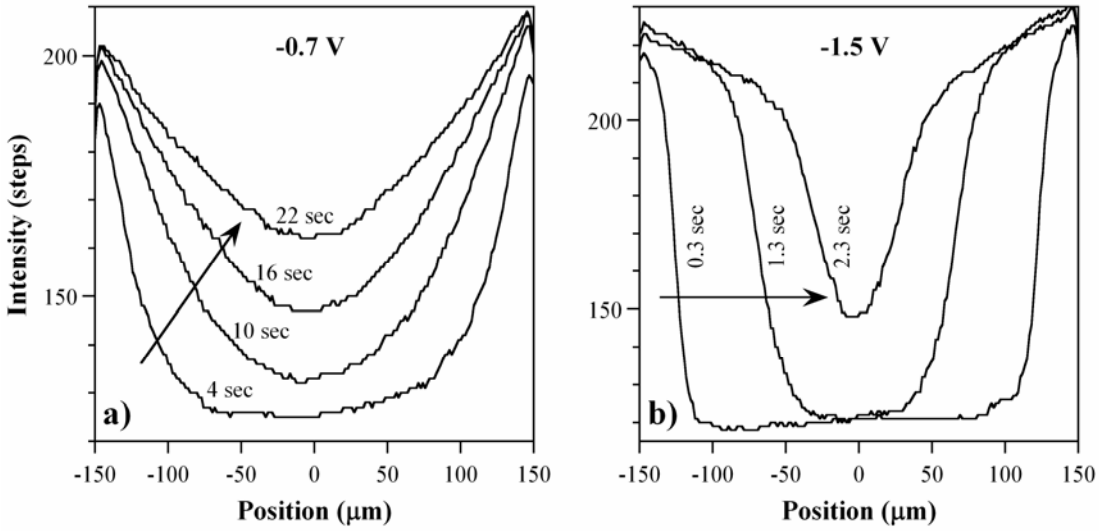

Figure 28. Intensity profiles during later-cycle reductions corresponding to the images in Figure 27 at a) -0.7 V, with curves separated by 6-second intervals, and b) at -1.5 V with 1-second intervals. Arrows indicate the direction of change. In b) at 2.3 seconds, the fronts from the two edges have met.

The absolute intensity values in Figure 24 and Figure 28a and b vary, but the absolute numbers on the y-axis are not meaningful since they depend on the lighting conditions. The only meaningful parameter is the normalized difference between oxidized and reduced states, which we divided into 20 levels. As shown below, the levels correspond to approximately 5% increments in oxidation (doping) level.

The front position versus time is shown for two potentials in Figure 29. The two primary differences from Figure 25 are the shorter time and the apparent increase in velocity when the fronts meet, since they are no longer perfectly sharp. The general shapes of the curves do not change with potential, but the (negative) slopes increase. As for the first reduction cycle, the curves have dependences on time that lie between

t and $\sqrt{t}$ depending on factors that are still not entirely clear (see the Supplementary Materials section for further information).

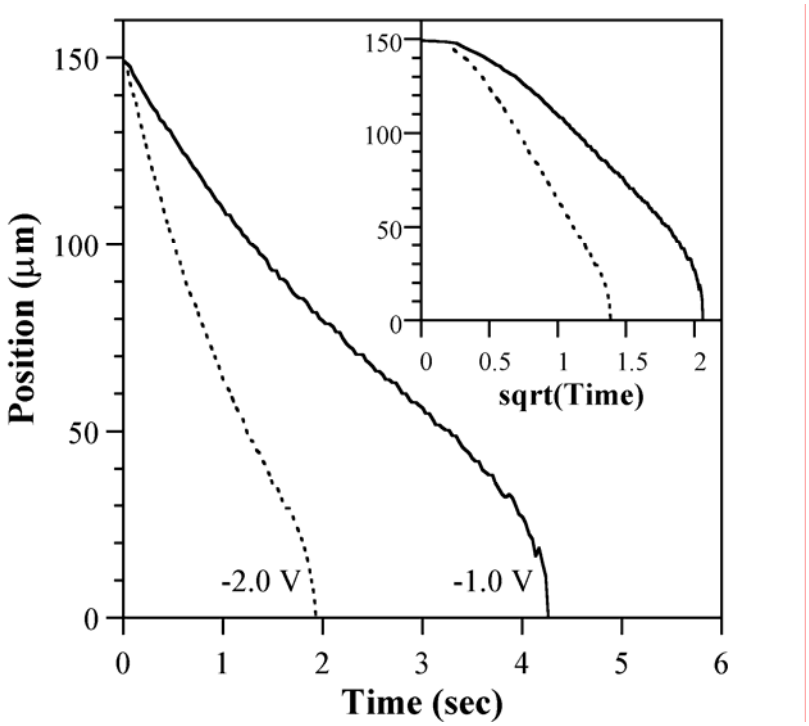

Figure 29. Front position (10th level, 50% doped) vs. time during steady-state reduction steps to -1.0 V and -2.0 V (vs. Ag/AgCl). The insert shows the same data versus the square root of time.

Front velocities vs. reduction potential are shown in Figure 30. The data points represent multiple reductions of 7 samples. Between -0.8 V and -1.6 V, the velocity increased linearly with applied potential, but for more negative potentials, the velocity saturated at between 70 and 80 μm/sec. This shows that the rate-limiting process has changed, perhaps from cation transport in the polymer to another process, not yet identified, but possibly the creation of free volume by chain conformational changes.

As was the case for the first-ever reduction cycle, the velocity extrapolated to zero near the onset of the reduction process. The difference between the first and later cycles is therefore only in the slope, which is related to the mobility, which was -3.3 for the first cycle and 20 times higher at -62 in later cycles. This is consistent with the more open, hydrated configuration of the polymer matrix after the first reduction.

The reproducibility of the results can be judged from Figure 30. Differences in velocity for the various samples were primarily caused by small differences in the PPy and SU8 thicknesses [28].

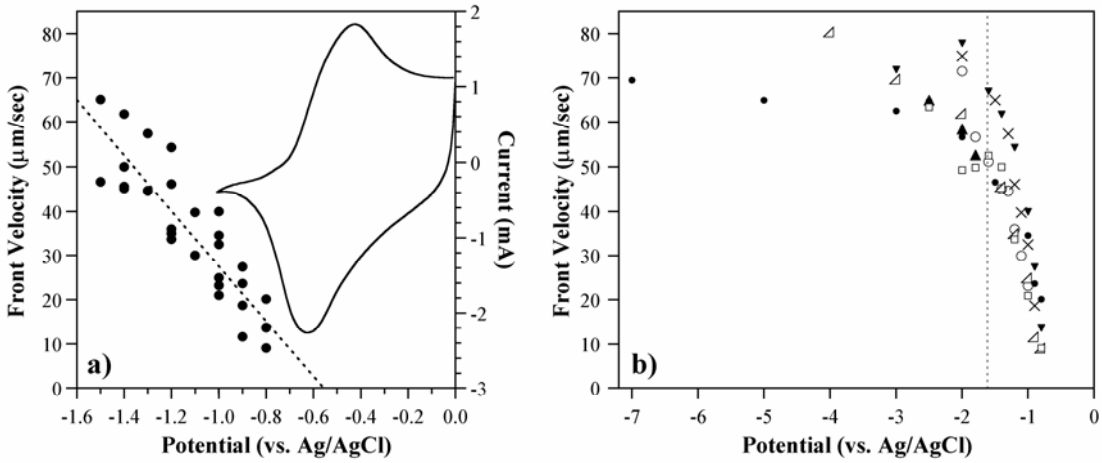

Figure 30. Front velocities during later cycles vs. reduction potential. a) A later-cycle CV of a film without an ion barrier is shown for reference. The line shows a linear fit to the data between -0.8 and -1.6 V. b) Data shown over a wider potential range. Different samples are indicated by different symbols. The range in *a* is indicated by the dashed vertical line.

For comparison, in PEDOT [33] with the Tezuka geometry (uncovered film contacted electrically on one side) the reaction front moved at a rapid 10 cm/sec (10,000 times faster than in our experiments) upon oxidation (anion ingress), suggesting that in this experiment electron transport may have been rate-limiting. In P3HT [34] the fronts

did not travel at constant velocity, nor were they straight; typically the front was faster in the center of the film than at the edges. The front velocity was proportional to $t^{-\gamma}$, where γ was less than the 0.5 (Diffusion process will create a front velocity proportional to $t^{-0.5}$, while a migration process under constant electrical field will create a constant front velocity.).

4.3.1.3 Front Broadening

The positions of the 5th and 15th levels, at the front and back of the phase front, respectively, are shown vs. time in Figure 31 for a sample reduced at -1 V from 0 V. The two lines are superimposed at the edge of the film, but diverge as the front propagates to the center.

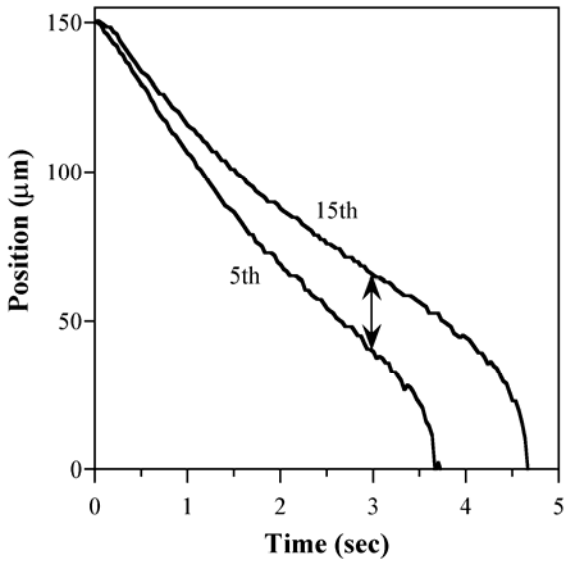

Figure 31. The front and back of the phase front versus time upon reduction (-1 V vs. Ag/AgCl). The arrow indicates the width of the front.

If the front broadening were due to classical Fickian diffusion, the broadening would go as the square root of time and would not depend on the applied potential. Figure

32 shows the time dependence of the front width for several potentials. These data came from scans on the same sample. (Additional data are presented in the Supplementary Materials.) The front width increases linearly with time in the vast majority of experiments, at the same rate for all potentials. This inconsistency with Fickian diffusion is not unexpected, given the change in the state of the polymer during reduction (Figure 17). Ion mobility has consistently been shown to depend on oxidation level [6, 13-25, 46], as have the polymer's mechanical properties [47, 48]. As a result, diffusion is in general not Fickian. (It can be Fickian if small potential steps are applied.)

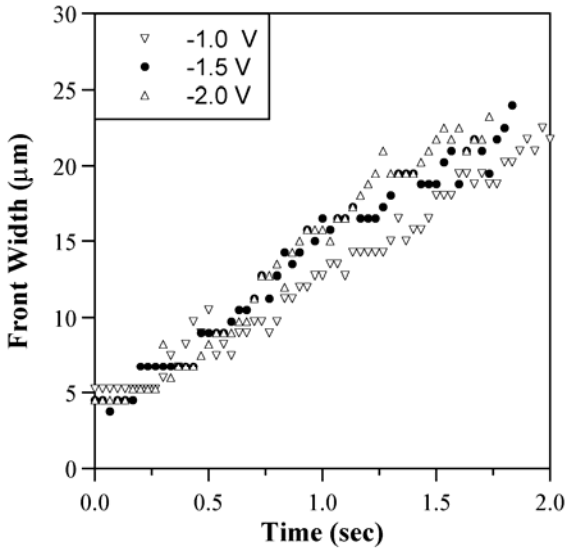

Figure 32. Front width during electrochemical reduction as a function of time at different reduction potentials (400 nm PPy, 2 μm SU8).

4.3.1.4 Effect of Oxidation Potential

The purpose of the experiments reported in this section was to ascertain the role of the state of the matrix on the ion mobility. This variable had been held constant in the sections above. The results of the first reduction cycle compared to later cycles

showed that diffusion and mobility in PPy(DBS) are oxidation-level dependent. Thus, a series of experiments was conducted in which the reduction was initiated at different oxidation potentials to vary the state of the film at the onset of switching to the fully reduced state.

In prior sections, the voltage was stepped from 0 to various negative voltages. In this section, the voltage was instead stepped from various initial voltages to -1.1 V. This changed the initial state of the polymer while keeping the same final state. The relationship between velocity and voltage will give us some qualitative insight into the dependence of the ion mobility (and diffusivity) on the ion concentration, C. To find the quantitative dependence, however, we need to solve $v = \mu(C)E$, but to do that we first require the electric field E throughout the material, which is done in the next two papers of this series. One must also take into consideration the fact that the initial potential varies not only the mechanical state of the polymer matrix, but also its electrical conductivity σ_e. To obtain the electric field correctly therefore requires a knowledge of $\sigma_e(C)$, which changes by at least 5 orders of magnitude between the conducting and insulating states.

Figure 33 shows the front velocity *plotted as a function of the initial potential*, which was held for 30 seconds prior to switching to ensure that the film had uniformly reached the given oxidation level; this was verified by monitoring the stabilization of the color of the film prior to reduction. Between -0.4 V and -0.65 V the front velocity shot up almost an order of magnitude. This potential range corresponds with the onset of the reduction peak in the cyclic voltammogram, and thus the onset of cation

entry into the film, which opens the polymer matrix and pulls in additional water. This result is intuitively obvious. At initial potentials more negative than -0.65 V, no phase fronts were discernable and color variations could not be tracked because the polymer was already reduced.

The data consistently showed a small peak in the velocity around +0.1 V. (This is also where the peak for anion transport occurs in electrolytes with mobile anions.) It is not clear why this small increase in velocity is seen in the NaDBS electrolyte; the peak is probably not due to OH^- transport since that peak appears as a shoulder on the Na^+ peaks [35].

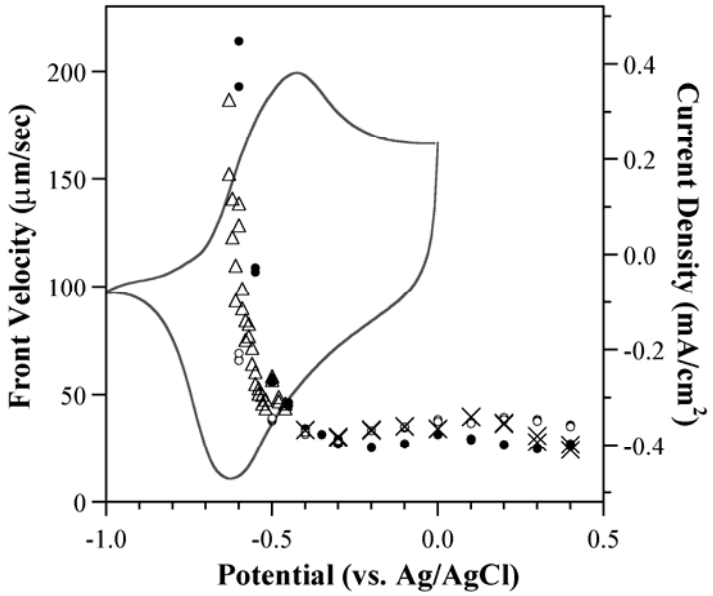

Figure 33. Effect of initial oxidation potential on front velocity. Different sample are represented by different symbols. A CV from an uncovered PPy(DBS) film is shown for reference.

The data below -0.4 V can be fit to an exponential with $y \sim e^9$ to e^{12x}, where x is the overpotential. This is an extreme dependence of velocity on the state of the polymer

hydration and chain conformation, and it is clear that the asymmetry sketched in Figure 17 must be considered in any modeling.

To convert these data to a dependence on charge, the dependence of charge on voltage between 0 and -1 V was obtained from cyclic voltammetry and chronoamperometry (Figure 34 insert). The voltage-charge curves obtained with both methods were similar. The dependence of velocity on the percentage of consumed charge, Q, is approximately $v \sim e^{2Q}$. It should be borne in mind that this dependence is on the total charge consumed, and not the number of ions in the film because, as is clear from Figure 33 and prior studies [35], some current is drawn that is unrelated to actuation (capacitive charging, electrolysis, OH^- exchange, reversible OH^- substitution onto the PPy backbone, etc.).

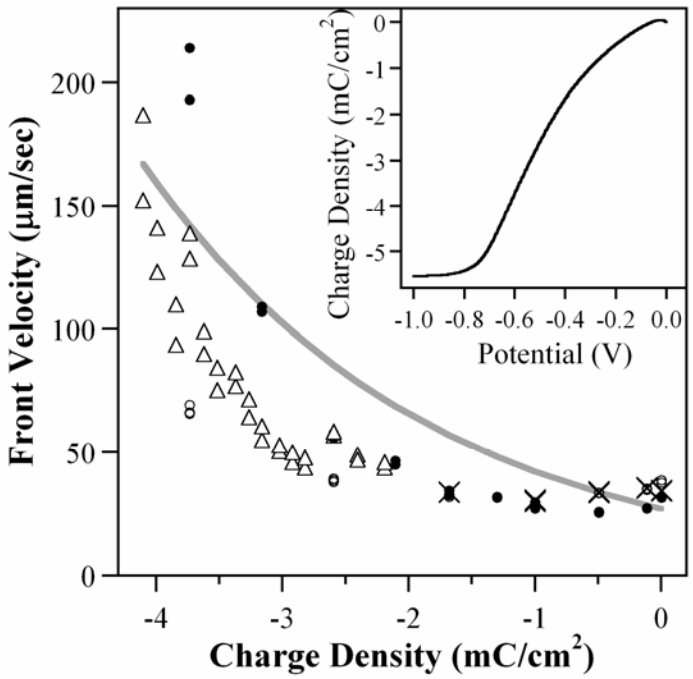

Figure 34. Dependence of front velocity on consumed reduction charge. Samples are represented by the same symbols as in Figure 33. The insert shows the C vs. V data used for the conversion. The grey line is an exponential curve of 27*exp(2*Q/-5.5)), where 27 is the velocity with zero charge density, Q is the consumed charged, and -5.5 is the total charge density.

4.3.2 Electrochemical Oxidation

In this section results from switching the potential from the reduced state (transparent, insulating) back to the oxidized state (red, conducting) are presented. In order to maintain charge neutrality, the cations that entered the film during reduction are now expelled. Since the polymer matrix started in the fully expanded state and was switched to the fully compacted state, polymer chain conformation was eliminated as a variable. Since the electrical, chemical, and mechanical states of the polymer are different at the two endpoints, reversing the voltage does not result in a simple reversal of the cation phase front. Instead, the behavior is substantially different upon oxidation than upon reduction.

4.3.2.1 Ion Transport Behavior

The color changes undergone by the PPy during the course of oxidation upon application of 0 V are shown in a series of images in Figure 35 and as intensity profiles in Figure 36. The first thing to note is that color change was greatest and fastest at the edges. This was unsurprising, since cations nearest the electrolyte interface would be the first to leave. Unlike during reduction, however, the color at the center of the film also changed rapidly (see the arrows labeled "1"). We postulated that this was due to the high diffusivity/mobility of the Na^+ in the reduced state (Figure 33). The average intensity change was thus initially more rapid than during reduction for the same overpotential. Although diffuse front-like intensity changes were seen in the earliest stages, they broadened rapidly to more closely resemble the behavior seen at low voltages during reduction (compare Figure 27a and b). Note that the color change direction was again from the edges inward, although the intensity dropped rather than rose (compare Figure 28a).

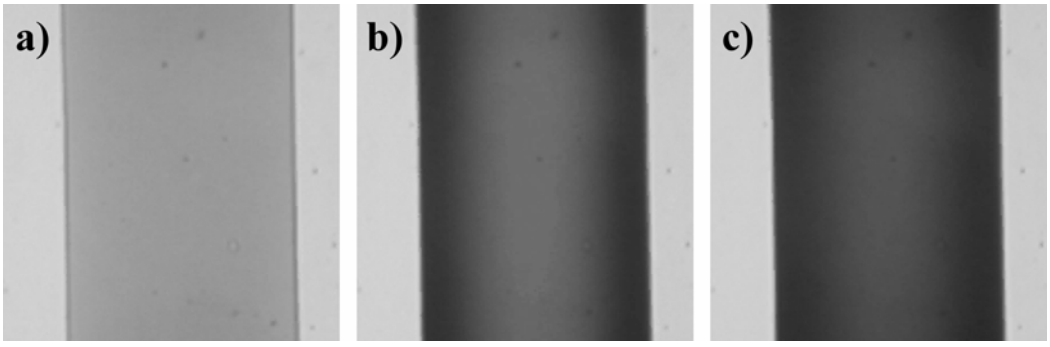

Figure 35. Overhead images of color change during oxidation at a) t = 0 seconds, b) 2 seconds, and c) 4 seconds (-1.1 V to 0 V step, 300 nm thick PPy(DBS), 2 μm thick SU8).

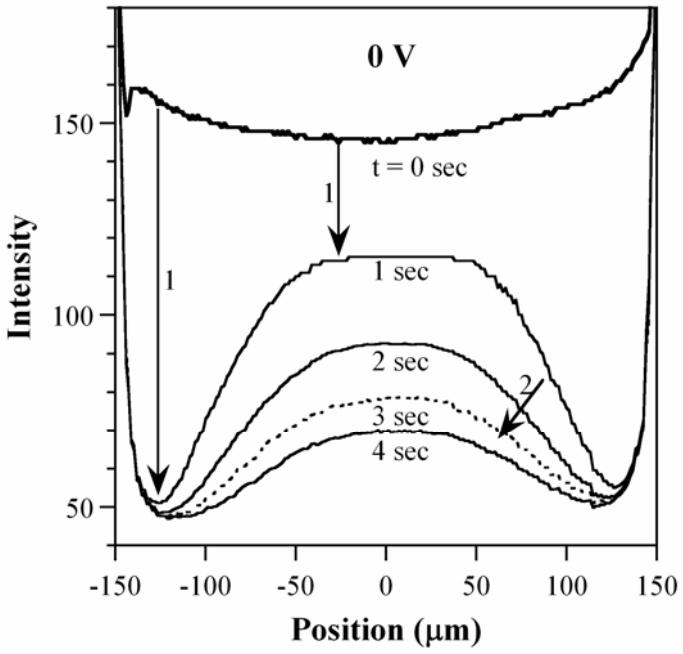

Figure 36. Red channel intensity profiles of the images in Figure 35 and of intermediate times. The arrows labeled "1" indicate changes at early times and "2" subsequent changes.

The rapid initial color change occurring over the whole film bears a resemblance to the behavior of anion-transporting films during reduction [32]. In that case, the phenomenon was attributed to the film starting in the conducting state, so that the electrical signal had control authority over the entire film. In our case, though, the film had a high electrical resistivity at t = 0, so the more likely explanations for the uniformity of the response in PPy(DBS) in our geometry are the high mobility/diffusivity of the cations in combination with the short path-length for the electrons and/or differences in the strengths of the electric fields. These questions will be examined in Part 2 of this series of papers.

After the initial intensity drop in the center of the film, further changes took longer and longer, as evident from the increasingly closer line spacing in Figure 36. A

reasonable explanation, which we evaluate in Part 2, is the potential drop main across the electrolyte during oxidation, leaving electrical field in the film negligible. Also collapse of the polymer matrix at the outer edges as it becomes increasingly oxidized continuously lowers the mobility of the remaining ions.

Even though there was no actual phase front propagation during oxidation, since the entire film was affected more or less immediately upon application of the potential step, oxidation level positions were determined using the same method as previously. The positions of the 5^{th}, 10^{th}, and 15^{th} color levels versus time are shown in Figure 37. The shapes of the curves are almost identical to the ones for reduction (Figure 29), but are of course upside-down. The position moved as the square root of time (see insert) until the oxidation levels moving in from either edge met (at that point the lines go almost straight up.). However, the broadening was considerably greater than during reduction, as seen by comparing the 5^{th} and 15^{th} levels (approx. 25% and 75% doping, respectively) to those in Figure 31. The 15^{th} levels from either edge met each other and disappeared very rapidly (< 0.5 sec), whereas the 5^{th} level took more than six times longer.

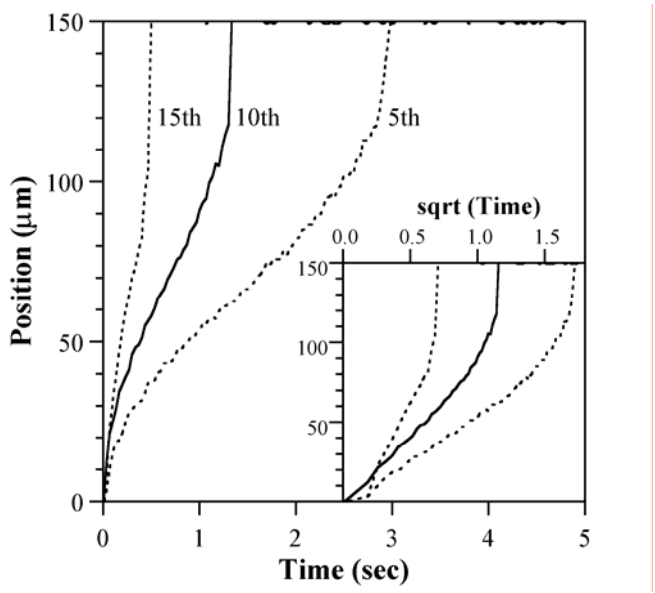

Figure 37. Positions of the 10th level (solid line, 50% doped) and the 5th and 15th levels (dotted lines) with time upon oxidation from -1.1 V to 0 V. (Same sample as in Figure 35 and Figure 36.)

4.3.2.2 Effect of Oxidation Potential

It is not possible to define a meaningful average velocity for the ions during oxidation because the entire film changes color, although at varying rates depending on position. Tracking the 5th color level gives an apparent velocity of 60 μm/sec, while tracking the 10th gives 125 μm/sec and the 15th gives 630 μm/sec. All of these velocities are high, the same as or higher than when -1.5 V or greater is applied during reduction (Figure 30b).

A different method was therefore utilized to compare the rates of oxidation and reduction and to investigate the effect of varying the oxidation potential. The average intensity over the entire 300 μm width of the film was tracked over time. This is essentially equivalent to tracking the flux of ions exiting the edges. The results are shown for oxidation from -1.1 V to +0.4, 0.0, and -0.4 V in Figure 38a and for

reduction from 0 V to -0.9, -1.1, and-1.5 V in Figure 38b. (For additional data, see the Supplementary Materials.) Unlike for reduction, during oxidation the change in intensity did not have any systematic dependence on potential. This finding has an important implication for actuator control: *it is impossible to speed up this half of the reaction by increasing the applied voltage*. In Part 2 we show how this is a result of how the electric fields are dropped over the polymer and the electrolyte.

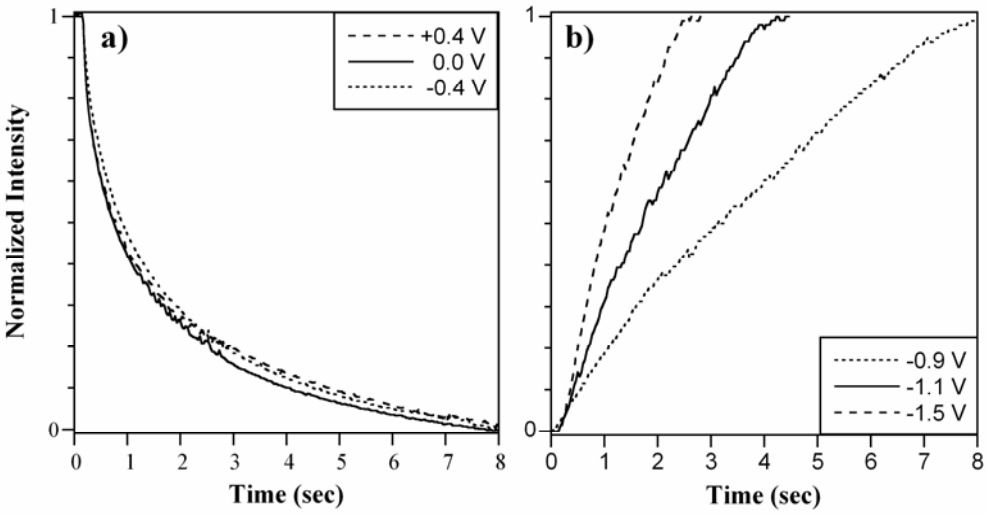

Figure 38. Average intensity over the width of the PPy stripe vs. time. An intensity of 1 corresponds to the fully reduced state, and that of 0 to the fully oxidized state. a) Intensity during oxidation from –1.1 V to three oxidizing potentials (PPy 400 nm, SU8 2 μm thick), and b) intensity during reduction from 0 V to three reducing potentials (PPy 450 nm thick, SU8 2 μm thick).

The oxidation process took ~8 seconds to complete in every case. Reduction took 8 seconds when -0.9 V was applied, longer for less negative potentials and shorter for more negative potentials. This may explain the discrepancy reported in the literature about whether ion ingress or egress is faster: it depends on how large a role migration plays in a given experiment.

The finding that ion expulsion is not speeded up by driving the reaction at higher potentials has also been observed in polyaniline films [48]. In both polyaniline films and fibers, speed was significantly affected by the material preparation method: spun fibers were much faster than cast films. At that time it was pointed out that which material properties affect switching rates remains a key question for future work.

The shapes of the curves during oxidation and reduction were quite different. The oxidation curve fell more or less exponentially with time, whereas the reduction curves, after the first 0.5 seconds, rose with the square root of time. The latter is consistent with the front velocity results (Figure 29).

4.3.2.3 Front Broadening

Front broadening during oxidation, once again defined as the distance between the 5^{th} and 15^{th} intensity levels, was also examined as a function of oxidation potential (Figure 39). The front width had an initial very rapid increase during the first 0.1 seconds, but then the slope changed abruptly and broadening became linear with time (until the fronts met). These data must be interpreted with caution because of the absence of an actual front, but the most important point is still valid: the front widths had no dependence on potential between -0.4 and +0.4 V.

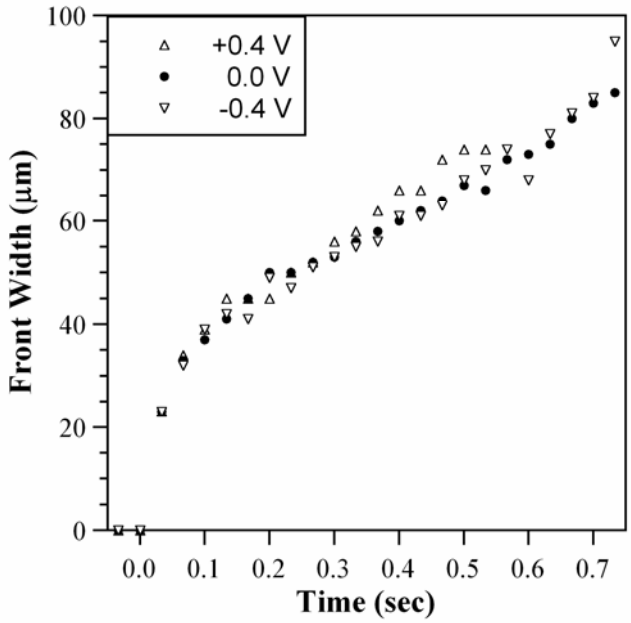

Figure 39. Oxidation phase front broadening at different oxidation potentials (400 nm PPy, 2 μm SU8).

The initial rapid increase in front width again most likely reflects the high mobility/diffusivity of the ions in the fully reduced state. After that, once the edge of the film is oxidized at the electrolyte interface, the ions face a similar environment as during reduction, in which the polymer matrix is sufficiently closed that the ions cannot move through the polymer without requiring chain conformational changes to create free volume. Therefore, a linear dependence is again established by the non-equal probabilities of moving one direction versus another (non-Fickian diffusion). The slope is nearly ten times greater than during reduction, however, indicating that the matrix is still considerably more open.

4.3.3 Intensity, Charge, and Strain

It is important to lay out a convincing argument that the color changes reported above are relevant for actuation, and moreover, for the modeling work that follows in Part 2,

that the color is correlated in some way with the Faradaic charge. This section presents that evidence. We have said above that the 10th intensity level corresponds to approximately 50% doping, and this statement is also justified. We first present out-of-plane actuation strain measurements and then examine the relationship between color, redox charge, and strain.

4.3.3.1 Out-of-Plane Actuation Strain

Out-of-plane strain is the change in the thickness of the film upon actuation [38, 49]. This is different from the inplane strain that is harnessed in bilayer actuators [50, 51]. Out-of-plane actuation strain is typically 10 times larger than inplane strain, and can thus be utilized for applications such as microfluidic valves [52].

The out-of-plane strain of an ion barrier-covered PPy(DBS) film reduced at -1.0 V is shown in Figure 40. The gray line shows the thickness of the as-deposited PPy with the overlying SU8 layer. The slow ion velocity during the first reduction scan, which takes approximately 3 minutes, allows snapshots of the process to be taken, since the height profiles are completed in only 2 seconds. The thin black lines in Figure 40a are profiles taken 40 seconds apart, and the thick black line shows the final, completely reduced state.

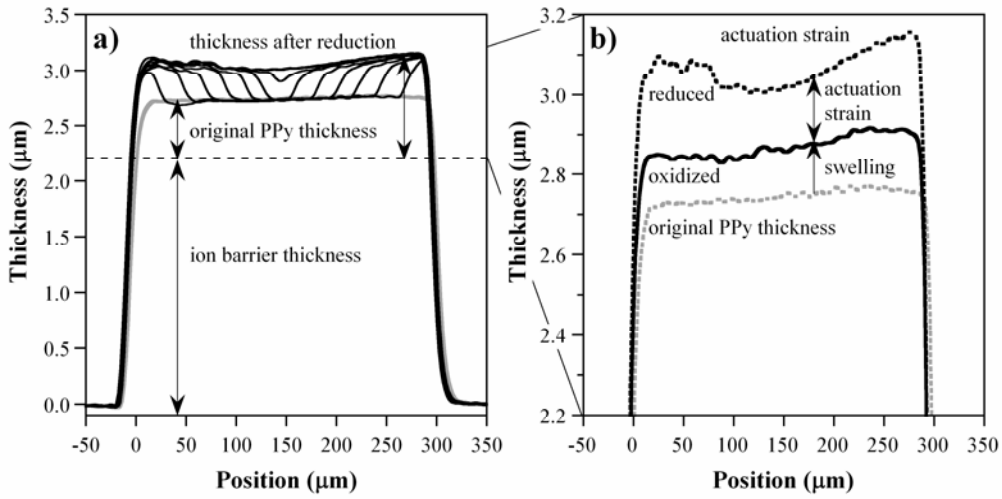

Figure 40. a) Height changes during the first-ever reduction (-1 V). The as-deposited PPy + SU8 thickness (gray line), thickness snapshots every 40 seconds during the reduction process (thin black lines), and completely reduced thickness (thick black line) are shown. b) Subsequent height changes during actuation. The quasi-irreversible swelling (24% of the original film thickness) between the oxidized and as-deposited state and the reversible actuation strain (28% of the oxidized film thickness) between later cycle oxidized and reduced states are shown.

The film thickness changes reflected the same ion phase fronts as the color intensity profiles above. The height increased stepwise to a value corresponding to the maximum ion concentration in the PPy, and the steps traveled from the edges of the film to the center.

Upon re-oxidation (shown in the close-up Figure 40b), the PPy thickness did not return back to its original, as-deposited value. Instead, in subsequent cycles the height changed reproducibly between the reduced state value and a thicker oxidized state value. This irreversible swelling is consistent with results obtained on uncovered PPy(DBS) films with atomic force microscopy [38] and with the hypothesis that water enters the film during the first reduction scan and remains in the film during re-oxidation.

One key thing to appreciate in Figure 40 is that *the strain reaches a maximum value beyond which it does not increase*. This fact confirms that the ion density in the polymer has an upper bound, C_{max}, as expected from the notion that the cations enter the material to re-establish charge neutrality by compensating the fixed density of DBS anions left behind by an equal concentration of holes upon reduction. Models of ion transport in conjugated polymers must take C_{max} into account, since it affects the driving forces that can be achieved by diffusion (as will be shown in Part 2).

Additional evidence for a maximum actuation strain, and therefore a maximum ion concentration, is that the strain did not depend on the applied potential (Figure 41). Thus, C_{max} is given by the number of charges to be neutralized in the polymer, and not by the driving force on the ions.

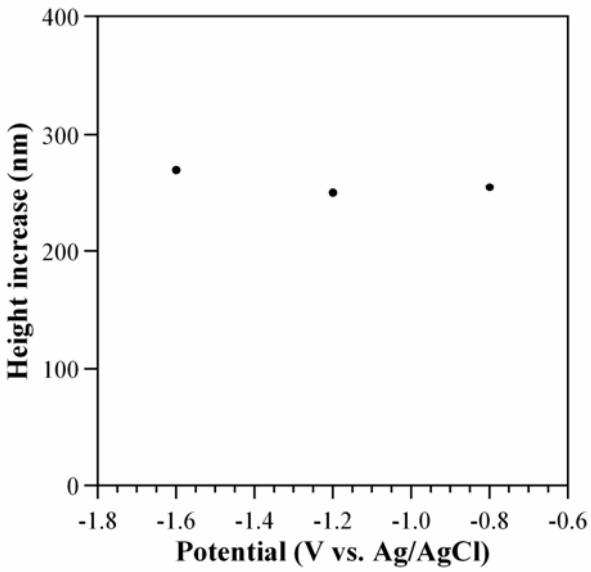

Figure 41. Height increase (actuation strain + swelling) as a function of applied potential. The sample (420 nm PPy, 2 μm thick SU8) was oxidized at 0 V for 30 seconds and then stepped to different reduction potentials, where it was held for 10 minutes before measurement.

Given the not-perfectly-flat-topped profiles (Figure 40b), actuation strain was determined in three ways. One was to "eyeball" the thicknesses, the second was to average the height values between x = 50 and 250 μm (x = 0 and 300 correspond to the edges of the film), and the third was to subtract the curves at different oxidation levels and obtain the average differences. The three methods yielded similar results, within 5% of each other.

To verify that the swelling shown in Figure 41 was due to water drawn in during the first reduction, rather than to the passive uptake which can occur upon initial immersion of the film into the electrolyte [38, 53], height changes due to swelling were measured at different immersion times in the electrolyte. The thickness increased 5% within the first 10 minutes, with no further increase over the next 6 hours. (In 11 μm thick uncovered films, the swelling was found to be 11% [38]; the difference may be due to the stiffness of the ion barrier [28].) All films were therefore immersed for at least 10 minutes before the strain measurements were performed.

4.3.3.2 Correlating Intensity and Charge

It is known that not all of the charge injected into the conjugated polymer is associated with volume change [35, 48]. Capacitive charging, charge consumed by the reversible addition of OH^- groups onto the backbone, and charge consumed by parasitic reactions can be significant, and moreover are essentially impossible to distinguish from redox charge [54] (by which we mean charge associated solely with the creation or annihilation of holes). Nevertheless, it is of interest to see what the

correlation is between the intensity and the consumed charge, even though we do not expect a one-to-one correlation. These studies were done on *ion-barrier-covered* PPy(DBS) films.

Charge and intensity during reducing and oxidizing potential steps are compared in Figure 42. The potential was stepped to/from 0 from/to -1.5 V, and the current and color were recorded simultaneously. The average, normalized intensity over the width of the covered PPy(DBS) stripe was obtained as in section 4.3.2.2, and the charge was obtained by integrating the corrected current data, in which the residual parasitic current was subtracted from the measured current.

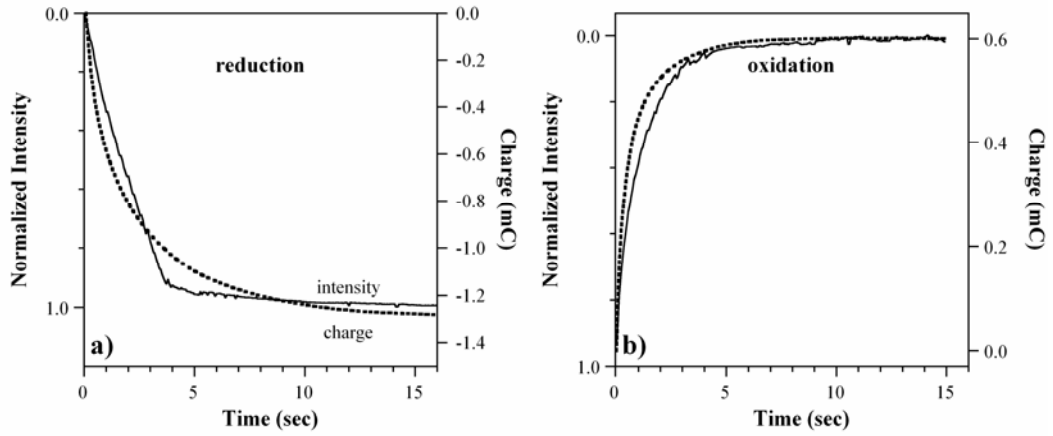

Figure 42. Average intensity over the entire width of the PPy stripe and the charge consumed for a) reduction (-1.1 V) and b) oxidation (0 V) (300 nm PPy, 2 μm thick SU8). Note that the intensity axes are reversed.

During reduction, the intensity and charge curves differed: the charge approximately followed ln(time), but the color change was almost linear for the first 3 seconds, and then did not change further. During oxidation, on the other hand, the charge and color curves superimposed, and both approximately followed ln(time).

The reason for the difference in the intensity and charge curves only during reduction is not immediately obvious and must be considered further. Two possible explanations for the mis-match are that either 1. parasitic processes draw current not associated with ion transport (only the redox charge density, not the total charge density consumed during switching, corresponds to the ion concentration in the film), and/or 2. absorption at wavelengths the camera defines as "red" is nonlinear with charge (it cannot be assumed a priori that the optical absorption would necessarily follow the ion concentration).

Looking at prior work for insight, a similar non-correlation of charge and strain was seen in polyaniline films and fibers during oxidation (the ion ingress step) [48]: strain had a step-like profile, while the charge followed a slower, smooth curve. (The stress was even less correlated with the charge.) Likewise, the strain and charge curves were more similar during reduction (ion egress). These facts make it unlikely that the non-superposition during reduction of PPy(DBS) is due to the parasitic reactions (primarily hydrogen generation) occurring only at negative potentials, since that would require parasitic reactions occurring only at positive potentials in the polyaniline system.

To explore the issue further, the color and current during cyclic voltammetry of a PPy(DBS) film *uncovered by an ion barrier* were measured simultaneously (Figure 43). During reduction, charge was consumed between 0 and -0.3 V (in the

pseudocapacitive region* labeled 3) and during the first cathodic peak centered at -0.53 V (possibly associated with OH^- transport [35], labeled 1), but the color did not start to change until the foot of the second cathodic peak centered at -0.67 V (associated with Na^+ transport and labeled 2). Upon oxidation, color change started at -0.73 V with the start of the first oxidation peak (2') and was completed by -0.4 V, prior to end of the second peak (1') and before the pseudocapacitive current. These data are strikingly similar to previously published actuation data (Figure 10 in [35]), which showed that there was no bilayer movement associated with either the pseudocapacitive current or the "OH^-" peak.

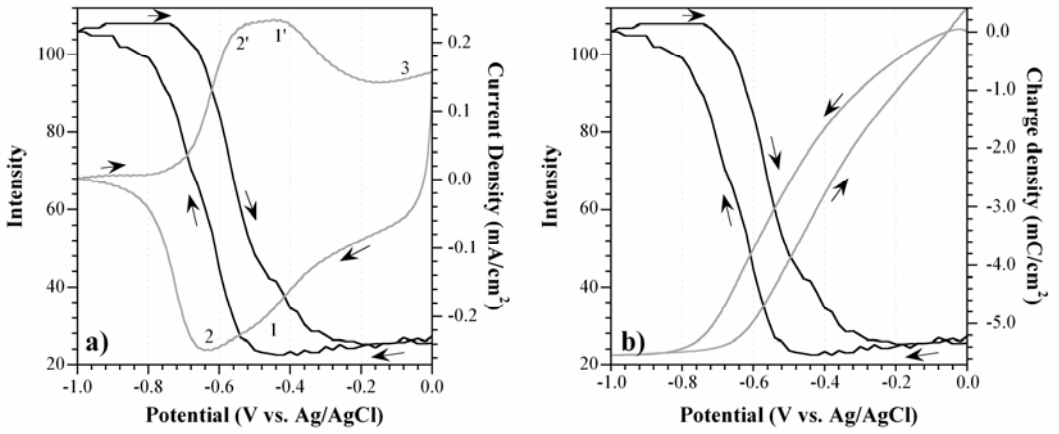

Figure 43. a) intensity as a function of potential (black line) during cyclic voltammetry (gray line) of an uncovered PPy(DBS) film (450 nm thick). b) comparison between intensity and charge obtained from cyclic voltammetry in a).

* The nature of the current above the oxidation peak has been the subject of debate for many years. It has the rectangular shape associated with the capacitive charging of an electrode surface, and hence has frequently been referred to as capacitive current. However, the magnitude of this current is strongly dependent on deposition conditions, being totally absent in some films that have otherwise identical cyclic voltammograms [55].

Although Figure 43 sheds some light on the reason that charge and intensity are not perfectly correlated during chronoamperometry, it does not answer a key question. Why does the color change occur *faster* than the current in Figure 42, since Na^+ transport requires a more cathodic potential, and thus greater energy, than the current-consuming processes 1 and 3? The combined data would suggest that Na^+ transport is faster than both the purported OH^- transport and/or the processes occurring during pseudo-capacitive charging when -1 V is applied, which does not seem reasonable. This is a topic that should be further investigated in future work.

4.3.3.3 Correlating Intensity and Strain

As an additional substantiation that actuation strain and color change in these devices occurred simultaneously, a gold film was deposited over part of the ion barrier surface to serve as a mirror. The gold surface was reflective when it was parallel to the substrate, but appeared dark where it was sloped over a height step. A partially reduced film is shown in Figure 44 with the mirror on the right during later cycles. This sample used Parylene C as the ion barrier since it has a lower Young's modulus than SU8-2002 and can be deposited in a thinner layer without pinholes. The interface between red and transparent regions of the film, and the dark line indicating the step in height (indicated by the arrows), occurred at approximately the same position and moved together in both the first cycle and in later cycles. The lines were less visible in later cycles because both the height change and slope were smaller.

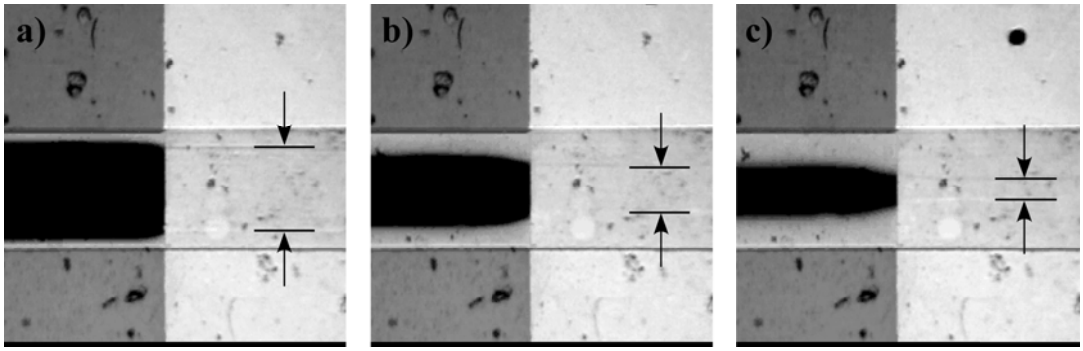

Figure 44. Color and volume change in a PPy(DBS) film (820 nm) with a Parylene C ion barrier (1000 nm), and on the right side of the device, a thin gold mirror (200 nm). The reduction potential was -1.5 V. Arrows indicate the two parallel, inward-moving shadows resulting from the slope of the Au film above the step in PPy thickness. a) 0.33 second b) 1 second c) 1.66 seconds.

The small difference in velocity of the phase front on the right and left sides of the images is due to the increase in Young's modulus of the ion barrier caused by the addition of the gold film [28]. During the first cycle, the phase front moved slower under the Au + Parylene, but in subsequent cycles it moved faster. We surmise that in the first cycle the higher barrier stiffness, and consequentially the higher force required to bend it, hinders the volume expansion. Upon oxidation, however, the higher stiffness hinders the collapse of the matrix, thus holding it more open and facilitating ion ingress during the next reduction. In Figure 44, the phase front in the right side (higher stiffness side) moved at an average velocity of 59.6 μm/sec, faster than the left side (47.5 μm/sec, lower stiffness side).

As a further corroboration of the link between intensity and strain, the actuation strain measured by mechanical profilometry and the red channel intensity are shown as a function of potential in Figure 41. The reduction potentials were stepped from 0 V to various negative potentials. Each potential was held for several minutes to establish equilibrium before the measurements were made. The strain and intensity had

identical relationships with the reduction potential below -0.5 V, and a plot of intensity vs. strain in that region is linear. The onset for both was at -0.5 V, and they saturated at -0.8 V: more negative potentials did not increase either one. Above -0.5 V, the height increased slightly, while the intensity was flat.

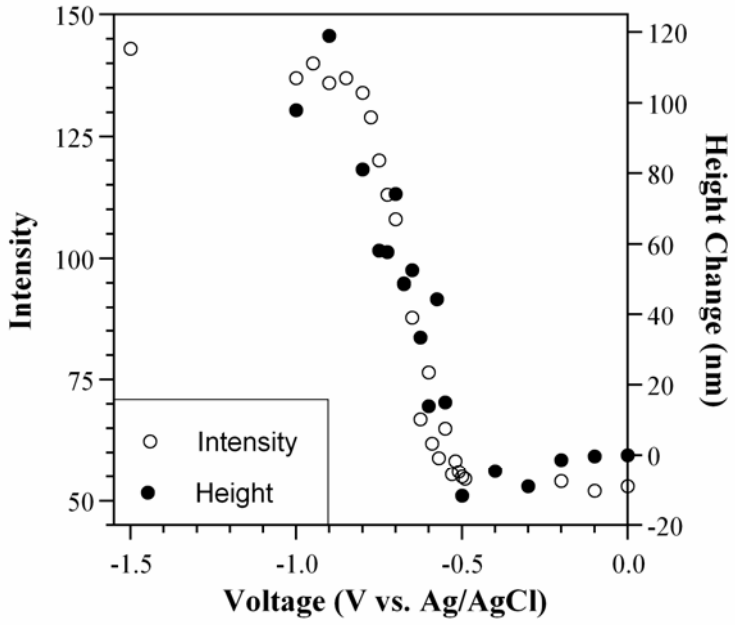

Figure 45. Final intensity in an uncovered PPy film 400 nm thick (left axis) and final thickness change in an SU8-covered PPy film 420 nm thick (right axis) vs. the applied reduction potential after stepping from 0 V and holding for several minutes.

4.4 Discussion

It is worthwhile to consider the various events that take place in a conjugated polymer during redox to shed some light on the experimental results presented above. These are the events that need to be considered by an eventual, complete physical model. (In Part 2 of this series, we present a partial model that treats charge transport.) First

we focus on the events that take place during redox from an electronic point of view, and then from a physical point of view.

Charge transport is triggered by an electrical stimulus such as a change in voltage. From a band structure point of view (Figure 46), a potential applied to the electrode changes the Fermi level of the electrons in the metal relative to the allowed energy levels in the polymer. (Energy E is related to the applied potential V by $E = -qV$, where q is the charge on an electron [56].) Without considering the nature of those levels*, we shall refer to them as the highest occupied levels (HOLs). These are actually a broad band of energy levels due to the distribution of different conjugation lengths in the polymer, seen in cyclic voltammograms as broad redox peaks. In the reduced state, these levels are fully occupied, and although the energy of electrons in the electrode (the Fermi level, E_{Fm}) is higher, no charge can be transferred to the polymer since the HOLs are full. As the applied potential is made more positive, the Fermi level in the metal drops, and when it is lower than some portion of the HOL band, electrons are transferred from the polymer backbones to the electrode, leaving behind positively charged polarons and bipolarons, which we have collectively referred to as holes in analogy with the charges in inorganic semiconductors. Transfer stops when no electrons occupy levels above E_{Fm}. The amount of charge that is transferred depends on the voltage, up to the point at which the Fermi level

*There is some disagreement about whether electrons in a reduced polymer are removed from the valence band edge or the polaron band (which does yet contain any states). As electrons are removed and the lattice relaxes, polarons are created, and the energy levels shift. Thus, electrons may be removed at one energy (associated with the oxidation potential) and returned at another (a more negative voltage, associated with reduction). To simplify the discussion, we treat the highest occupied level as unchanging.

drops below the HOL band, when the polymer is fully oxidized (doped). Raising the potential further does not produce more holes; rather, it results in other, unwanted chemical reactions that may be reversible (such as the addition of carbonyl groups to the chain) or irreversible (such as hydrolysis). Between the fully oxidized and reduced states, the number of electrons that can be transferred for each incremental change in energy can be found approximately from the cyclic voltammogram, although as pointed out above, the CV also reflects other charge transfer processes.

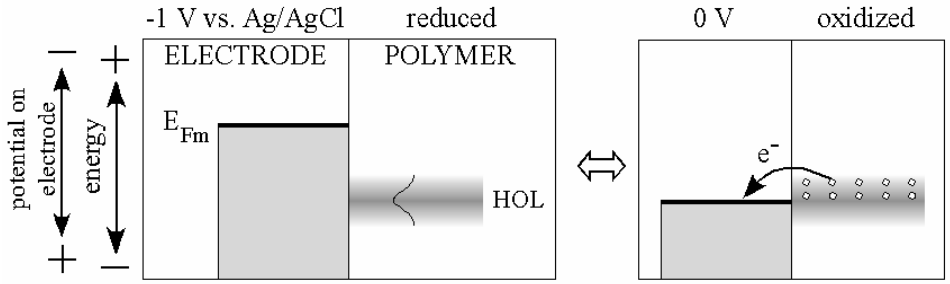

Figure 46. Band structure representation of the oxidation reaction, assuming instantaneous charge compensation by ions. Allowed energy levels are indicated in gray. Electron have a distribution of energies in the polymer. Positively charged holes are represented schematically as empty circles.

This description of the oxidation process assumed that at equilibrium the holes were compensated by an equal number of anions that entered the polymer from the electrolyte or, for cation transporting materials, by the egress of cations. However, ion transport is slow relative to electron transport, and cannot occur instantly upon application of a potential. Figure 47 illustrates what happens if a voltage is applied and compensating ions do not arrive immediately, where the electrolyte is now explicitly shown. For simplicity, we describe the events in an anion-transporting material.

The film again begins in the reduced state, and a sufficiently positive potential is applied that the conjugated polymer can be oxidized, which lowers E_{Fm}. Electrons start to be transferred from the HOLs to the electrode. Without compensating anions, the resulting holes build up, creating an electric field that increases until it balances the voltage on the electrode, thereby lowering the relative energy of the electrons in the polymer. At that point, charge transfer stops. The amount of energy E by which the levels are lowered depends on the dielectric constant ε of the polymer and the net charge Q.[*] When the Fermi energy levels in the metal and polymer are equal, there is no further driving force for charge transfer. The higher the applied potential, the greater the number of electrons that can be removed before the voltages balance. Ions in the electrolyte move into the polymer under the applied electric field, neutralizing the net charge. (The anions are shown schematically: they do not occupy states in the polymer band structure.) This raises the energy levels in the polymer, since the field depends on the *net* charge. This allows additional electrons to be removed from the polymer (without changing the potential applied to the electrode). The process continues until the energy levels in the electrode and film are equalized, or until the polymer is fully oxidized. Of course, in a real system these steps occur simultaneously and continuously, not discretely as in the figure and the foregoing description. Upon reduction, these steps are reversed.

[*] $E \sim [Q]/r\varepsilon \sim [h^+ - C^-]/r\varepsilon$, where r is the distance to the net charge, $[h^+]$ is the concentration of holes, and C^- is the concentration of ions.

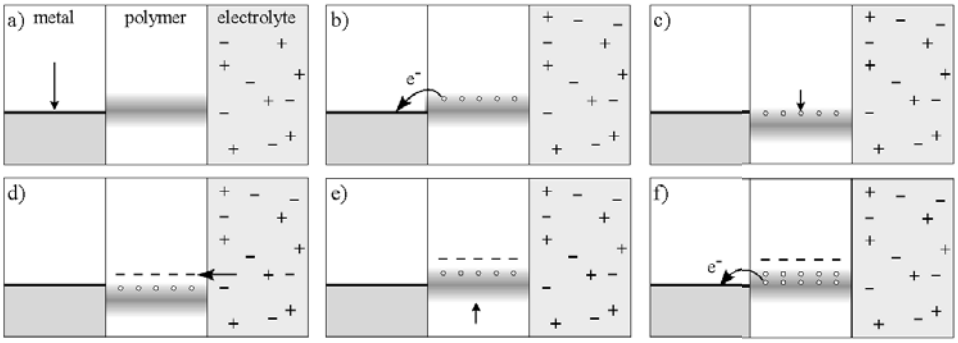

Figure 47. Schematic illustration of the driving energies for charge transport, assuming non-instantaneous charge compensation by ions. a) An anion transporting polymer initially in the reduced state. A positive potential is applied to the electrode, lowering its Fermi level, E_{Fm}. b) Electrons are transferred from the polymer to the electrode, creating positively charged holes on the polymer backbone. c) This net charge in the polymer lowers its Fermi level , E_{Fp}, relative to that of the electrode, halting further electron transfer. d) The applied potential attracts anions from the electrolyte, which restore charge neutrality. e) The removal of the net charge raises the Fermi level in the polymer back to its original position in (b). f) Since the Fermi level in the metal is now lower, electron transfer to the metal can resume. The process repeats from step c until the electron energy levels are equal or until the polymer is completely oxidized.

From a physical point of view, the various steps that occur during oxidation are illustrated schematically in Figure 48. 1) Electrons are removed from the polymer chains. In the fully doped state, a hole is created for every 3-4 monomer units of polypyrrole. 2) The holes move away from the electrode along the polymer chains. In the most general case, they move by both drift (also known as migration, due to an electric field) and diffusion (due to a concentration gradient). a) The polymer backbones undergo conformational changes in response to their altered electronic structure [14, 57, 58]. 3) Anions move through the electrolyte, in the most general case through a combination of drift*, diffusion, and convection. 4) Anions enter the polymer, possibly shedding some of the molecules in their solvation shell. (This step

* If the ions are depleted in the electrolyte, then drift may not be negligible

is often represented as a charge transfer resistance in impedance models.) 5) Ions move through the polymer, between the chains, in the most general case by a combination of drift and diffusion (convection is negligible). They are typically solvated. b) Space must be created in the polymer for the ions to enter by chain conformation changes. 6) Solvent enters the polymer that is not bound to ions but is in response to osmotic pressure created by the ions [26]. It moves solely by diffusion, since it is uncharged. Which of these steps is rate limiting depends on the experiment that has been performed, which is one reason for the fact that different research groups have reported apparently contradictory results.

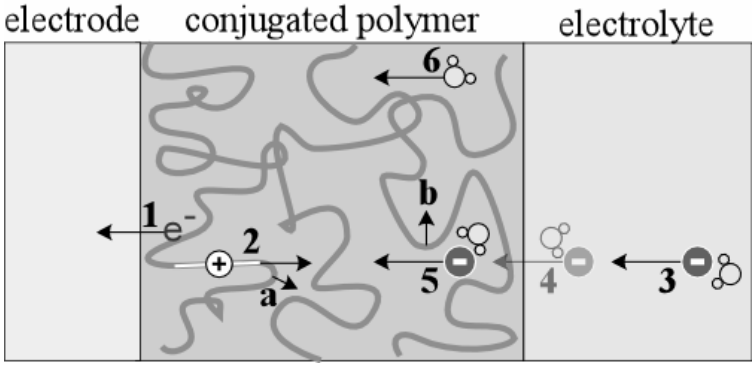

Figure 48. Schematic illustration of the physical processes occurring during electrochemical oxidation.

In Part 2 of this series we build a model of charge transport in conjugated polymers based on first-principle physics and the reduction behavior of PPy(DBS) in the above experimental geometry. We then use the model to predict the oxidation behavior, as well as oxidation and reduction in anion-transporting materials, in this and other geometries.

Referring back to Figure 15 and Figure 48, what additional research is needed to complete our understanding of the redox process? Let us put aside, for the moment, structure-property relationships that link the deposition conditions to the material properties and these properties to the behavior, and also put aside the effect of cycling conditions, such as the solvent, electrolyte concentration, electrode material, cell geometry, etc. These issues still require a substantial amount of experimental study. What is needed to complete a physics-based model that will take us, for a particular material and set of cycling-condition-specific charge transport coefficients, from a given electrical input to predictions of device behavior, including speed, strain, stress, etc.? The next obvious step of the modeling effort should be to include the polymer chain movements, for example by combining our charge transport model with Otero et al.'s conformational relaxation model, which is mature and has been extensively experimentally validated. With that advance, the effect of cycling history and sample temperature can be taken into account, which will give the state of the polymer matrix at any given time, on which the coefficients in the charge transport model depend. It should then be possible to produce a rudimentary control algorithm that applies the appropriate potentials to achieve a desired actuator motion. The next large step will be more difficult, since there has been less prior theoretical work in this area: linking the solvent content to the polymer's electrical and mechanical properties.

4.5 Summary and Conclusions

We have described an experimental configuration in which ion transport is the rate-limiting step in the redox reaction and have conducted experiments that ensure that

chain conformational changes are constant. As a result, the reduction reaction does not take place at a given location until the cations arrive there, and oxidation does not take place until they leave. It should be borne in mind that this configuration gives information about ion transport parallel to the film surface, which may be quite different from transport perpendicular to the surface if the material is anisotropic, as PPy(DBS) is known to be. The simplicity of device fabrication should allow this configuration to be used by other groups with different materials, and we particularly encourage its use to study anion-transporting conjugated polymers. Our results are summarized in Table I.

Upon reducing the PPy(DBS) for the first time, cations and water are introduced into a tightly compacted matrix. As a result, they form a sharp phase front that stays sharp and moves relatively slowly in response to a cathodic potential step, with a velocity that is linear with the applied over-potential. This implies that the dominant transport mechanism is migration (drift), rather than diffusion. The front is identical whether it is imaged using color or mechanical strain.

Upon re-oxidation, fronts are not seen. Instead, the film becomes darker everywhere at once, although the process is faster at the edges. This behavior indicates that the process is dominated by diffusion, a conclusion that is confirmed by the observation that the time course of the oxidation reaction is completely insensitive to the applied oxidation potential. This means that this half of the reaction cannot be accelerated by applying higher voltages.

The film does not return to its original thickness when the cations exit during oxidation, but it remains swollen with water, which remains semi-permanently in the film. This change is invisible in the current and color measurements since it does not involve the electronic states of the polymer. The reversible component of out-of-plane actuation strain, which is the only component that is useful in actuators cycled more than once, is caused by solvated cation transport. The first-cycle water ingress merely causes anomalously large strains in the first cycle, or first several cycles in thick films.

In the following reduction steps, the cations enter a more open, hydrated polymer. Fronts are again seen for sufficiently large overpotentials, but they move much faster and they broaden with time. These fronts are still linear with the overpotential, but the slope is 20 times larger, indicating that the cation mobility is greater by that factor. The mobility is increased even further if the polymer is stepped from a partially reduced state, which has an even more open structure, rather than from the fully oxidized state. For small overpotentials, the color lightens over the whole film with a u-shaped profile, indicating that the process is dominated by diffusion. The broadening of the ion fronts is linear with time, but does not depend on potential, consistent with non-Fickian diffusion.

Cation transport occurs solely to reestablish charge neutrality, so the color and the strain do not change any further once the film reaches its fully oxidized or reduced state: there is a maximum ion concentration in the film. Color and strain were found to be linearly correlated and to directly reflect the oxidation level, but the total

consumed charge comprises currents from capacitive charging and reactions other than PPy redox, which can occur with other time constants. In particular, under the experimental conditions used in this paper, there were two pairs of peaks in the cyclic voltammogram, as well as pseudocapacitive current in the oxidized state. Only the more cathodic pair of peaks is associated with color change and actuation strain.

The oxidation and reduction processes are not symmetric in two very significant respects. First, upon reduction the polymer starts as a conductor and becomes an insulator, and upon oxidation it goes from an insulator to a conductor, so the potential drops seen by the ions are different. In addition, in the oxidized state the polymer matrix is more compact and contains less water, so ion mobility is significantly lower than in the reduced state. These differences were reflected in the phase front behavior and are the subject of the modeling work in Part 2 of this series.

Table I. Summary of the main experimental findings.

	First-Ever Reduction	**Later Reductions**	**Oxidation**
Existence of Fronts	Ion fronts travel from edges to center for V < -0.6 V	Ion fronts travel from edges to center. No phase fronts below -0.75 V, but a gradual reduction over the entire film.	No fronts, regardless of potential.

Front Velocity	1 μm/sec at -1.1 V.	30 μm/sec at -1.1 V. Front velocities increase if scan is begun in partially reduced state, $v \sim e^{2Q}$ where Q is the consumed charge.	NA
Front Broadening	Fronts remain sharp throughout reduction.	Fronts broaden linearly with time, and broadening does not depend on voltage.	NA
Voltage Dependence	Front velocity is linear with voltage, going to zero at V_o.	Front velocity is linear with voltage, going to zero at V_o. Slope is 20x higher than for first reduction. Velocities saturate at ~70 μm/sec below -1.6 V.	Oxidation speed was independent of potential. Oxidation was faster than reduction at less than -0.9 V, but reduction was faster if V <-0.9.
Front Position vs. Time	Varies from $v \sim t$ to $v \sim \sqrt{t}$.	Varies from $v \sim t$ to $v \sim \sqrt{t}$.	

Strain	Thickness increases by actuation strain + swelling, 55%.	Thickness increases by actuation strain 28%. Actuation strain does not depend on potential once fully reduced.	Thickness decreases by actuation strain, 28%; swelling strain of 24% does not go away.
Current vs. Color	Charge increases exponentially, while intensity increases almost linear with time.	Current is not perfectly correlated with color change.	Current is fairly well correlated with color change.
Color during Cyclic Voltammetry	NA	Color change is associated with the more cathodic reduction peak.	Color change is associated with the more cathodic oxidation peak.
Strain and Color	Completely correlated fronts.	Intensity and strain have identical dependence on potential.	NA

4.6 Acknowledgements

We would like to acknowledge funding through DuPont's Young Professor Grant and the Laboratory for Physical Science, as well as thank the U. S. Army Research Laboratory for use of equipment while completing this research. We also would like

to thank Dr. Donald DeVoe and Dr. Likun Zhu for helping us with Parylene C deposition.

4.7 References

[1] B. Francois, N. Mermilliod, and L. Zuppiroli, "Swelling of polyacetylene when doped by iodine or sodium," *Synth. Met.*, vol. 4, pp. 131-8, 1981.

[2] Q. Pei and O. Inganäs, "Conjugated polymers and the bending cantilever method: electrical muscles and smart devices," *Adv. Mat.*, vol. 4 (4), pp. 277-278, 1992.

[3] T. F. Otero, E. Angulo, J. Rodriguez, and C. Santamaria, "Electrochemomechanical properties from a bilayer: polypyrrole/non-conducting and flexible material -- artificial muscle," *J. Electroanal. Chem.*, vol. 341, pp. 369, 1992.

[4] R. H. Baughman, L. W. Shacklette, R. L. Elsenbaumer, E. Plichta, and C. Becht, "Conducting polymer electromechanical actuators," in *Conjugated Polymeric Materials: Opportunities in Electronics, Optoelectronics, and Molecular Electronics*, vol. 182, *NATO ASI Ser., Ser. E*, J. L. Brédas and R. R. Chance, Eds. Dordrecht: Kluwer Academic Publishers, 1990, pp. 559-82.

[5] R. H. Baughman, "Conducting polymer artificial muscles," *Synth. Met.*, vol. 78, pp. 339-353, 1996.

[6] T. F. Otero, "Artificial muscles, electrodissolution and redox processes in conducting polymers," in *Conductive Polymers: Transport, Photophysics, and Applications*, vol. 4, *Organic Conductive Molecules and Polymers*, H. S. Nalwa, Ed. New York: John Wiley & Sons, 1997, pp. 517-594.

[7] J.-M. Sansiñena and V. Olazábal, "Conductive polymers," in *Electroactive Polymer (EAP) Actuators as Artificial Muscles: Reality, Potential, and Challenges*, Y. Bar-Cohen, Ed. Bellingham: SPIE Press, 2001, pp. 193-222.

[8] M. T. Cortés and J. C. Moreno, "Artificial muscles based on conducting polymers," *e-Polymers*, vol.041, pp. 1-42, 2003.

[9] E. Smela, "Conjugated polymer actuators for biomedical applications," *Adv. Mat.*, vol. 15 (6), pp. 481-94, 2003.

[10] D. Leo, E. Smela, J. Madden, K. Kim, Z. Ounaies, and D. F. Infante, "Standard testing methods for extensional and bending electroactive polymer actuators," Proc. ASME 2005, International Mechanical Engineering Congress and Exposition (IMECE), Orlando, FL, 2005, pp. 2005-82440.

[11] Q. Pei and O. Inganäs, "Electrochemical applications of the bending beam method; a novel way to study ion transport in electroactive polymers," *Sol. State Ion.*, vol. 60, pp. 161-166, 1993.

[12] X. Wang, B. Shapiro, and E. Smela, "Visualizing ion transport in conjugated polymers," *Adv. Mat.*, vol. 16 (18), pp. 1605-1609, 2004.

[13] T. F. Otero and E. Angulo, "Oxidation-reduction of polypyrrole films -- kinetics, structural model and applications," *Solid State Ionics*, vol. 63-5, pp. 803-809, 1993.

[14] T. F. Otero, H. Grande, and J. Rodriguez, "A new model for elecrochemical oxidation of polypyrrole under conformational relaxation control," *J. Electroanal. Chem.*, vol. 394, pp. 211, 1995.

[15] T. F. Otero, H. Grande, and J. Rodriguez, "Conformational relaxation during polypyrrole oxidation: from experiment to theory," *Electrochim. Acta*, vol. 41 (11/12), pp. 1863-1869, 1996.

[16] T. F. Otero, H. Grande, and J. Rodriguez, "An electromechanical model for the electrochemical oxidation of conducting polymers," *Synth. Met.*, vol. 76, pp. 293, 1996.

[17] T. F. Otero, H. Grande, and J. Rodriguez, "Electrochemical oxidation of polypyrrole under conformational relaxation control. Electrochemical relaxation model," *Synth. Met.*, vol. 76, pp. 285, 1996.

[18] T. F. Otero and H. Grande, "Thermally enhanced conformational relaxation during electrochemical oxidation of polypyrrole," *Electroanal. Chem.*, vol. 414, pp. 171, 1996.

[19] T. F. Otero, H.-J. Grande, and J. Rodriguez, "Reinterpretation of polypyrrole electrochemistry after consideration of conformational relaxation processes," *J. Phys. Chem. B*, vol. 101, pp. 3688-3697, 1997.

[20] T. F. Otero, H. Grande, and J. Rodriguez, "A conformational relaxation approach to polypyrrole voltammetry," *Synth. Met.*, vol. 85, pp. 1077, 1997.

[21] T. F. Otero, H. Grande, and J. Rodríguez, "Role of conformational relaxation on the voltammetric behavior of polypyrrole. Experiments and mathematical model," *J. Phys. Chem. B*, vol. 101, pp. 8525-33, 1997.

[22] T. F. Otero and M. Bengoechea, "UV-visible spectroelectrochemistry of conducting polymers. Energy linked to conformational changes," *Langmuir*, vol. 15, pp. 1323-1327, 1999.

[23] T. F. Otero and I. Boyano, "Comparative study of conducting polymers by the ESCR model," *J. Phys. Chem. B*, vol. 107 (28), pp. 6730 -6738, 2003.

[24] T. F. Otero and I. Boyano, "Potentiostatic oxidation of polyaniline under conformational relaxation control: experimental and theoretical study," *J. Phys. Chem. B*, vol. 107 (18), pp. 4269-4276, 2003.

[25] T. F. Otero and J. Padilla, "Anodic shrinking and compaction of polypyrrole blend: electrochemical reduction under conformational relaxation kinetic control," *J. Electroanal. Chem.*, vol. 561 (1), pp. 167-71, 2004.

[26] L. Bay, T. Jacobsen, S. Skaarup, and K. West, "Mechanism of actuation in conducting polymers: osmotic expansion," *J. Phys. Chem. B*, vol. 105 (36), pp. 8492-8497, 2001.

[27] X. Wang, E. Smela, and B. Shapiro, "Understanding ion transport in conjugated polymers," Proc. SPIE 11th Annual Int'l. Symposium on Smart Structures and Materials, EAPAD, vol. 5385, San Diego, CA, 2004, pp. 146-154.

[28] X. Wang, E. Smela, and B. Shapiro, "Understanding ion transport in conjugated polymers," Proc. SPIE 12th Annual Int'l. Symposium on Smart Structures and Materials, EAPAD, San Diego, CA, 2005.

[29] J. H. Kaufman, N. Colaneri, J. C. Scott, and G. B. Street, "Evolution of polaron states into bipolarons in polypyrrole," *Phys. Rev. Lett.*, vol. 53 (10), pp. 1005-8, 1984.

[30] J. L. Brédas, J. C. Scott, K. Yakushi, and G. B. Street, "Polarons and bipolarons in polypyrrole - evolution of the band structure and optical spectrum upon doping," *Phys. Rev. B*, vol. 30 (2), pp. 1023-1025, 1984.

[31] Y. Tezuka, S. Ohyama, T. Ishii, and K. Aoki, "Observation of propagation speed of conductive front in electrochemical doping process of polypyrrole films," *Bull. Chem. Soc. Jpn.*, vol. 64, pp. 2045-51, 1991.

[32] Y. Tezuka, T. Kimura, T. Ishii, and K. Aoki, "Concentration distribution of conducting species with time resolution in electrochemical undoping process at the polypyrrole-film-coated electrode in the light of electric percolation," *J. Electroanal. Chem.*, vol. 395, pp. 51-55, 1995.

[33] J. C. Carlberg and O. Inganas, "Fast optical spectroscopy of the electrochemical doping of poly(3,4-ethylenedioxythiophene)," *J. Electrochem. Soc.*, vol. 145 (11), pp. 3810-3814, 1998.

[34] T. Johansson, N. K. Persson, and O. Inganas, "Moving redox fronts in conjugated polymers studies from lateral electrochemistry in polythiophenes," *J. Electrochem. Soc.*, vol. 151 (4), pp. E119-E124, 2004.

[35] S. Shimoda and E. Smela, "The effect of pH on polymerization and volume change in PPy(DBS)," *Electrochim. Acta*, vol. 44 (2-3), pp. 219-238, 1998.

[36] S. Skaarup, L. Bay, K. Vidanapathirana, S. Thybo, P. Tofte, and K. West, "Simultaneous anion and cation mobility in polypyrrole," *Sol. State Ion.*, vol. 159 (1-2), pp. 143-147, 2003.

[37] H. Mao and P. G. Pickup, "Ion transport in a polypyrrole-based ion-exchange polymer," *J. Phys. Chem.*, vol. 93 (17), pp. 6480-6485, 1989.

[38] E. Smela and N. Gadegaard, "Volume change in polypyrrole studied by atomic force microscopy," *J. Phys. Chem. B*, vol. 105 (39), pp. 9395-9405, 2001.

[39] H. Yang and J. Kwak, "Mass transport investigated with the electrochemical and electrogravimetric impedance techniques 1. Water transport in PPy/CuPTS films," *J. Phys. Chem. B*, vol. 101 (5), pp. 774-781, 1997.

[40] C. K. Baker, Y.-J. Qiu, and J. R. Reynolds, "Electrochemically induced charge and mass transport in polypyrrole/poly(styrenesulfonate) molecular composites," *J. Phys. Chem.*, vol. 95, pp. 4446-4452, 1991.

[41] J. C. Lacroix, K. Fraoua, and P. C. Lacaze, "Moving front phenomena in the switching of conductive polymers," *J. Electroanal. Chem.*, vol. 444 (1), pp. 83-93, 1998.

[42] M. R. Gandhi, P. Murray, G. M. Spinks, and G. G. Wallace, "Mechanism of electromechanical actuation in polypyrrole," *Synth. Met.*, vol. 73 (3), pp. 247-256, 1995.

[43] G. L. Duffitt and P. G. Pickup, "Enhanced ionic conductivity of polypyrrole due to incorporation of excess electrolyte during potential cycling," *J. Chem. Soc. Faraday Trans.*, vol. 88 (10), pp. 1417-1423, 1992.

[44] Y. Li, "On the large overpotential of the first reduction of polypyrrole perchlorate films in organic solutions," *Electrochim. Acta*, vol. 42 (2), pp. 203-210, 1997.

[45] L. Lizarraga, E. M. Andrade, and F. V. Molina, "Swelling and volume changes of polyaniline upon redox switching," *J. Electroanal. Chem.*, vol. 561 (1), pp. 127-35, 2004.

[46] K. West, T. Jacobsen, B. Zachau-Christiansen, M. A. Careem, and S. Skaarup, "Electrochemical synthesis of polypyrrole: influence of current density on structure," *Synth. Met.*, vol. 55-57 (2-3), pp. 1412-1417, 1993.

[47] P. Murray, G. M. Spinks, G. G. Wallace, and R. P. Burford, "In-situ mechanical properties of tosylate doped (pTS) polypyrrole," *Synth. Met.*, vol. 84 (1-3), pp. 847-848, 1997.

[48] E. Smela, W. Lu, and B. R. Mattes, "Polyaniline Actuators,Part 1: PANI(AMPS) in HCl," *Synth. Met.*, vol. 151 (1), pp. 25–42, 2005.

[49] E. Smela and N. Gadegaard, "Surprising volume change in PPy(DBS): an atomic force microscopy study," *Adv. Mat.*, vol. 11 (11), pp. 953-7, 1999.

[50] M. Christophersen, Y. Liu, B. Shapiro, and E. Smela, "Characterization and modeling of PPy bilayer microactuators. Part 1: Curvature," *Sens. Act. B*, vol. 115 (2), pp. 596-809, 2006.

[51] B. Shapiro and E. Smela, "Bending actuators with maximum curvature and force and zero interfacial stress," *J. Intell. Mater. Syst. Struct.*, in press, 2005.

[52] Y. Berdichevsky and Y.-H. Lo, "Polymer microvalve based on anisotropic expansion of polypyrrole," Proc. Mat. Res. Soc. Symp. Fall 2003 Meeting, vol. 782, Boston, 2003, pp. A4.4.1.

[53] A. Della Santa, D. De Rossi, and A. Mazzoldi, "Performances and work capacity of a polypyrrole conducting polymer linear actuator," *Synth. Met.*, vol. 90 (2), pp. 93-100, 1997.

[54] S. W. Feldberg, "Reinterpretation of polypyrrole electrochemistry. Consideration of capacitive currents in redox switching of conducting polymers," *J. Am. Chem. Soc.*, vol. 106, pp. 4671-4674, 1984.

[55] S. Maw and E. Smela, "Effects of monomer and electrolyte concentrations on actuation of PPy(DBS) bilayers," *Synth. Met*., vol.155 (1), pp. 18-26, 2005.

[56] B. G. Streetman and S. Banerjee, *Solid State Electronic Devices*, 5th ed, Upper Saddle River, Prentice-Hall, 2000.

[57] X. Lin, J. Li, E. Smela, and S. Yip, "Polaron-induced conformation change in single polypyrrole chain: an intrinsic actuation mechanism," *Int. J. Quant. Chem.*, vol. 102, pp. 980-5, 2005.

[58] J. P. Aime, F. Bargain, M. Schott, H. Eckhardt, G. G. Miller, and R. L. Elsenbaumer, "Structural study of doped and undoped polythiophene in solution by small-angle neutron scattering," *Phys. Rev. Lett,*, vol. 65 (1), pp. 55-58, 1989.

[59] J. D. Madden, P. G. Madden, P. A. Anquetil, and I. W. Hunter, "Load and time dependence of displacement in a conducting polymer actuator," Proc. MRS Symposium Proceedings, vol. 698, Electroactive Polymers and Rapid Prototyping, Boston, Massachusetts, 2001, pp. 137-144.

Chapter 5 Charge Transport in Conjugated Polymers: Part 2. Modeling and Simulation Results[1]

5.1 Introduction

Ion transport occurs along with electron transport in all applications of conjugated polymers in which the operation of the device depends on significant changes in the oxidation level of the polymer, including batteries and super-capacitors, electrochromic displays, actuators, and chemical sensors. Since the oxidation level of the material changes substantially, the resulting changes in material properties, such as variations in conductivity, cannot be considered to be small perturbations.

The goal of the work in this paper was to develop a model that would correctly predict the dominant features of charge transport in conjugated polymers during electrochemical switching between fully oxidized and reduced states based on fundamental physical equations. The model should therefore make predictions that hold for both oxidation and reduction, under a wide range of experimental conditions, and for all conjugated polymers. Thus, the model was initially developed with the fewest restricting assumptions, and then the consequences of imposing more restrictions was systematically examined. (This is not a black-box model, such as a lumped parameter equivalent circuit model, although such models have been successfully applied to some aspects of switching behavior; see for example [1, 2].)

[1] To be submitted as:

X. Z. Wang, B. Shapiro, and E. Smela, "Charge Transport in Conjugated Polymers: Part 2. Modeling and Simulation Results."

This work expands upon that done by Lacroix et al. [3], who modeled the movement of electrons and ions in conjugated polymers, examining several limiting cases analytically. Here, we take the same basic equations governing electron and ion movements, subject them to boundary conditions, and simulate them, allowing us to examine virtually any case of interest. Simulations offer the advantage of allowing one to visualize the charge concentrations, electric fields, and other variables as they evolve over time. By simulating the geometry described in Part 1 of this series, we are able to qualitatively compare the results of the simulations with the experimental results.

Other prior modeling based on first principles has been done with the aim of predicting the shape of cyclic voltammograms. Those models used simplifying assumptions to make the problem tractable, such as that ions moved solely by ordinary diffusion, that changes in the number of charges on the backbone did not need to be considered, or that charge neutrality held everywhere [4-6]. The current model does not make these assumptions. However, in this paper we do not consider the energetics or kinetics of electron transfer between the polymer and the electrode, and only examine switching to potentials at which this transfer is possible and fast. Including the information on polymer energy levels contained in cyclic voltammograms is outside the scope of this work.

This paper makes two main contributions to our understanding of redox in conjugated polymers. First, it presents a model that accounts for most of the behavior observed during reduction and oxidation (redox) in cation-transporting films over a wide range

of experimental conditions. Second, the model is used to make predictions of the behavior under different conditions and in different systems. These are the first steps toward being able to design devices with particular switching characteristics.

The paper is divided into two parts. In *Part A*, the model is developed. First, an overview of the model is given in section 5.2. (The reader who is not interested in the modeling details but wishes to cut right to the chase can skip from here to *Part B*.) The modeling methods are detailed in section 5.3: the assumptions, governing equations, boundary conditions, etc. The code that was used is available upon request [*]. Section 5.5 explores the behavior of a bare-bones model. Simulations are run to verify that the model gives reasonable results, and the effect of varying the model parameters is examined. This yields a qualitative understanding of the roles of the material constants and experimental conditions in the model. In section 5.6, the complexity of the model is increased to better reflect the physical system, resulting in a "full model". Section 5.7 summarizes the results of *Part A*. In *Part B*, the full model is run for various conditions of interest, since it can be readily adapted to handle different geometries and materials. Section 5.8 includes the oxidation of the ion-barrier covered, cation-transporting film, the removal of the ion barrier, and changing the polymer to an anion-transporter. These scientific results are summarized and discussed in section 5.8.5.

[*] A license for the commercial software package FEMLAB will be required to run the code.

Part A: Model Development

5.2 Model Overview

The model presented here explicitly accounts for the movement of both ionic charge and electronic charge (polarons and bipolarons on the polymer backbone, referred to as "holes" herein in analogy to the positive charges in inorganic semiconductors). In prior versions of this model, hole transport was either neglected [7] or the assumption was made, based on experimental estimates in the literature of the relative mobilities of the polarons and the ions, that the holes moved instantaneously relative to the ions [8]. The latter allowed us to formulate an analytical solution for the hole transport. This simplifying assumption has been lifted here.

There are three mechanisms for charge transport: diffusion, drift (also called migration), and convection. Diffusion occurs in the presence of concentration gradients; Fickian diffusion arises when the probabilities for particle movement are equal in all directions, i.e., if the medium is isotropic. Migration is the movement of a particle under a force, such as the movement of a charged particle under an applied voltage. Since both polarons and ions are charged species, one cannot *a priori* neglect their movement in electrical fields, nor their charge interactions. As reviewed by Lacroix [3], charge transport cannot be described solely by diffusion: the existence of electrical fields in the polymer, particularly in the reduced regions, must be taken into account. Electrochemists have traditionally combined the drift and diffusion terms into one term, called the *electrochemical potential*[*]. For transparency, they are kept

[*] $\Delta\mu_{(2\text{-}1)} = RT \ln a_{A2} / a_{A1} + zF\Delta\psi_{(2\text{-}1)}$

separate here. Lastly, convection is the movement of a particle that is carried in the flow of a fluid, like a boat in a current. This last mechanism is neglected in our model. For ion transport, it is neglected because there are no significant fluid flows through the conjugated polymer**, and for hole transport it is neglected because the polymer chains do not flow as a liquid does (although the chains do undergo local movements such as changes in conformation and reptation). In the electrolyte convection is also neglected since the solution is unstirred. Thus, the model includes one partial differential equation (PDE) for the ion current due to drift and diffusion, and a second PDE for the hole drift and diffusion.

The electric field under which the charges move arises from two sources. Physically, fields are produced by applied voltages on electrodes and by local imbalances between the concentrations of positively and negatively charged species. It only takes a minute charge imbalance to create a large electric field, which means that even if charge neutrality is satisfied almost everywhere, net charge can still become the dominant driver for ion transport [3]. In the model, boundary conditions are used to specify the potentials at key interfaces, and Poisson's equation, a third PDE, relates the gradient of the electrical field inside the polymer to the net charge.

The three PDEs are coupled because the concentrations of holes and ions in the polymer are not independent. In a cation-transporting polymer like PPy(DBS), as holes are withdrawn at the electrode, charge compensating cations enter from the electrolyte. The negatively charged counterions are immobile in the polymer and are

** Solvent diffuses into the polymer independently of ion transport [9], but there is no evidence that it carries ions.

treated as a fixed background in the model. The concentrations of holes H and cations C sum to the concentration of anions almost everywhere, and where they do not, charge neutrality is violated and electrical fields are produced that result in charge migration.

The equations used in our work are the standard ones used for describing charge transport in crystalline inorganic semiconductors like silicon [10] and therefore may be too simple to account for all the physics occurring in the conjugated polymer during redox, a process that has no inorganic analog. However, they provide a first approximation, a starting point in the model-building process. We show in this paper that they do, in fact, account for much of the dominant physics.

Since the equations are coupled, they cannot be solved analytically for any general case. Thus, they are solved numerically using finite element modeling. After solving for the initial conditions (the polymer is fully oxidized or fully reduced before a switching potential is applied at the boundaries), the ion, hole, and potential profiles are allowed to evolve in response to each other, simulating the redox process.

Model development was informed only by experimental results obtained during electrochemical reduction of an ion-barrier covered film of PPy(DBS). Comparison between simulation and experimental results guided the choice of initial and boundary conditions, the meshing and other details of the simulation mechanics, and choices such as how to stipulate the maximum concentration of ions in the material. Since the same governing equations should also hold during oxidation, simply running the model "backwards" by reversing the voltage at the boundaries, with no

other changes, provided an independent check of model validity. By modifying the third PDE to reflect anion transport, we have also been able to make predictions for redox in materials such as PPy(ClO_4). The generality of the model can thus be tested in the future.

5.3 Modeling Methods

This section goes into detail in describing the governing equations, assumptions, boundary conditions, and so forth, used in the model.

5.3.1 Model Properties

5.3.1.1 Continuum Treatment

Since the length scale of the polymer chain segments is small compared to the μm or larger length scales of devices, it is appropriate to use a continuum assumption. That means that the finite element model volume elements are small compared to the device length scales, but large compared to the polaron length scales. Within each volume element there are many ions and/or holes (there are ~10^3 holes in a volume element 10 nm on each side[*]), so it is appropriate to consider concentrations of species instead of tracking individual molecules.

5.3.1.2 Physics and Equations

5.3.1.2.1 Governing Equations

[*] Calculated using the fact that to deposit a film 1 μm thick consumes 200 mC/cm^2, and that approximately 10% of that charge is used for the creation of charge carriers: $0.1*[200*10^{-3}\ C/(10^2*10^6*10^6)]/1.6*10^{-19}$ electrons/C ≈ 1000 electrons/(10 nm)^3).

The first modeling equation (the continuity equation [11]) expresses the conservation of species:

$$\frac{\partial C_i}{\partial t} = -\nabla \bullet \vec{J}_i \tag{7}$$

where C_i is the concentration of species *i* (mol/cm^3) and J_i is the flux (mol/sec-cm^2). C_i is a dynamic variable that depends on space and time, so $C_i = C_i(x,y,z,t)$. This equation holds in the absence of species generation (e.g. by light) or annihilation.

The flux J_i must be expressed in terms of the physical conditions. As mentioned previously, we ignore convection but consider diffusion and drift, $\vec{J}_i = \vec{J}_i^{diff} + \vec{J}_i^{drift}$. Commonly used models for each of these components in inorganic semiconductors are [10, 12] $\vec{J}_i^{diff} = -D_i \nabla C_i$, where D_i is the diffusion coefficient (cm^2/sec), and $\vec{J}_i^{drift} = z_i \mu_i C_i \vec{E}$, where z_i is the positive or negative charge per species molecule, μ_i is the mobility (cm^2/V-sec), and $\vec{E}$ is the electric field, and where $\vec{E} = -\nabla \phi$ and ϕ is the electric potential[**]. The assumptions contained in these two equations are described in [10, 15]. The expression for the diffusion flux, for example, assumes that the particles take a random walk that is unaffected by other particles (dilute solution approximation), and the equation does not apply in systems in which the particles hop between a fixed number of sites.

Substituting the flux equations into (7) results in a PDE for the rate of change of the concentration of species *i* (the cations or the holes) at any location inside the polymer

[**] There are of course other ways of formulating the currents, involving e.g. quasichemical potentials [13], particle jump probabilities in different directions [14], etc.

(8) $$\frac{\partial C_i}{\partial t} = -\nabla \bullet \vec{J}_i = -\nabla \bullet \left(-D_i \nabla C_i - z_i \mu_i C_i \nabla \phi\right)$$

In this framework, D_i and μ_i are not constants, but are functions of the oxidation level of the polymer. (It is possible that they are also functions of other variables, and part of the job of future modeling will be to determine the complete functional dependence of these coefficients.)

In systems at equilibrium with non-interacting particles that undergo random walks and that have a density given by the Boltzmann distribution, D_i and μ_i are related through the Einstein relation: $D_i/\mu_i = kT/q = RT/F$ [10, 13, 14]. In these systems, equation (8) is equivalent to the Nernst-Planck equation [12]. The advantage of the Einstein relation is that it reduces the number of independent coefficients that must be determined. Unfortunately, since diffusion during redox is not Fickian (as shown experimentally in Part 1) and since the density of the ions (or holes) is so high in the fully reduced (oxidized) states that they cannot realistically be considered to be non-interacting, this assumption cannot be made, and the model must examine the effect of a varying **D/μ**. For example, in systems with memory, in which the direction of a previous step affects the direction of the next step, the ratio **D/μ** is concentration-dependent [14]. A more general relationship is

(9) $$\frac{D_i}{\mu_i} = \frac{C_i}{q\frac{\partial C_i}{\partial \eta}}$$

where η is the chemical potential. It has been shown that using this relationship with a Gaussian density of states accounts well for the increase in $\mathbf{D/\mu}$ with concentration that is seen in disordered organic semiconductors [16].

Maxwell's electrostatic equation (Poisson's equation) is used to model the electrical fields, giving the potential in terms of the net charge density $\boldsymbol{Q}$ (C/cm^3).

$$\varepsilon_0 \nabla(\varepsilon \nabla \phi) = Q = \sum_{i=1}^{n} z_i C_i \quad . \tag{10}$$

Here ε_o is the permittivity of a vacuum, ε is the dielectric constant of the material, and z_i is the (positive or negative) charge of the ion or hole. In this paper we used $z_i = 1$ for both the holes and the ions and did not consider e.g. divalent cations.

Equations (8) and (10) encompass the Nernst equation, which is derived by balancing the drift and diffusion terms at equilibrium. In fact, the formulation here is more general since the system is not at equilibrium.

In this model, ion transport is not coupled to mechanical stress using a PDE. Rather, this coupling is handled (section 5.6.1) artificially through using an empirical form for the dependence of the diffusion coefficient on ion concentration: the exponential relationship obtained in Part 1 (Figure 34). Coupling in mechanical effects, such as due to polymer stiffness, conformational changes, or actuation strain, is the subject of future work.

5.3.1.2.2 Boundary and Initial Conditions

To solve the PDEs of equation (8), one for the holes and one for the ions, together with the PDE in equation (10), it is necessary to define reasonable boundary and initial conditions. The boundary conditions should correspond to the physical conditions imposed at the polymer/electrode and polymer/electrolyte interfaces. They therefore require careful consideration in order that they both make physical sense and allow the simulations to run.

At the polymer/electrode boundary there is no ion flux across the interface, as shown in Figure 49 ($\vec{J}_C \cdot \hat{n} = 0$, where $\hat{n}$ is a unit vector oriented perpendicular to the boundary). For the holes, a flux boundary condition was used at the electrode*. During reduction, we set

(11) $$\vec{J}_H = \mu_H H \vec{E}\,.$$

With this expression, the higher the electric field $\vec{E}$ and the higher the hole concentration H in the polymer, the higher the current density crossing from the polymer to the electrode. When the hole concentration falls to 0, current flow between he polymer and the electrode ceases. Since the simulation cannot solve for **H** if **H** is also used in the boundary condition, in the model this is actually phrased as $\vec{J}_H = \mu_H (1 - C)\vec{E}$, which is true almost everywhere by charge neutrality. During oxidation, this boundary condition was changed to

(12) $$\vec{J}_H = \mu_H C \vec{E}$$

* This BC is only used in the 1D model; in the 2D model, a constant hole concentration of C_0 is set at the polymer/electrode boundary.

because the current now depends on the number of available sites onto which a hole can potentially be placed, which is equal to the number of sites occupied by cations. The question arises as to whether to use the ion or hole mobility in these expressions, since ion transport is the rate-limiting step. It turns out that using either μ_H or μ_C gives identical results.

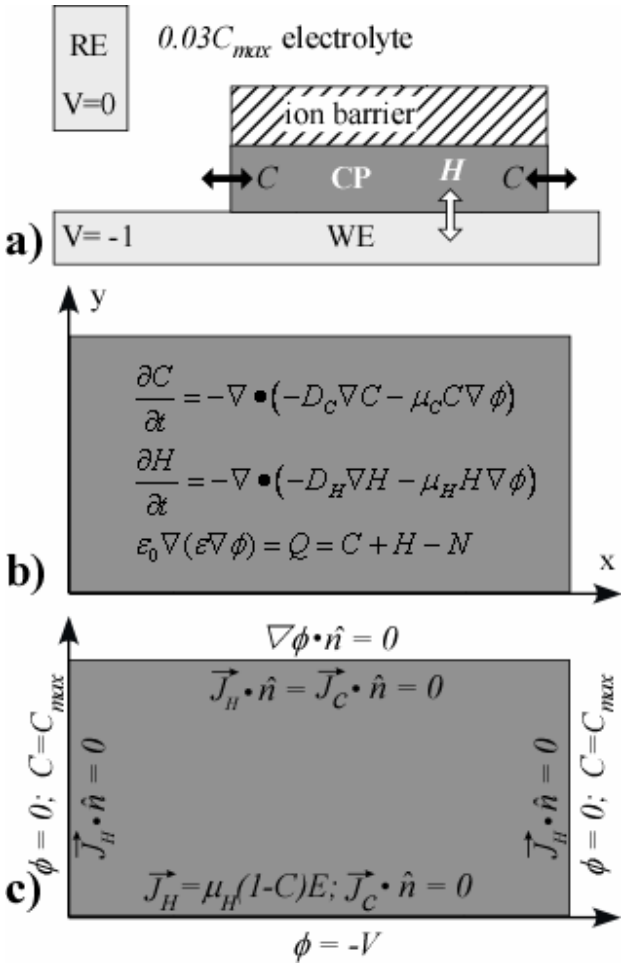

Figure 49. a) Schematic of the physical system, showing the potentials on the working and counter electrodes during electrochemical reduction of a cation-transporting polymer, the bulk concentration of cations in the electrolyte, and the interfaces that ions and holes can cross. b) The PDEs used in modeling the cation-transporting conjugated polymer. c) The boundary conditions used at the polymer interfaces for a basic model that does not include ion transport in the electrolyte (the "base case" model of section 5.5).

The potential at the electrode boundary in the model is, effectively, the applied *overpotential* in the experiments, i.e. the difference between the applied potential and the potential at which reduction (or oxidation) begins. This is distinct from the experimental applied potential (vs. Ag/AgCl) because only fully oxidizing or reducing potentials can be applied in the model, since the model does not yet take into account the energetics of charge transfer seen in the cyclic voltammogram. The electrode/polymer boundary condition used in the model is equivalent to stipulating that there is sufficient energy to allow the holes to cross the interface, in either direction, in response to the electric fields. Note also that in the model, setting ϕ = -1 V at the electrode and ϕ = 0 V at the electrolyte interface is equivalent to setting ϕ = 0 V at the electrode and ϕ = +1 V at the electrolyte, since only the potential *difference* is significant in the mathematics.

At the polymer/electrolyte boundaries, there is no hole flux ($\vec{J}_H \cdot \hat{n} = 0$) since holes cannot enter the electrolyte. In the initial modeling cases (section 5.5), which do not include transport in the electrolyte, a constant ion concentration ($C = C_{max}$) is imposed at the boundary, where C_{max} is the maximum concentration of ions in the polymer. (The effect of varying this boundary condition is shown in the Supplementary Materials, section 1.2.2.7.) Also in the initial cases, the potential is set to zero ($\phi = 0$). This is not physically reasonable, since it ignores the resistive drop in the electrolyte, and thus causes the model to neglect the effects of changing electrical conductivity during redox. Therefore, in section 5.6.4 we expand the model to include the electrolyte.

The top polymer/insulator boundary has no ion or hole flux ($\vec{J}_C \cdot \hat{n} = 0$ and $\vec{J}_H \cdot \hat{n} = 0$), and it is electrically insulating ($\nabla\phi \cdot \hat{n} = 0$). This boundary does not appear in the 1-D simulations.

The initial conditions were an ion concentration of 0 and a hole concentration of $\boldsymbol{H} = \boldsymbol{H_{max}}$ everywhere, representing the fully oxidized state. The initial potential profile was found by solving the electrostatic PDE (equation (10)) based on these ion and hole concentrations.

5.3.1.2.3 Capping the Charge Carrier Density

One of the most difficult but important aspects of model phrasing involved limiting, or "capping", the ion and hole concentrations in the polymer so that they did not exceed $\boldsymbol{C_{max}}$ or $\boldsymbol{H_{max}}$. Physically, $\boldsymbol{H_{max}}$ arises from the fact that the maximum number of polarons is approximately 1 per every 3-4 monomer units in PPy; removing additional electrons requires much higher voltages and results in reactive cation radicals that lead to polymer degradation. The number of holes reversibly removed from the polymer during reduction is equal to the number added during oxidation. By charge neutrality, the number of cations in the reduced polymer cannot exceed the number of holes that were removed, so $\boldsymbol{H_{max}} = \boldsymbol{C_{max}}$. Thus, when the polymer is fully oxidized, $\boldsymbol{H} = \boldsymbol{H_{max}}$ and $\boldsymbol{C} = 0$, and when it is fully reduced, $\boldsymbol{H} = 0$ and $\boldsymbol{C} = \boldsymbol{C_{max}}$.

As mentioned above, in the physical system there is a significant difference in energy (voltage) between electrons removed from the polymer backbones reversibly during redox and electrons removed irreversibly due to chemical reactions. The model,

though, does not include such energetic considerations, and thus without capping, $\boldsymbol{H}$ and $\boldsymbol{C}$ can reach unrealistically high values in the simulations, particularly at the boundaries and particularly during oxidation. This is a result of using a too-large dielectric constant (which was necessary for the simulations to run, as discussed in section 5.4.1): by equation (10), the larger the value of $\boldsymbol{\varepsilon}$, the larger the allowed charge imbalance.

To cap the concentrations, the migration term was set to zero when either the ion or hole concentration went above 1. This was implemented by multiplying the migration term with a step function. This method of enforcing physically reasonable concentrations in the polymer is itself unphysical, in that it does not correspond to a physical process for regulating the charge. However, since this model included neither the energetics of charge injection nor an appropriate dielectric constant, it was necessary to resort to this stratagem. Two other methods were also used to cap the concentrations, including strict enforcement of charge neutrality and dramatically increasing diffusivity once charge concentration was higher than the maximum.

5.3.2 Reducing Model Complexity

In modeling a complex system, it is important to build up the model with simple, *verifiable* pieces. For each piece, it is necessary to understand the numerical problems, the dependence on parameters, and the limiting cases, before moving on to include more degrees of freedom in the model. We discuss three strategies to do this: a) non-dimensionalizing the model to reduce the number of free parameters, b) reducing the number of spatial dimensions by exploiting symmetry or physics, and c)

showing that some parameters are so small or large that their behavior needs not be tracked.

5.3.2.1 Non-Dimensionalization

The modeling was carried out in non-dimensional units and variables. Non-dimensional (i.e. normalized) variables better illustrate the balance between competing physical effects, reduce the number of parameters required to define the model, and allow a single modeling run to predict the behavior in systems with any dimensions. An excellent discussion of the benefits of non-dimensionalization is provided in [17].

Essentially, each non-dimensional variable such as x, y, z, t, ϕ, C, and H, is normalized by a characteristic scale of the system (see Table II). For example, the non-dimensional length x is obtained by taking the dimensional length $\boldsymbol{x}$ (μm) and dividing it by the ion path length $\boldsymbol{L}$ = 150 μm, $x = \boldsymbol{x/L}$, since $\boldsymbol{L}$ is the length that characterizes the size of the experimental system. The boldface variables denote dimensional quantities, and the plain text variables denote non-dimensional variables. Likewise, the non-dimensional potential $\phi = \boldsymbol{\phi} / \boldsymbol{V}$, where $\boldsymbol{\phi}$ is the overpotential and $\boldsymbol{V}$ = 1 Volt. Ion and hole concentrations are non-dimensionalized by $\boldsymbol{C_{max}} = \boldsymbol{H_{max}}$ = 3 M, the maximum concentration of ions/holes in the polymer. All non-dimensional variables are unitless, since the units cancel when dividing by the characteristic quantities.

Table II. Non-dimensional units and variables.

Unitless variable	**Definition (from dimensional variables)**	**Normalization**
x, y, z	$\boldsymbol{x/L, y/L, z/L}$	L = maximum ion path-length
∇	$\boldsymbol{L\nabla}$	
ϕ	$\boldsymbol{\phi/V}$	$\boldsymbol{\phi}$ = applied over-voltage on electrode, $\boldsymbol{V}$=1 Volt
C, H	$\boldsymbol{C/H_{max}, H/H_{max}}$	$\boldsymbol{H_{max}}$ = maximum concentration in the polymer = number of immobile dopant anions
t	$\boldsymbol{t / t_0 = \mu_C V t/L^2}$	time is normalized by ion drift over characteristic length
$\partial / \partial t$	$\left[L^2 / \boldsymbol{\mu_C V} \right] \partial / \partial \boldsymbol{t}$	from definition of t, by chain rule
μ_C	1	get unit non-dimensional mobility by choice of $\boldsymbol{t_0}$
μ_H	$\boldsymbol{\mu_H/\mu_C}$	$\boldsymbol{\mu_C}$
D_C	$D_C = \boldsymbol{D_C / \mu_C V}$	$\boldsymbol{\mu_C}$ and $\boldsymbol{V}$
ε	$\varepsilon = \boldsymbol{\varepsilon V / L_0^2 z H_0}$	by characteristic voltage gradient and charge concentration

Systems parameters such as t_0, L, μ_C, and V are inter-related: characteristic length and voltage scales lead to a characteristic time, t_0, the time that it takes an ion with a mobility of μ_C to traverse a distance L under a voltage V as $t_0 = L^2/(\mu_C V)$. Under this choice of non-dimensionalization, the non-dimensional ion mobility is unity, $\mu_C = 1$. A unit non-dimensional electric field ($\vec{E} = -\nabla\phi = 1$) and a unit ion concentration ($C = 1$) will cause a unit ion drift flux ($\vec{J}_C^{\,drift} = \mu_C C\vec{E} = 1$). The remaining variable non-dimensionalization and the resulting PDEs are derived in detail in the Supplementary Materials (SM 1.2.1.1).

The non-dimensional governing equations for cation-transport are

$$\text{a)}\quad \frac{\partial C}{\partial t} = -\nabla \bullet \left(-D_C \nabla C - C\nabla\phi\right)$$

$$\text{(13) b)}\quad \frac{\partial H}{\partial t} = -\nabla \bullet \left(-D_H \nabla H - \mu_H H\nabla\phi\right)$$

$$\text{c)}\quad \nabla(\varepsilon\nabla\phi) = Q = C + H - 1$$

where μ_C is not shown in the first equation because it is equal to 1. The dimensional model, equations (8) and (10), has 8 free parameters: D_C, μ_C, D_H, μ_H, ε, V, L, and H_0. The non-dimensional model, equation (13), has four: D_C, D_H, μ_H, and ε.

5.3.2.2 Reduced Spatial Dimensions

PDEs are solved in finite element models by meshing the computational region in space into cells (nodes), and then iterating all the variables (ion and hole concentrations and electric potential) in time across all the spatial nodes. Increasing the number of spatial dimensions increases the computational cost, by the square in

going from 1-D to 2-D and by the cube in going to 3-D. Therefore, we started with fast-running 1-dimensional models for initial model development (less than 1 minute of run time), and proceeded to 2-D models (20 to 30 minutes to run each time) once we were satisfied with the qualitative predictions. By the symmetry of the experimental geometry, which had no variation along the long axis of the polymer stripe, 3-D models were not required.

The1-D models were numerically more robust than the 2-D models because they had fewer nodes and required less computer memory. When numerical issues arose, such as resolving steep gradients, including sharp cut-off functions for charge capping, or capturing small dielectric coefficients, they could be solved by increasing the mesh resolution. For the 2-D models, which already operated near the limit of computer memory and speed, this was not a viable option. Thus, the 2-D models were more fragile. They "broke" in several cases, often when large gradients were created. For example, during reduction when ions reached the electrode, the concentration increased to values >> 1, forming a large gradient that was not well resolved by the mesh. Also, high voltages often created large gradients at the electrolyte boundary, which "crashed" the simulation.

At $t = 0$, the electric field lines form arcs through the polymer between the electrode and the electrolyte. Conceptually, the 1-D simulation can be considered to be along one of these lines, as shown in Figure 50. Note that this is the case only because no nucleation occurs in PPy(DBS); to simulate polymers such as PPy(ClO_4) in which ion ingress begins along vertical lines [18], a 2-D or 3-D model would be needed.

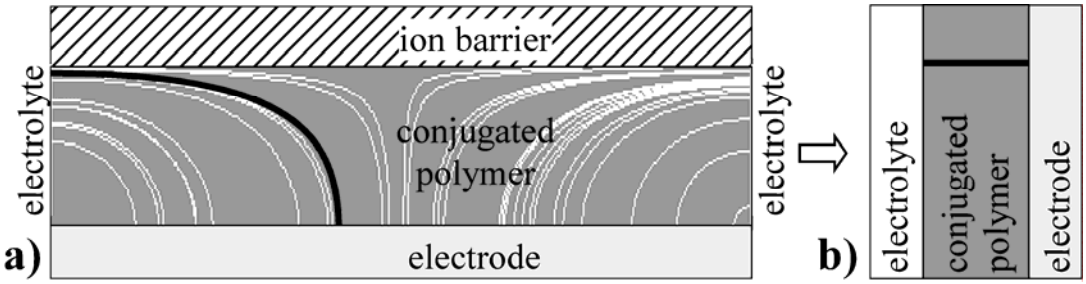

Figure 50. a) A schematic 2-D slice across an ion-barrier-covered, oxidized PPy(DBS) strip at t = 0, showing calculated electric field lines (white) going from the electrode to the electrolyte prior to any ion ingress. The 1-D model can be considered to represent ions and holes traveling along one of these field lines (such as indicted by the black line). For clarity, the vertical axis is much exaggerated in comparison with the experimental geometry. b) The geometry studied in the 1-D models can be considered to be line between the electrolyte and the electrode, although the potentials are not the same as they would be if this were the actual geometry.

Figure 50b is the same geometry as for a layer of conjugated polymer on an electrode uncovered by an ion barrier, so the model should correctly predict the behavior for this case as well. The question arises, how much does the transport differ in the ion-barrier covered case, due to the distortion of the field lines, from the thin film case? This question is taken up in section 5.5.2, in which the 1-D simulation is compared to a 2-D simulation.

5.3.2.3 Parameters

As noted in the introduction, one goal in this paper was to develop a qualitative understanding of how the model behaves as some parameters are increase or decreased relative to the other parameters. These trade-offs are inherent in the non-dimensional parameters. For example, the nondimensional diffusion coefficient, defined as $D_C = \boldsymbol{D_C} / \boldsymbol{\mu_C V}$, represents the ratio of the relative strengths of diffusion to migration (given by the drift coefficient times the applied voltage).

Of the 8 dimensional model parameters $\boldsymbol{D_C}$, $\boldsymbol{\mu_C}$, $\boldsymbol{D_H}$, $\boldsymbol{\mu_H}$, $\boldsymbol{\varepsilon}$, $\boldsymbol{V}$, $\boldsymbol{L}$, and $\boldsymbol{H_0}$, four are known: $\boldsymbol{V}$ is 1 Volt, $\boldsymbol{L}$ is 150 μm, and $\boldsymbol{H_0}$ is 3 M. The value of ε ranges from 10 to 10^4[19-23]. D_C and μ_C only come into the model as a ratio, and initially a ratio of 0.026 was used, taken from the Einstein relation D/μ = kT/q = 0.026 V. The coefficients for the holes were defined relative to those for the ions, and in the baseline model case (Section 5.5.1), they were taken to be 1000 times larger: D_H = 26 and μ_H = 1000. The choice of the factor of 1000 was somewhat arbitrary; it has been assumed in the literature [24] that hole transport is much faster than ion transport. The choice of 1000 was enough to make hole transport virtually infinitely fast relative to ion transport for the experimental configuration reported in Part 1.

5.4 Numerical Methods

5.4.1 General

The non-dimensional PDEs were solved using the PDE modeling software COMSOL, version 3.2. Of the 3 PDEs listed in equation (13), the first two are dynamic (they contain time derivatives *d/dt*) and the last one is static (no time derivative). We proceeded by choosing physical? initial conditions for *C* and *H* at $t = 0$, and then solving the electrostatic PDE (equation (13)c) for a potential ϕ that satisfied the boundary conditions and was consistent with the chosen initial conditions. Using these 3 starting variables $C(x,y,t=0)$, $H(x,y,t=0)$, and $\phi(x,y,t=0)$, the COMSOL software then solved the PDEs at each time step and updated the variable values to find *C*, *H*, and ϕ at $t = \Delta t, 2\Delta t, 3\Delta t, \ldots T$, where *T* is the simulation end time.

We used a number of techniques to enable, and then improve, the numerical simulations. Numerical solution schemes for drift/diffusion PDEs can suffer from numerical instability and spurious oscillations, particularly in simulations with sharp propagating fronts. As is standard in numerical methods, a small amount of artificial diffusion was added to stabilize the simulations (this does not change the character of the solutions). Specifically, we added Petrov-Galerkin compensated artificial diffusion [25], available within FEMLAB, to both hole and ion transport (tuning parameter 0.25). For consistency, we used this in all the simulations, even in cases that already had a significant amount of diffusion.

The smaller the dielectric constant ε, the thinner the regions in which charge neutrality does not hold. For the experimentally reasonable values given above, the non-dimensional dielectric constant $\hat{\varepsilon} = \varepsilon_0 \varepsilon \phi_0 / L_0^2 N_0$ is on the order of 10^{-11}, yielding regions that are so thin that the mesh density required to resolve them was beyond our computing capabilities, even for the 1-D model. Therefore, the models were run with the smallest dielectric constant that could be resolved, $\varepsilon \sim 10^{-3}$. We then verified that as ε decreases, the behavior of the model converged (Supplementary Materials section 1.2.2.1, or SM 1.2.2.1). We also ran cases with charge neutrality strictly enforced ($\varepsilon = 0$). (In the Supplementary Materials, we show that the charge neutral behavior is exactly the limit of the small-ε behavior as $\varepsilon \to 0$.)

5.4.2 2-D Simulations

For the 2-D simulations, there were additional issues. First, finer meshing was needed in regions where the electric field changed rapidly. This was done by solving

the initial potential, then allowing FEMLAB to adapt the mesh spacing given that electric field profile, and using the same mesh in the subsequent simulation steps. In addition, the 2-D simulations were more fragile (prone to "crashing") than the 1-D cases, and the geometry posed some additional challenges. The methods used for dealing with these issues are described here.

In the experiments, the thickness of the polymer (300 nm) was small compared to its half-width (150 μm), giving an aspect ratio (thickness:width) of 1:500. This configuration could not be used directly because it was numerically unstable: if the thickness was discretized into 10 nodes and the width into 100 nodes, then each grid element had an aspect ratio of 1/50 (= 0.3/1.5), but numerical errors increase as mesh elements deviate away from an aspect ratio of 1. To address this problem, the simulated film thickness was set to be 100 times thicker than the actual film thickness so that the grid elements had an aspect ratio of 1:5, close to 1. To correct for the increased thickness, D, μ, and ε in the y-direction (thickness direction) were increased, creating anisotropic diffusion, migration, and dielectric coefficients and in effect making the film act as if it were thinner. To compensate for the 100-fold increase, these parameters should have been increased by a factor of 100^2, with the square arising from the spatial 2nd derivatives in equations (13). However, the largest anisotropy for D and μ that was stable in the simulations was 1000. Thus, the simulation geometry was equivalent to a film with an aspect ratio of 1:158. The dielectric constant in the simulation was only increased by a factor of 10 since it was already too large, and increasing it would have moved ε even further away from realistic values.

The boundary conditions were as shown in Figure 49c. The sharp square corners, where the electric fields became highly concentrated, led to numerical instabilities. The electrode/electrolyte and ion-barrier/electrolyte intersections were beveled to a 45° angle. Also, two different potentials were applied at the polymer/electrode and polymer/electrolyte interfaces, giving a step function at the vertices (see Figure 49c). In practice, this does not arise because electrolyte is not a perfect conductor, and the voltage at the corners will blend smoothly from $\phi = -V$ (polymer/electrode) to $\phi = 0$ (polymer/electrolyte). An exponential decay was used to smoothly change the voltage from the electrode/electrolyte corner to the electrode edge.

5.5 Results 1: Base Case Model and Variations

As discussed above, the model was built based on electrochemical reduction of a cation-transporting material, which displays a rich set of behaviors. To begin the modeling effort, we started with a base case, which was the simplest case, and then increased the model complexity step by step, proceeding to the more difficult, and realistic, cases. This first Results section is thus presented as a theme (the base case) with variations. The latter were used both to confirm that the model was behaving reasonably, i.e., predicting behavior that was qualitatively consistent with the experiments, and to give a firm understanding of how the model behaved and why. After this, in section 5.6, the model complexity is increased by adding non-constant coefficients as well as transport in the electrolyte. Finally, in Part B, the model is used to make predictions of behaviors under new conditions: the potentials are reversed to mimic oxidation, boundary conditions are modified to predict uncovered

films, and equation (13) is modified to predict behavior in an anion-transporting polymer. Results are primarily from the 1-D model, with 2-D simulations run when necessary for confirmation.

Since the base case is the simplest, it does not include transport in the electrolyte, only in the polymer. As mentioned above, the material coefficients D_C, D_H, μ_C, μ_H, and ε depend on the state of the material; they can be functions of ion concentration C, hole concentration H, and the electric potential ϕ. However, in the base case these coefficients were all treated as constant.

5.5.1 Base Case Simulation Results

Figure 51a shows the ion and hole concentrations, and the net charge, as a function of position along the line in Figure 50b partway through the reduction process. As in that figure, the electrolyte is on the left and the electrode on the right; this will be the case in all the figures in this paper. There are several things to note in this figure. In this partially reduced case, the reduced material is on the left, since the cations enter from that side, the oxidized material is on the right, and there is a phase front between them. The nondimensional ion concentration on the left is 1, which means that the material is completely reduced, and it transitions to zero at the phase front. The hole concentration goes the opposite way, from zero on the left to 1 on the right, corresponding to fully oxidized material. The ion and hole concentration mirror each other because they are tied together through equation (13)c.[*] Note, however, that there is a small net charge at the phase front. It is negative, showing that in this

[*] For this reason, in a simulation in which ions were not permitted into the polymer from the left side, nothing happened after a small initial build-up of holes at that interface.

region the retreating holes have not been completely replaced by cations. The holes cannot leave the material any faster than the ions can arrive (or the net charge and electric fields would grow without limit), and, as will be shown below, the velocity of the front is thereby limited by the ion mobility. Another thing to observe in this figure is that with the parameter settings of the base case, the migration component makes a substantial contribution to the transport, as evidenced by the existence of a phase front (since we are using constant coefficients with a Fickian diffusion equation, the front cannot arise from the diffusion component).

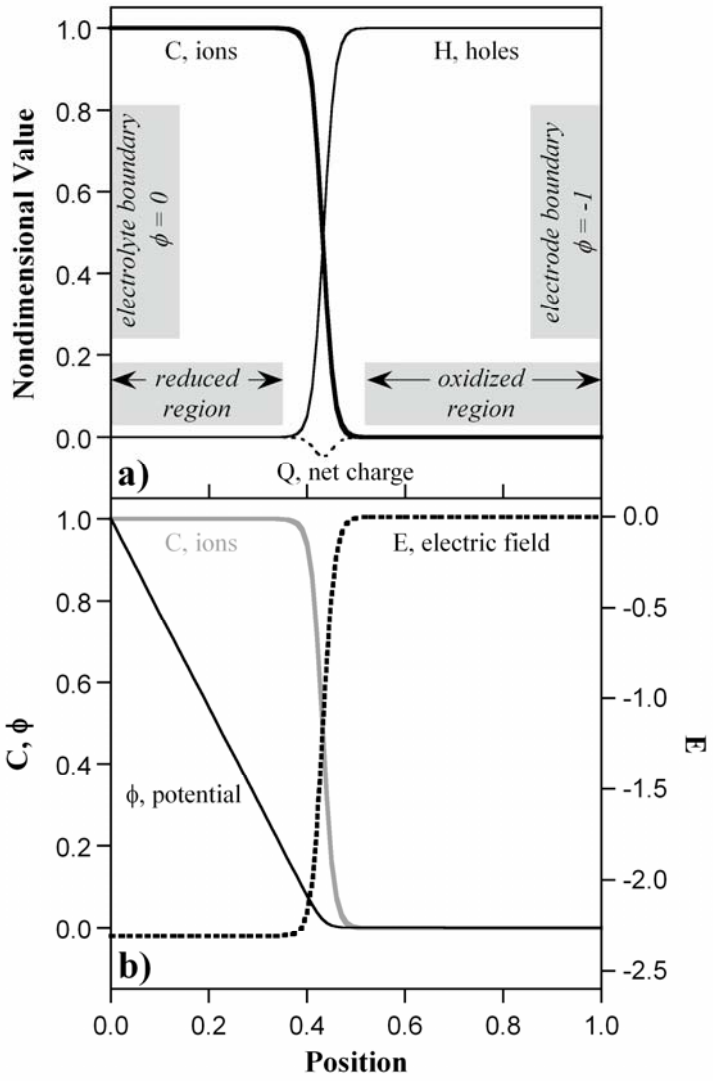

Figure 51. A snapshot during the reduction process in the base case model. a) Ion, hole, and net charge concentrations as a function of position. b) The corresponding potential and electric field, with the ion concentration shown in gray for comparison. Note that the electric field has a different scale.

To relate these curves to the experimental work, the ion concentration should be compared with Figure 28b in Part 1 (see also [7]). The ion concentration in Figure 51a, when mirrored around the y-axis, corresponds to intensity in the experimental profiles. There is reasonable qualitative agreement.

Figure 51b shows the electric field and the potential at the same instant of time. There is almost no potential drop across the oxidized region of the film; instead, the voltage is dropped across the reduced region. This is the result one would expect from a consideration of material conductivity, given by

(14) $\sigma = q(C\mu_C + H\mu_H) \sim qH\mu_H.$

since $\mu_H/\mu_C = 1000$. In the model, this outcome arises automatically from the transport equations. The cation and hole fluxes due to migration are expressed as $J_C = z_C \mu_C C_C E = \sigma_C E$ and $J_H = z_H \mu_H C_H E = \sigma_H E$ (where $z_C = z_H = 1$). Therefore, the migration current density is:

(15) $J = (\sigma_C + \sigma_H)E,$

which is immediately recognizable as a variant of Ohm's law. (A plot of conductivity versus position is given in SM 1.2.2.2). Thus, in Figure 51b the voltage drop is linear with position in the fully reduced region, since this area behaves essentially as a resistor.

The results obtained from using equation (13)b with $\mu_H/\mu_C = 1000$ are virtually the same as were obtained from using an analytical equation for the holes, which was published in [8]. The two sets of curves are plotted together in SM 1.2.2.3.

Figure 51 showed a single snapshot in time, but how do these curves evolve, and how fast does the front travel? Figure 52a shows the ion concentration profile at three times. Initially, the phase front, at which the ion concentration drops from 1 to 0, is narrow, with the curve nearly vertical. As the front travels into the film, it broadens,

and the “foot” at the base goes from an abrupt 90° turn to a concave curve. The profile is convex at the top and concave at the bottom, with an inflection point at a normalized ion concentration of ~0.5. At the inflection point, the movement of the curve can be described using only a forward-directional vector parallel to the position axis.

The net charge Q at these times is shown in Figure 52b, and the electric fields in Figure 52c. The net charge does not remain constant as the front propagates, but diminishes. Its magnitude is determined by $\hat{\varepsilon}$, which is constant, and by the gradient of electrical field across the front, which decreases overtime due to broadening of the front.

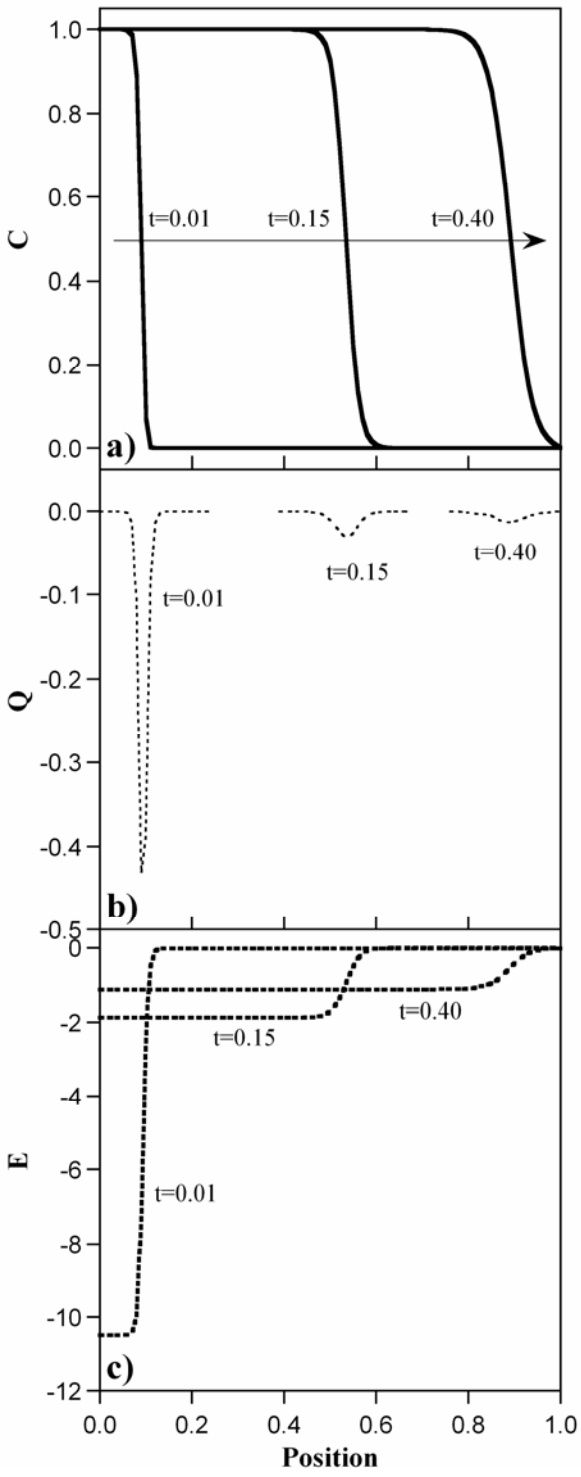

Figure 52. At three times during reduction in the base case, the a) cation concentration, b) net charge, and c) electric field.

By analogy with the Haynes-Shockley experiment [10], one could attribute front movement to drift, and front broadening to diffusion. In a bar of silicon, the front velocity is constant, and the front broadens with the square root of time. It is clear from the time labels in Figure 52a, however, that the front in the conjugated polymer does not move linearly with time. This is because the doping in inorganic semiconductors is constant, whereas the doping level in conjugated polymer changes, so the electric field is not constant.

The front velocity and width are shown as a function of time in Figure 53. The front position x is defined as the position at which the ion concentration is 0.5, and the front width is the distance between the positions at which the ion concentrations are 0.25 and 0.75. Both the front position and broadening have a $\sqrt{t}$ dependence. The total number of ions, obtained by integrating the ion concentration profile, corresponds to the experimental average intensity (Figure 42a in Part 1); this also increases with $\sqrt{t}$. The current is obtained from the time derivative of the total number of ions in the film, and therefore goes as $1/\sqrt{t}$. (It should be noted that the simulation current does not, of course, include capacitive or parasitic currents.)

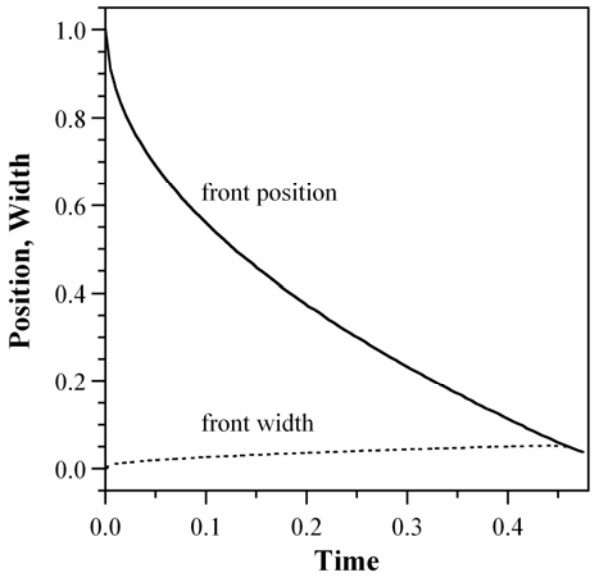

Figure 53. Front position and broadening vs. time during reduction in the base case. Both go as the square root of time. The front broadening curve was obtained by averaging 3 simulations with different meshes to reduce numerical noise.

The reason for the square root of time dependence of the front position is that the voltage is dropped primarily across the insulating region, which grows wider as the reduction front propagates; thus, the electric field in the insulating region, $E = dV/dx$, drops. To explain the $\sqrt{t}$ dependence, we reason thusly. With the transport equations used in the model, the velocity of ions v_C is given by $v_C(t) = \frac{dx}{dt} = \mu_C E(t)$ everywhere in the film, where x is the front position. Since the potential drops linearly with position in the reduced region, $E(t) = \frac{V}{x}$. Substituting, $\frac{dx}{dt} = \mu_C \frac{V}{x}$. In the base case μ_C is constant, and since V, the applied potential, does not change during the reduction process, it is also constant. The solution is therefore $x = \sqrt{2\mu V}\sqrt{t}$.

It is instructive to separate the ion flux into diffusive and drift components, as shown in Figure 54. The cations drift in the reduced region due to the voltage drop, and they diffuse at the phase front, where the concentration gradient lies. This result, together with the others for the base case, shows that the model is functioning properly and behaving reasonably, and that our hypothesis that front movement is by drift and front broadening by diffusion is correct.

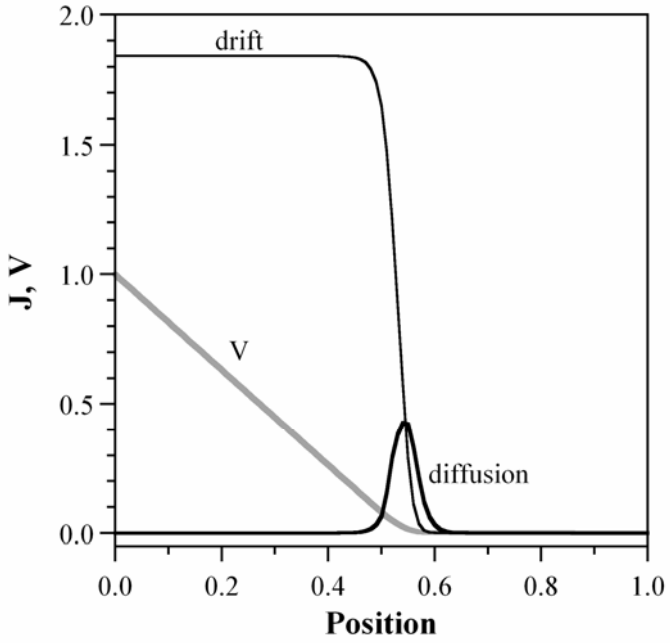

Figure 54. The diffusive and drift components of the ion flux at t = 0.15 during reduction in the base case model, with the potential indicated for reference.

5.5.2 2-D Confirmation of 1-D Results

Before varying the base case parameters, it was important to check that the 1-D simulations had given essentially the same results as a full 2-D simulation. Therefore, the base case was run in 2D (Figure 50a) with the capping function described in 5.3.1.2.3. Figure 55 shows snapshots of the ion, hole, and net charge

concentrations half-way through the reduction process. As in the 1-D case, the ions entered the film as a front, with a net negative charge between them and the holes.

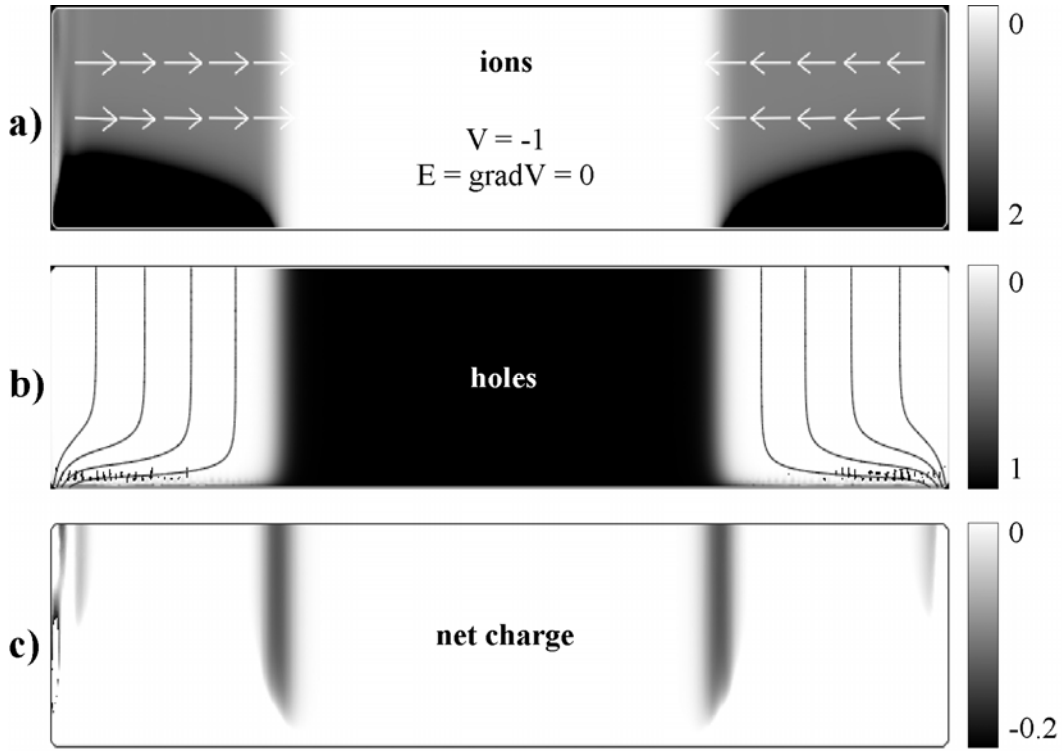

Figure 55. Concentration profiles resulting from running the base case in a 2-D simulation. a) Ion concentration, indicated by gray-scale intensity, with black representing 2 and white 0; the gray in the reduced area corresponds to C = 1. The arrows show the electric field direction and strength. b) Hole concentration, with the lines showing contour plots of constant potential. c) Net charge, shown with a magnified gray scale for clarity.

The most important thing to note in Figure 55a is the electric field direction. After time t = 0 (shown in Figure 50a), the field lines become parallel with the bottom electrode, leading the ions inward in a straight line. The field magnitude is constant in the reduced area and drops to almost zero in the oxidized area. Correspondingly, the lines of constant potential Figure 55b are uniformly spaced in the reduced region, showing that the potential drops linearly along x, and the lines are vertical, showing that along the film thickness the potentials are essentially constant. As a

consequence, the 1-D and 2-D simulation results are virtually identical, as shown in Figure 56*. The Supplementary Materials shows that the front velocity in the two models is almost the same.

It should be noted that the fields are distorted at the bottom electrode, as seen in both the ion concentrations and the potential contours. The reasons for this are twofold. One is the too-large dielectric constant that had to be used in the simulation, which allowed the net charge to grow to high values, despite the use of the capping function. The second was the high field concentrations at the corners. Only the upper portion of the simulated film was therefore used to derive Figure 56.

* A scaling factor for time was needed when comparing the 1D and 2D results. The Supplementary Materials contains a mathematical derivation of this factor.

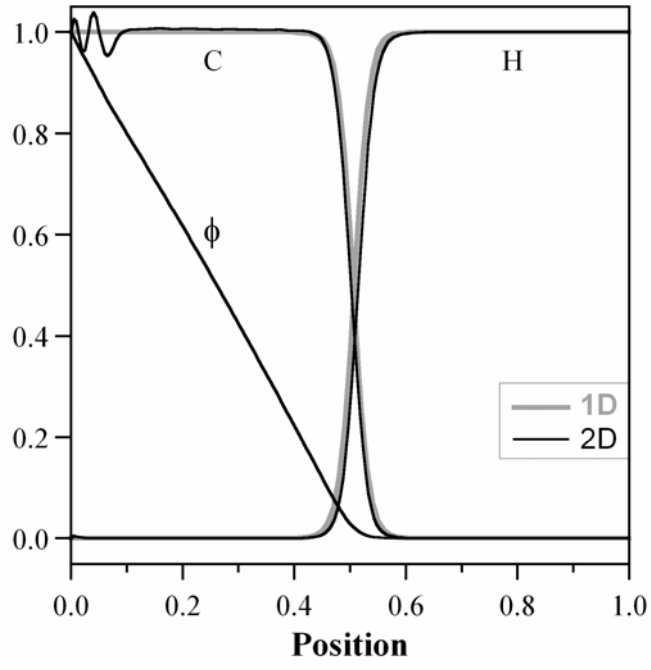

Figure 56. Comparison of ion, hole, and potential profiles from the 1D and 2D simulations at the same electrochemical reduction level. (The wiggles in the 2D ion profile on the upper left are from numerical noise.)

5.5.3 Parameter Variation

In this section, the outcomes from varying the base case parameters are presented so that the basic model can be fully understood. Only one parameter is varied at a time, with the others kept the same as in the base case. Once the effect of these variations is understood, and the reasonableness of these results is confirmed, then the model complexity can be increased to represent the experimental configuration more realistically.

5.5.3.1 Voltage

Changing the voltage at the polymer/electrode boundary corresponds to changing the applied overpotential in the experiments. The model was run with potentials at the boundary between 0.001 and 10 (Figure 57a).

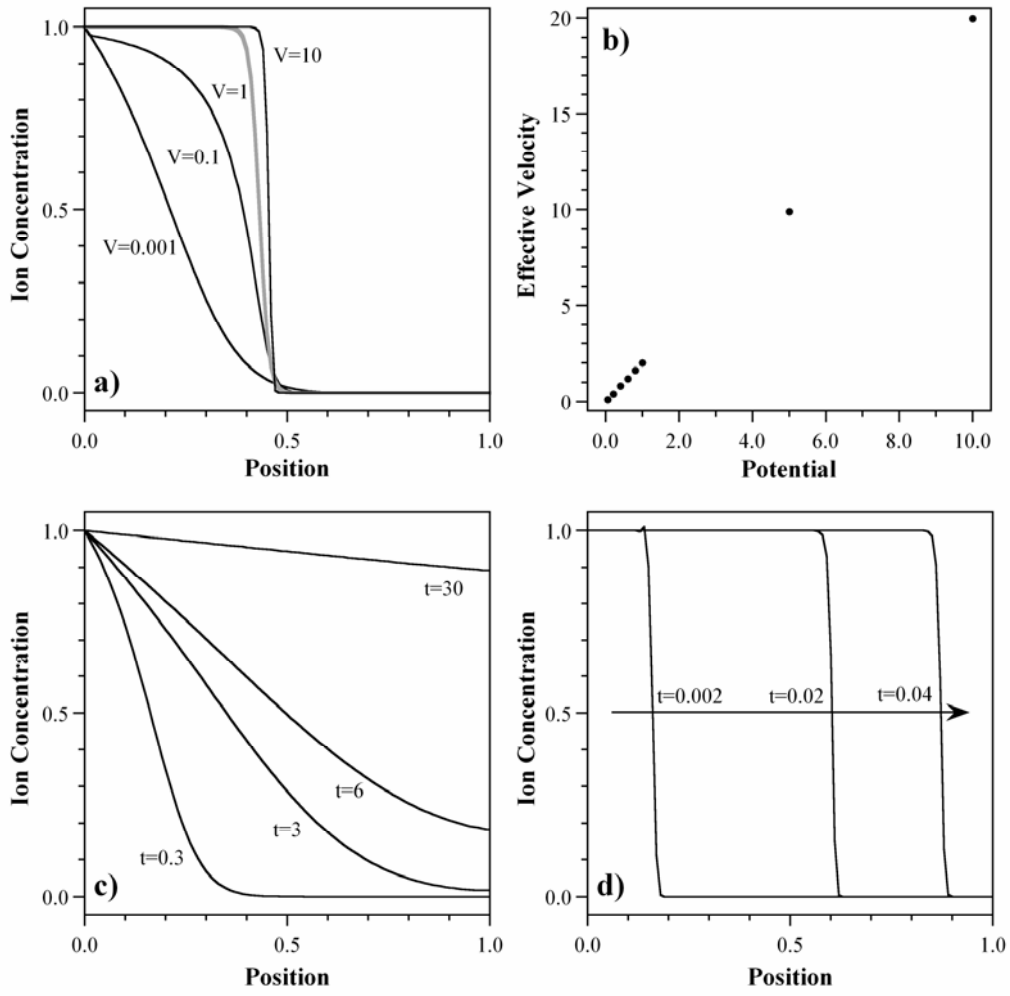

Figure 57. a) Ion concentration profiles for a range of reducing voltages applied at the polymer/electrode boundary in the base case model. The profile with the standard base case parameters is indicated by the gray line. b) Front velocity as a function of voltage. c) Ion profiles at different times for V = 0.001. These ion concentration profiles are similar to those obtained when the ion move under diffusion only (compare Figure 63). d) Ion profiles at different times for V = 10, which is essentially a migration-only case.

Lower-voltage profiles are broader, and the ions move more slowly. In fact, when the voltage is close to zero, at V=0.001, the ion concentration profile has no phase front. This happens because the diffusion and drift terms add linearly in the transport PDEs. The drift term increases linearly with the field, and thus at each point in the material, it increases linearly as the voltage is raised. Changing the voltage therefore dials the size of the drift term relative to the diffusion term. (To qualitatively compare the experimental data, see Figure 28 in Part 1.) The net charge at the front also decreases when the reduction potential is lowered, as shown in SM 1.2.2.4, because lowering the potential lowers the gradient of the electric field, to which Q is proportional by equation 7c.

In Figure 57b, the front velocity is plotted as a function of the voltage. Since the velocity decreases with time, an *effective velocity* had to be defined. This was taken as the distance traveled by the front divided by the time it took to get there, where the distance that was used was from the electrolyte to the electrode (1 in normalized distance), and the front position was, as above, the point at which the ion concentration was 0.5. The effective front velocity was linear with voltage. Qualitatively, this is what occurred in the experiments (Figure 30a, Part 1).

One limiting case arises when the voltage is turned off completely, giving a profile for diffusion only, and another arises when the voltage is very high, giving a profile for drift only. However, V cannot be set identically to zero in the model, because if the migration term vanishes, then charge neutrality cannot be enforced and the motion of the ions and holes becomes uncoupled, leading to non-physical results (SM

1.2.2.8). Instead, a very small value of V was used, $V = 0.001$. To emulate transport under migration only, a large value of V was used, $V = 10$. These limiting cases show what each component of the PDE does separately, as illustrated in Figure 57c and d. (Note that the times in these two panels differ by two orders of magnitude.) Under diffusion only, ions initially (see $t = 0.3$) enter the polymer rapidly, forming something like a front, in that the part of the film on the left is reduced and the part on the right is oxidized. A short time later, however, the polymer is partially reduced everywhere. The ion concentration at $x = 0$ stays fixed at 1 by the boundary condition, and the level throughout the rest of the polymer gradually rises. The polymer requires a long time ($t > 30$) to become fully reduced. In the limiting case of migration only, there is a definite front, on one side of which $C = 1$ and on the other side of which $C = 0$, that moves into the film. This front does not broaden over time.

The *effective broadening velocity* was determined from the width of the front at time $t = 0.4$. If the front broadening were due only to diffusion, then it would not depend on the potential. The front width as a function of potential and the effective front broadening velocity are shown in Figure 58. There is a strong voltage dependence, with broadening decreasing logarithmically as the potential is raised.

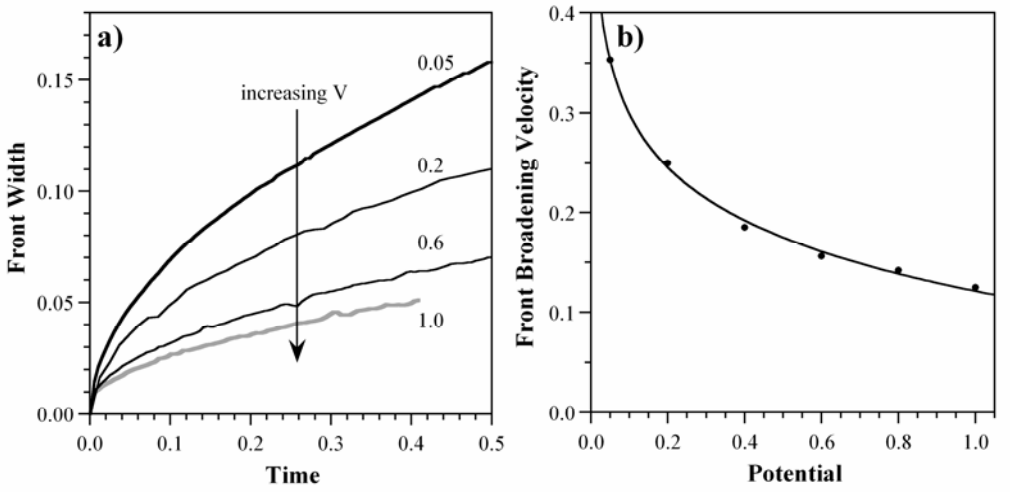

Figure 58. a) Front width over time at different applied potentials (indicated) during reduction obtained using the base case model. b) Effective front broadening velocity vs. potential. (The squiggles are due to numerical noise.) The curve is a logarithmic fit to the simulated points.

The front broadening is under the influence of both diffusion and migration. Diffusion tries to increase the front width to lower the concentration gradient, while migration decreases the front width to lower the net charge. The migration term increases with the overpotential, and the front broadening is thus found to be slower, as expected. The effective front broadening velocity does not decrease linearly with potential: higher voltages also create sharper phase fronts that further lower the diffusion contribution to front broadening. A theoretical analysis of the front broadening is presented in the Supplementary Materials (SM 1.2.1.3).

5.5.3.2 Relationship between D and μ

Another, essentially equivalent, way to vary the relative contribution of the diffusion and migration terms in the base case model, in which the diffusivity and mobility are constant, is through their ratio. This was set to $D/\mu = 0.026$ for both ions and holes in

the base case, where that value arose from assuming that the Einstein relation was valid. Increasing the ratio has the same effect as lowering the reduction potential (as shown in SM 1.2.2.10). Also, as pointed out previously, since the density of ions (or holes) is so high in the fully reduced (oxidized) state that the charges cannot realistically be considered to be non-interacting, the assumption that the Einstein relation is valid cannot be made blindly, and the model must examine the effect of a varying D/μ.

We therefore examined how varying the D/μ ratio based on the more general relationship between diffusivity and mobility given in equation (9) changed the concentration profiles. Specifically, Figure 59 shows the effect on the ion profile if D_C/μ_C was proportional to C. Since it is not clear how to choose the magnitude of this function to best compare with the base case, three relationships were used: 1. $D_C = 0.026(1+5C)$, 2. $D_C = 0.026(1+5C)/3.5$, and 3. $D_C = 0.026(1+5C)/6$ ($\mu_C = 1$ for all cases). The first gives an averaged (over concentration) D/μ 6 times higher than the 0.026 of the base case, the second gives the same average D/μ, and the third gives ~2 times lower average D/μ but the same maximum D/μ, thereby bracketing the base case. In Figure 59, these three relationships are noted as higher, same, and lower, respectively.

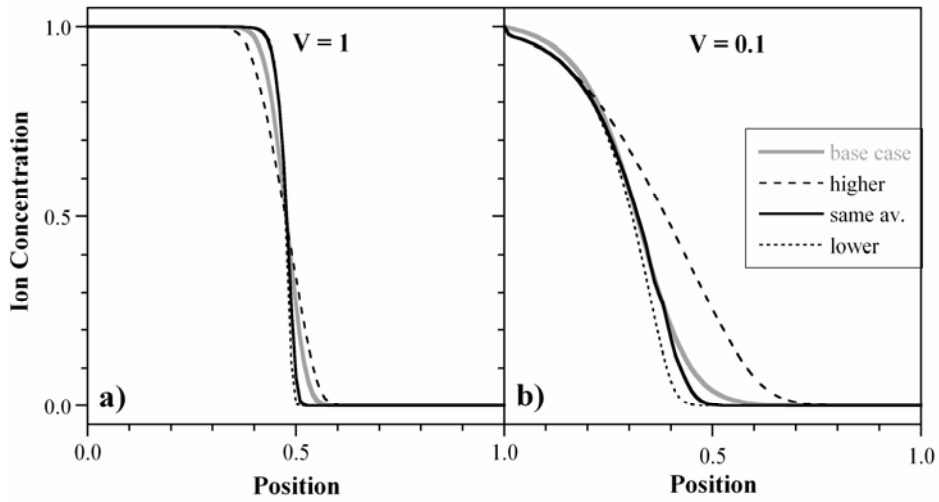

Figure 59. Ion concentration profiles in the base case model during reduction when D_C/μ_C is not constant (base case, gray line) but proportional to C (other lines). a) $V = 1$, $t = 0.12$. b) $V = 0.1$, $t = 0.52$.

For ϕ = -1, the speed of the front is not significantly changed by the alteration in D_C/μ_C because front propagation speed is dominated by migration, so a variation in the diffusivity has a negligible effect. The front width is affected, however. For the relationship labeled "same", the front is narrower than the base case, particularly at the foot where C is small. The difference between "same" and "lower" is also seen at the foot, becoming even sharper for the latter. For "higher", the front is broader everywhere. The same basic behavior was seen for ϕ = 0.1. Thus, using a more general relationship between D_C and μ_C only has a minor effect on the simulation predictions, and one that would be difficult to observe experimentally.

5.5.3.3 Finite Hole Mobility

Whether the electron movement or the hole movement is rate-limiting depends on their relative mobility. Experimental studies have suggested that hole transport is orders of magnitude faster [27-29]. Even so, hole transport may be the rate-limiting

step in some experiments, such as those of Tezuka et al. [30-32]. The value of adding equation (13)b to the model, over our prior work in which an analytical equation was used, is that it allows us to examine such cases.

The ion concentration profile resulting from setting the hole mobility equal to the ion mobility is shown in Figure 60a in comparison with the base case, in which hole mobility was 1000 times higher. (Additional ion concentration profiles can be found in SM 1.2.2.4.) The corresponding potentials as a function of position are shown in Figure 60b.

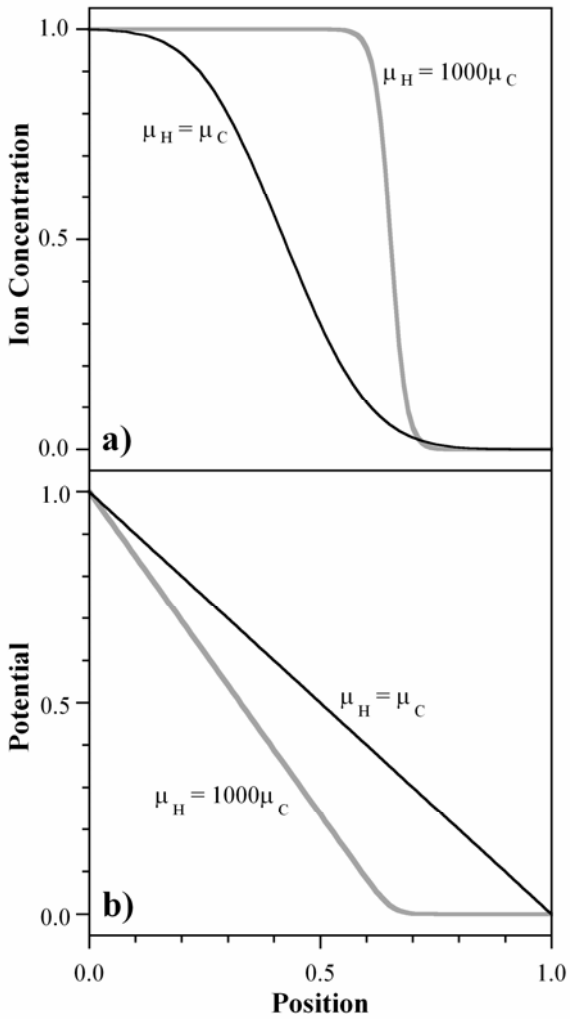

Figure 60. a) Ion concentration profiles from the base case simulation when the hole mobility is set equal to the ion mobility during reduction. The gray line shows the base case with the usual 1000:1 ratio of hole mobility to ion mobility at the same time (t=0.22). b) The corresponding potential profiles.

The voltage profile changes significantly, dropping linearly between 0 and 1. This can, of course, be seen by examining equation (14): since the conductivity and charge density of the oxidized and reduced regions are identical, Ohm's law dictates a constant potential drop. As a general rule to understanding the simulation results, the key is the potential profile that develops in the polymer under different conditions. Lowering the hole mobility, changing the boundary conditions, or introducing

concentration-dependent coefficients changes the potential profile, and thus the charge transport. The lower potential drop over the reduced region, since the drop now occurs over the entire film, lowers the front velocity. The front is also wider than in the base case since the electric field in the film is smaller, which allows diffusion to broaden the fronts more quickly (see Figure 58).

The front position is shown as a function of time in Figure 61. As noted above, the front moves more slowly when the mobilities are equal, but more importantly the velocity is *constant*, a direct result of the unvarying potential across the film. In PPy(DBS), there is 4 orders of magnitude difference between the conductivities in the oxidized and reduced states, so this does not explain experimental results in Part 1 (Figure 25. Phase fronts propagate between $\sqrt{t}$ and t.). However, this case might be observed in other organic systems having poor hole mobility arising from defects or other energy barriers; a change from $\sqrt{t}$ to t might also occur upon polymer degradation, which would have the effect of lowering the conductivity in the oxidized state.

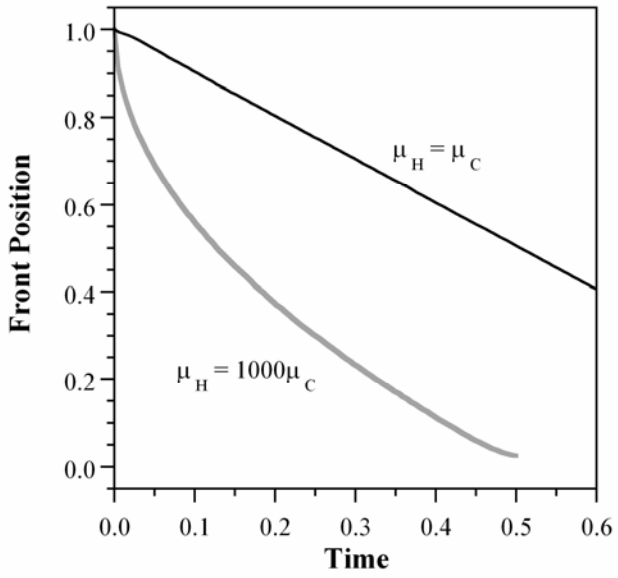

Figure 61. Position of the phase front vs. time when the hole mobility is set equal to the ion mobility in the base case model during reduction; the gray line shows the usual base case result.

5.5.3.4 Charge Neutrality Strictly Enforced

The argument has been made that charge neutrality cannot be violated during redox in a conjugated polymer because the high hole mobility will produce near-perfect charge shielding. Equation (13)c was therefore modified as follows to explore the effect of enforcing zero net charge*:

$$\nabla \bullet (\mu_C C \nabla \phi + \mu_H H \nabla \phi) = 0 \qquad (16)$$

This has the same effect as setting $\varepsilon = 0$ in equation (13)c and setting the diffusion terms in equations (13)a,b equal. When $\varepsilon = 0$, there can be no net charge, so the drift

* Adding the hole and ion transport equations, $\frac{\partial (C+H)}{\partial t} = -\nabla \bullet [(-D_C \nabla C - \mu_C C \nabla \phi) + (-D_H \nabla H - \mu_H H \nabla \phi)]$. By charge neutrality, we have $H + C = 1$. Substituting, $-\nabla \bullet [(-D_C \nabla C - \mu_C C \nabla \phi) + (-D_H \nabla H - \mu_H H \nabla \phi)] = 0$. Neglecting diffusion leads to equation (16).

flux $J_{drift} = \mu_C C\nabla\phi + \mu_H H\nabla\phi$ is constant. These simulations were less stable, and so the maximum ratio of μ_H/μ_C that could be used was 5. Otherwise, the settings were the same as those used in the base case.

The simulated polymer still reduced under these conditions, and this occurred through migration of a front that broadened over time and whose velocity was proportional to the applied voltage, just like in the base case. In addition, the front shapes were similar. The ion and potential profiles and the front position vs. time are shown in the Supplementary Materials (SM 1.2.2.9). (They are not shown here because the ratio $\mu_H/\mu_C = 5$ makes direct comparison with the base case impossible; these results are more comparable to those in the previous finite hole mobility section.)

The results of this simulation are significant because only the voltage drop over the polymer provided the driving force for reduction; there was no contribution from net charge, yet the results were essentially the same. The question of whether charge neutrality is or is not strictly enforced everywhere is therefore largely moot, at least as concerns predictions of charge transport behavior.

5.6 Results 2: Increased Model Complexity

The simplicity of the base case model allowed good demonstrations of how the model parameters (drift, diffusion, voltage, hole mobility, and charge neutrality) affected the simulated behavior. However, this simplified model did not take into account the experimentally observed concentration-dependence of the mobility, nor did it include the electrolyte, assuming that ion transport in the electrolyte was not a rate-limiting

process. In this section, the model complexity is increased to take these into account with the aim of making more realistic predictions.

5.6.1 Nonconstant Coefficients

Constant diffusivity and mobility are appropriate when neither the polymer structure nor the movement of solvent affect ion transport, and diffusion is consequently Fickian. Experimentally, however, ion transport has been found to depend strongly on the state of the polymer matrix [33], and Otero et al. [18] have developed a very successful conformational relaxation model to predict peak positions in chronoamperograms that takes the state of the matrix into account. Thus, our model needed to have a mechanism for handling non-Fickian diffusion. One way that non-Fickian diffusion has been dealt with in the literature (albeit with varying degrees of success) has been through a concentration-dependent diffusion coefficient [34, 35]. In this section, we explore the results of taking this approach.

It should be pointed out that in order to properly handle polymer relaxation effects, a mechanical model needs to be incorporated into our transport model, which will be the subject of future work. Nevertheless, it is of value to study the incorporation of a rudimentary mechanism to make diffusion non-Fickian.

5.6.2 Diffusion and Migration

Previously studied polymers in which case II diffusion occurs [36, 37] did not have charged species moving in an applied electric field, as in our case. We therefore ran two scenarios. In the first, drift was included, and the link between diffusivity and mobility that was imposed in the base case, $D/\mu = 0.026$, was maintained so that the

mobility had the same concentration dependence as the diffusivity. This case was expected to give results that agreed more closely with our experiments than the base case with constant coefficients. We had shown that the experimental front velocity vs. ion concentration data in Part 1 (Figure 34, showing the velocity vs. consumed charge) could be reasonably well fit with coefficients of the form

(17) $D_C = D_0 e^{2C}$

(18) $\mu_C = \mu_0 e^{2C}$,

so this was the form used in the PDE for ions. The PDE for the holes was left unaltered, and no other changes were made to equation (13).

Figure 62 shows the resultant ion concentration profile. Using a concentration-dependent diffusivity and mobility created a sharper front than did the base case. The phase front and front broadening still propagate with $\sqrt{t}$, but with an artificially higher velocity because of the larger magnitude of the coefficients. (In the figure, the ion concentration profile of the base case was taken when t = 0.12, while that of the new case was taken at t = 0.02.)

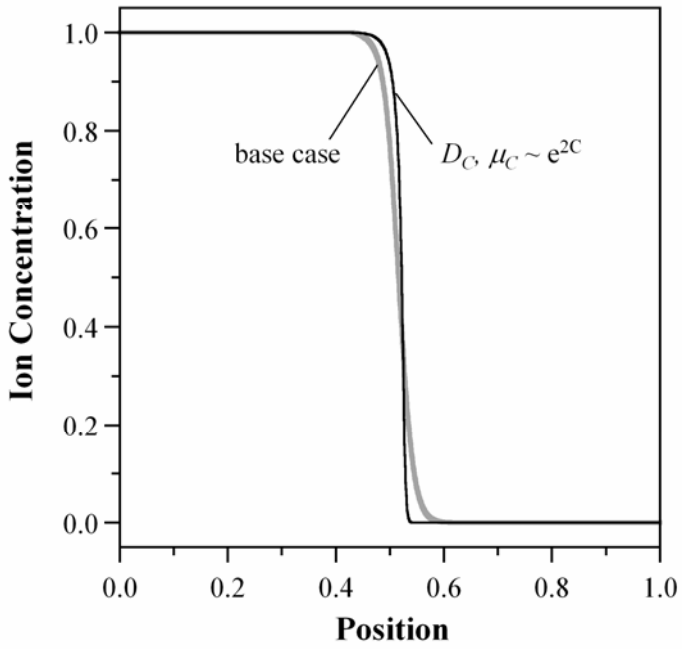

Figure 62. The ion concentration profile that results from using non-constant coefficients (equations (17) and (18)) at a point when the film is approximately halfway reduced compared to the base case when the front is in the same position.

The differences in the predictions of this model versus the base case would again be difficult to distinguish experimentally. This addition to the model is therefore not critical if charge transport is dominated by migration. We include it, however, in all the sections that follow, unless otherwise noted, because we know with certainty from experimental results that diffusion in these systems is not Fickian.

5.6.3 Diffusion Only

In a second case run with non-constant coefficients, the migration term in equation (13)b was removed so that the ion transport PDE had only a diffusion term. The motivation for simulating this case was to determine the form of the dependence of D_C on C that would be needed to produce a front in the absence of migration. Lacroix

et al. [3] had previously shown that a hole diffusivity D_H that increased steeply with the concentration of oxidized sites could lead to a moving front, and for completeness we now did this for ion diffusivity. Furthermore, this case is of interest because a number of theories have assumed that charge moves only due to diffusion. Once again, only the diffusivity of the ions was made concentration-dependent, and the PDE for holes was left unaltered.

Figure 63 shows ion concentration profiles for three relationships between diffusivity and ion concentration: a linear relationship,

(19) $D_C = D_0 (1 + 5C)$,

the exponential relationship from the experiments (equation (17)), and an even steeper exponential relationship,

(20) $D_C = D_0 e^{5C}$.

The linear relationship was designed to have the same diffusivity as equation (17) at an ion concentration of 1.

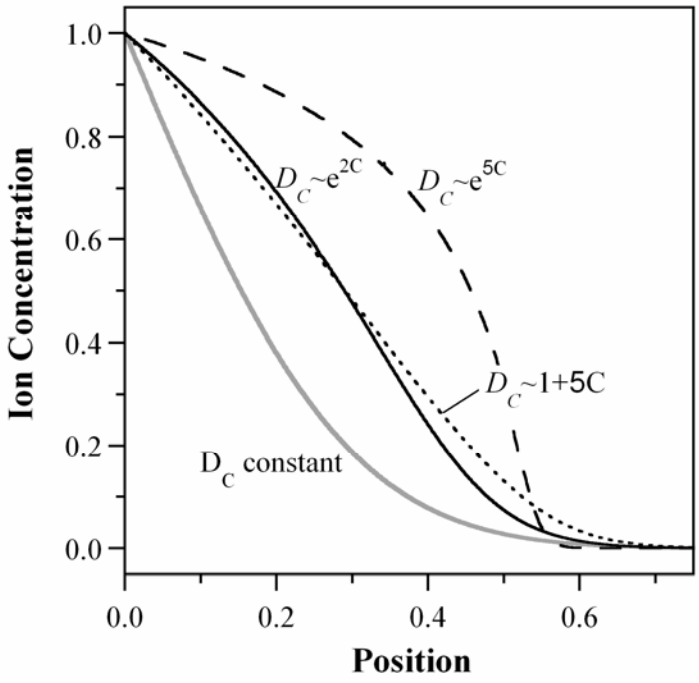

Figure 63. Ion concentration profiles resulting from three concentration-dependent ion diffusivities when ion transport is solely by diffusion during reduction in the base case model. The case with diffusion only and constant coefficients is shown for comparison (gray line).

The linear relationship, unsurprisingly, produces no front in the event that transport is by diffusion alone. The experimental relationship $D_C \sim e^{2C}$, however, results in a curve with an inflection point, which is thus quasi-front-like. The very steep exponential relationship of equation (20) produces a clear front, and its position changes with the square root of time. However, since there is no migration in this model, the front velocity is independent of the voltage. Of these curves, D_C = constant most closely resembles the experimental color profiles. This may indicate that D_C does not have the same exponential dependence on C as μ_C does, but rather is constant. Alternatively, it indicates that the form of the diffusion term in the model is fundamentally incorrect, and is not helped by using non-constant coefficients; rather,

a different method of handling the non-Fickian diffusion is needed to correctly model transport at low V.

5.6.4 Addition of the Electrolyte

The next step in increasing model complexity was to add ion transport within the electrolyte, retaining the non-constant coefficients. With this addition, the model was as complete as it could be made based only on charge transport PDEs and the Poisson equation. We therefore refer to this as the "full model" and use it in Part B of this paper to examine how changes in the polymer or the experimental configuration change the ion transport behavior.

In the model up to this point, the same voltage drop was imposed across the polymer throughout the reduction process, regardless of whether it was oxidized, and thus highly conductive, or reduced and highly resistive. In reality, however, the potential is instead dropped across the electrolyte when the polymer is conductive. Considering the polymer and the electrolyte as if they behave as two resistors in series, the potential across the polymer (which has a variable resistance) depends on the magnitude of its resistance versus that of the electrolyte through a simple voltage-divider relation. Thus, this full model was expected to give more accurate predictions of the electric fields in the film, which translates directly to better predictions of ion profiles and front velocities vs. time.

Another reason that it was important to add the electrolyte was to examine the effect of ion depletion and ion double-layer buildup at the polymer/electrolyte boundary. It has been postulated that even if ion transport is by diffusion only, a high ion

concentration in the double layer may account for the observed faster redox speeds with higher applied voltages (diffusive elastic metal model [38]). This could only be investigated by the addition of the electrolyte.

5.6.4.1 Full Model

The electrolyte was added as a second material, as illustrated in Figure 64. Charge transport was governed by the following PDEs. These are essentially identical to those used in polymer, but instead of holes, equation (22) accounts for the anions, and the net charge in equation (23) is simply given by the difference between the anion and cation concentrations at a given location. Convection, which is small in unstirred solutions, was not included in the electrolyte model.

$$\frac{\partial C_e}{\partial t} = -\nabla \bullet (-D_{Ce} \nabla C_e - \mu_{Ce} C_e \nabla \phi) \tag{21}$$

$$\frac{\partial A}{\partial t} = -\nabla \bullet (-D_A \nabla A + \mu_A A \nabla \phi) \tag{22}$$

$$\varepsilon_o \nabla (\varepsilon_e \nabla \phi) = Q = C_e - A \tag{23}$$

Here C_e is the cation concentration in the electrolyte, A is the anion concentration in the electrolyte, D_{Ce} is the diffusivity and μ_{Ce} is the mobility of the cation in the electrolyte, D_A is the diffusivity and μ_A is the mobility of the anion in the electrolyte, and ε_e is the dielectric constant of the electrolyte. The ion diffusivity and mobility in the polymer are as given by equations (17) and (18), so we now have a complete model that also takes into account the concentration-dependence of μ_C and D_C.

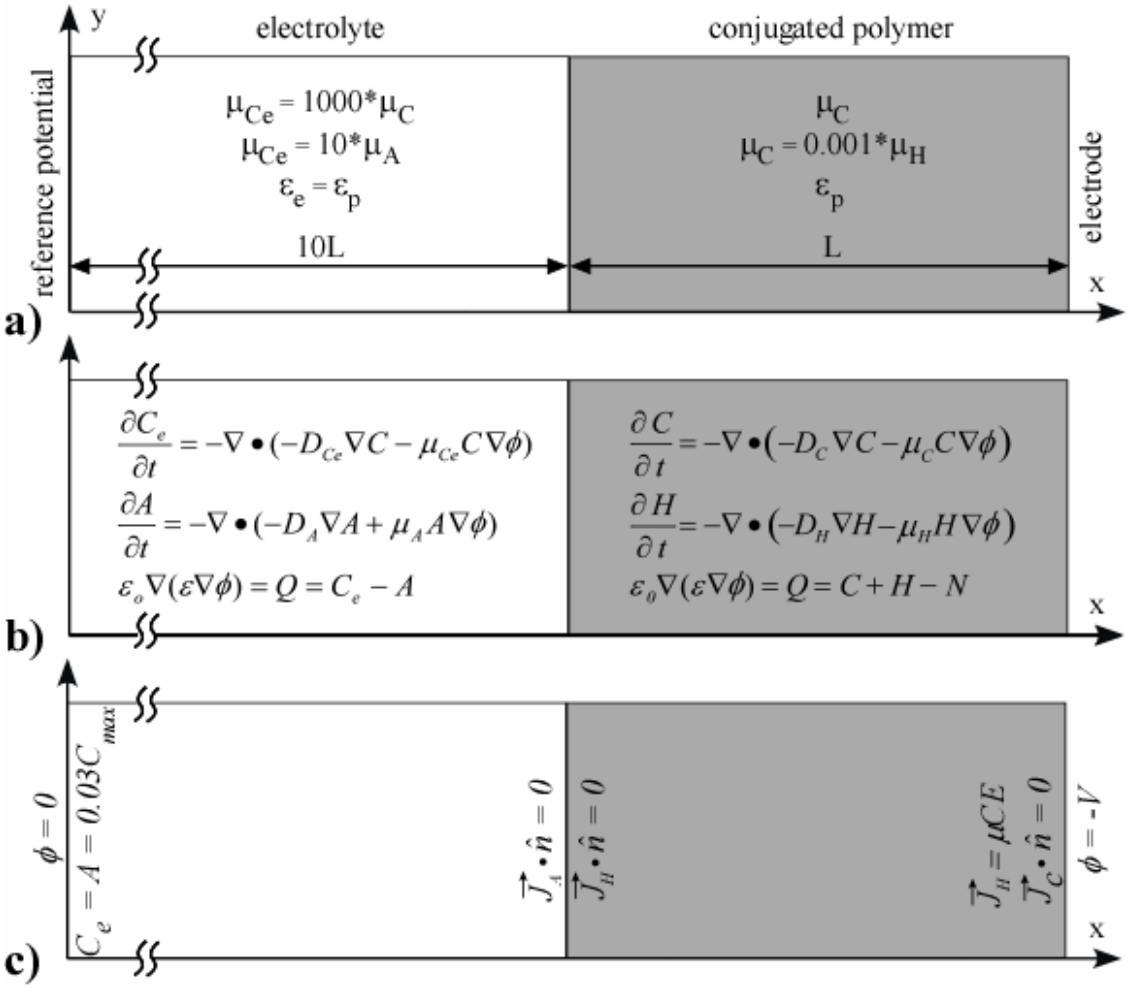

Figure 64. The a) parameters, b) PDEs, and c) boundary conditions used during reduction in the full model, a 1-D model that included the electrolyte and non-constant coefficients. On the left side of the electrolyte is the equivalent of a reference electrode shorted to a counter electrode.

As in the previous section, we began with a starting point case. Both anions and cations were treated as singly charged. In the electrolyte, the cations were assumed to have a 10x higher mobility than the anions since in our experiments the Na^+ is much smaller than the DBS^- (Figure 64a). The cation mobility in the electrolyte was assumed to be 1000 times higher than in the polymer, based on reported diffusivity values in the literature [39, 40]. The Einstein relation was assumed to be valid. The dielectric constant in the electrolyte was set to the same value as for the polymer.

The electrolyte was set to be 10x longer than the polymer, which was also based on our experimental configuration. The parameters in the polymer were the same as those used in the base case, except for the implementation of non-constant coefficients.

There were three boundaries in the new model (Figure 64c). On the left-hand side (x = -10) is a second electrode, equivalent to an experimental configuration in which the counter and reference electrodes are shorted. At this electrode/electrolyte boundary, the anion and cation concentrations were set equal to the salt concentration in the bulk of the electrolyte. Since we used a 0.1 M electrolyte concentration for the experiments, this was also used in the model system (equal to 0.033 C_o, since $\boldsymbol{C_{max}}$ = 3 M). The potential at that boundary was zero during the reduction process. The interface between the electrolyte and the polymer (x = 0) had a no-flux condition for anions and holes, keeping them confined in the electrolyte and polymer, respectively. Lastly, the polymer/electrode interface (x = 1) had the same boundary conditions as in the base case.

In the initial conditions for the simulation, anion and cation concentrations throughout the electrolyte were equal to 0.033*C_o. In the polymer, the initial conditions were the same as used in the base case: C = 0 and H = 1.

5.6.4.2 Full Model Results

The concentrations of the charged species are shown when the front has reached half-way into the polymer in Figure 65a. In the new electrolyte region, both anions and cations are depleted near the surface of the polymer, their concentrations returning to

bulk values by x = -4. Just at the interface, though, the cation concentration rises steeply, forming a thin double-layer (clearly seen in the insert of Figure 65a). The profiles in the polymer are qualitatively similar to those in the base case, without the electrolyte.

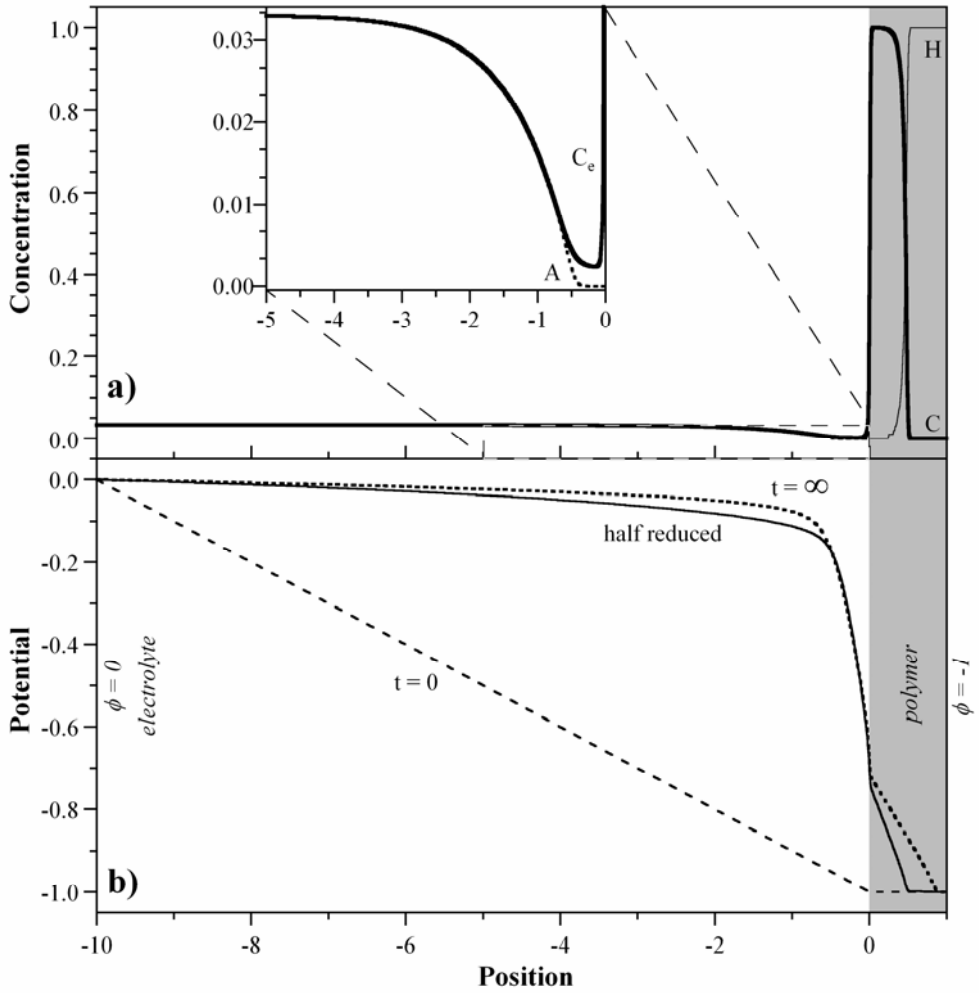

Figure 65. Simulation results for reduction using the full model, which included the electrolyte and nonconstant coefficients. a) Anion, cation, and hole concentrations as a function of position. The insert shows a close-up of the electrolyte adjacent to the polymer. b) The potential as a function of position at three different times.

There are two competing effects acting on the cations in the electrolyte. The first is their attraction to the negative potential on the electrode, which produces the double-layer. The second is depletion of cations in the electrolyte as they are pulled into the polymer faster than they can be supplied. This results in a near-zero concentration of cations between the double-layer and $x = -0.5$. The development of a depletion layer suggests that ion transport in the electrolyte might become rate-limiting under some conditions. The anions, on the other hand, are depleted because of the requirement for charge neutrality (equation (23)), and they do not build up at the surface because they are repelled by the negative potential.

The potential as a function of position is shown at three time snapshots in Figure 65b. Initially, when the polymer is in its conducting, oxidized state, all of the voltage is applied across the electrolyte. As the polymer is reduced, the potential across it rises, but even so, half-way through the reduction process approximately 70% of the potential drop is still across the electrolyte. The largest part of this drop occurs across the depletion and double layer regions. The profile does not change significantly thereafter: at the end of the process, only slightly more of the potential is dropped across the polymer.

The front position still moves essentially as $\sqrt{t}$ in the polymer. This is because after an initial rapid increase, up to $t = 0.01$, the potential across the polymer grows so slowly. (The potential drop across the polymer over time is shown in SM 1.2.3.2). Likewise, the effective front velocity is still linearly proportional to the applied

potential. Regardless of the size of the applied voltage, this model did not show a limiting velocity due to transport in the electrolyte.

Comparing with the base case, it is clear that electrolytes play an important role for ion transport in conjugated polymers. First, potential drop across the electrolyte is substantial especially across the depletion layer. It lowers the migration effect in the polymer. As a result, the phase front speed is lowered, and it takes longer time to fully reduce polymer films. Since the potential in the full model is not the overpotential over the polymer, a V=0.25 is used for the base case (Nonconstant coefficient is also adopted.) to compare with the full model with V=1. The two cases show identical results as shown in SM 1.2.3.3.

5.6.4.3 Variation: Diffusion Only

Because of the continued discussion in the literature maintaining that ion transport is due only to diffusion, this question was examined once again using the full model. In the diffusive elastic metal model [38], the force for ion transport into the polymer is a high concentration of ions in the double layer at the polymer/electrolyte interface, and diffusion is linked to the applied potential through changes in the double-layer ion concentration.

Migration was removed in the full model in four different ways, taking away, without any other alterations in the model, 1. the cation migration term in the polymer, 2. the cation and hole migration terms in the polymer, 3. the cation and anion migration terms in the electrolyte, or 4. the migration terms for cations, anions, and holes everywhere. Here we present the results of the first case because it corresponds

directly to the diffusive elastic metal model. Results from the other three cases are given in the Supplementary Materials (SM 1.2.4) since they do not have clear physical meanings. The first case is further subdivided into two: using the experimentally determined dependence of mobility on concentration, equation (17), and using the steeper relationship of equation (20), which yields a phase front even when transport is by diffusion only.

The consequences of using e^{2C} with the cation migration term in the polymer set to zero are shown in Figure 66. For these simulations, no capping was used. For $t < 2$, there is quasi-frontlike behavior, in that the concentration at $x = 1$ does not change immediately (Figure 66a & b) and the curve has an inflection.

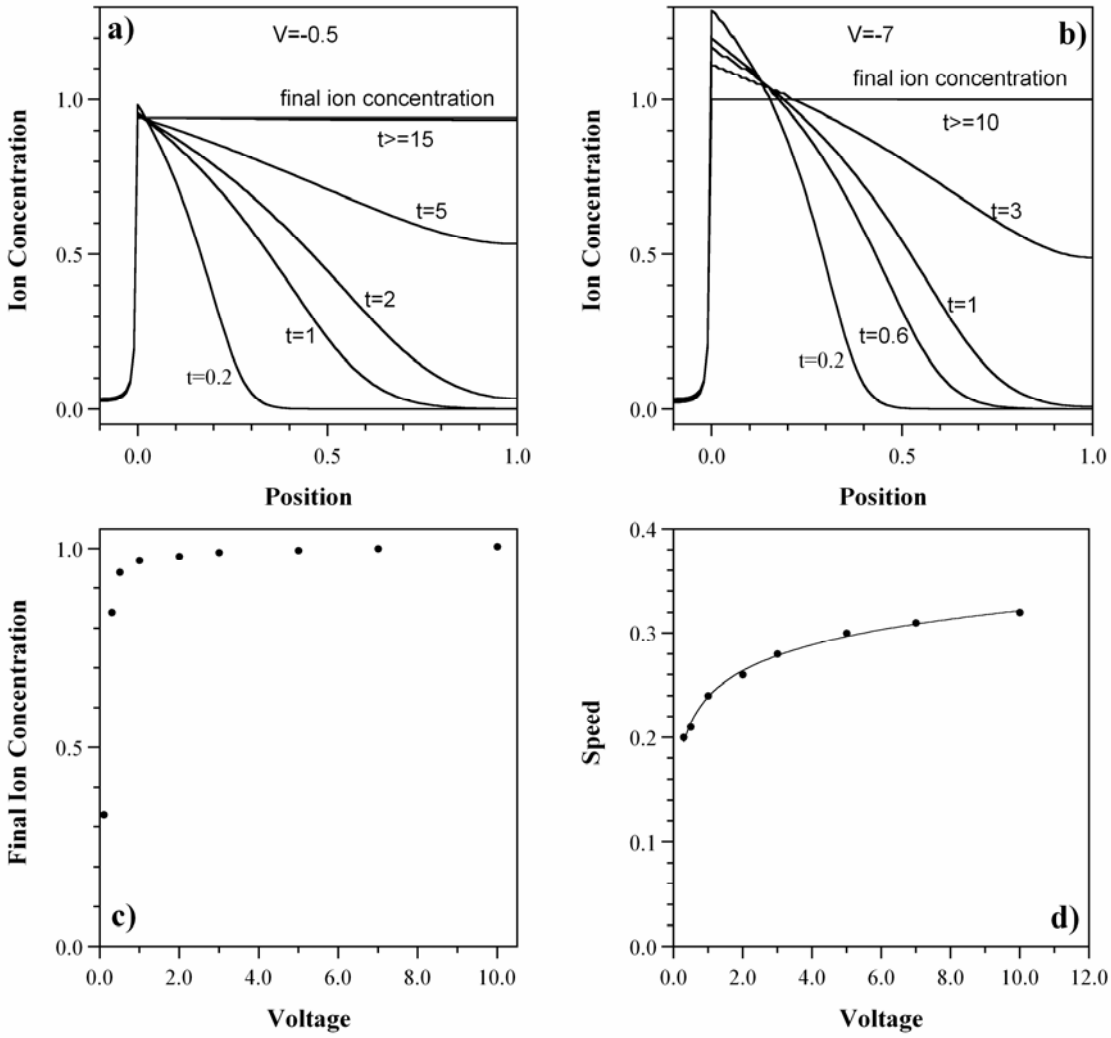

Figure 66. Results of the full model during reduction when the migration of ions in the polymer is turned off and $D_C = D_0 e^{2C}$. Ion concentration profiles for a) V = 0.5 and b) V = 7. c) Final ion concentration in the polymer under different potentials. d) Phase front velocity vs. potential. The line shows a log fit.

For $\phi < 10$, the polymer does not fully reduce (Figure 66a & c). For example, for $\phi =$ 0.5, the ion concentration in the film only reaches 0.32. For voltages below 1 V, the cations reach a maximum value in the polymer equal to their value in the double layer, and the ion concentration eventually reaches this value throughout the film. This is not a physically meaningful result: it only occurs experimentally when a voltage below the reduction potential is applied, resulting in a partially oxidized film,

but in the model, all applied potentials are sufficient to fully reduce the polymer. The final ion concentration in the polymer increases with the applied potential, as shown in Figure 66c, because a more negative reduction potential can pull more ions into the double layer. However, the polymer can only be completely reduced for V > 10.

Without capping, at high voltages C went to unrealistically large values at the interface (Figure 66b). (Not only have ion high concentrations > 1 not been seen experimentally, but out-of-plane volume measurements have expressly shown that they do not occur at any point during reduction [33, 41].) The high initial concentrations drop over time, and at the end of the reduction process, $C \approx 1$ throughout the polymer.

The most important question to be answered by the simulation was, "Is the reduction speed voltage-dependent?". As shown in Figure 66d, it was: the speed went as $0.24+0.08\log(\phi)$. This is because, unlike in the base case with diffusion-only (compare section 5.6.3), the concentration at $x = 0$ is not fixed at 1, but varies with the concentration in the double layer. Using a higher reduction potential increases the ion concentration in the double layer through a stronger migration term in the electrolyte. This occurs even for voltages at which C stays below 1, and is thus not just an artifact of not using capping. This is a demonstration of the ion transport mechanism postulated in the diffusive elastic metal model. However, the fact that the polymer does not fully reduce, that fronts are produced only using extreme dependences of D_C on C, and that the velocity is logarithmic rather than linear with V indicate that this case is not physically meaningful.

With the migration term turned off, capping could not be enforced by the strategy of increasing the migration term. To examine the effect of capping, therefore, the diffusion term was raised when C went above 1, using the relation $D_C = D_0 (1+ 0.01e^{15(C - 0.8)})$. The simulation can only run potential as high as 1.2. When higher potentials were used, the simulation crashed. The capping function shows negligible effect on ion transport even when potential is 2, as shown in SM 1.2.4.1. This is because ion concentration in the double layer is not high enough to dramatically increase the diffusion.

The results of using a diffusivity proportional to e^{5C} to force the emergence of a phase front are shown in the Supplementary Materials (SM 1.2.4.1). The outcomes are basically the same as those in Figure 66, but the concentration profiles have a pronounced front. Again, the polymer does not fully reduce below $\phi \sim 2$, and the reduction velocity goes as the ln of the voltage. As usual, the front propagates with $\sqrt{t}$ since they are driven by only diffusion.

5.7 Summary of Model Development Results

The key findings of each simulation in Part A are summarized in Table III. The simulations are for electrochemical reduction of an ion-barrier-covered cation-transporting polymer unless otherwise noted. Also, unless otherwise noted the simulation parameters were the same as in the 1-D Base Case (upper half of the table) or in the Full Model (lower half of the table)

Table III. Summary of the cases examined in Part A for model development and the key findings of each.

Section, Case	**Simulation Settings**	**Questions Posed**	**Key Findings**
5.5.1 **1-D Base Case**	1. Constant D_C, D_H, μ_C, μ_H, ε 2. $\mu_H = 1000\mu_C$ 3. $D/\mu = 0.026$ $\varepsilon = 10^{-3}$ 4. $\phi = -1$ on electrode	What behaviors are predicted by the simplest possible model?	1. Charge transport is due primarily to migration. 2. A cation front moves through the film. 3. The front velocity $v_f \sim \sqrt{t}$, even though transport is by migration rather than diffusion. 4. The front broadens due to diffusion, with front width $w_f \sim \sqrt{t}$. 5. The applied potential is dropped over the reduced region; E fields are large there. 6. E and the net charge Q decrease over time as the width of the reduced region grows.

Section, Case	**Simulation Settings**	**Questions Posed**	**Key Findings**
5.5.2 2-D Base Case	Same as previous.	Is it valid to perform the 1-D simulations, or are 2-D simulations needed?	1. Yes, virtually the same results are obtained as in the 1-D case. 2. Cations travel along E field lines that are primarily parallel to the surface.
5.5.3.1 1-D Base, Vary V	Vary ϕ: $0.001 < \phi < 10$	What is the voltage-dependence of the behavior?	1. Front velocity is linearly proportional to voltage: $v_f \sim \phi$. 2. Diffusion makes a significant contribution to the behavior when ϕ is small.
5.5.3.2 1-D Base, Change D/μ	$D = 0.026(1+5C)/n$, n is 1, 3.5, and 6 to make diffusivity at C=0.5 higher than the base case, or the same as the base case, and lower than the base case respectively. $\mu = \mu_0$	What happens if the Einstein relation is not assumed, but D/μ depends on charge concentration?	1. Fronts are all wider than in the base case. 2. At high voltages, phase front velocities are the same. 3. At lower voltages, higher diffusivity creates higher velocities.

Section, Case	**Simulation Settings**	**Questions Posed**	**Key Findings**
5.5.3.3 1-D Base, Low Hole Mobility	$\mu_H = \mu_C$	What happens if we do not assume that the holes are much faster than the ions?	1. The cation front propagates linearly with time: $v_f \sim t$. 2. ϕ drops linearly across the polymer. 3. Front broadening increases. 4. Front velocity decreases.
5.5.3.4 1-D Base, Charge Neutral	1. $H = 1 - C$ 2. $\mu_H = 5\mu_C$	How does the behavior change if charge neutrality is strictly enforced in the polymer (no net charge permitted)?	Essentially the same results as in the base case, but reflecting the lower hole mobility that was used.

Section, Case	**Simulation Settings**	**Questions Posed**	**Key Findings**
5.6.2 Base Case with Non-Constant Coefficients	1. $D_C = D_0 * e^{2C}$, $\mu_C = \mu_0 * e^{2C}$	Increase the model complexity to better reflect the physical system. What changes if diffusion is non-Fickian?	1. No substantial differences from the base case, but the fronts are sharper. 2. Front width still goes as $w_f \sim \sqrt{t}$. 3. Front velocity still goes as $v_f \sim \sqrt{t}$ and $v_f \sim V$. 4. Higher front velocities (approximately 2.7 times higher, $e^{2*0.5}$=2.7), which are an artifact of the larger magnitudes of the coefficients. 5. At low V, concentration profiles with these non-constant coefficients do not resemble the experimental data. The model does not correctly handle diffusion.

Section, Case	**Simulation Settings**	**Questions Posed**	**Key Findings**
5.6.3 Base Case, Diffusion Only, Non-Constant Coefficients	1. $D_C = D_0(1+5C)$, $D_0 * e^{2C}$, or $D_0 * e^{5C}$ 2. $\mu_C = 0$	If cation diffusion is non-Fickian, can a front be formed if the ions move only by diffusion?	1. Yes, a phase front is formed in the film if the exponent is large enough. For $D_0 e^{2C}$, there is quasi-frontlike behavior, and for $D_0 e^{5C}$, a real front is formed. 2. The front velocity goes as $v_f \sim \sqrt{t}$. 3. Voltage has no effect on the reduction speed.
5.6.4.2 **Full Model**	1. $D_C = D_0 * e^{2C}$, $\mu_C = \mu_0 * e^{2C}$ 2. New anion, cation PDEs in an electrolyte layer 3. New boundary conditions, including $\phi = 0$ at edge of electrolyte	Increase the model complexity to better reflect the physical system. How is the behavior affected by including the potential drops and ion transport in the electrolyte?	1. There is a significant voltage drop across the electrolyte. At the end of the reduction process, only 30% of the voltage is across the insulating polymer. 2. Depletion and double layers form in the electrolyte. 3. Front velocity still goes as $v_f \sim \sqrt{t}$ and $v_f \sim \phi$. 4. When the same overpotential is applied to the polymer, ion transport is identical between the full model and the base case.

Section, Case	Simulation Settings	Questions Posed	Key Findings
5.6.4.3 Full Model, Diffusion Only	1. $D_C = D_0 * e^{2C}$ 2. $\mu_C = 0$	How is non-Fickian diffusion-only cation transport affected by the inclusion of an electrolyte layer?	1. The cation concentration in the polymer equals the cation concentration in the double-layer. 2. The polymer does not fully reduce unless extreme voltages are applied (ϕ = 10). 3. Quasi-frontlike behavior is again seen. 4. The reduction speed does depend on voltage, but it goes as log(ϕ).

As reviewed by Lacroix [3], charge transport cannot be described solely by diffusion: the existence of electric fields in the polymer must be taken into account. Several diffusion-only models were tested, and none could reproduce the experimentally-observed behavior. Specifically, they did not result in a linear dependence of the reduction rate on the applied voltage. Using constant coefficients, i.e., assuming Fickian diffusion, the base case simulation without a migration term was completely insensitive to voltage, and the ions entered without forming a front. If the diffusion coefficient had a large exponential dependence on C, making the diffusion non-Fickian, then a front was generated, but its speed still did not depend on potential. In the full model, using an exponential dependence of the diffusion coefficient resulted

in a voltage-dependent reduction speed as a result of a voltage-dependent cation concentration in the double-layer, but the speed went as ln(ϕ) rather than ϕ.

Lacroix [3] had also discussed that the driving force for ion movement was a local violation of charge neutrality from an imbalance in the concentration of electrons and ions. Our modeling confirmed this result, showing that regions with net charge can result in significant potential drops. However, it also showed that even in the absence of net charge, achieved by enforcing absolute charge neutrality throughout the system, essentially the same results were obtained. Therefore, it is unnecessary to postulate the existence of net charge in order to explain the reduction behavior.

The modeling results also shed light on the time-dependence of the reduction process. A square root of time dependence of the current should not lead one to conclude that the process is necessarily due to diffusion. In the base case simulation, $x \sim \sqrt{t}$ even when ion transport was dominated by migration. This arose coincidentally because the insulating region grew wider as the front propagated.

The addition of the electrolyte layer affects the behavior in the simulations in at least three ways. First, it changes the voltage at the surface of the polymer from a fixed to a variable value that changes as the relative resistance of the polymer vs. the electrolyte changes with doping level. Second, the ion concentration at the electrolyte boundary of the polymer is also changed from a fixed to a variable value through the introduction of a "double layer", or spike in ion concentration, which builds up in response to charges on the polymer. Third, it changes the ion flux from the electrolyte to the polymer because of the development of a depletion layer, which

arises because of the high concentration of ions pulled into the polymer in comparison with the much lower bulk electrolyte concentration.

Nevertheless, the modeling results during reduction were not strongly affected by these alterations, or, as mentioned previously, by the use of non-constant coefficients. In fact, the only significant difference arose during the diffusion-only case, where the base case model showed no dependence of the reduction speed on applied voltage, and, because of the introduction of the double-layer, the full model did. However, we will use the full model in the simulations below because it incorporates more realistic physics, and this is important in other geometries or conditions, such as examining the effect of electrolyte concentration or studying thin films.

Front broadening is not well accounted for by the model, even using non-constant coefficients. This method of handling non-Fickian diffusion does not make a strong enough "correction" of the underlying Fickian behavior given by the transport PDEs. Thus, the broadening always goes as $\sqrt{t}$, although the experimental broadening is linear with time. In other non-Fickian polymers, sharp fronts move into polymers linearly with time and do not broaden.

Part B: Full Model Results/Predictions

In this second half of the paper, comfortable that the model is behaving in a reasonable way and that we understand how the various parameters in the model change the simulation outcomes, we turn to using the model to simulate various important experimental configurations. In all the work presented below, except for the 2D simulations, the full model is used.

5.8 Results 3: Model Predictions

The full model was developed based only on the behavior experimentally observed during the reduction of the cation-transporting material PPy(DBS), and it accounts reasonably well for those observations. In this section, the model is validated against new and known experimental conditions, beginning with reduction of the ion-barrier-covered, cation-transporting material in electrolytes of different concentration and then turning to the *oxidation* process. We then move to the reduction of such films *uncovered* by an ion barrier. This section ends with predictions of the as-yet unknown redox behavior of ion barrier covered *anion-transporting* materials, examining how they are expected to differ from cation-transporting materials.

5.8.1 Effect of Electrolyte Concentration

The concentration of ions in the electrolyte would be expected to affect the front velocity if cation flux within the electrolyte became the rate limiting step. Although the mobility of the ions is much higher in the electrolyte than in the polymer (1000x in the previous section), the concentration required by the polymer is 30x higher than is present in the bulk of the electrolyte. Recall that flux is proportional to both mobility and concentration, $J = zC\mu E$, and that there is a depletion layer just outside the polymer where C_e goes to very small values. In addition, the electric fields across the polymer and the electrolyte change over time. To explore this dynamic, the bulk concentration in the electrolyte was varied from very dilute (C_e = 0.0033 at x = -10, equivalent to 0.01 M) to highly concentrated (C_e = 1, 3 M).

Figure 67a shows the ion concentration profiles in the polymer at t = 0.05 for 6 concentrations under a voltage of V = -1. The ion velocity increases strongly with electrolyte concentration, as shown by the greater depth into the film of the ion front. In fact, for concentrations $\leq$ 0.066, the outer edge film was only partial reduced: C did not equal 1 anywhere. Note also the corresponding cation concentrations in the electrolyte. The position of the front, taken as the point at which C = 0.5, is plotted vs. bulk electrolyte concentration in Figure 67b, illustrating that the velocity increases rapidly with concentration until, above C_e = 0.1, the velocity approaches a maximum value.

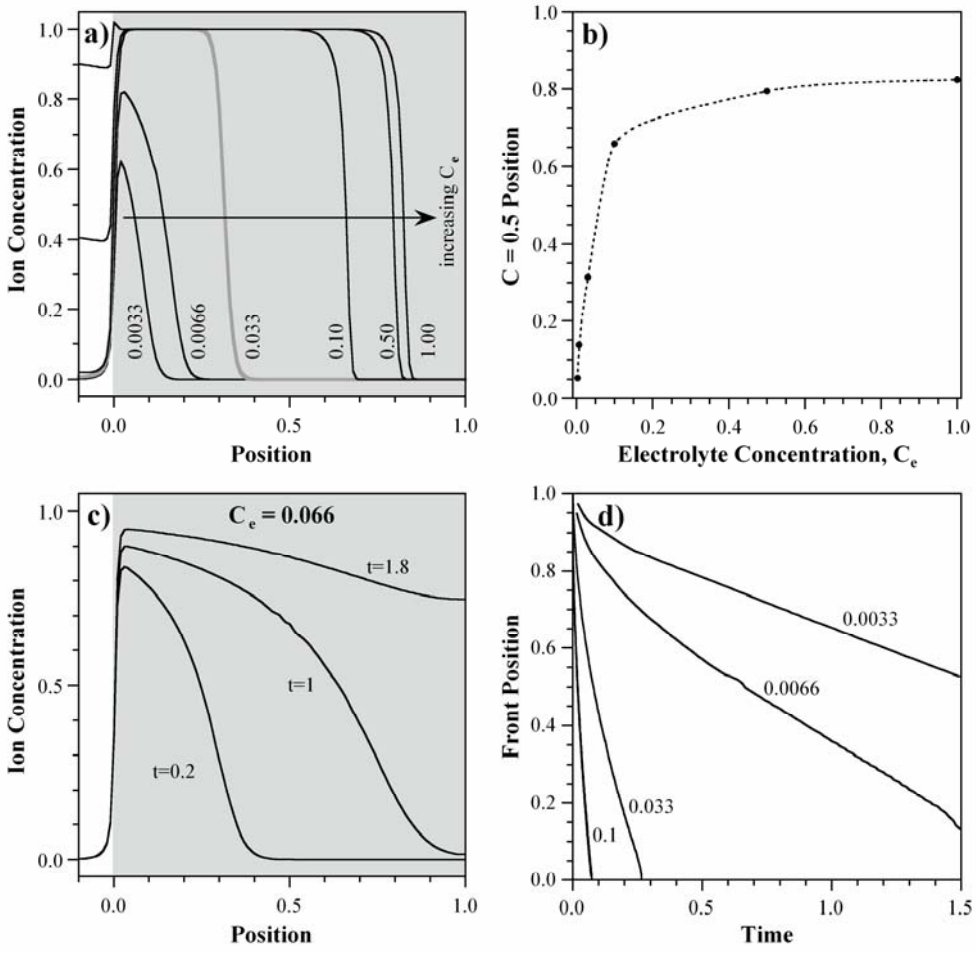

Figure 67. a) Ion concentration profiles during reduction for different electrolyte concentrations at *t* = 0.05 under V = -1 in the full model. b) Phase front position (taken as the point where C = 0.5) at t = 0.05 vs. electrolyte concentration. c) Ion concentration profiles at different times for an electrolyte concentration of 0.0066. d) Phase front positions vs. time for different concentrations. The lines for C_e = 0.1, 0.5, and 1.0 overlie each other on this scale.

Figure 67c follows the profiles for C_e = 0.0066 over time. For this and lower concentrations, there were no real phase fronts, and even at the outer edge, the concentration only slowly approached C = 1. These profiles show that ion transport in the electrolyte, rather than in the polymer, is the rate limiting step at this concentration.

Figure 67d shows the front positions for the various concentrations vs. time. For high concentrations, the fronts propagate with $\sqrt{t}$, but for the lowest concentration the front moves linearly with time, with a transitional curve seen at 0.0066. This result is significant: when ion transport in the electrolyte is the rate limiting step, the velocity becomes constant with time.

These results raise the question, "How does the reduction speed depend on *C* and *V*?" The time it takes to completely reduce the film, defined as the time it takes the point $C = 0.5$ to reach $x = 1$, is plotted as a function of these variables in Figure 68. Reduction time, rather than front velocity, was used because of the lack of clear fronts at low concentration. If the same potential is applied such as V=-1, the reduction time decrease exponentially with concentration till 0.1, as shown in Figure 68a. The reduction time also decrease exponentially with applied voltage, as shown in Figure 68b.

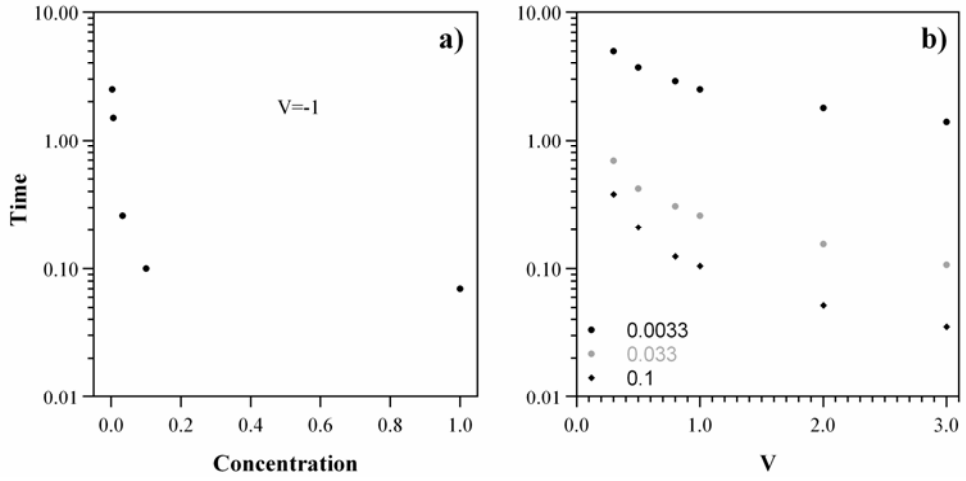

Figure 68. Reduction time as a function of a) electrolyte concentration (V=-1. The y axis has a log scale.), b) applied potential (The y axis is the same as that in a))

As pointed out in previous sections, the potential profile is the key to the behavior since it determines the migration term, which is the major flux component in most cases. The potential drops vs. time across the polymer are shown in Figure 69a for electrolyte concentrations from 0.03 to 1. As would be expected, the higher the electrolyte concentration, the higher the electrolyte conductivity, and thus the greater the fraction of the potential that is dropped over the polymer, leading in turn to faster ion velocities. The potential at t = 0.05 is plotted vs. electrolyte concentration in Figure 69b. Note the close resemblance of this relationship with that in Figure 67b.

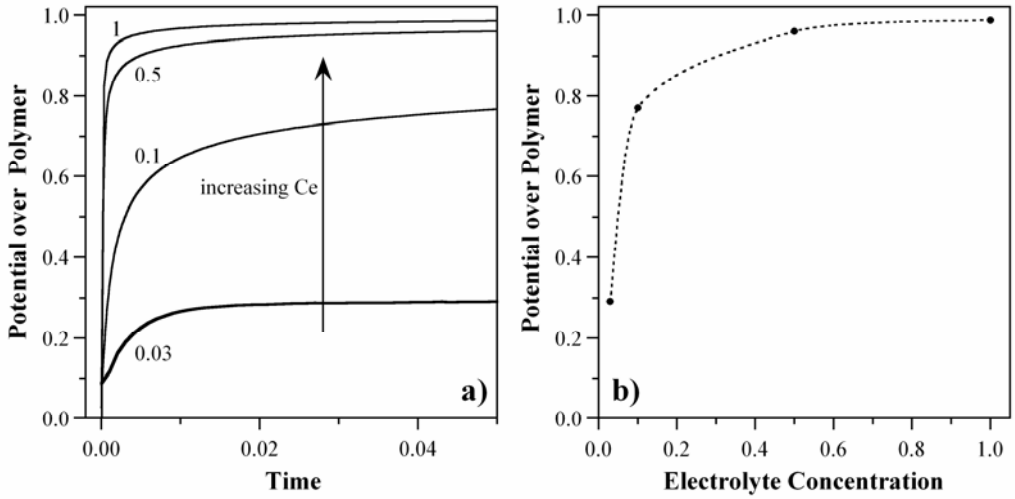

Figure 69. a) The voltage dropped over the polymer vs. time during reduction for different electrolyte concentrations in the full model. b) The potential of the polymer when *t* = 0.05.

5.8.2 Oxidation of a Cation-Transporting Material

In the experiments, the reduced film was oxidized by switching to an anodic potential on the working electrode. Thus, with the fully reduced state as the initial condition, simply changing the applied voltages at the boundaries of the model system should

correctly predict the behavior if the model correctly accounts for the dominant physical effects.

5.8.2.1 Oxidation Model

To model the conjugated polymer during oxidation, the full model was simply run "backwards", meaning that the potentials at the outer interfaces were interchanged. The other boundary conditions were the same as during reduction, except for the hole flux condition at the polymer/electrode interface. As explained in section 5.3.1.2.2, the flux boundary condition for holes at the electrode was modified according to equation (12), which in non-dimensional variables is

(24) $J_h = C * E$.

The initial conditions were inherited from the final state achieved in the reduction simulation: the hole concentration was zero everywhere in the polymer, while the ion concentration was 1, and in the electrolyte the ion concentration was equal to C_e everywhere. The initial potential was calculated based on the ion and hole concentrations and the potentials applied at the boundaries.

During oxidation, it was necessary to "cap" the hole concentrations near the polymer/electrolyte interface. This was accomplished by turning off migration when the hole concentration went above 1. The results of two other capping methods are described below in 5.8.2.3.

5.8.2.2 Results

The ion concentration profiles during oxidation are shown in Figure 70a, and the corresponding potential profiles in Figure 70b. The inserts show close-up snapshots within the polymer at different times. Note that to more effectively display the data, the *x*-axis in the electrolyte has been scaled by a factor of 10 relative to the *x*-axis in the polymer.

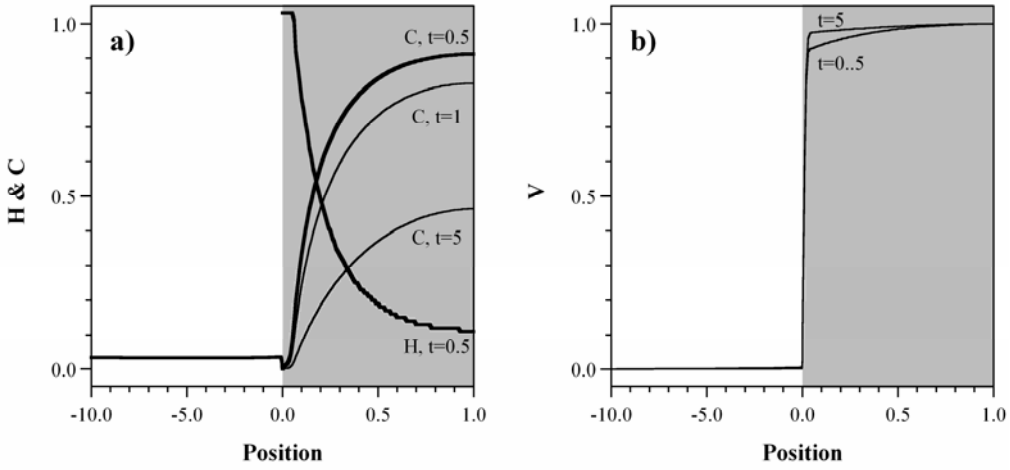

Figure 70. a) Ion and hole concentration profiles during oxidation in the full model. b) Potential profiles at *t* = 0.5 and 5.

Looking at the t = 0.5 curve in Figure 70a, the ion concentration at the electrolyte boundary dropped essentially instantly from C = 1 at t = 0 to C = 0 at the electrolyte boundary as the cations exited the film. Interestingly, even at very early times the ion concentration profile had a bell shape: all other parts of the film also lost ions simultaneously. The oxidation level increased without a phase front: at later times the bell shape remained, but dropped in height. These predictions are consistent with the experimental data (Figure 36 in Part 1).

The reason for this behavior can be found in the potential profiles. As shown in Figure 70a, holes build up at the polymer/electrolyte interface because they are

repelled by the positive voltage on the electrode but cannot leave the polymer. In the oxidized area, holes reach their maximum concentration of 1, while ions gradually decrease to zero, resulting in a net positive charge and thus a potential drop. Because the polymer is partially oxidized, there are no significant potential drops elsewhere in the system. Without them, there is little contribution to ion transport due to migration, and the system becomes diffusion-dominated. The oxidation speed does not, as a result, depend on the applied voltage.

The oxidation voltage is varied to find out how it affects the oxidation process. Two types of curves are presented: ion concentration profiles (Figure 71a) at the same time and total ions in the film (Figure 71a). The ion concentration profiles keep the same shape when oxidation potential is varied from 0.5 to 2. With higher voltages, ions leave the polymer slightly faster. Since no phase fronts are formed during cation oxidation, the second curve, total ions vs. sqrt(t), is used to reveal effect of oxidation voltage. As shown in Figure 71b, when different voltages are applied, they have large effects on ion egress at the beginning of oxidation but have negligible effect once the oxidation occurs certain time (such as 0.7). This is evidence on the total ion vs. sqrt(t) curve: the difference of total ions in the film is mainly formed at the very beginning. After certain time, the curves are parallel with each other, meaning that ions leave the film with the same rate. The difference in offset is understandable. At the very beginning, polymer has large potential drop due to low conductivity. At the very beginning, ions are kicked out by both migration and diffusion, but later one, ion egress is controlled only by diffusion. Therefore, when oxidation voltage is

increased, the ions are kicked out quicker at the beginning and then resume the same rate as controlled by diffusion.

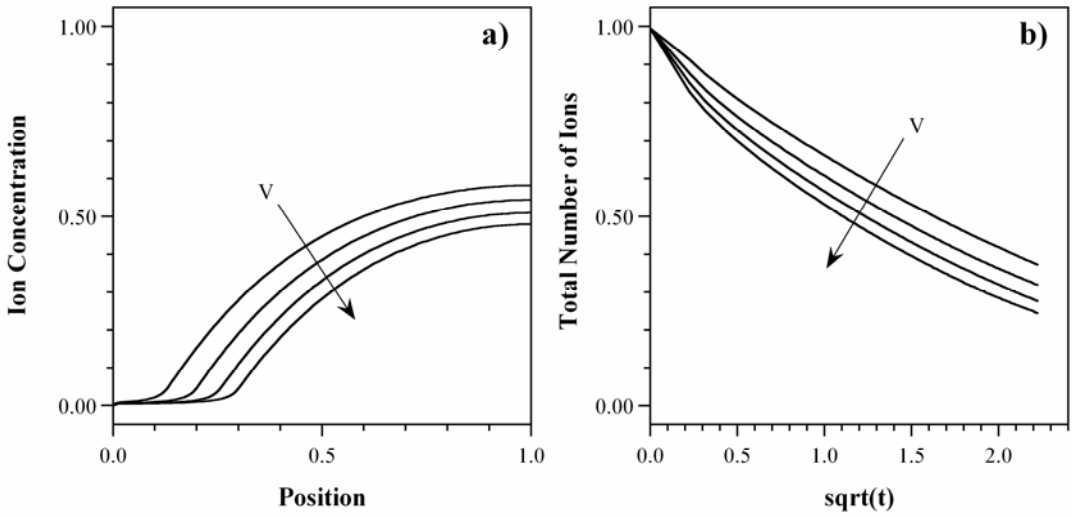

Figure 71. Effect of oxidation voltage (V = 0.5, 1.0, 1.5, and 2. The arrow shows the voltage increase.) on a) ion concentration profiles (t = 5) and b) total number of ions in the film.

5.8.2.3 Role of the Capping Technique

The results presented above were obtained by capping the ion and hole concentrations by turning off migration when they went above 1. Without capping, the hole concentrations went to values as high as 10^4, which we deemed to be unacceptable because it was so far from what we understand to be true in the physical system. In order to ensure that the capped outcome was reasonable, two other methods of controlling the charge were examined: enforcing charge neutrality everywhere and exponentially increasing the diffusivity when the charge density rose above 1. The results of not using capping are also presented. The uncapped and charge-neutral simulations provide limiting cases of large versus zero net charge, against which it is useful to compare the capped simulations.

5.8.2.3.1 Charge Neutrality

To enforce charge neutrality in the electrolyte, equations analogous to those in section 5.5.3.4 were used. The potentials in the electrolyte and polymer were governed by:

(25) $$\nabla \bullet (\mu_{Ce} C_e \nabla \phi + \mu_A A \nabla \phi) = 0$$

(26) $$\nabla \bullet (\mu_C C \nabla \phi + \mu_H H \nabla \phi) = 0$$

Otherwise, the same boundary conditions and parameter settings were employed as in the full model.

During oxidation, it was possible to use the usual $\mu_H = 1000*\mu_C$, whereas during reduction the hole mobility was limited to $\mu_H = 5*\mu_C$. The reason for this is that the hole concentration goes to zero during reduction. A slightly negative hole concentration introduced by numerical noise creates a negative conductivity, which creates even more simulation error. During oxidation, on the other hand, the hole concentration grows, which eliminates the possibility of creating a negative conductivity.

5.8.2.3.2 Increasing Diffusivity

One method of capping the concentrations is to increase the diffusivity and mobility for ions (and holes), having them grow exponentially large as *C* and/or *H* approach 1, so that the charge diffuses rapidly away from such regions.

(27) $$D_C = D_0 (1 + 0.01 e^{15(C - 0.8)})$$

(28) $$\mu_C = \mu_0 (1 + 0.01 e^{15(H - 0.8)})$$

These functions start to apply when C or H go above 0.8, but have a negligible effect on transport when C or H is below 1. The multiplier of 15 is the largest that ran stably.

Figure 72 shows the ion and potential profiles with three capping functions and those without any capping functions. Turning off mobility and increasing diffusivity produced quite similar results, while the charge neutrality case and no capping function case are close to each other. Ion concentration profiles in the polymer are similar for all cases. But charge neutrality and no capping cases tend to create larger depletion layer in the electrolyte, this is because they have larger potential drop across the electrolyte, as shown in Figure 72b. The reason is that the charged area at polymer/electrolyte interface is larger of no migration and high diffusion cases than that of no capping and charge neutrality cases. None of these cases show dependence on the applied voltage. Ion concentration profiles for further oxidation such as $t = 5$ is consistent with the above analysis, as shown in Supplementary Materials (SM 1.2.5.3). For cation oxidation, using capping functions alter ion concentration profiles slightly. But they have a larger effects on potential profiles because they lower the hole concentration greatly at the polymer/electrolyte interface.

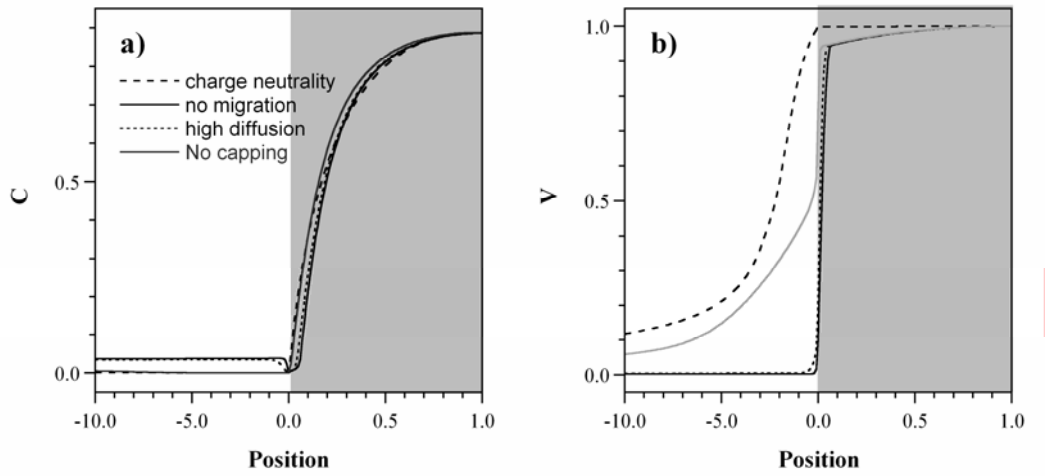

Figure 72. a) Ion concentration profiles using the three capping methods at t = 0.4. The results without capping are shown with the gray line for comparison. b) The corresponding potential profiles.

5.8.2.4 Conclusions, Oxidation

In summary, to simulate the oxidation process, the full model was run using the reduced state as the initial condition and reversing the potentials on the electrode. The full model was run without capping, with two different capping methods, and with charge neutrality strictly enforced to provide limiting cases for the oxidation behavior, and all showed that oxidation is dominated by diffusion and therefore unaffected by the voltage on the working electrode. The reason for this is the relatively high conductivity of the polymer in the partially oxidize state combined with the high conductivity of the electrolyte; the potential is dropped instead across the net charge layer and/or the electrolyte close to the polymer, depending on the model.

5.8.3 Uncovered Thin Film

So far, we have modeled the experimental configuration used in Part 1, a PPy stripe covered by an ion barrier. As shown in Part A, in the 1-D model this is equivalent to

modeling a thick PPy film. In our micro-actuator work, however, we use thin PPy films, on the order of 1 μm thick. We now use the models we have developed to simulate redox in a thin, uncovered cation-transporting film.

5.8.3.1 2D Model

Using the 2-D geometry allows one to explore the competition between out-of-plane and in-plane ion transport in an uncovered film. Due to the fragility of 2-D simulations, the model did not include the electrolyte, and utilized a constant mobility and diffusivity. In other words, these results are not from the full model, but from the base case model. The only change to the model that was used in section 5.5.2 was to the boundary condition on the top of the polymer. There, the ion concentration was set to 1, a zero hole flux was imposed, and the potential was set to zero.

5.8.3.2 Uncovered Films with Isotropic Transport Coefficients

Figure 73 shows the simulation results for a film that is approximately halfway reduced, with the model parameters chosen to mimic isotropic ion and hole transport in the polymer[*]. This figure should be compared with Figure 55, although the intensity gray-scales have been changed to reflect the different minima/maxima. (Unlike in Figure 55, in which the ions accumulated at the electrode, the potentials and concentrations near the electrode are correct here since the snapshot shows a time prior to the ions reaching the electrode.) The noise at the left and right edges is numerical.

[*] As a reminder, to achieve the coefficients were scaled as described in section 5.4.2.

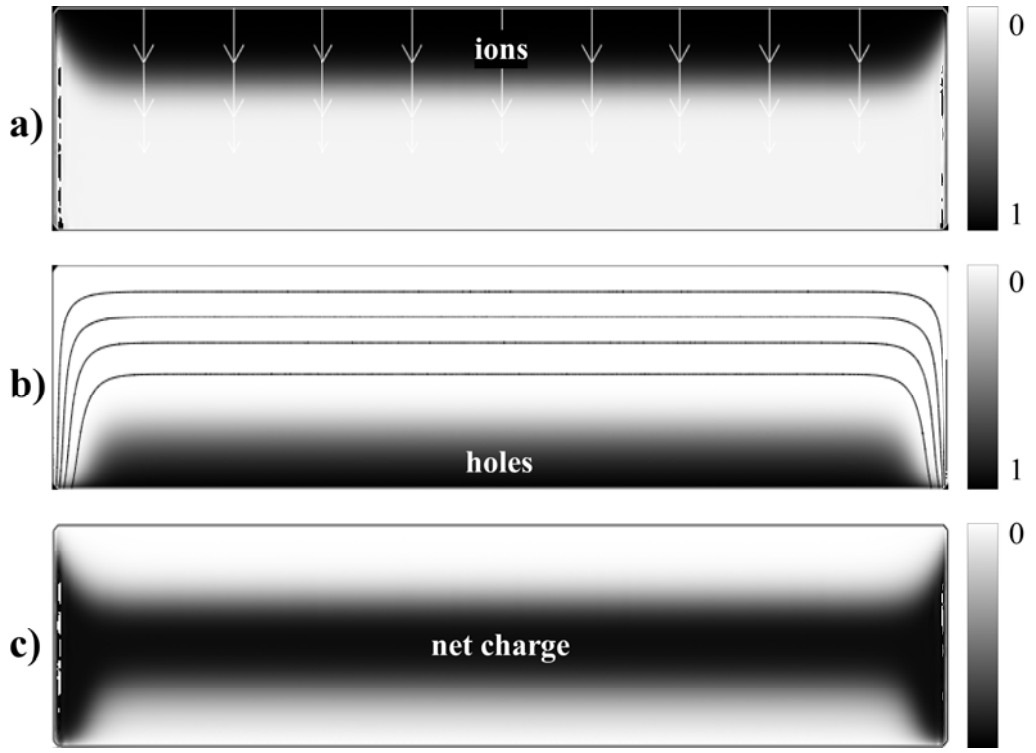

Figure 73. 2-D simulation results for an *uncovered* cation-transporting film approximately halfway through the reduction process using the base case model. a) Ion, b) hole, and c) net charge concentrations. The white lines indicate the electric field magnitude and direction, and the black lines show contours of equal potential. (Figure not to scale.)

Since the ions mainly enter the film from the top boundary (Figure 73a), the reduced area grows from there to the bottom electrode, with a front between the reduced and oxidized areas. (Ions also enter the film from the sides, but since the effective film width in the simulation is 100 times greater than the thickness, the reduced area on the sides is too small to see.) Along most of the film width, the electric field lines, along which the ions travel, are parallel to the *y*-axis. However, the V = 0 boundary condition at the three polymer/electrolyte interfaces causes the equipotential lines to curve (Figure 73b). This would not have happened had the electrolyte been included in the 2-D simulation.

At the two upper corners, the y-component of the electric field is zero, and the x-component is small: although in the figure the equipotential lines are spaced close together, this is not actually the case because the figure is not to scale but is compressed by a factor of 200 in the x-direction. Due to the small inplane fields and the curvature of the lines at the corners, the ion concentration is lower there, and the net charge higher. The magnitude of the net charge is greater than in Figure 55 because the snapshot in Figure 73c was taken at an earlier time, and the magnitude of the net charge decreases with time as shown in Figure 52b.

Ion and hole concentration profiles along the field lines were similar to those in the base case (see SM 1.2.6.1), except that the front width was proportionally much greater in relation to the film thickness: the front width spanned the entire film almost immediately. As a consequence, the front did not have a sqrt(t) propagation.

5.8.3.3 Uncovered Films with Faster In-Pane Transport

In general, the morphology of conjugated polymers is anisotropic, and thus the transport will be anisotropic. As shown in Part 1, cation transport in PPy(DBS) is strongly anisotropic because of its lamellar structure [42, 43], with inplane velocities approximately 2 orders of magnitude higher than out-of-plane. The 2-D model readily supports modeling of anisotropic transport since Femlab allows independent x (inplane) and y (out-of-plane) coefficients. Anisotropic transport was implemented by setting $D_x = kD_y$ and $\mu_x = k\mu_y$ for both ions and holes.

It should be emphasized that the electric field in the uncovered film favors out-of-plane transport since the field lines are mainly in the vertical direction (Figure 73a).

Thus, in order to produce appreciable in-plane transport in the uncovered film, D_x needed to be increased to at least $D_x \sim 10^3 D_y$.

Figure 74 shows two examples of ion concentrations in partially reduced films with anisotropic transport coefficients. For an anisotropy of $k = 10^3$ (Figure 74a) the fronts converged from both the top and the sides. Upon increasing the anisotropy to $k = 10^5$ (Figure 74b), the fronts moved primarily inplane.

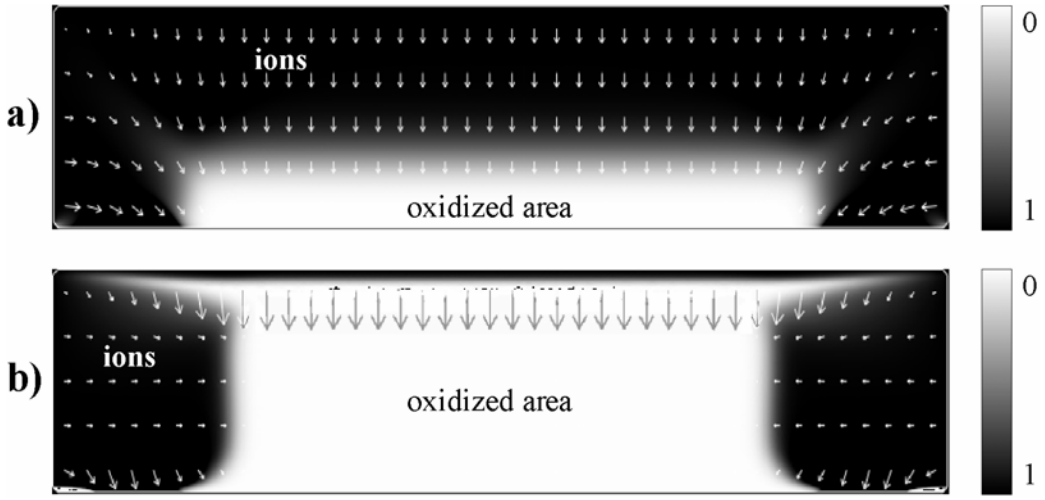

Figure 74. Ion concentrations in a partially reduced, uncovered film using a) $D_x = 10^3 D_y$ and b) $D_x = 10^5 D_y$ in the 2D base case model. Arrows indicate the direction and magnitude of the electric field. (Figure not to scale.)

These simulations indicate that the anisotropy in the transport coefficients in PPy(DBS) may be significantly greater than one would estimate from a comparison of the inplane and out-of-plane velocities. This is because $\frac{v_x}{v_y} = \frac{\mu_x}{\mu_y}\frac{E_x}{E_y}$. Thus, since $E_x << E_y$ in an uncovered film, in order to see inplane transport μ_x must be >> μ_y in order for $v_x > v_y$ as seen experimentally. The simulations indicate that $\mu_x \approx 10^3 \mu_y$.

5.8.3.4 1D Model

Ions transport along the electric field lines in thin films was further explored using the full model in a 1D geometry, since this would permit the inclusion of the electrolyte. Recall that the ion-barrier-covered thin film model was equivalent to a model for an uncovered film 150 μm thick. To adapt the model for a thin uncovered film, the diffusivity, mobility, and permittivity of the polymer were scaled, setting them 1000 times higher. This effectively decreased the film thickness by a factor of $\sqrt{1000}$ =33, or 4.5 μm.

5.8.3.4.1 Reduction

The ion concentration profiles in the thin film are dramatically different than in the thick film, as shown in Figure 75a. There is no phase front. Instead, the ion distribution is flat and increases uniformly until the polymer is reduced. Two important points relating with thin films need to be emphasized here to understand the results. First, since the film is thin, it takes a negligible time for ions traveling from the polymer/electrolyte interface to the electrode compared to the time it takes ions in the electrolyte to reach the polymer surface. Second, since the film is thin, potential drop is small, even when the film is fully reduced, which greatly lowers the migration term in the polymer. Considering these two effects, ion transport in a thin film is rather governed by diffusion rather than migration, and diffusion smooth out the concentration gradient in no time since the polymer is thin.

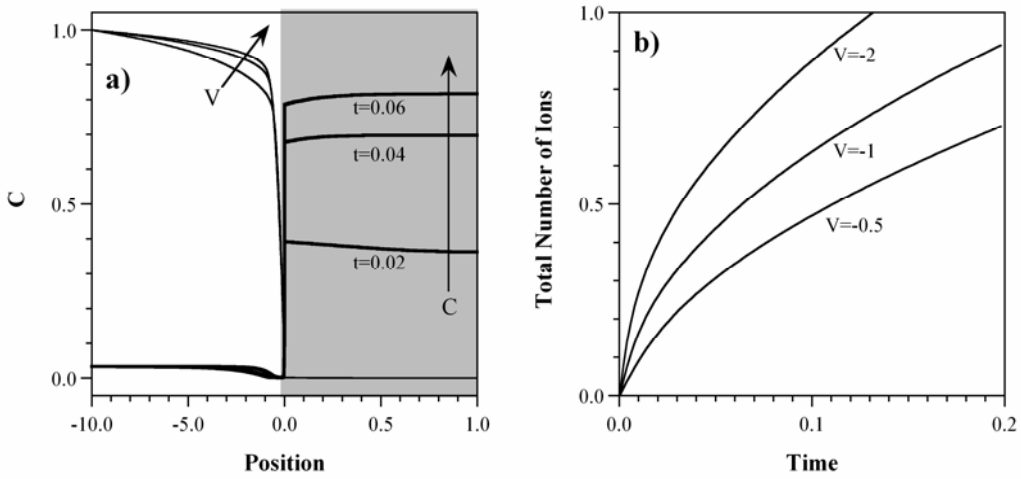

Figure 75. Cation and hole profiles in a thin film during reduction. (The x axis of the electrolyte has been scaled 10 times smaller.) b) Total number of ions in the film. The profiles in Figure 75a are quite different from those obtained in the 2D case, which did show a front. The key different in the 2D model is that it ignores the transport in electrolytes. Therefore, the 2D model has a larger potential drop or migration term than it should be, which creates the phase front. In the 1D model, electrolytes have most of the potential drop because the film is thin and it is not a surprise that the film has no phase fronts

The total number of ions in the film is shown versus time at different voltages in Figure 75b. The reason why more negative voltages increase the ion entering rate is that they enhance the ion transport in the electrolyte, which limits the transport in the polymer. Since ion transport in the polymer is controlled by diffusion, the total number of ions in the film rises with $\sqrt{t}$. The time when the total number of ions reaches 0.5 is used to characterize the reduction. It decreases exponentially with applied voltage, as shown in Figure 76.

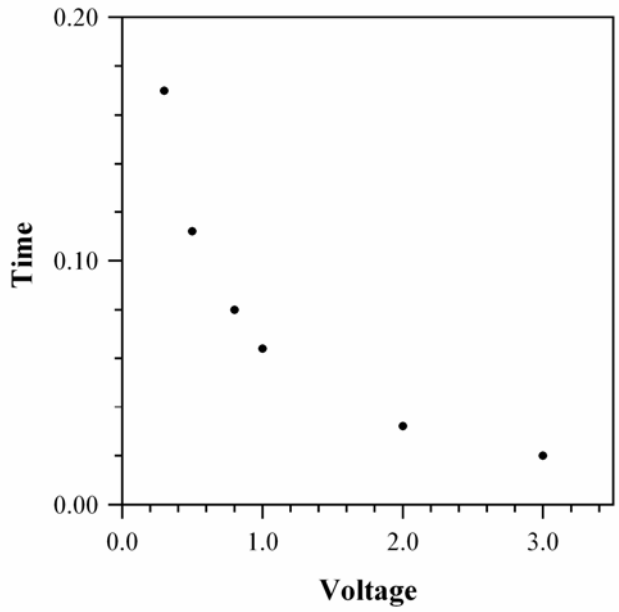

Figure 76. Reduction time of thin film (the time when total ions reach 0.5.) vs. applied voltage.

5.8.3.4.2 Oxidation

The potential profile and concentration profiles (t = 0.01) and during thin film oxidation are shown in Figure 77a. Again, potential drop across the polymer is negligible. Both ion and hole concentration profiles show no phase fronts. Hole concentrations at the polymer/electrolyte interface do not reach the maximum concentration immediately after the oxidation, because the potential drop across the polymer is not high enough. Ions change their concentration abruptly at the polymer interface. This is caused by the high electrical field at the interface generated by the net charge, as shown in Figure 77b.

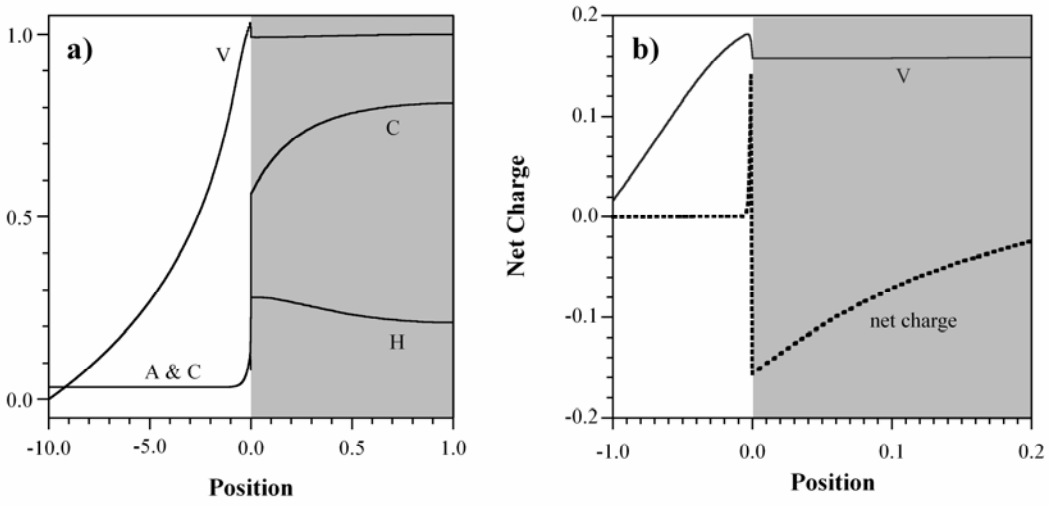

Figure 77. a) Concentration profiles and potential profiles during oxidation of a thin film. *t* = 0.01. b) the corresponding net charge profile across the polymer/electrolyte interface.

The oxidation process in the thin film is shown in Figure 78. No phase fronts are formed during the oxidation. Potential drop in the electrolyte decreases with oxidation, while potential drop across the polymer increase a little bit. Another observation is that a large potential drop occurs at the polymer/electrolyte interface due to net charges generated there. The oxidation process is found to depend on oxidation potentials. The higher the oxidation potential, the quicker the ions leave the film (Figure 78b). Two reasons may account for this observation. As shown in thick film oxidation, the applied voltage affects the ion egress especially at the beginning of the oxidation. Since the thin film oxidation is short, oxidation potential will have stronger effect on thick films than on thin films. Second, the film is thin, even a small potential variations can result large change of the electrical field. Therefore, the migration term is largely altered in thin films.

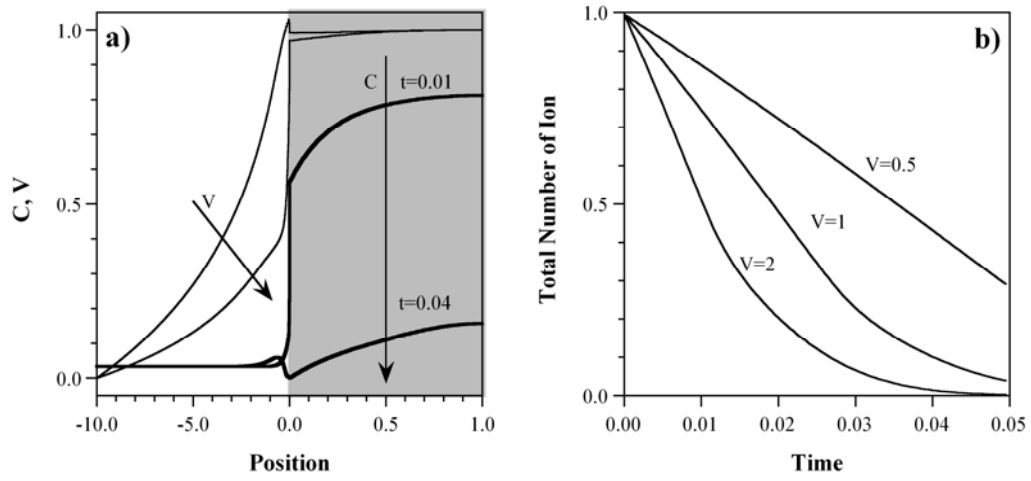

Figure 78. a) Cation and potential profiles in a thin film during oxidation. (Note x-axis scaling.) b) The total number of ions in the film versus time.

Anion-transporting Conjugated Polymers

We now turn to simulations of anion-transporting polymers. As mentioned previously, the key difference between cation and anion transporting materials is that in the former, ions enter an initially conducting film, while in the latter the ions enter an insulating film. These results will thus allow a closer examination of the roles of electrical conductivity and hole transport in redox. No experiments of the type described in Part 1 have been performed with anion-transporting conjugated polymers, such as PPy(ClO_4) or polyaniline, so a correct predictions of future experimental results would represent a true validation of the model.

Inplane ion transport was simulated with the full model for the equivalent cases of a thick film or a barrier-covered thin film. Equations (13) were modified to reflect the change in the sign of the ionic charge as well as the absence of immobile anions in the film.

$$\frac{\partial A}{\partial t} = -\nabla \bullet (-D_A \nabla A + \mu_A A \nabla \phi)$$

(29) $$\frac{\partial H}{\partial t} = -\nabla \bullet (-D_H \nabla H - \mu_H H \nabla \phi)$$

$$\nabla(\varepsilon \nabla \phi) = H - A$$

Here, A is the anion concentration and D_A and μ_A are the anion diffusivity and mobility in the polymer. Equations (17) and (18) were used with D_A and μ_A, and D_H/D_A = 1000, the same as in the cation-transport full model. Transport in the electrolyte was the same as in section 5.6.4.2 except that the coefficients for anions and cations were set to be equal, which are1000 times higher than ion mobility in the polymer, to reflect the fact that in anion-transporting systems, the anions are typically small, comparable in size to the cations. The concentrations were capped by setting mobility to zero, as described in section 5.3.1.2.3.

The boundary conditions were rewritten to reflect the altered relationship between holes and ions: the hole flux at the polymer/electrode interface was $J_H = \mu_H (1 - A)E$ during oxidation and $J_H = \mu_H AE$ during reduction. At the electrolyte interface, the cation flux was zero: only anions could be exchanged between the electrolyte and the polymer.

The initial concentrations of holes and anions were 0 for oxidation, 1 for reduction. As usual, the initial potential profile was solved statically based on these concentrations and the voltages at the boundaries, and the simulation started with this profile.

In comparing the results of cation reduction and anion oxidation, it should be kept in mind that all the simulation parameters were identical except for the anion mobility in electrolyte. Thus, differences between the two cases did not originate from the parameter values.

5.8.4.1 Anion Oxidation

As previously, we start with ion ingress. For an anion-transporting film, this takes place during oxidation. Figure 79a shows the anion concentration in the electrolyte and the polymer at different times during the oxidation process, and Figure 79b shows the corresponding potential profiles.

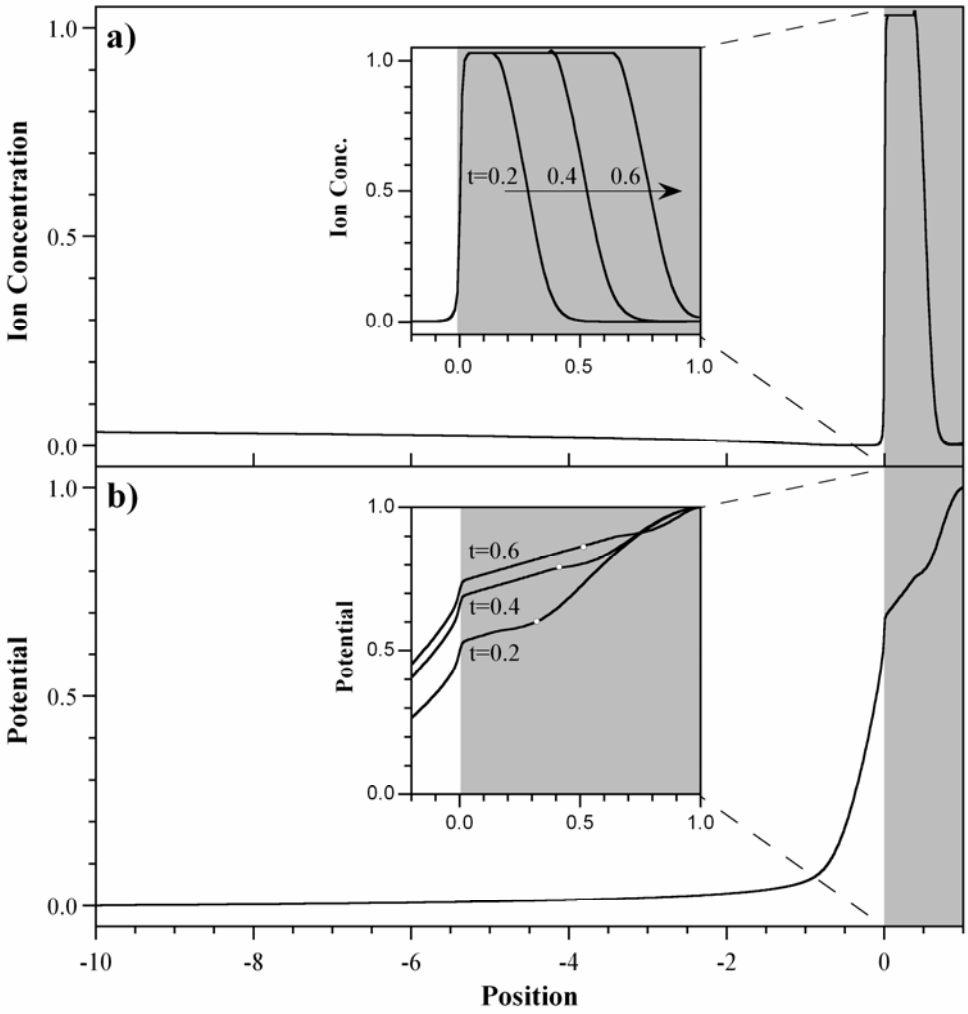

Figure 79. a) Anion concentration in an anion-transporting polymer at three times partway through oxidation (ϕ = 1); note the scaling of the *x*-axis in the electrolyte. The hole concentration profile, not shown, is nearly identical. The insert shows a close-up in the electrolyte at t = 0.4. b) The corresponding potential profiles, with front positions indicated by white points. The wiggle in the potential profile is due to the net charge at the phase front.

As during cation ingress, oxidation begins at the polymer/electrolyte interface (x = 0) because of the much higher mobility of the holes than the anions. Again, a phase front separates the oxidized and reduced regions. The front is comparatively (approximately 3 times at a similar doping level.) wider (compare Figure 65) but it

does not significantly broaden with time. In the electrolyte, the depletion region extends further (also compare to Figure 65).

The potential profiles are complex. While the majority of the voltage is dropped across the depletion layer in the electrolyte, some is also dropped over the reduced region of the polymer and some is dropped across the oxidized region. The latter grew linearly with the width of the oxidized area, as can be seen by looking at the potential curves between the interface and the front position, marked by the points.

Figure 80 shows the anion, hole, potential, and net charge profiles (t = 0.4). Anion and hole follow in most arrears of the polymer except a large deviation at the polymer/electrolyte interface. At the interface, the anion concentration rapidly increases from that of the electrolyte to 1, while hole concentrations there are readily 1. Therefore, a large positive charge is formed at the polymer/electrolyte interface, as shown in Figure 80b. Tow other noticeable charged area in the polymer are also found. A small but sharp positive net charge shows up at the start of the phase front, whose cause is not clear yet. The other area is the reduced area, which has even smaller positive charge all the time. In the electrolyte that is adjacent to the polymer, a negative charge is formed because of the increase of anions. Another area that has net charge is the reduced area, which has a slightly positive charge because oxidation potential slightly increases hole concentration in the reduced area. The electrolyte adjacent to the polymer/electrolyte interface is negative charged due to the increased anion co concentration there.

To explain the potential profile in the polymer, both the net charges and the conductivity of the film need to be considered. Since the electrolyte and the reduced area have low conductivity, they attract large potential drops. The potential drop across the oxidized area is small due to the high conductivity and proportional with the size of the oxidized area. This is unlike the potential drop across the oxidized area in the base case or in the full model. The possible explanation is that the oxidized area is in the middle of two charged regions that create potential difference across the oxidized area. At the same time, we must realize that it is necessary to have potential drop across the oxidized area. Noticing no concentration gradient in the oxidized area, ion ingress will not occur if no electrical field presents.

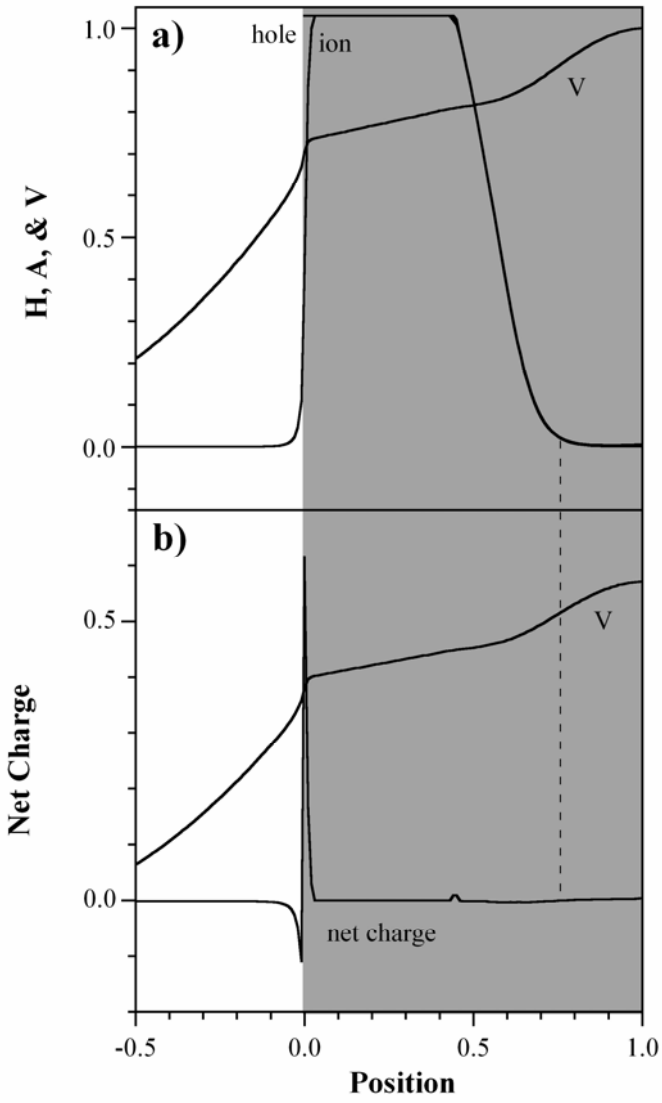

Figure 80. a) ion, hole, and potential profile at t = 0.4. b) the corresponding net charge. The dash line is to show the end of phase front.

The front position and width are shown in Figure 81a versus time, and the velocity is shown as a function of voltage in Figure 81b. Unlike for ion ingress into a cation-transporting film, the front propagated linearly with time rather than with the square root. A linear fit yielded y = 1 – 1.37x with R = 0.999. The reason for this striking difference in behavior is the increase in the small potential drop across the oxidized

region as oxidized area grew. This produced a constant electric field in the oxidized region, resulting in a constant front velocity.

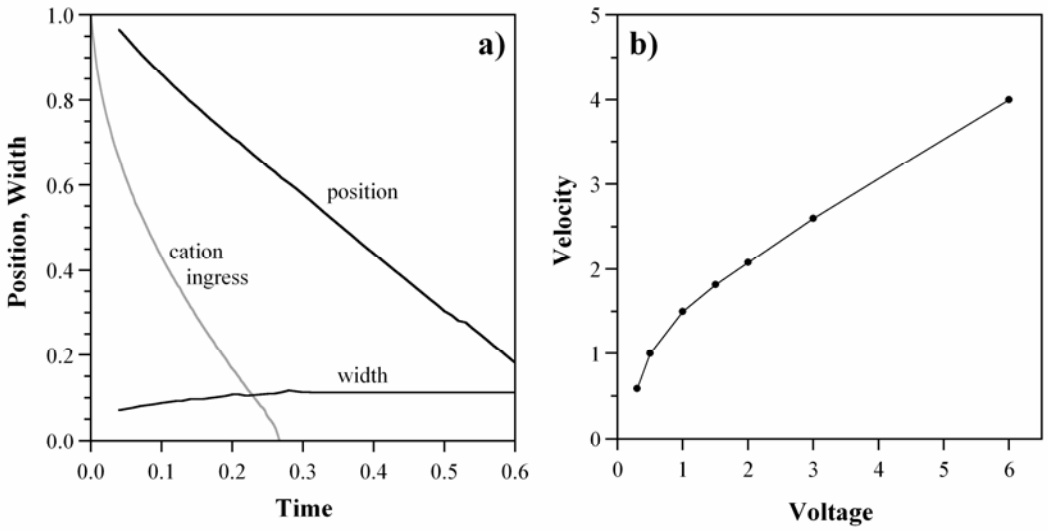

Figure 81. a) Front position and width during oxidation of an anion-transporting film in the full model. The front position for ion ingress into a cation-transporting film under identical model parameters is shown for comparison (gray line). b) Velocity of the front vs. voltage.

The front width increased with $\sqrt{t}$ until t = 0.3, and then it stopped broadening. The exact reason is not clear due to similar reasons regarding with the voltage drop across the oxidized area. The square root dependence arises from the Fickian form of the diffusion term. As discussed previously, despite the fact that nonlinear coefficients were used, the model did not adequately handle the non-Fickian behavior observed experimentally.

From Figure 81a it can be seen that cation ingress occurs more quickly than anion ingress. This is because the cations need to pass through the previously reduced area of the polymer to reach the oxidized area, while the anions need to pass through previously the oxidized area. Since the potential drop across the reduced area is

larger, the velocity of the ions is larger ($v = \mu E$). Secondly, the potential drop in the polymer versus the electrolyte increases during cation reduction, while it decreases during anion oxidation because the reduced area grows in the former case and shrinks in the latter.

5.8.4.2 Anion Reduction

Using the endpoint of the oxidation simulation as the initial state, the potentials at the boundaries were switched to simulate the reduction process. Figure 82 shows the anion concentrations and potential profiles in the polymer as they evolve over time.

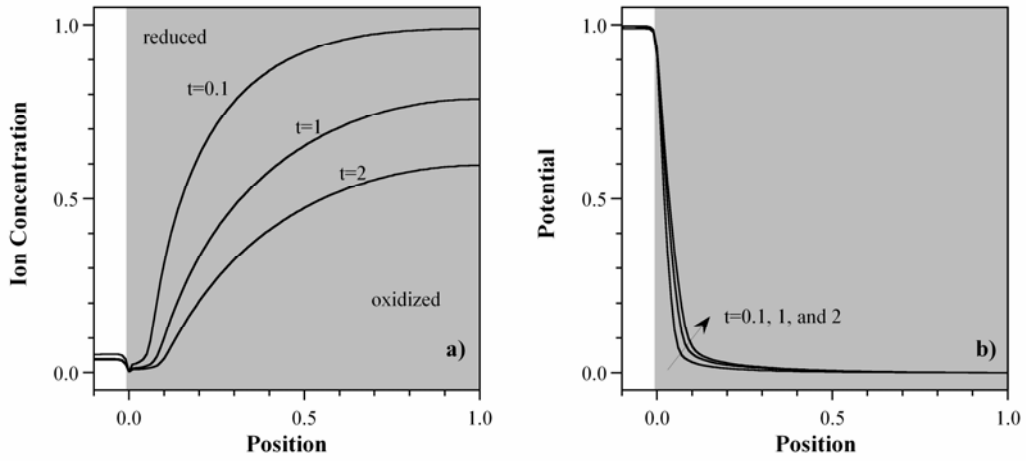

Figure 82. a) Anion concentrations and b) potentials in an anion-transporting polymer during reduction (V = -1) using the full model.

As during the oxidation of a cation-transporting polymer, the ions closest to the polymer/electrolyte interface quickly left the film, producing a short-lived front (as seen at t = 0.1). Thereafter, the ion concentration decreased everywhere. The potential dropped primarily over the reduced area, as expected since it had the lowest conductivity in the system.

The applied potential had only a small effect on the ion transport rates (shown in SM 1.2.6.2). This is because in the reduced area $J_{A,drift} = \mu_A AE \approx 0$ since A $\approx$ 0, and in the oxidized area, E $\sim$ 0, so again $J_{A,drift} \approx 0$. Thus, reduction in the anion-transporting film was diffusion controlled.

5.8.5 Discussion of Model Predictions

5.8.5.1 Summary of Key Scientific Results

The key results of modeling the various systems of Part B are summarized in Table IV. The major scientific findings of the paper are presented in

Figure 83: ion ingress is compared with ion egress for a thick anion-transporting film, a thick cation-transporting film, and a thin cation-transporting film.

Table IV. Summary of predictions made using the full model, which includes nonlinear diffusivity and mobility and an electrolyte layer. Unless otherwise noted, the simulation parameters were the same as for the case of an ion-barrier-covered thin film.

Section, Case	**Simulation Settings**	**Questions Posed**	**Key Findings**
5.6.4.2 Cation-Transport, Reduction	1. $D_C = D_0 * e^{2C}$, $\mu_C = \mu_0 * e^{2C}$ 2. New anion, cation PDEs in an electrolyte layer 3. New boundary conditions, including $V = 0$ at edge of electrolyte	Increase the model complexity to better reflect the physical system. How is the behavior affected by including the potential drops and ion transport in the electrolyte?	1. Voltage drop occurs in the electrolyte. 2. A depletion layer forms in the electrolyte.

Section, Case	**Simulation Settings**	**Questions Posed**	**Key Findings**
5.8.1 Cation-Transport, Reduction	1. Electrolyte concentration varied from 0.0033 (0.01 M) to 1 (3 M)	How does electrolyte concentration affect ion transport?	1. Higher electrolyte concentration reduces the voltage drop. 2. When electrolyte concentration is low, ion transport in the electrolyte is the rate limiting step. The phase front propagates linearly with time. contradicts next item. 3. At low concentration (0.033), front moves with $\sqrt{t}$. 4. At low concentration, broader front width. 5. Front velocity increases with concentration up to 0.1, then approaches a constant value.
5.8.2 Cation-Transport, Oxidation	V = +1 at the polymer/electrode interface, V = 0 at edge of electrolyte	What happens during oxidation of a cation-transporting film, using the same model run "backwards"?	1. There is a negligible potential drop across the film. Thus, ion transport occurs by diffusion and there are no phase fronts. 2. Voltage has no effect on ion transport.

Section, Case	**Simulation Settings**	**Questions Posed**	**Key Findings**
5.8.3.2 Cation-Transport, No Barrier, Reduction (2D Sim.)	1. On top surface, $C = C_0$, $J_H = 0$, $V = 0$ 2. No electrolyte layer 3. Constant D, μ	What does the model predict for the geometry used in actuators, electrochromic devices, batteries, etc.?	1. Cations travel primarily perpendicular to the surface (along E field lines). 2. Charge concentrations and potentials along the field lines are essentially the same as in the base case.
5.8.3.3 Cation-Transport, No Barrier, Reduction, Fast In-Plane Transport (2D Sim.)	1. Same as previous, plus: 2. $\mu_{C,\ inplane} = 10^x \mu_{C,\ out\text{-}of\text{-}plane}$	Increase the inplane diffusivity to reflect anisotropic cation velocities in PPy(DBS).	1. One must set $\mu_{C,\ inplane} = 10^3 \mu_{C,\ out\text{-}of\text{-}plane}$ to get any noticeable inplane transport, and $\mu_{C,\ inplane} = 10^5 \mu_{C,\ out\text{-}of\text{-}plane}$ for inplane transport to dominate.

Section, Case	**Simulation Settings**	**Questions Posed**	**Key Findings**
5.8.3.4 Cation-Transport, No Barrier, Reduction (1D Sim.)	1. Same as full model except: 2. μ_C and D_C increased by 1000x 3. ε increased by 1000x	How does the prediction of thin-film behavior change with the inclusion of the electrolyte?	1. For very thin films, transport in the electrolyte is the rate-limiting step. 2. There is no front in the film. Instead, C rises uniformly with time everywhere in the polymer. 3. Oxidation speed increases with V 4. Ions still enter or leave the film with $\sqrt{t}$
5.8.4.1 Anion-Transport, Oxidation	1. PDEs adapted to reflect change in sign of ion charge and no background charge. 2. $V = +1$ on polymer/electrode interface	How does ion ingress into an anion-transporting film differ from ion ingress into a cation-transporting film?	1. Just as in a cation-transporter, anions enter the polymer with a front. 2. Unlike in a cation-transporter, the front moves linearly with time: $v_f \sim t$. 3. The front velocity increases with V, but non-linearly.

Section, Case	Simulation Settings	Questions Posed	Key Findings
5.8.4.2 Anion-Transport, Reduction	1. PDEs adapted to reflect change in sign of ion charge and no background charge. 2. V = -1 on polymer/electrode interface	How does ion egress from an anion-transporting film differ from ion egress from a cation-transporting film?	1. Just as in a cation-transporter, ions move mainly by diffusion and no front is formed. 2. V has a negligible effect on ion transport speed.

The behavior in a given system under an applied potential of $\phi = 1$ is governed by the magnitude and location of the potential drops. As a rule of thumb, the potential drops are located where there is a net charge: at double layers and depletion layers. To a lesser extent, potential is also dropped across the reduced portions of the polymer. If there is no significant potential drop across the polymer, then the behavior is dominated by diffusion rather than drift, making the switching speed largely unresponsive to voltage.

The results are most intuitively understood in a cation-transporting thick film during reduction. Even though there is a large voltage drop across a depletion layer in the electrolyte just at the polymer surface, there is still a significant potential drop across the reduced part of the film, setting up an electric field responsible for charge migration. The migration of ions from the electrolyte into the film leads to a front.

The distance over which the potential is dropped increases as the front advances, reducing the migration term and yielding a $\sqrt{t}$ dependence of current on time.

The reason for the diffusion-dominated behavior during oxidation is less obvious. In thick cation-transporting films, after an initial loss of cations near the interface due to migration, a potential drop builds up at the polymer/electrolyte interface. Without a migration term in the polymer, transport occurs almost entirely by diffusion. The cause of this drop differs somewhat depending on the model assumptions. Using a capping function to limit the charge concentrations to maximum values near 1, the drop arises at the outer edge of the polymer due to a small net positive charge arising from a build-up of holes, which move as far as possible from the positively charged electrode. Using a strictly charge-neutral model, on the other hand, shifts the voltage drop to the electrolyte just outside the polymer because of the large net charge in the depletion layer.

In anion-transporting films, ion ingress is again characterized by a front, but this front moves with a linear dependence of current on time. The reason for the front is, however, slightly different than for cation ingress. The polymer is initially entirely insulating, so it has a significant potential drop across it, thus leading to a significant migration term. The growing conducting region has only a small potential drop, but it winds up increasing as the conducting region widens.

During ion egress, the behavior is again diffusive. At the start of the reduction of the anion-transporter, the film is oxidized and highly conductive, so the potential is dropped primarily over the electrolyte. After the initial anion egress at the electrolyte

interface, the film becomes reduced there, and thus highly resistive. The electric fields in the rest of the polymer are small, however, and thus there is no driving force causing migration. The location of the potential drop is the same as in the cation-egress case in, but the causes for it are somewhat different.

When the thickness of a cation-transporting film is decreased, all of the material is essentially in the interface region and there is no longer any bulk. The thinness of the film has at least two effects on ion transport. First, the potential drop across the film is necessarily small, since there is so little material. Second, the ion transport time across the film is much shorter than in the electrolyte, and thus ion transport in the electrolyte becomes the rate-limiting step in the reduction process. The concentration profiles are flat. Even in this case, however, the redox goes as $\sqrt{t}$. The number of different conditions that lead to a square root dependence is remarkable, actually.

Unlike in a thick film, the oxidation speed of a thin film depends on the oxidation potential since a thin film falls into the influence of the polymer/electrolyte interface. The ion concentration does not drop to zero within the polymer, but rather just outside it.

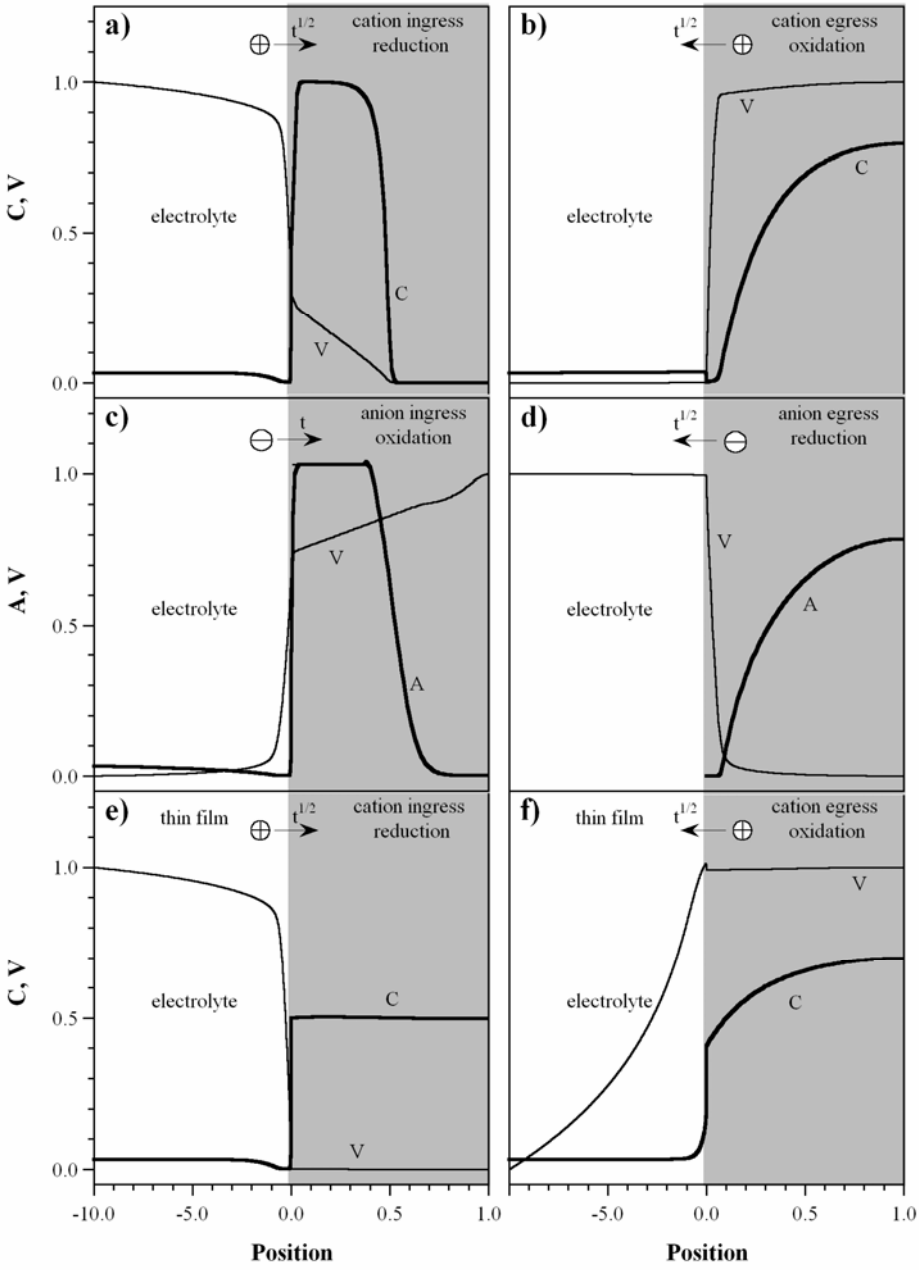
a)
cation ingress
reduction
electrolyte
C
V
b)
cation egress
oxidation
electrolyte
V
C
c)
anion ingress
oxidation
electrolyte
V
A
d)
anion egress
reduction
electrolyte
V
A
e)
thin film
cation ingress
reduction
electrolyte
C
V
f)
thin film
cation egress
oxidation
electrolyte
V
C
C, V
A, V
1.0
0.5
0.0
-10.0
-5.0
0.0
0.5
1.0
Position

Figure 83. Summary of the major scientific findings of the paper: simulation results for an anion-transporting thick film, a cation-transporting thick film, and a cation-transporting thin film during ion ingress and egress. Note that the voltage is here represented as going from 1 to 0 instead of the equivalent 0 to -1.

Figure 84 shows the net charges for different cases. Net charges are always found at the polymer/electrolyte interface, where flux of holes is stopped. Close to the interface, holes are readily zero or 1, but ions need to change from concentrations in electrolytes to concentrations in polymers. Net charges are created in this transition area. Another area is where the film is either fully reduced or fully doped, the transition zone between the fully reduced and fully oxidized area. Where the area is positive charged or negative charged depends on whether holes are removed or donated. The electrolyte adjacent to the polymer/electrolyte interface is also charged. Net charges at the polymer/electrolyte interface affect the potential profile greater than net charges at the transition zone, most likely because of their high magnitude. The net charges of the transition zone also affect the potential drop but in much lower magnitude, possibly because the transition zone is till conductive.

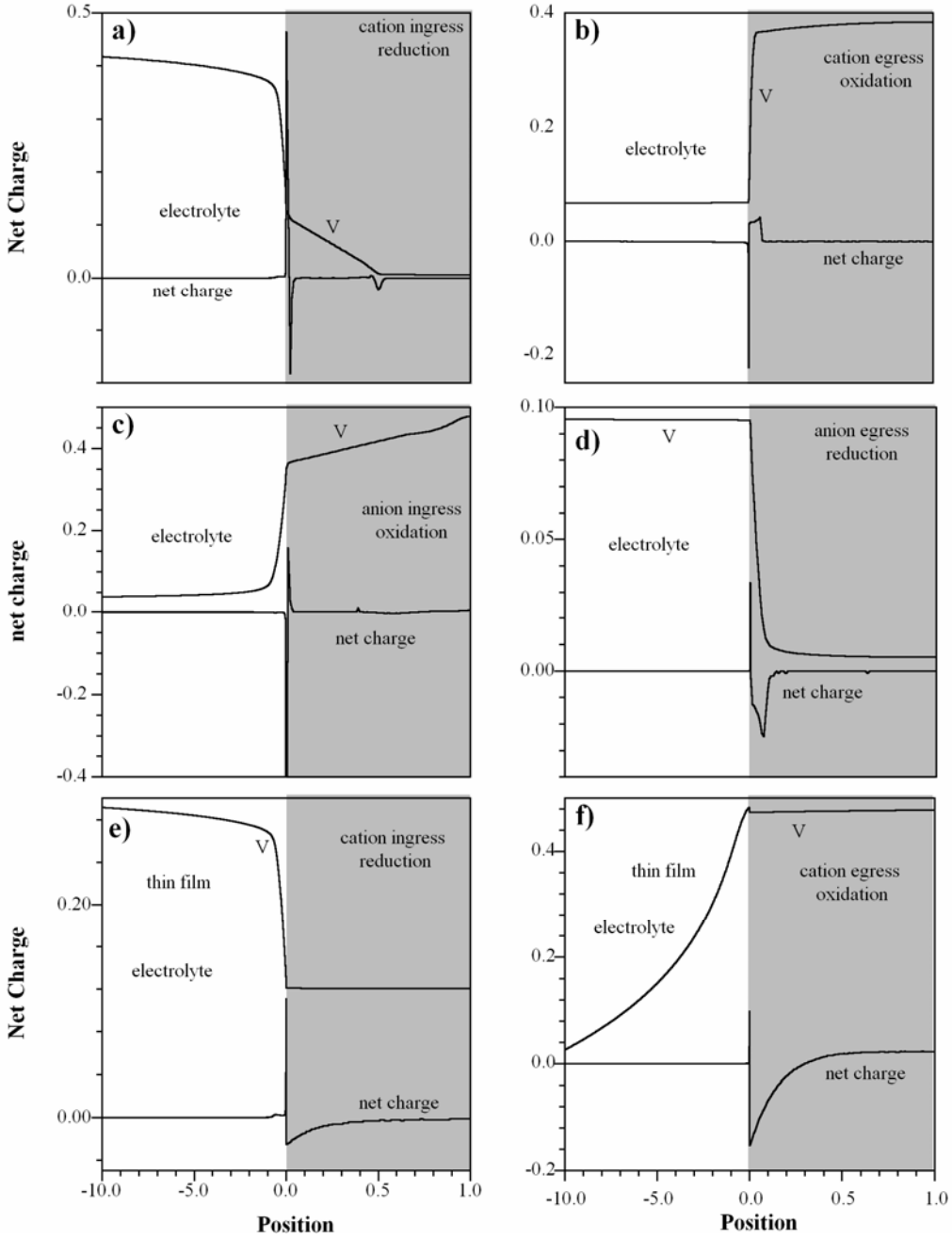

Figure 84. Summary of net charge profiles. The corresponding potential profiles are plotted together. The y axis is for the net charge only (Values of potentials are not shown.) The scale of y axis is also different. The electrolyte is also scaled down 10 times in this plot.

5.8.5.2 Comparison of the Speeds of the Redox Processes

Figure 85 compares the total number of ions in the film as a function of time during ion ingress and egress for cation- and anion-transporting thick films. Figure 85a shows that cations enter the polymer faster than anions do. To understand this, we examine the ion fluxes J across the "reacted" areas near the electrolyte interface. Since no charge accumulates in the fully reduced region during cation reduction, or in the oxidized area during anion oxidation, the ion flux over those areas yields the ion accumulation rate in the remainder of the polymer. These ion fluxes are driven by migration, since there are no concentration gradients in the fully reduced or oxidized polymer. From equation (8), $J = zC\mu E$ (where $z = 1$), and we have used the same C and μ values for both cations and anions. Therefore, E is the only parameter that correlated with rate of ion ingress. Since the reacted material in the case of cation ingress is insulating, versus the conducting material generated during anion oxidation, E is larger, resulting in a faster rate.

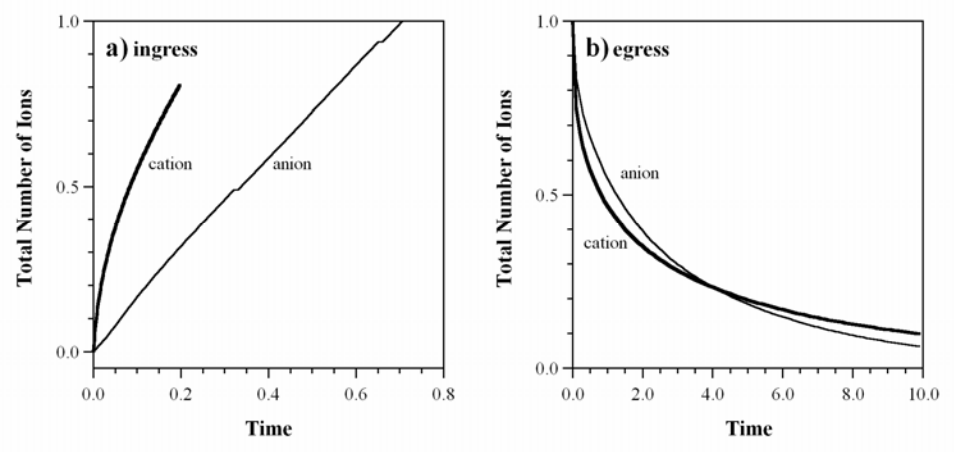

Figure 85. Total number of ions in the film during a) Ion ingress and b) Ion egress. Note the 10x difference in the time scales in the two plots. For all cases, the potential drop is 1 across the polymer and the electrolyte.

Figure 85b compares ion egress among cation transporting films and anion transporting films. Cation egress is initially faster than anion egress. The difference between cation egress and anion egress become smaller, and eventually, anion egress becomes faster than that of cation egress. Potential drop across the polymer, again, is the key to understand these observations. Cation egress starts with a low conductivity film (reduced), over which there is a large potential drop, while anion egress starts with a highly conductive film, with a negligible potential drop. As a result, the migration term is larger for cation egress at the beginning of the process. As time goes on, however, and the cation-transporting film becomes conductive while the anion-transporting film becomes insulating, the ion egress slows in the former and accelerates in the latter.

5.9 Conclusions

Nernst-Planck and Poisson's equations are used to model charge transport in conjugated polymers and electrolytes. The model includes both diffusion and migration as the driving mechanisms for all charged species (cation, anion, and holes). The model uses the Poisson's equation to calculate the potential profile. But, the model does not include polymer relaxation and energetics that occur in conjugated polymers. Numerical simulations are conducted in FEMLAB, attempting to give insights on several important issues that have long been debated in the literature.

The first issue is whether migration contributes to ion transport in conjugated polymers. To examine the migration effect, two types of cases are conducted. First, the reduction voltage is varied from 0.1 to 10. The effective velocity of the phase

front is found to increases linearly with the reduction potential, which is consistent with experimental observation and confirms the migration dominance undoubtedly. The concentration profile at low reduction potentials shows more diffusion controlled features, which is also consistent with experimental observations. The second case type is to remove migration term in the transport equations and then vary the reduction potential. The simulation results have large deviations with experimental observations. For example, phase fronts are formed in the film only when an unrealistic concentration dependent diffusivity (e^{5C}) is used. Phase front velocities increase with reduction potentials in a logarithm manner, which contradicts the experimental observations. The above simulations clearly suggest that diffusion alone is not enough for ion transport in conjugated polymers and migration needs to be included in the modeling work.

Another important finding is that the phase front may move linearly with square root of time even migration is dominant driving force. This prediction clearly points out that an experimental relationship that is linearly with square root of time does not necessarily infer a diffusion controlled process.

The third issue is that how to handle the diffusion in conjugated polymers. Experiments clearly suggest non-Fickian diffusion in conjugated polymers. Our model used concentration dependent diffusivity to improve the predictions but is not successful. Phase fronts broaden linearly with square root of time, which contradicts experimental observations. At low reduction potentials, predictions with variable diffusivity are more deviated from experimental observations that that with constant

diffusivity. For future improvement, a diffusion term that addresses the chain relaxation process needs to be included in the model.

Another issue is how ion transport in electrolytes affects the ion transport in polymers. In the literature, a common understanding is that ion transport in electrolytes is negligible. The simulation showed that potential drop in the electrolyte is not negligible. When the same overpotential is applied to conjugated polymer films, ion transport in the electrolyte has negligible effect.

Simulations clearly show differences between ion ingress and ion egress. Simulations and experiments showed that ion ingress and ion egress show completely different properties. For a cation transporting material such as PPy(DBS), the reduction, which has ion ingress, is found to be controlled by migration evidenced by the phase front formed in the polymer and a linearly relationship between phase front velocities and reduction potential. On the contrary, oxidation shows a bell shape ion concentration profile, which suggests a diffusion controlled process. Furthermore, the oxidation potential shows no effects on the oxidation process, which strongly supports the conclusion that oxidation of PPy(DBS) is diffusion dominant.

Simulations further compare cation transport and anion transport. Simulations show that both ion ingress (reduction of PPy(DBS) and oxidation of PPy(Cl)) shares the same behavior. The same conclusion also applies to ion egress (oxidation of PPy(DBS) and reduction of PPy(Cl)).

5.10 Acknowledgements

We would like to acknowledge Laboratory for Physical Sciences and DuPont for financial support for this work. We acknowledge the FEMLAB technical staff for helping us solve several simulation issues. We also want to thank Kevin Lewy, Mario Urdaneta, Jason West, and Pramod Mathai for helping us on issues with a simulation server.

5.11 References

[1] W. J. Albery and A. R. Mount, "Transmission-line model for conducting polymers including cations and Donnan exclusion," *J. Chem. Soc. Faraday Trans.*, vol. 89 (14), pp. 2487-2497, 1993.

[2] S. Fletcher, "Contribution to the theory of conducting-polymer electrodes in electrolyte solutions," *J. Chem. Soc. Faraday Trans.*, vol. 89 (2), pp. 311-320, 1993.

[3] J. C. Lacroix, K. Fraoua, and P. C. Lacaze, "Moving front phenomena in the switching of conductive polymers," *J. Electroanal. Chem.*, vol. 444 (1), pp. 83-93, 1998.

[4] F. Berthier, J.-P. Diard, and C. Montella, "Numerical solution of coupled systems of ordinary and partial differential equations. Application to the study of electrochemical insertion reactions by linear sweep voltammetry," *J. Electroanal. Chem.*, vol. 502, pp. 126-31, 2001.

[5] E. Deiss, O. Haas, and J. B. Schlenoff, "Numerical-simulation of the cyclic voltammogram of polyacetylene," *J. Electrochem. Soc.*, vol. 142 (10), pp. 3256-3262, 1995.

[6] J. Bisquert and V. S. Vikhrenko, "Analysis of the kinetics of ion intercalation. Two state model describing the coupling of solid state ion diffusion and ion binding processes," *Electrochim. Acta*, vol. 47 (24), pp. 3977-3988, 2002.

[7] X. Wang, B. Shapiro, and E. Smela, "Visualizing ion transport in conjugated polymers," *Adv. Mat.*, vol. 16 (18), pp. 1605-1609, 2004.

[8] X. Wang, E. Smela, and B. Shapiro, "Understanding ion transport in conjugated polymers," Proc. SPIE 12th Annual Int'l. Symposium on Smart Structures and Materials, EAPAD, San Diego, CA, 2005.

[9] L. Bay, T. Jacobsen, S. Skaarup, and K. West, "Mechanism of actuation in conducting polymers: osmotic expansion," *J. Phys. Chem. B*, vol. 105 (36), pp. 8492-8497, 2001.

[10] B. G. Streetman and S. Banerjee, *Solid State Electronic Devices*, 5th ed, Upper Saddle River, Prentice-Hall, 2000.

[11] H. M. Schey, *Div, Grad, Curl, and All That: An Informal Text on Vector Calculus*, New York, W. W. Norton & Company, 1973.

[12] A. J. Bard and L. R. Faulkner, *Electrochemical Methods: Fundamentals and Applications*, 2nd ed, New York, John Wiley & Sons, Inc., 2001.

[13] N. W. Ashcroft and N. D. Mermin, *Solid State Physics*, Philadelphia, Saunders College, 1976.

[14] S. E. Guidoni and C. M. Aldao, "On diffusion, drift and the Einstein relation," *Eur. J. Phys.*, vol. 23, pp. 395–402, 2002.

[15] R. P. Feynman, R. B. Leighton, and M. Sands, *The Feynman Lectures on Physics*, Addison-Wesley Publishing Company, 1964.

[16] Y. Roichman and N. Tessler, "Generalized Einstein relation for disordered semiconductors—implications for device performance," *Appl. Phys. Lett.*, vol. 80 (11), pp. 1948-50, 2002.

[17] R. L. Panton, *Incompressible Flow*, 2 ed, New York, NY, John Wiley & Sons, Inc., 1996.

[18] T. F. Otero and I. Boyano, "Comparative study of conducting polymers by the ESCR model," *J. Phys. Chem. B*, vol. 107 (28), pp. 6730 -6738, 2003.

[19] D. Comoretto, G. Dellepiane, F. Marabelli, P. Tognini, A. Stella, J. Cornil, D. A. dos Santos, J. L. Bredas, and D. Moses, "Experimental and theoretical studies of the anisotropical complex dielectric constant of highly stretch-oriented poly(p-phenylene-vinylene)," *Synthetic Metals*, vol. 116 (1-3), pp. 107-110, 2001.

[20] A. J. Epstein, A. P. Lee, and V. N. Prigodin, "Low-dimensional Variable Range Hopping in Conducting Polymers," *Synth. Met.*, vol. 117, pp. 9-13, 2001.

[21] A. Kaynak, J. Unsworth, G. E. Beard, and R. Clout, "Study of Conducting Polypyrrole Films in the Microwave Region," *Mat. Res. Bull.*, vol. 28 (11), pp. 1109-1125, 1993.

[22] C. Y. Lee, H. M. Kim, J. W. Park, Y. S. Gal, J. I. Jin, and J. Joo, "AC electrical properties of conjugated polymers and theoretical high-frequency behavior of multilayer films," *Synthetic Metals*, vol. 117 (1-3), pp. 109-113, 2001.

[23] G. Phillips, R. Suresh, J. Waldman, J. Kumar, J. Ichen, S. Tripathy, and J. C. Huang, "Dielectric-Properties of Polypyrrole Doped with Tosylate Anion in the Far Infrared and Microwave," *Journal of Applied Physics*, vol. 69 (2), pp. 899-905, 1991.

[24] C. D. Paulse and P. G. Pickup, "Chronoamperometry of polypyrrole: migration of counterions and effect of uncompensated solution resistance," *J . Phys. Chem.*, vol. 92 (24), pp. 7002-7006, 1988.

[25] T. J. R. Hughes, L. P. Franca, and M. Balestra, "A New Finite-Element Formulation for Computational Fluid-Dynamics .5. Circumventing the Babuska-Brezzi Condition - a Stable Petrov-Galerkin Formulation of the Stokes Problem Accommodating Equal-Order Interpolations," *Computer Methods in Applied Mechanics and Engineering*, vol. 59 (1), pp. 85-99, 1986.

[26] J.-C. Lacroix and A. F. Diaz, "Electrolyte effects on the switching reaction of polyaniline," *J. Electrochem. Soc.*, vol. 135 (6), pp. 1457-63, 1988.

[27] R. John and G. G. Wallace, "Doping-dedoping of polypyrrole: a study using current-measuring and resistance-measuring techniques," *J. Electroanal. Chem.*, vol. 354, pp. 145-61, 1993.

[28] E. M. Genies, G. Bidan, and A. Diaz, "Spectroelectrochemical study of polypyrrole films," *J. Electroanal. Chem.*, vol. 149, pp. 101-113, 1983.

[29] T. Osaka, K. Naoi, S. Ogano, and S. Nakamura, "Dependence of film thickness on electrochemical kinetics of polypyrrole and on properties of lithium/polypyrrole battery," *J. Electrochem. Soc.*, vol. 134 (9), pp. 2096-2102, 1987.

[30] Y. Tezuka and K. Aoki, "Concentration profiles of conducting species in polypyrrole films in cyclic voltammetry by means of a diode array detector," *Journal of Electroanalytical Chemistry*, vol. 425, pp. 167-172, 1997.

[31] Y. Tezuka and K. Aoki, "Direct demonstration of the propagation theory of a conductive zone in a polypyrrole film by observing temporal and spatial variations of potentials at addressable microband array electrodes," *J. Electroanal. Chem.*, vol. 273, pp. 161-168, 1989.

[32] Y. Tezuka and T. Kimura, "Concentration distribution of conducting species with time resolution in electrochemical undoping process at the polypyrrole film coated electrode in the light of electric percolation," *Journal of Electroanalytical Chemistry*, vol. 395, pp. 51-55, 1995.

[33] X. Wang and E. Smela, "Ion transport in conjugated polymers: Part 1. Experimental studies on PPy(DBS)," in preparation, 2006.

[34] N. E. Schlotter and P. Y. Furlan, "A Review of Small Molecule Diffusion in Polyolefins," *Polymer*, vol. 33 (16), pp. 3323-3342, 1992.

[35] D. A. Edwards, "Non-Fickian diffusion in thin polymer films," *Journal of Polymer Science Part B-Polymer Physics*, vol. 34 (5), pp. 981-997, 1996.

[36] M. Ilg, B. Pfleiderer, K. Albert, W. Rapp, and E. Bayer, "Investigation of the Diffusion Process in Cross-Linked Polystyrenes by Means of Nmr Imaging and Solid-State Nmr-Spectroscopy," *Macromolecules*, vol. 27 (10), pp. 2778-2783, 1994.

[37] N. L. Thomas, "A theory of case II diffusion," *Polymer*, vol. 23 (pp. 529-542, 1982.

[38] P. G. A. Madden, J. D. W. Madden, P. A. Anquetil, N. A. Vandesteeg, and I. W. Hunter, "The relation of conducting polymer actuator material properties to performance," *IEEE J. Ocean Eng.*, vol. 29 (3), pp. 696-705, 2004.

[39] P. Burgmayer and R. W. Murray, "Ion gate electrodes. Polypyrrole as a switchable ion conductor membrane," *J. Phys. Chem.*, vol. 88, pp. 2515-21, 1984.

[40] M. J. Ariza and T. F. Otero, "Ionic diffusion across oxidized polypyrrole membranes and during oxidation of the free-standing film," *Colloids and Surfaces a-Physicochemical and Engineering Aspects*, vol. 270, pp. 226-231, 2005.

[41] E. Smela and N. Gadegaard, "Surprising volume change in PPy(DBS): an atomic force microscopy study," *Adv. Mat.*, vol. 11 (11), pp. 953-7, 1999.

[42] W. Wernet, M. Monkenbusch, and G. Wegner, "A new series of conducting polymers with layered structure: Polypyrrole n-alkylsulfates and n-alkylsulfonates," *Macromolecular Rapid Communications*, vol. 26 (6), pp. 430-437, 2005.

[43] K. Naoi, "Electrochemistry of surfactant-doped polypyrrole film: formation of columnar structure by elelctropolymerization," *J. of Elelctrochemical Society*, vol. 142 (2), pp. 417-421, 1995.

[44] X. Wang, B. Shapiro, and E. Smela, "Modeling charge transport in conjugated polymers," Proc. SPIE 13th Annual Int'l. Symposium on Smart Structures and Materials, EAPAD, vol. 6168, San Diego, CA, 2006.

Chapter 6 Summary of Scientific Contributions

The dissertation makes a list of scientific contributions to the community of conjugated polymer actuators. They are:

- Designed and developed a new experimental technique that directly displayed ion concentration in conjugated polymers. This technique successfully decoupled ion transport from electron transport. It provided a quantitative measurement on ion concentration and velocity in conjugated polymers.

- Provided solid experimental data and simulation results suggesting that migration is a driving mechanism for ion transport in conjugated polymers. Diffusion of ions in conjugated polymers was found to be non-Fickian diffusion.

- Provided clear experimental data showing that ion egress and ion ingress had different behavior. Cation egress of PPy(DBS) was found to be independent with applied potential, which was different from cation ingress. An important suggestion of this discovery is that increasing overall actuation speed of PPy(DBS) actuators may not be achievable by varying applied potentials.

- Modeled charge transport in conjugated polymers using Nernst-Planck-Poisson's equations and conducted numerous simulation cases for various experimental situations. The model for the first time successfully predicted both ion ingress and ion egress in PPy(DBS) correctly.

- Characterized effect of initial oxidation potentials on phase front velocity. The experimental data showed that velocity of phase front propagation increase exponentially with initial oxidation potential, suggesting that ion mobility increases with polymer swelling.

- Correlated volume change with ion concentration and electronic charge. A linear relationship between intensity and strain was found, suggesting ion concentration, instead of electronic charge, may be a better parameter to control conjugated polymer actuators.

Chapter 7 Future Work

The long-term goal of this project is to have a comprehensive and clear understanding of actuation behavior of PPy(DBS) with various experimental situations. Eventually, constitutive equations need to be built that relate volume change (both magnitude and speed) with major actuator parameters including film thickness, applied voltage, time, temperature, ion type, solvent type, electrolyte concentration, external load, and cycle history. Although this dissertation made a solid start toward these constitutive equations, current understanding is still not enough to produce the desired constitutive equations. Following understandings of conjugated polymer actuators must be achieved in order to move forward with this project.

- An immediate step is to implement non-Fickian diffusion term in the model. The model in this dissertation used a non-constant diffusivity to describe the non-Fickian diffusion, which can not correctly predict the diffusion phenomena in experiments such as front broadening and the shoulder behind the phase front. From the modeling of Case II diffusion, a stress term determined by polymer relaxation can better hand the non-Fickian diffusion. The right description of the diffusion process will allow us to better predict the actuation speed and ion concentration profile in the polymer especially for cation egress of PPy(DBS).

- The effect of ion type, ion mixture, and electrolyte concentration on ion transport speed and volume change must be characterized and understood. For the biomedical application of conjugated polymer actuators, it is inevitable to

operate these actuators in biofluids. Constitutive equations without these parameters bare no applications.

- Effect of external load and cycle history on volume change and ion transport speed must be understood. Creep and hysterisis are most likely occurs when actuators experience with relative heavy load and many cycles.

- Stress-strain curves of conjugated polymers must be obtained and understood. Critical information of mechanical properties needs to be extracted from these data including modulus, yield strain, break strain, creep behavior, and hysterisis.

Appendix

1.1 Supplementary Experimental Results

1.1.1 Reduction

1.1.1.1 Phase Front Propagation Curves

As discussed in section 3.1.1, the velocities of the phase fronts varied in their time dependence between $v \sim t$ and $v \sim \sqrt{t}$, and Figure 25 showed a case intermediate between the two. Figure SM 1 shows data at the two limits.

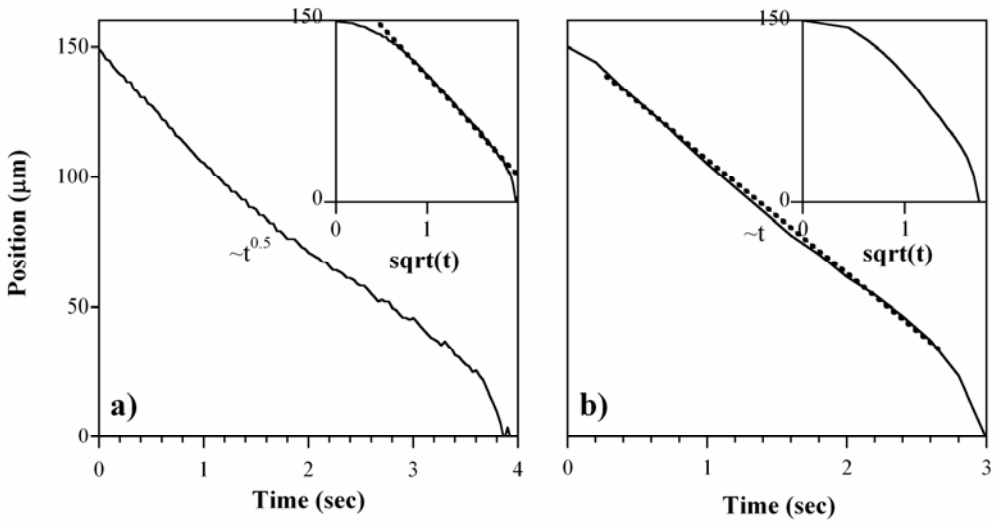

Figure SM 1. a) An example of a phase front propagating at a velocity proportional to $\sqrt{t}$. (V = -1 V vs. Ag/AgCl, PPy 300 nm, SU8 2 μm) b) An example of a phase front propagating linearly with t. (PPy 400 nm, SU8 2 μm) The reduction potential was -1.2 V.

1.1.1.2 Break-In during Initial Cycles

The "break-in" effect of conjugated polymers during the first few cycles is well known. This effect was also observed in samples that had been cycled and then left in the electrolyte without an applied potential at 0 V for some time. Figure SM 2

shows the measured ion velocity as a function of cycle number and the corresponding chronoamperograms.

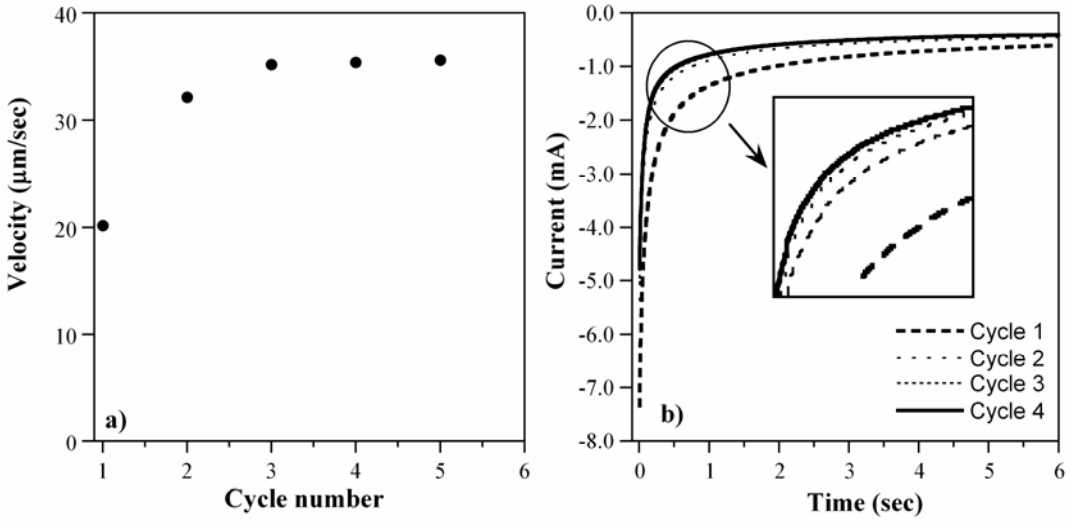

Figure SM 2. a) Ion front velocity during reduction at -1 V as a function of cycle number. b) Corresponding current response of the same sample. (PPy, 600 nm, SU8, 2 μm)

During the first 3 cycles, the velocity increased. After that, the speeds reached a constant value. The currents followed the same pattern. This dependence on cycle number was observed again when films were recycled after they rested in the oxidized state for more than 10 minutes.

The corresponding front broadening is shown in Figure SM 3. The front broadening during the 1st cycle was the lowest. The 2nd cycle had a higher broadening rate, and it increased slightly more in the 3rd cycle, but remained constant after that.

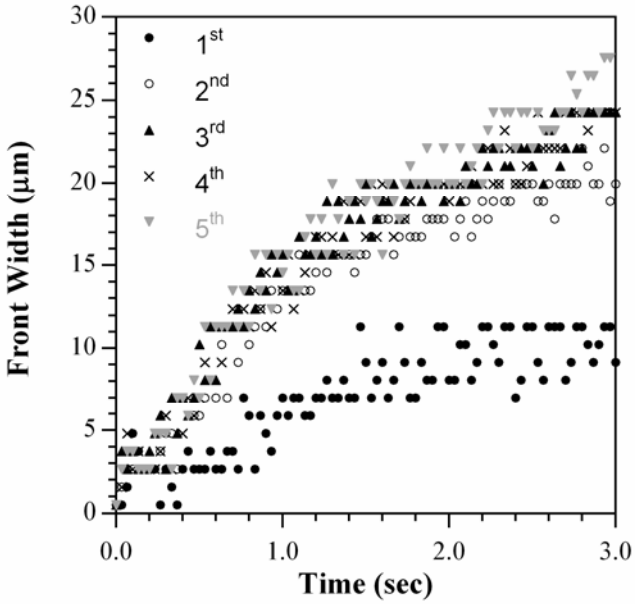

Figure SM 3. Front broadening at different cycle numbers. The experimental situations are the same as those in Figure SM 2. Note : The 1st cycle in this plot is not the "very first cycle". It is the first one during recycling.

1.1.1.3 Charge and Intensity during the Very First Cycle

During the very first cycle, charge and intensity do not follow each other. The intensity of the film increases almost linear with *t* since phase front moves into the film almost linear with *t*. Charge data, however, decreases exponentially and reached a plateau at 200 second, which is 90 seconds earlier than when phase fronts reach center of the film. Again, the results suggest that electronic charge and ions (intensity) may not have a linear relationship.

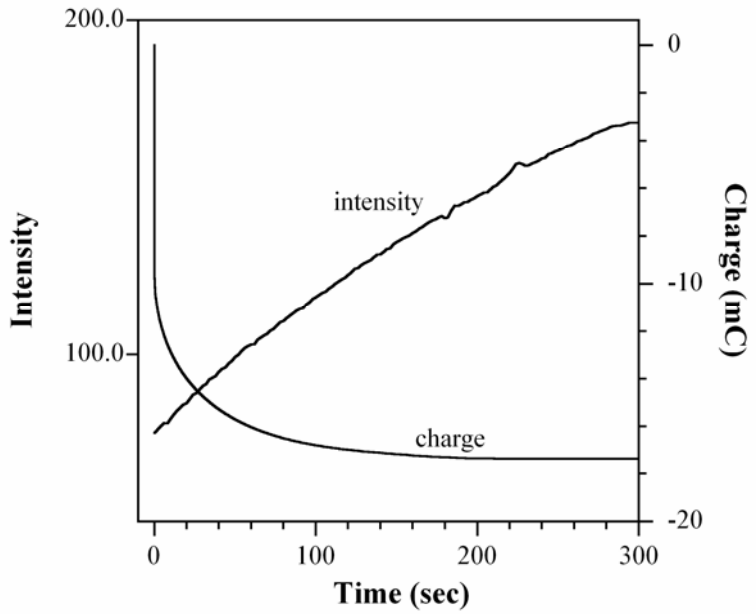

Figure SM 4. Intensity and charge during the very first cycle. Phase fronts reached center of the film at 290 seconds. Charge was obtained through integration of the current data.

1.1.2 Oxidation

1.1.2.1 Average Intensity Change vs. Oxidation Potential

Section 3.2.2 showed the average intensity change at oxidation potentials at 0.4, 0, and -0.4 V. Additional data from two samples are shown in Figure SM 5. The oxidation potential was increased from -0.5 V to 0.4 V at 0.1 V intervals.

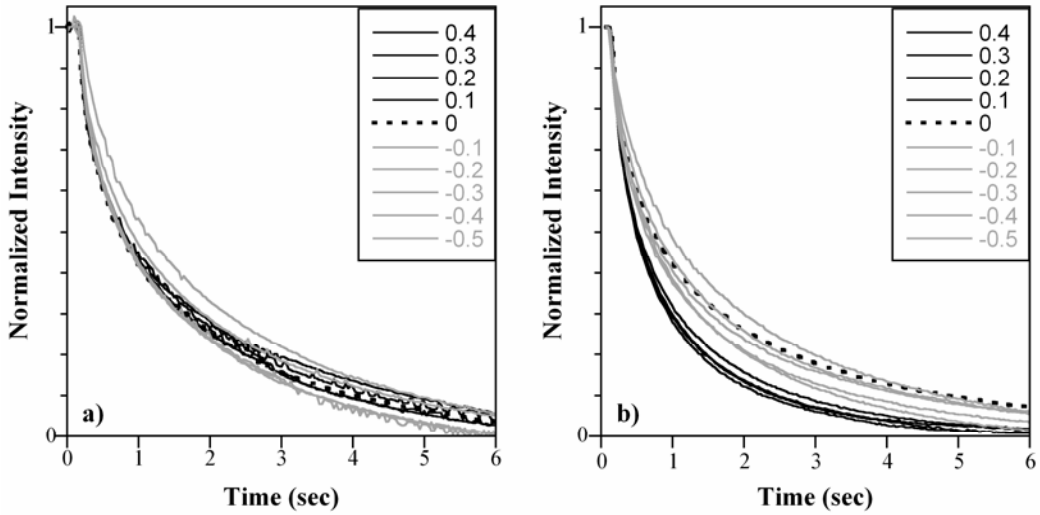

Figure SM 5. PPy stripe average intensity vs. time at different oxidation potentials for two samples. An intensity of 1 corresponds to the fully reduced state, and that of 0 to the fully oxidized state. a) PPy 400 nm, SU8 2 μm thick. b) PPy 500 nm, SU8 2 μm thick.

The data in Figure SM 5a have no systematic dependence on the oxidation potential. In Figure SM 5b, the oxidation is initially faster for potentials above 0 V, but all the curves are of similar shape and reach the fully oxidized state at the same time.

1.1.2.2 Color Profiles vs. Oxidation Potential

Two sets of intensity profiles during oxidation are shown in Figure SM 6, taken at oxidation potentials of -0.4 V and 0.4 V vs. Ag/AgCl.

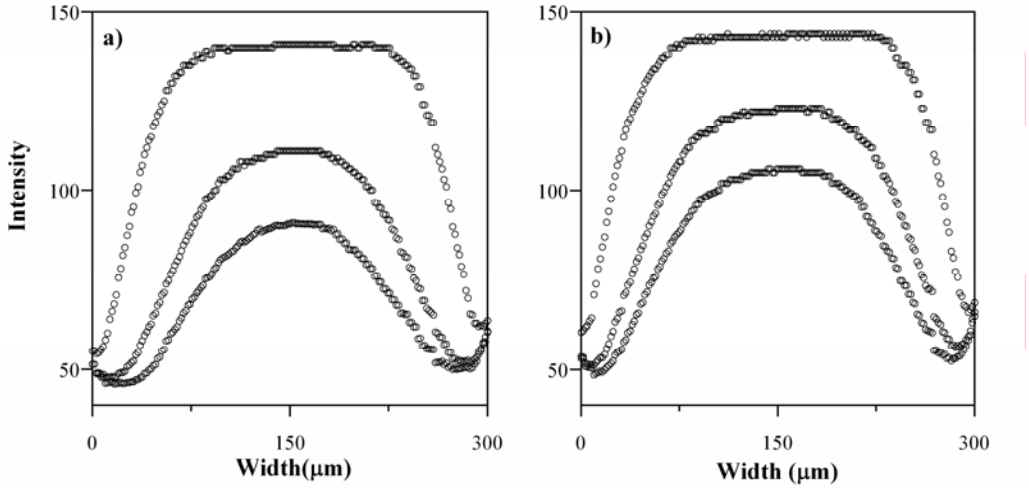

Figure SM 6. Intensity profiles across the PPy stripe during oxidation at 0.5 second time intervals, a) 0.4 V, b) -0.4 V. (PPy 400 nm, SU8 2 μm)

Step-like shapes at the beginning change to bell shapes. The data at the two potentials are almost identical and show clear no dependence on the oxidation potential.

1.1.3 Effect of Electrolyte Concentration

The phase front propagation experiments were also used to study effects of concentration on ion transport in PPy(DBS) {Wang, 2005 #3268}. Concentrations of NaDBS electrolytes varied from 0.01, 0.02, 0.05, 0.1, 0.2, and 0.3 M (NaDBS solutions saturated at concentrations higher than 0.3 M.). Velocities at lease three reduction potentials were obtained from each concentration. Since the reduction peak in the cyclic voltammograms shifted with electrolyte concentrations, velocities at the same overpotential were compared. In order to obtain velocities at the same

overpotentials, a linear equation was fit to the three measured velocities for each concentration, and velocities at the -0.5 V overpotential was calculated. The velocities essentially showed no dependence on electrolyte concentrations as shown in Figure SM 7.

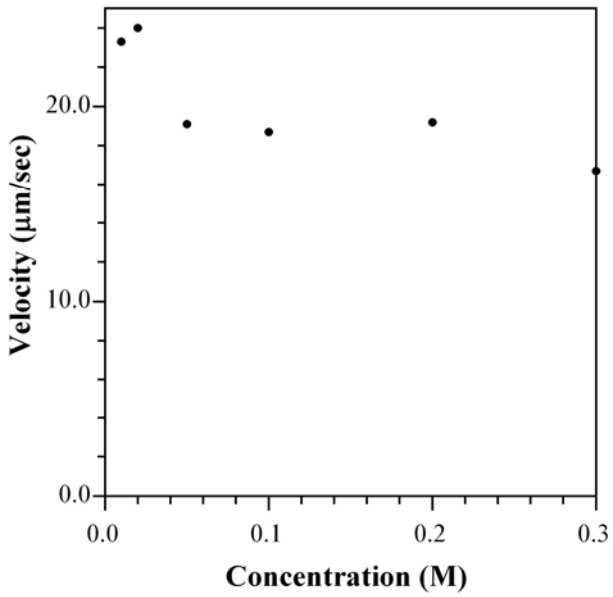

Figure SM 7. Front velocity as a function of NaDBS solution concentration upon reduction at -0.5 V more negative then the reduction peak.

The front broadening data are shown in Figure SM 8. Front broadening with 0.01 M is slightly slow than the others. Front broadening with the rest concentrations shows no difference.

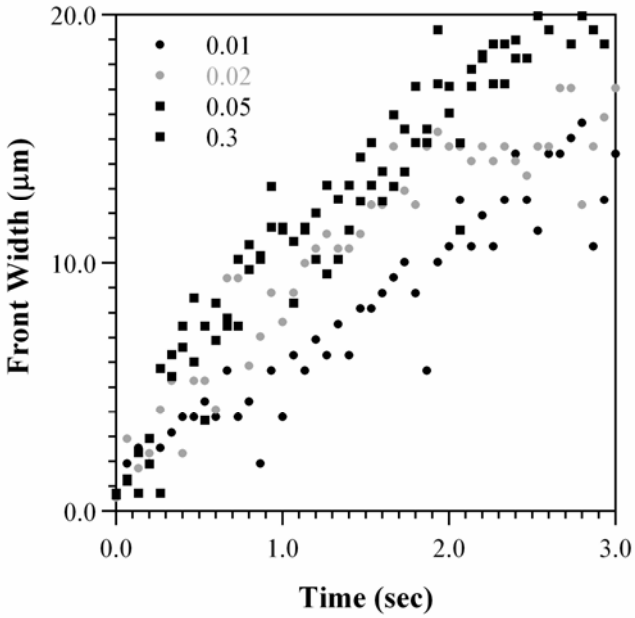

Figure SM 8. Front broadening with various electrolyte concentrations.

Figure SM 9 shows the intensity changes during oxidation with various electrolyte concentrations. The average intensity vs. time curves does not show any dependence on electrolyte concentrations.

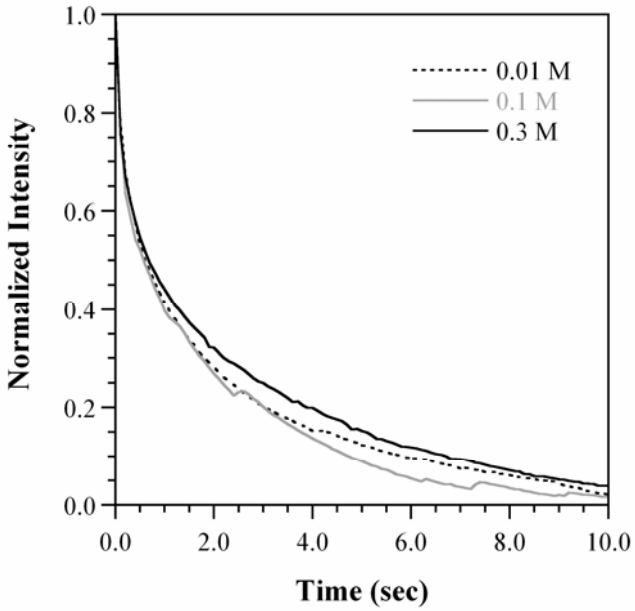

Figure SM 9. Intensity change during oxidation at various electrolyte concentrations.

1.1.4 Effect of Temperature

The phase front propagation experiments were also used to study effects of temperature on ion transport in PPy(DBS) {Wang, 2005 #3268}. Temperatures of 0.1 M NaDBS solutions were varied between 20 and 40 ^{o}C. Data from other temperatures were not obtainable because at temperatures lower than 20 ^{o}C, the NaDBS precipitated, and above 40 ^{o}C, condensation coated the microscope lens. Velocities at –1 V vs. Ag/AgCl were measured for each temperature. The results are shown in Figure SM 10. The reduction velocity increased slightly with temperature, approximately 0.24 μm/sec per Celsius degree.

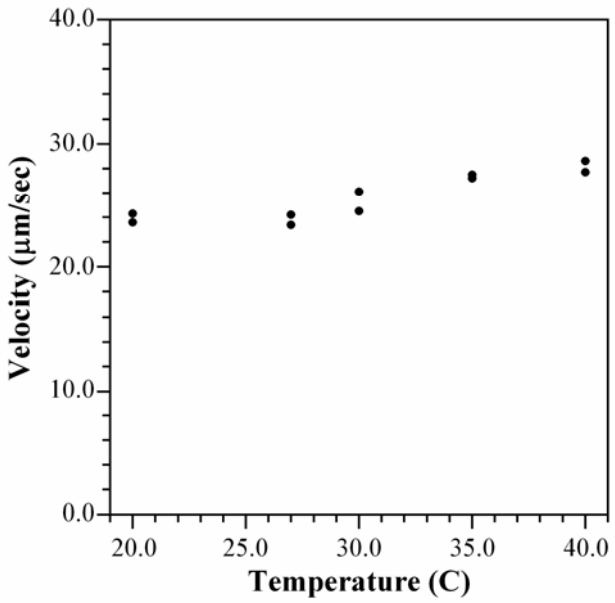

Figure SM 10. Front velocity as a function of temperature upon reduction at -1 V.

Figure SM 11 shows the front broadening with various temperatures. At 20 ^{o}C, fronts broadened slightly faster than those at 30 and 40 ^{o}C. However, 30 and 40 ^{o}C had similar front broadening rate.

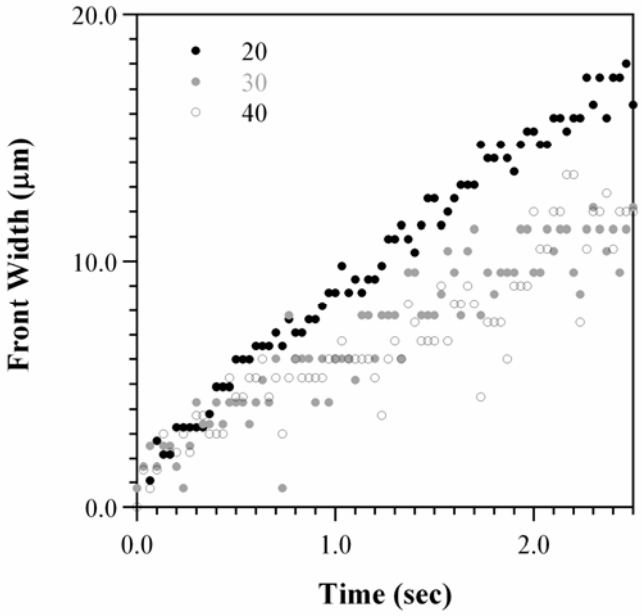

Figure SM 11. Front broadening with various temperatures.

Film intensity decreases faster when temperature is increased, as shown in Figure SM 12. At 20 ^{o}C, it took approximately 8 seconds for intensity of films to reach a plateau. At higher temperature, the required time was reduced to approximately 4 to 5 seconds.

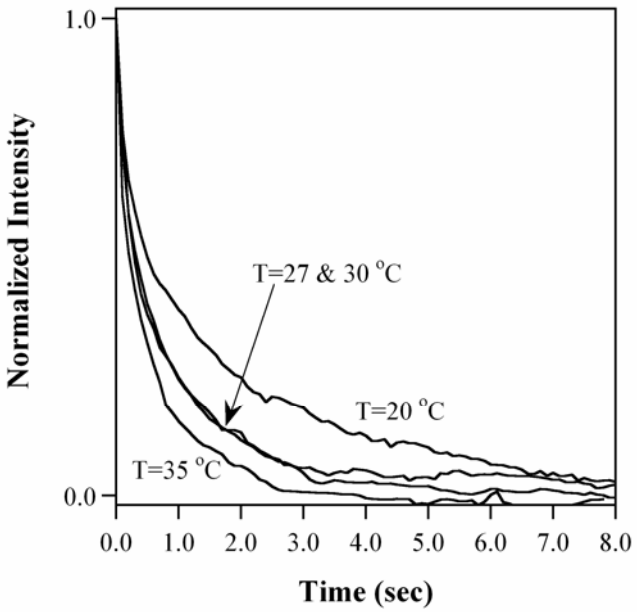

Figure SM 12. Oxidation intensity change at temperatures of 20, 27, 30, and 35 °C.

1.1.5 Effect of Ion Barrier Thickness

The ion barrier mechanically constrains the deformation of the film, and may thus interfere with the electrochemical reaction: Madden has reported that ion transport is a function of load [59]. To determine the effect of the ion barrier, the SU8 ion barrier thickness was varied from 2 μm to 25 μm, and 1 μm thick ion barriers were fabricated of Parylene C, which has a similar modulus (Parylene C has a modulus of 2.7 GPa given by the product specification sheet, and SU8 has a modulus of 2.4 GPa). A stiffness parameter was used to quantify the magnitude of the constraint. The stiffness parameter is the product of the ion barrier cross-sectional area seen by the ion front (8 mm * film thickness) and the barrier modulus.

1.1.5.1 Velocity

Reduction velocities are shown in Figure SM 13 as a function of ion barrier stiffness during the first cycle and subsequent cycles. Six samples were examined, all having a PPy thickness of 800 nm. (Recall that SU8 ~2 μm thick, corresponding to a stiffness of 38.4 N, was used for the other experiments in this paper.)

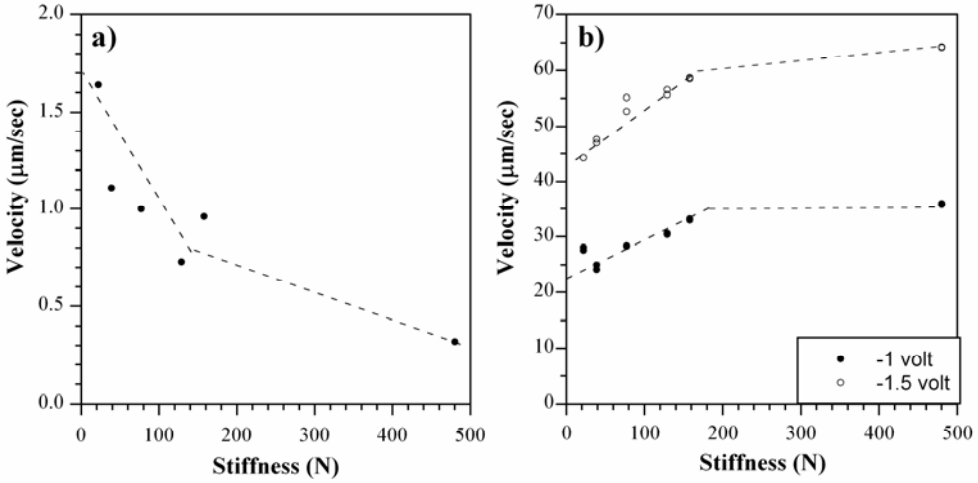

Figure SM 13. Dependence of ion velocity on ion barrier stiffness in a) the first cycle and b) later cycles during reduction at -1 V. (PPy 800 nm) Multiple points at the same stiffness represent different scans. Solid lines are linear fits for samples whose stiffness is less than 200 N.

During the first cycle, stiffer barriers reduced the velocity. Extrapolating to a stiffness of 0, the velocity under a perfectly compliant ion barrier would be approximately 1.7 μm/sec. The velocity dropped rapidly to half this value for a stiffness of 160 N, but then less rapidly to settle at approximately 0.3 μm/sec, 6 times less. Additional data are needed to more fully explore this relationship.

Contrary to the first cycle results and initial expectations, during later cycles stiffer ion barriers *increased* the ion velocity. At -1 V, the velocity went from ~20 μm/sec at

0 N to ~30 μm/sec at 160 N, an increase of 50%. At -1.5 V, the velocity also increased by 50%, from ~40 to ~60 μm/sec.

We propose a possible explanation for the reduced velocity in the first cycle with thicker barriers, but increased velocity in later cycles, based on the fact that it takes more energy to bend the stiffer layers. Thus, during the first reduction cycle, when the PPy film goes from a compacted state to an expanded one, stiffer barriers hinder the expansion, which is needed for ion ingress, to a greater extent. However, stiffer barriers also hinder the re-compaction of the polymer during oxidation, thereby holding the polymer matrix open. Thus, during subsequent cycles the ions encounter a more open structure. (It should further be kept in mind that the volume change during the first cycle is almost twice that during later cycles, so the bending energy required is significantly greater.)

1.1.5.2 Front Broadening

The front broadening for different ion barrier stiffnesses is shown in Figure SM 14 and Figure SM 15 for reduction at -1 V.

Ion barriers of 21.6 N and 76.8 N stiffness have slower broadening rates than the other four. Since 38 falls with the others, there is no clear pattern. Figure SM 15 shows that front broadening is linear with time for ion barriers that have stiffness below 100 N. For higher stiffness, the broadening has two slopes. A power function is used to fit the front broadening at higher stiffness as shown in Figure SM 16. The powers are found to fall between 0.75 and 1.

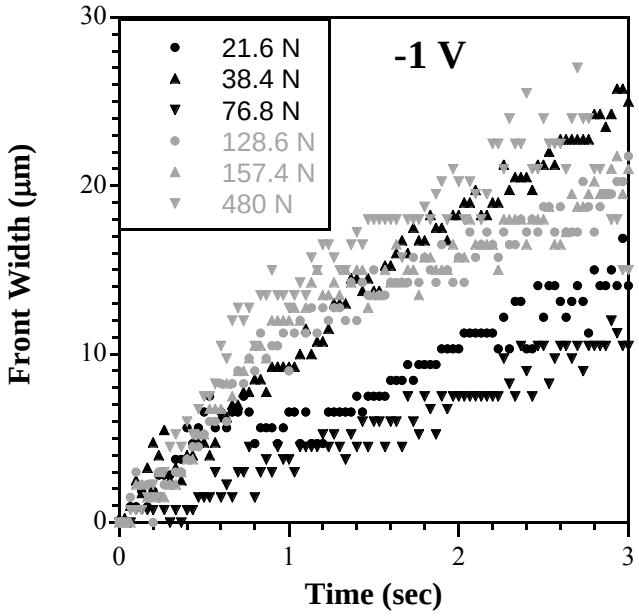

Figure SM 14. Front broadening as a function of ion barrier thickness at two potentials.

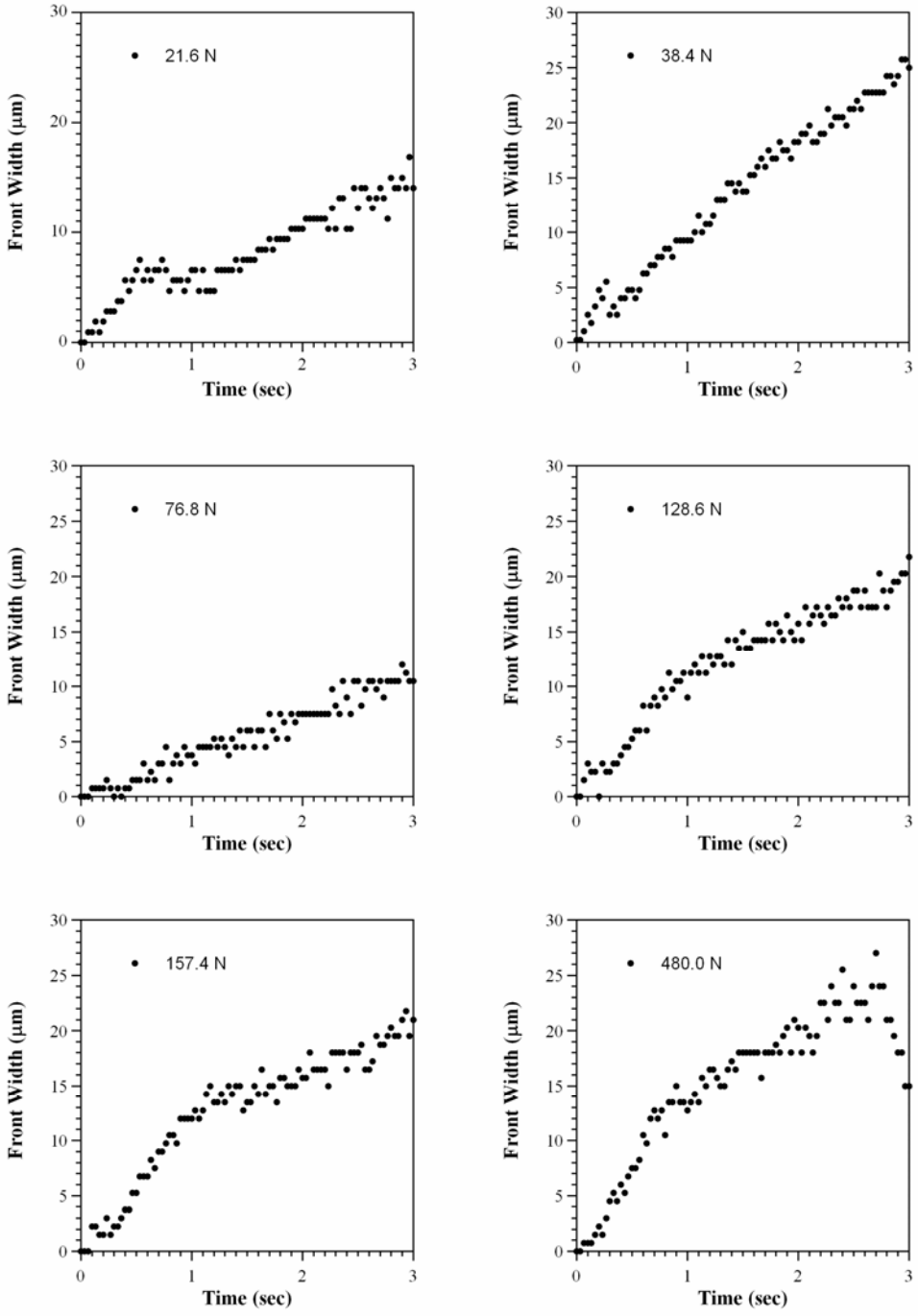

Figure SM 15. Front broadening for different ion barrier stiffnesses, -1 V.

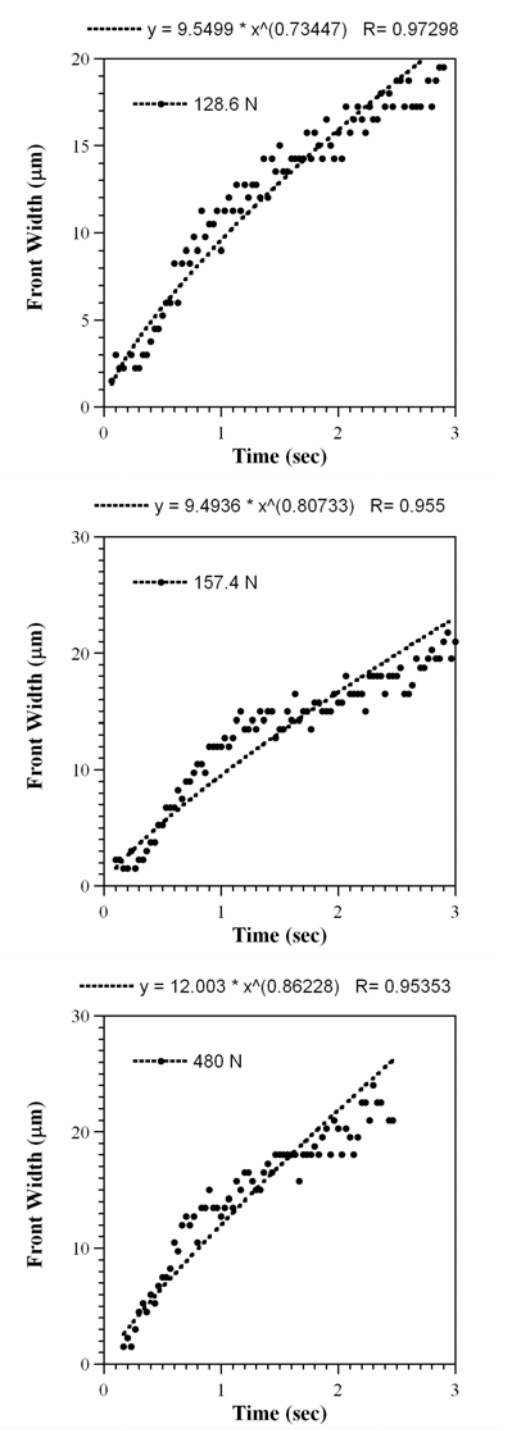

Figure SM 16. Power fit of front broadening curves with higher stiffness.

Figure SM 17 shows front propagation and front broadening have the same relationship with time. The comparison clearly shows that front broadening and front

propagation are independent from each other. This is not a surprise since front propagation is dominated by migration, and broadening is dominated by diffusion.

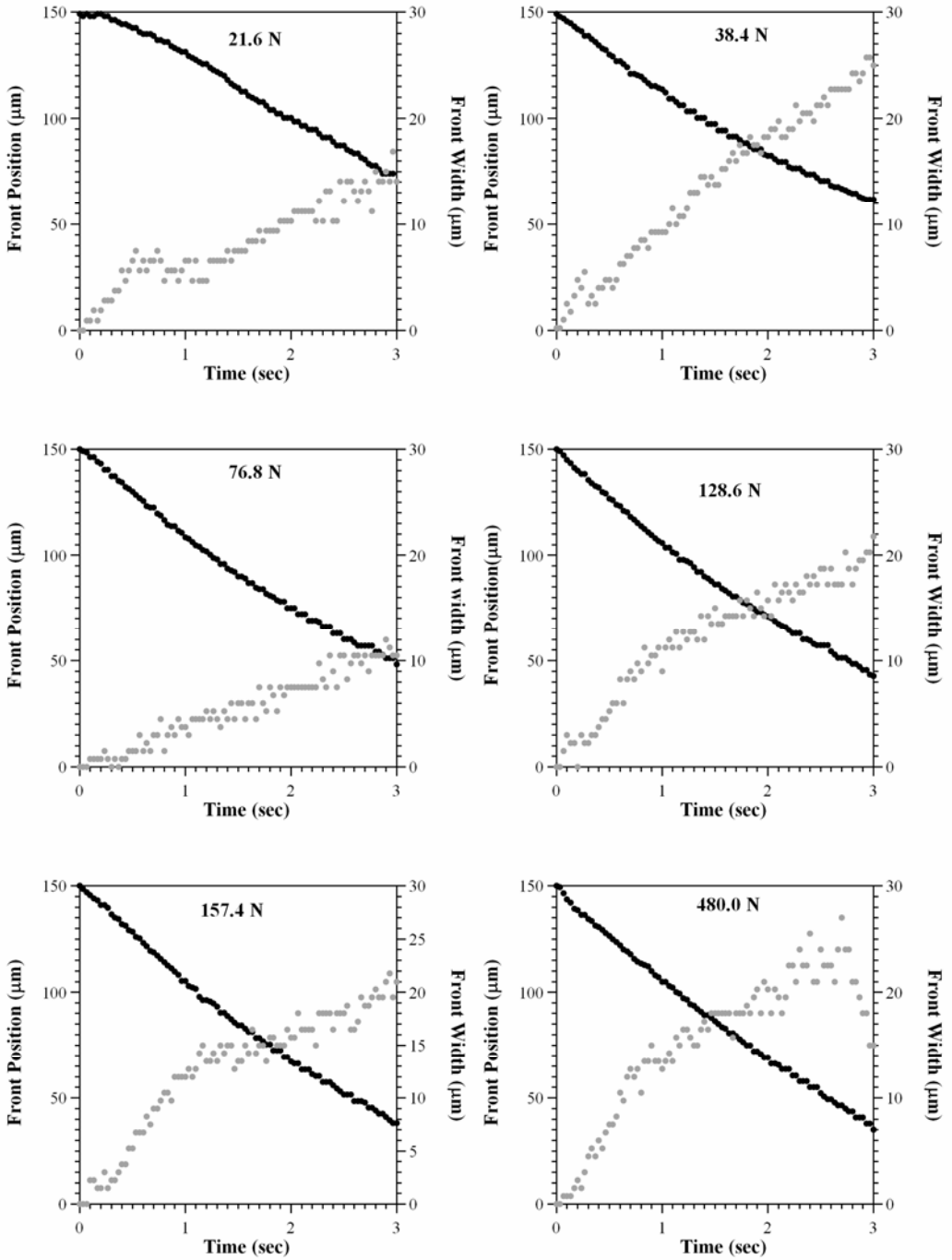

Figure SM 17. A comparison between front broadening and front propagation.

Front width of the first cycle is also tracked and shown in Figure SM 18. The front width is between 0 and 4 μm. With such small width, the analysis does not produce a continuous changing front width. It only produces oscillations of front width.

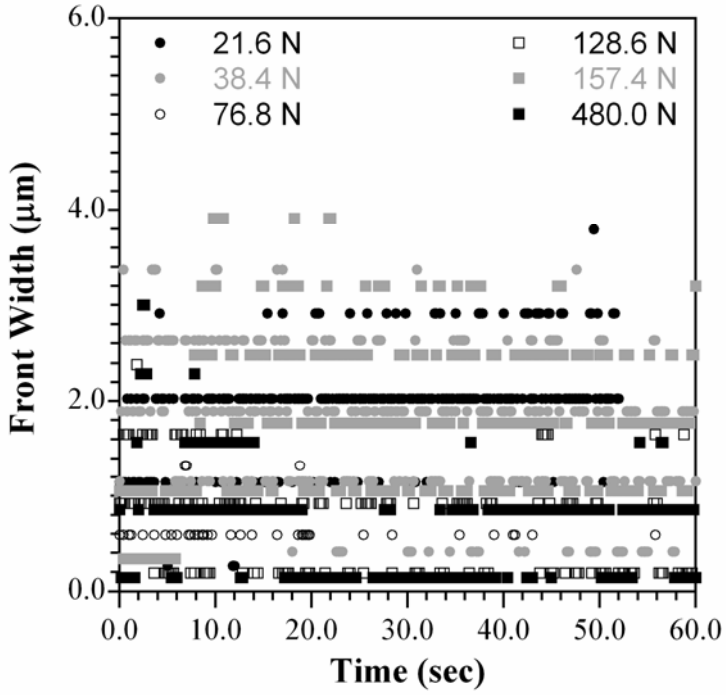

Figure SM 18. Front broadening in the very first cycle with different ion barrier stiffness. Films were never cycled before. No front broadening is observed.

1.1.5.3 Oxidation

Figure SM 19 shows the intensity change during oxidation with various ion barrier stiffness. Although front velocity during reduction increases with ion barrier stiffness, intensity change during oxidation does not show any dependence on ion barrier stiffness.

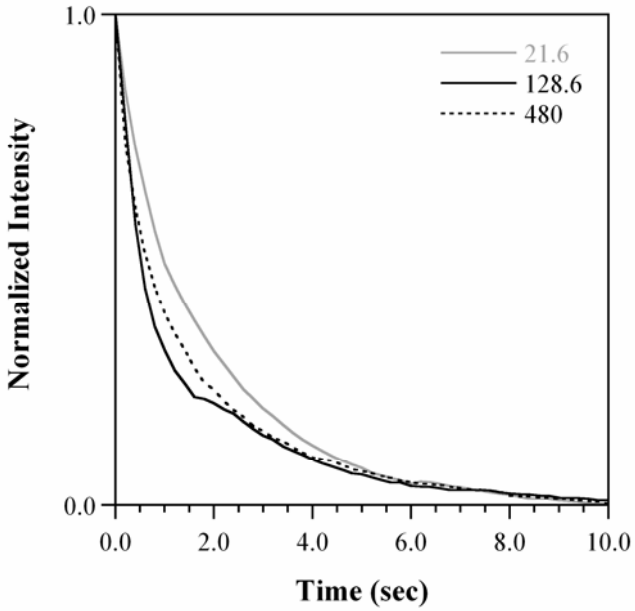

Figure SM 19. Intensity change during oxidation with different ion barrier stiffness.

1.1.6 Effect of PPy Thickness

If the ion front moves predominantly parallel to the electrode surface, and if the vertical outer edge of the PPy is uniform, then one might expect the ion velocity to be independent of the PPy(DBS) film thickness, provided that the polymer morphology, crosslinking degree, etc. is unchanged with thickness. To test this supposition, the thickness was varied between 0.3 and 1.85 μm, keeping the ion barrier thickness at 2 μm.

1.1.6.1 Velocity

First-cycle velocities at -1 V are shown in Figure SM 20a, and later cycle velocities in Figure SM 20b. (Velocities in later cycles could only be measured for film thicknesses less than 1 μm because hydrogen bubble generation was too severe for

thicker films.) Since only a single scan was performed, and only a single sample prepared at each thickness, these data are preliminary.

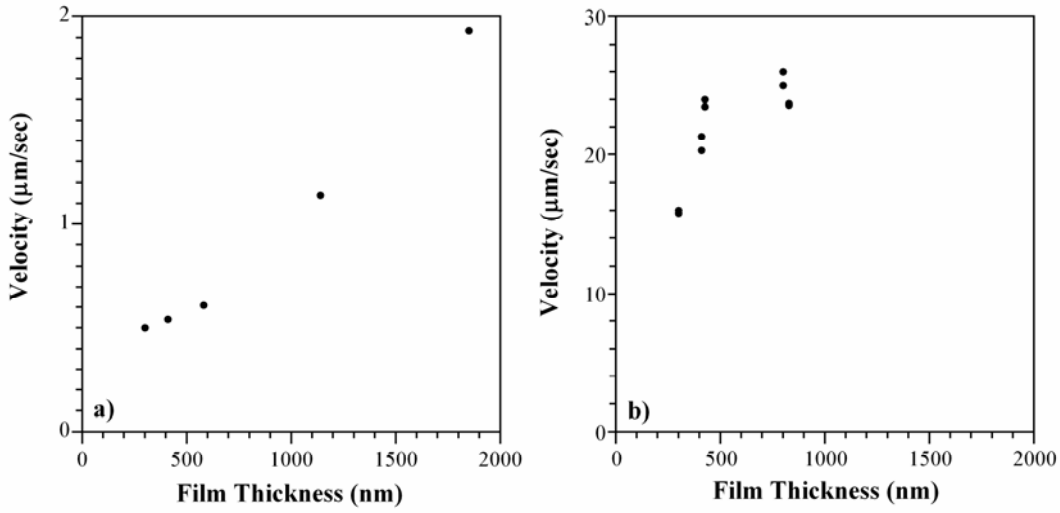

Figure SM 20. Reduction velocities at -1 V as a function of PPy(DBS) thickness. The ion barrier was 2 μm thick SU8. a) First cycle. b) Later cycles.

In both the first and subsequent cycles, reduction velocities increased with film thickness. During the first cycle, the velocity went from 0.5 μm/sec at 300 nm to 1.8 μm/sec at 1850 nm: both thickness and velocity increasing by a factor of 6. This suggests the hypothesis that, *since thicker films are proportionally stronger, they are thus able to deform the ion barrier more readily*, thereby increasing the velocity in both the 1st and later cycles.

The velocities in later cycles were also higher for thicker films, increasing from16 μm/sec at 410 nm to 26 μm/sec at 920 nm, a factor of only 1.6 for the speed vs. 2.1 for the thickness. This suggests that in the water-swollen state after the first reduction, the ion barrier plays a less influential role, completely consistent with the results of Figure SM 20b versus those of Figure SM 20a.

1.1.6.2 Front Broadening

The corresponding broadening data are plotted in Figure SM 21. There show no dependence on the PPy thickness.

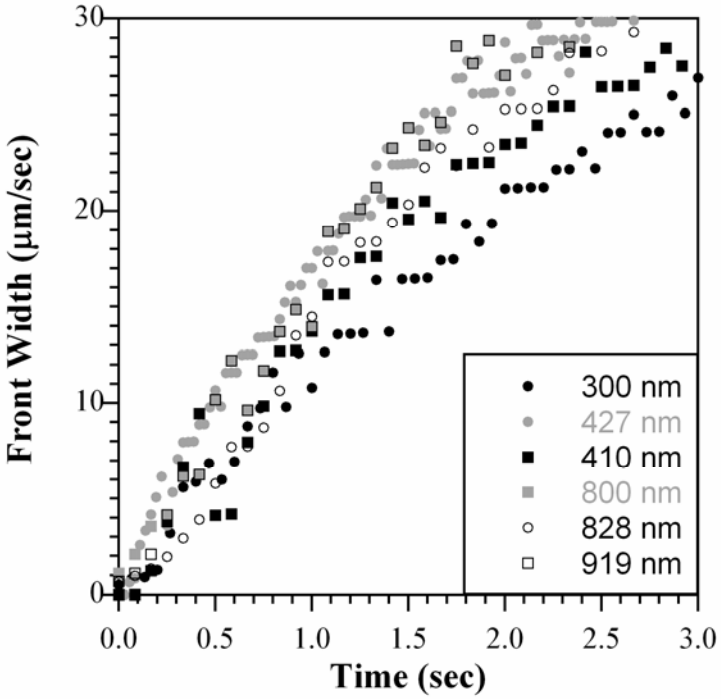

Figure SM 21. Phase front broadening as a function of film thickness. When fit to a power law, the slopes go as ~$t^{0.75}$.

1.1.6.3 Oxidation

Figure SM 22 shows the intensity change during oxidation with various film thicknesses. The data clearly show that intensity change increases with film thickness, this is consistent with the results of phase front velocity.

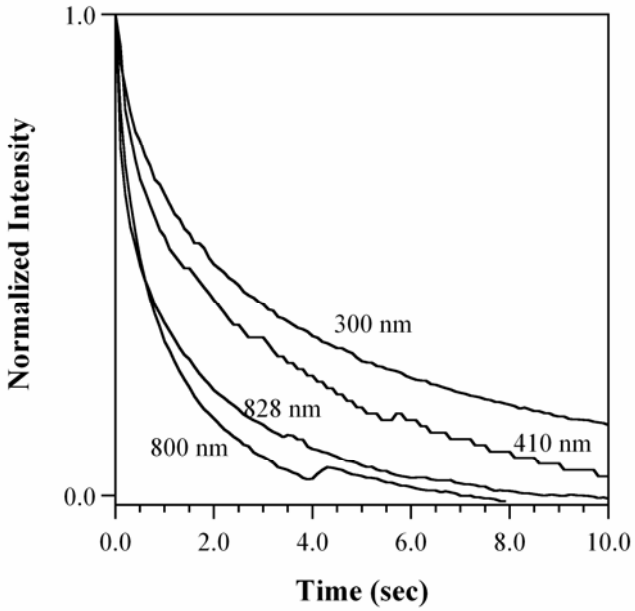

Figure SM 22. Intensity changes during oxidation with various film thickness.

1.1.7 Effect of Ion Type

1.1.7.1 Phase Front Velocity at Reduction

Reduction phase front velocities PPy(DBS) films with 0.1 M alkali cation electrolytes (Anions were DBS.) were measured to find out how alkali cations affect the redox speed of PPy(DBS). Date of the first-ever reduction cycle under -1 V is shown in Figure SM 23. Lithium has the highest velocity, which is twice as fast as Na and ten times as fast as K. Velocities of Rb and Cs are very small, which is close to zero. Because velocities of Rb and Cs were so slow, it took approximately 6 hours for the phase front to reach the center of the film.

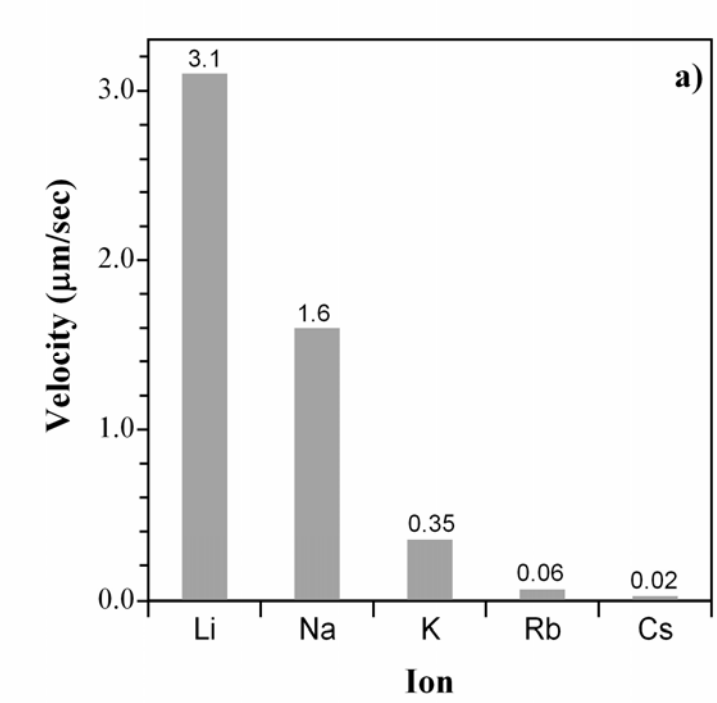

Figure SM 23. Inplane velocity of cations in PPy(DBS) during a) the first reduction step to -1 V and b) subsequent steps to -1.1 V. (Ion barrier thickness 2.2 μm.)

Figure SM 24 shows the phase front velocities during later cycles with different ions. For each ion, velocities of at least three potentials were measured. Apparently, velocities of ions follow the order of Li=Na > K > Rb > Cs. Measurements were repeated on different samples, and velocities with each ion all follow the same order.

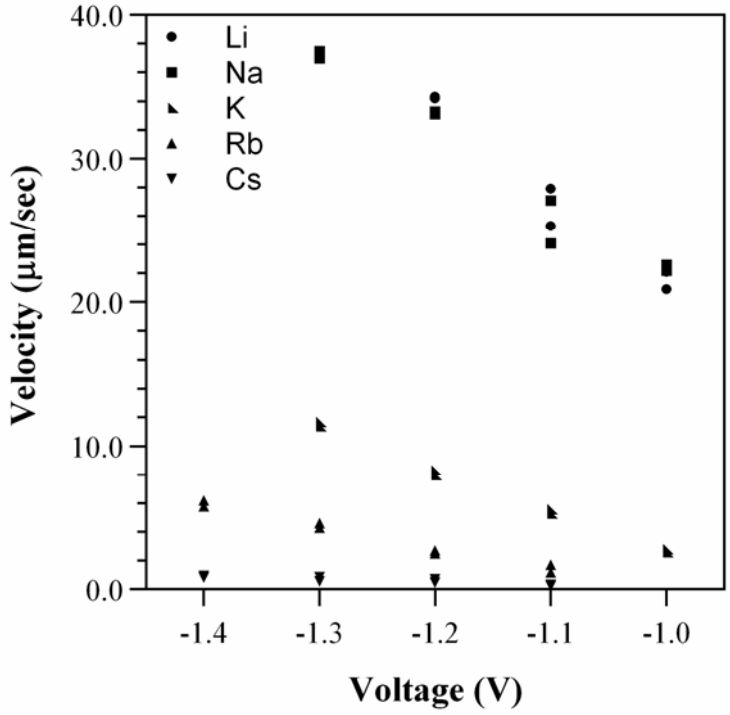

Figure SM 24. Alkali cation inplane velocity as a function of voltage. Duplicate points indicate duplicate measurements on the same sample.

1.1.7.2 Out of Plane Strain

Figure SM 25 shows how swelling of PPy(DBS) varies with each ions. Every column represents data of one sample. The error bar of each bar is the variation of height across the sample. The swelling of PPy(DBS) does not show huge difference among alkali cations. All swelling data fall between 20% and 45%. The averaged swelling of Li, Na, and Rb is close to 40%, while the averaged swelling of K and Cs is close to 30%. The importance of swelling is that it determines how open the polymer is before the reduction. Larger swelling means a more open polymer matrix, in which ions will have higher diffusivity. The relative constant swelling of PPy(DBS) tells us that the polymer openness with each ion is similar and should not cause large difference in diffusivity. Since swelling of conjugated polymers with

alkali cations has never been reported before, a comparison with literature is not available.

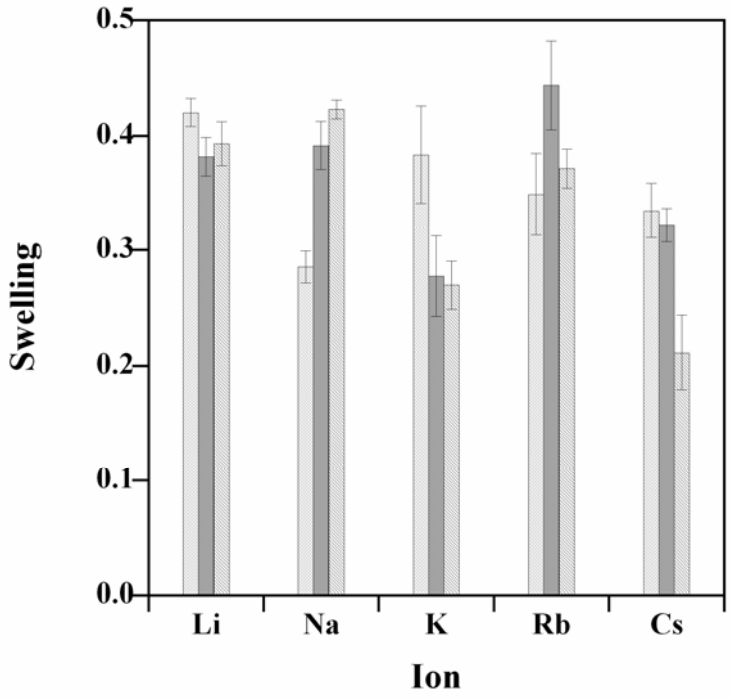

Figure SM 25. Swelling with alkali ions. Swelling is calculated based on the as-deposited film thickness.

Figure SM 26 shows the actuation strain with each ion. Lithium has the largest strain, then Na, K, Rb, and Cs. The order is consistent with the size of hydration shell of alkali cations in aqueous electrolytes. Since Li has the highest charge density, it has the largest hydration shell. Therefore, it brings in more water molecules into PPy(DBS) films, and produced the largest actuation strain. The order is also consistent with findings in literature.

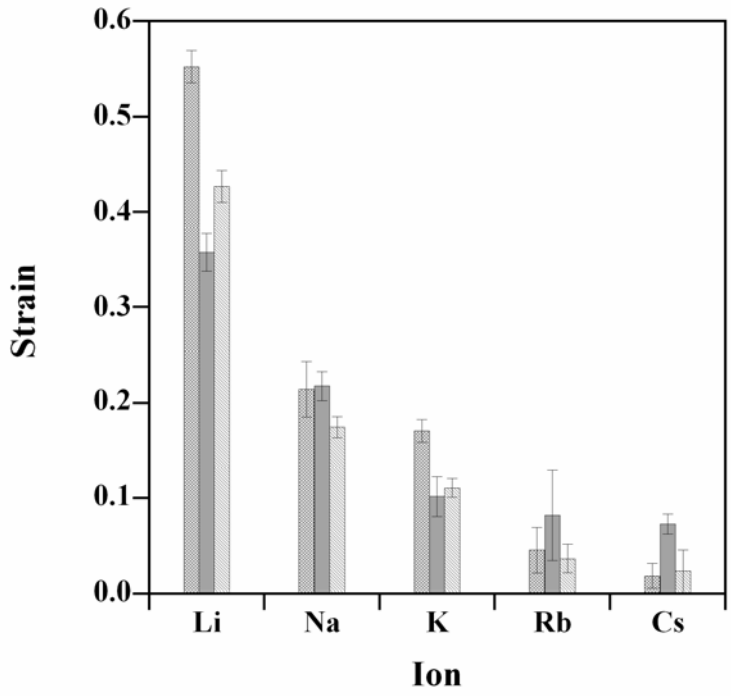

Figure SM 26. Actuation strain with alkali ions.

1.2 Supplementary Modeling and Simulation Results

1.2.1 Modeling and Theoretical Analysis

1.2.1.1 Derivation of Non-Dimensional PDEs (5.3.2, Reducing Model Complexity)

This section shows the derivation of non-dimensional PDEs. After implementing the characteristic scale, the non-dimensional transport equations are:

$$
\begin{aligned}
&\frac{\partial C}{\partial t} = -\nabla \bullet (-\frac{\boldsymbol{D_C t_0}}{\boldsymbol{L^2}} \nabla C - \frac{\boldsymbol{\mu_C V t_0}}{\boldsymbol{L^2}} C \nabla \phi) \\
&\frac{\partial H}{\partial t} = -\nabla \bullet (-\frac{\boldsymbol{D_H t_0}}{\boldsymbol{L^2}} \nabla H - \frac{\boldsymbol{\mu_H V t_0}}{\boldsymbol{L^2}} H \nabla \phi) \\
&\nabla (\frac{\boldsymbol{\varepsilon V}}{\boldsymbol{L^2 z C_0}} \nabla \phi) = C + H - 1
\end{aligned}
\qquad (30)
$$

By selecting $t_0 = L^2/(\mu_C V)$, based on the ion migration term, the non-dimensional ion mobility is a unity. Then, the non-dimensional PDEs are transformed to:

$$
\begin{aligned}
&\frac{\partial C}{\partial t} = -\nabla \bullet \left(-D_C \nabla C - C\nabla\phi\right) \\
&\frac{\partial H}{\partial t} = -\nabla \bullet \left(-D_H \nabla H - \mu_H H\nabla\phi\right) \\
&\nabla(\varepsilon\nabla\phi) = Q = C + H - 1
\end{aligned}
\tag{31}
$$

where $D_C = \boldsymbol{D_C} / \boldsymbol{\mu_C V}$, $D_H = \boldsymbol{D_H} / \boldsymbol{\mu_C V}$, $\mu_H = \boldsymbol{\mu_H} / \boldsymbol{\mu_C}$, and $\varepsilon = \boldsymbol{\varepsilon V} / \boldsymbol{L_0^2 z H_0}$.

D_C, is given by the ratio between dimensional diffusion $\boldsymbol{D_C}$ and drift magnitude $\boldsymbol{\mu_C V}$. Here $\boldsymbol{D_C}$ has units m^2/s, $\boldsymbol{\mu_C}$ has units C s / kg = m^2/sV, and $\boldsymbol{V}$ has units of volts = kg m^2 / C s^2. Hence D_C has units of $\frac{\mathrm{m}^2}{\mathrm{s}}\frac{\mathrm{kg}}{\mathrm{C\ s}}\frac{\mathrm{C\ s}^2}{\mathrm{kg\ m}^2} = 1$ and is non-dimensional. The remaining non-dimensional PDEs are derived in the same way.

For our choice of non-dimensionalization, each non-dimensional diffusion coefficient is scaled by the ion mobility timing the applied voltage, . The non-dimensional mobilities are $\mu_C = 1$ and $\mu_H = \boldsymbol{\mu_H} / \boldsymbol{\mu_C}$. Finally, the non-dimensional dielectric coefficient is the dimensional coefficient $\boldsymbol{\varepsilon}$ normalized by the characteristic gradient of the electric field , divided by the characteristic charge concentration $\boldsymbol{zH_0}$.

The dimensional model, equations (8) and (10), has 8 free parameters: $\boldsymbol{D_C}$, $\boldsymbol{\mu_C}$, $\boldsymbol{D_H}$, $\boldsymbol{\mu_H}$, $\boldsymbol{\varepsilon}$, $\boldsymbol{V}$, $\boldsymbol{L}$, and $\boldsymbol{H_0}$. The non-dimensional model, equation (13), has four: D_C, D_H, μ_H, and ε. Choosing the 8 dimensional parameters corresponds to a unique choice of the 4 non-dimensional parameters: $D_C = \boldsymbol{D_C} / \boldsymbol{\mu_C V}$, $D_H = \boldsymbol{D_H} / \boldsymbol{\mu_C V}$, $\mu_H = \boldsymbol{\mu_H} / \boldsymbol{\mu_C}$,

and $\varepsilon = \boldsymbol{\varepsilon V} / \boldsymbol{L_0^2 z H_0}$. Using these 4 non-dimensional parameters, one can solve the non-dimensional model. The resulting non-dimensional solution gives back the dimensional variable solutions via the relations $\boldsymbol{C}(\boldsymbol{x},\boldsymbol{y},\boldsymbol{z}) = \boldsymbol{H_0} C(\boldsymbol{x}/\boldsymbol{L},\boldsymbol{y}/\boldsymbol{L},\boldsymbol{z}/\boldsymbol{L})$, $\boldsymbol{H}(\boldsymbol{x},\boldsymbol{y},\boldsymbol{z}) = \boldsymbol{H_0} H(\boldsymbol{x}/\boldsymbol{L},\boldsymbol{y}/\boldsymbol{L},\boldsymbol{z}/\boldsymbol{L})$, and $\boldsymbol{\phi}(\boldsymbol{x},\boldsymbol{y},\boldsymbol{z}) = \boldsymbol{V}\phi(\boldsymbol{x}/\boldsymbol{L},\boldsymbol{y}/\boldsymbol{L},\boldsymbol{z}/\boldsymbol{L})$. Further, this same non-dimensional solution also provides the dimensional answer for any other choice of the 8 dimensional variables that yield the same 4 non-dimensional parameters – in this way, one non-dimensional solution provides a whole family of dimensional solutions.

1.2.1.2 Derivation of Governing Equations with Enforced Charge Neutrality (5.5.3.4, Charge Neutrality Strictly Enforced)

Knowing charge neutrality is enforced, we have C+H=1. Adding hole and ion transport equation:

$$\frac{\partial(C+H)}{\partial t} = 0 = -\nabla \bullet [(-D_C \nabla C - \mu_C C \nabla \phi) + (-D_H \nabla H - \mu_H H \nabla \phi)] \tag{32}$$

Then, assuming diffusion term is negligible, we have the following equation to determine potential profiles in polymer films.

$$0 = \nabla \bullet [(-\mu_C C \nabla \phi) - \mu_H H \nabla \phi)] \tag{33}$$

When ε is zero, Poisson's equation automatically creates zero net charge (right side of the equation) in polymer films.

1.2.1.3 Theoretical Analysis of Front Broadening Velocity (5.5.3, Parameter Variation)

We will give a theoretical analysis on front broadening velocity in this section to find out the main factors that affect the front broadening. The front broadening is determined by the ion velocities at different concentrations. The ion velocity, *v*, is connected with the transport equation through ion flux as:

(34) $$J = vC = -D\frac{\partial C}{\partial x} + \mu EC$$

Therefore, at concentration C_1: $J_1 = v_1 C_1 = -D\frac{\partial C_1}{\partial x} + \mu E_1 C_1$, then $v_1 = -D\frac{\partial C_1}{\partial x}/C_1 + \mu E_1$. Similarly, the ion flux at concentration C_2: $v_2 = -D\frac{\partial C_2}{\partial x}/C_2 + \mu E_2$. After time of t, ions of C_1 is at the position of x_1: $x_1 = \int_0^t v_1 dt = \int_0^t (-\frac{D}{C_1}\frac{\partial C_1}{\partial x} + \mu E_1)dt$, and ions of C_2 is at the position of x_2: $x_2 = \int_0^t v_2 dt = \int_0^t (-\frac{D}{C_2}\frac{\partial C_2}{\partial x} + \mu E_2)dt$.

Therefore, the effective front broadening is:

$$x_1 - x_2 = \int_0^t [-(\frac{D}{C_1}\frac{\partial C_1}{\partial x} - \frac{D}{C_2}\frac{\partial C_2}{\partial x}) + \mu(E_1 - E_2)]dt$$

Knowing $C_1 << C_2$ and $E_1 << E_2$, the equation becomes:

(35) $$x_1 - x_2 = \int_0^t [-\frac{D}{C_1}\frac{\partial C_1}{\partial x} - \mu E_2]dt$$

The equation tells that increasing V will lower the front width by increasing E_2. This also lowers the front broadening speed. One the contrary, lowering V will increase front width as well as the speed.

1.2.1.4 Scale Factor of Time between 1D and 2D Simulations (5.5.2, 2-D Confirmation of 1-D Results)

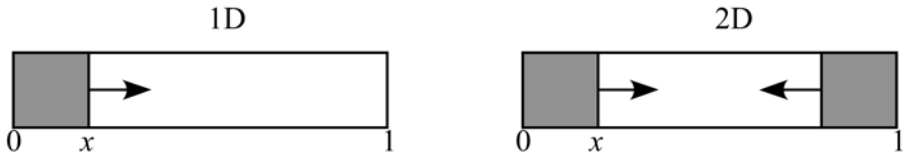

Figure SM 27. Reduced areas in 1D and 2D geometries. The 2D geometry has 2 phase fronts. Therefore, when phase front reaches the same position in the film, reduced area in 2D geometry is 2 times as that in the 2D geometry.

This section shows the mathematical derivation of the scale factor of time between 1D simulation and the 2D simulation. Results are compared when the film reaches the same doping level, which is approximately determined by the phase front position. If the phase front enters x = a (a represents the position) into the film in the 1D simulation, we will compare the results when the phase front enters x = a/2 into the film in the 2D simulation since ions enter the film from 2 edges in the 2D simulation.

The simulation results showed that in both 1D and 2D the phase fronts propagate linearly with square root of time. Based on the theoretical analysis of phase front propagation in section 5.5.1, the relation between phase front position is $x = \sqrt{2\mu_C V}\sqrt{t}$. Therefore, for 1D base case, the phase front moves with time as $x^1 = \sqrt{2\mu_C V}\sqrt{t^1}$, where x^1, and t^1 are the phase front position and time in 1D

simulation respectively. Similarly in 2D simulation, the phase front position along the electrical field line is expressed as $x^2 = \sqrt{2\mu_c V}\sqrt{t^2}$, where x^2 and t^2 are the phase front position and time.

To find the scale factor of time, the time when the phase front reaches a in 1D and the time when the phase front reaches a/2 in 2D need to be solved. When $x^1 = a$, then $t^1 = (a/\sqrt{2\mu_c V})^2$. When $x^2 = a/2$, then $t^2 = (a/\sqrt{2\mu_C V})^2/4$. The ratio between t^2 and t^1 is:

$$t^2 = \frac{t^1}{4}$$

The scale factor is not affected by the constants used in the non-dimensionalization.

1.2.2 Base Case Simulations

1.2.2.1 Variation of Dielectric Constant (5.4, Numerical Methods)

This section shows that using a non-dimensional dielectric constant 0.001, which is 8 orders of magnitude larger than the actually value (10^{-11}~10^{-8}), will not affect the results. The actual value of dielectric constant is not used in the simulation because it is much smaller than the other variables which are close to 1 and requires very dense meshes that FEMLAB can not handle it due to the limitation of computer memory.

Four different dielectric constants are used in the simulation from 0.1 to 0.01, 0.001, and 0.0001. The simulation results showed that when the dielectric constant was smaller than 0.001, simulation results converge as shown in Figure SM 28.

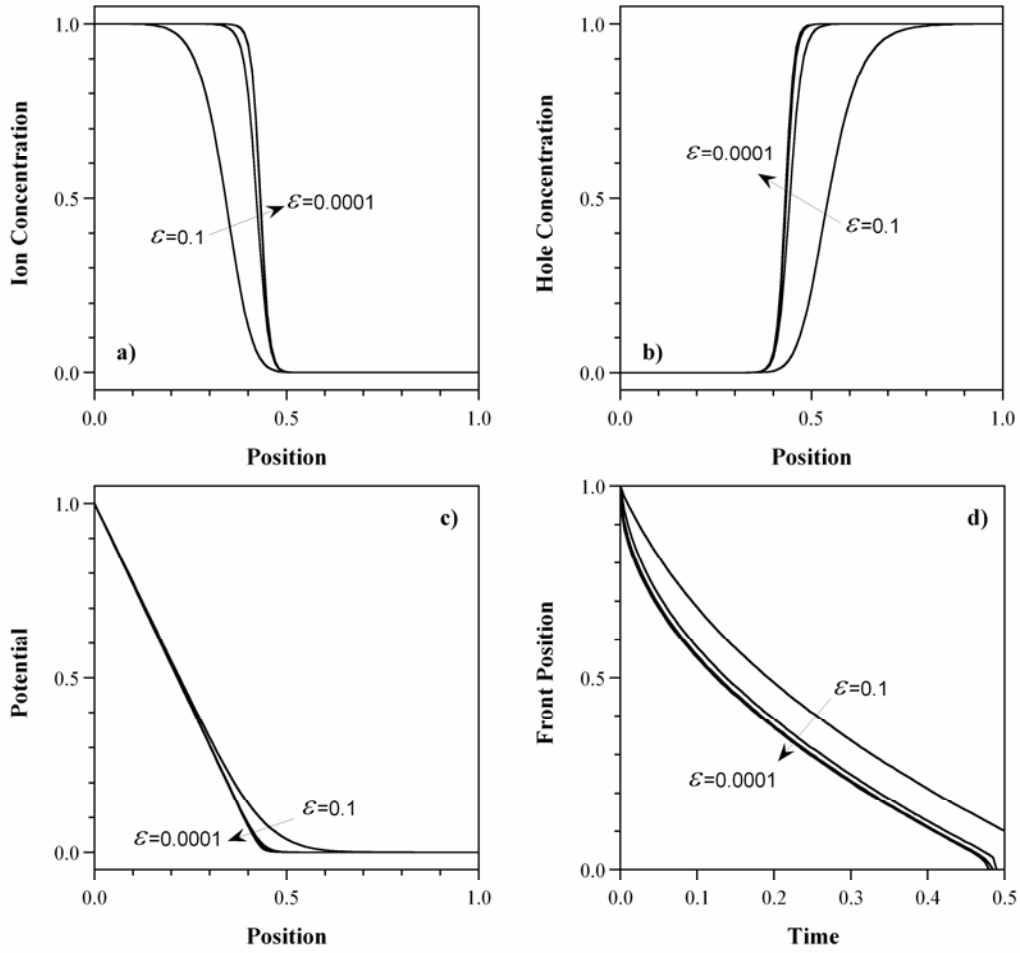

Figure SM 28. Convergence of simulation results using different ε. a) Ion concentration b) Hole concentration c) Potential d) Front position. When the ε is smaller than 1E-3, the simulation results are identical.

1.2.2.2 Conductivity vs. Position (5.5.1, Base Case Simulation Results)

This section shows the conductivity of the film. The conductive is calculated based on the equation: $\sigma(x) = C(x)\mu_C + H(x)\mu_H$. Ion and hole concentrations in Figure 51 are used in the calculation. Ion mobility is 1. Hole mobility is 1000. Film conductivity decreases from 1000 in the oxidized region to 1 in the reduced region as shown in Figure SM 29.

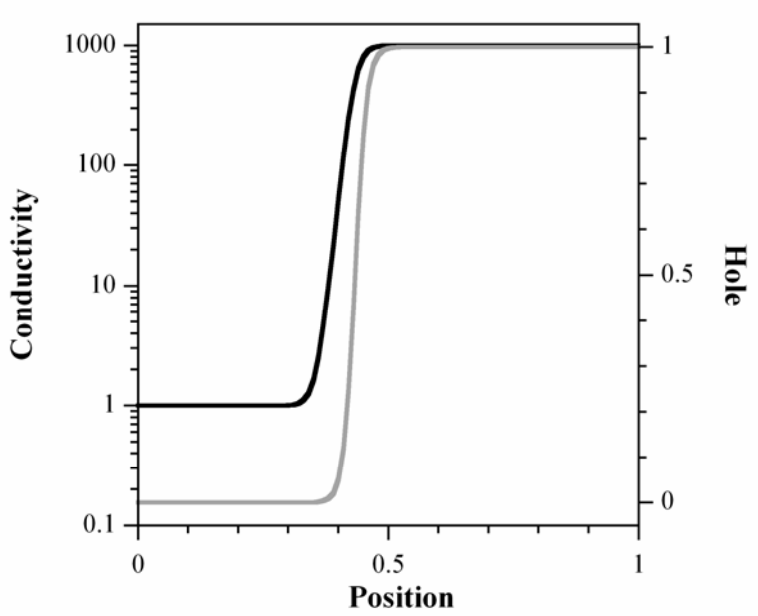

Figure SM 29. Conductivity (solid line) vs. position for the base case shown in Figure 51. Grey line is the hole concentration.

1.2.2.3 Analytical Solution vs. Solving PDE for Holes (5.5.1, Base Case Simulation Results)

This section compares the simulation results from PDEs with and without an analytical solution of holes. The ion concentration profiles from our previous model [8, 44], which used an analytical solution of holes, and from the base case are compared in Figure SM 30. Results from the two models are identical.

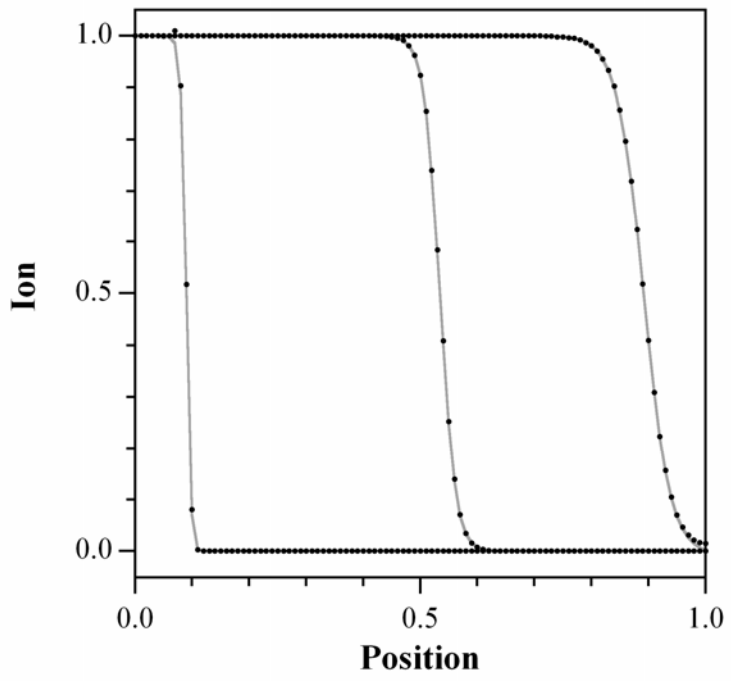

Figure SM 30. Comparison of the ion concentration profiles solved by three PDEs (grey line) with those from hole analytical solution (dots).

1.2.2.4 Net Charge for Different Reduction Potentials (5.5.3.1, Voltage)

Figure SM 31 shows the net charge in the film under higher (V = 1.5) and much lower (V = 0.001) reduction potentials than in the base case (V = 1). At very low potential, the film is basically charge-neutral everywhere. With increasing reduction potential, the net charge at the front increases, and its distribution narrows.

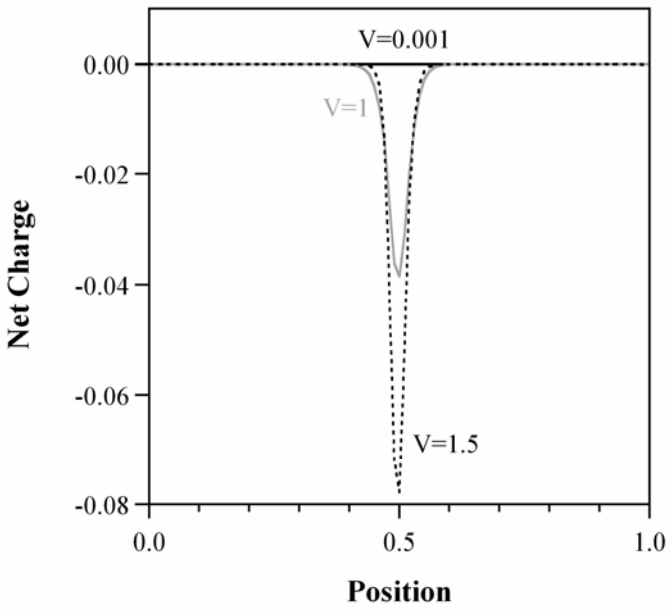

Figure SM 31. Net charge in the polymer for different reduction potentials when the polymer is approximately half-way reduced.

1.2.2.5 Front Propagation along the Electric Field Line in the 2-D Base Case (5.5.2, 2-D Confirmation of 1-D Results)

Figure SM 32 compares the phase front propagation along the electric field line in the 2D simulation with front propagation in the 1D simulation. The front moves slightly faster in the 2D case.

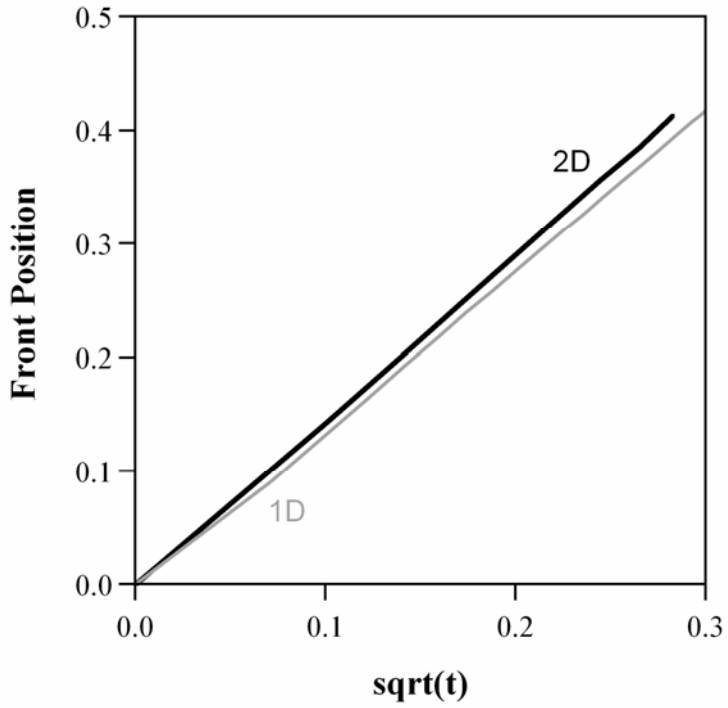

Figure SM 32. Front position vs. the square root of time for the 1D and 2D simulations. The front position for the 2D simulation was obtained from the ion concentration profiles along the electrical field streamline at *y*=0.15.

1.2.2.6 Ion Concentration Profiles when Hole Mobility Equals Ion Mobility (5.5.3.3, Finite Hole Mobility)

Figure SM 33 shows ion concentration profiles of the simulation with hole mobility equal to ion mobility. The concentration profiles show larger front width that those of the base case. Since the potential profile in this case drops across the whole polymer and does not change with time, the migration effect in the reduced area is smaller than the base case. As a result, diffusion makes the front wider than the base case.

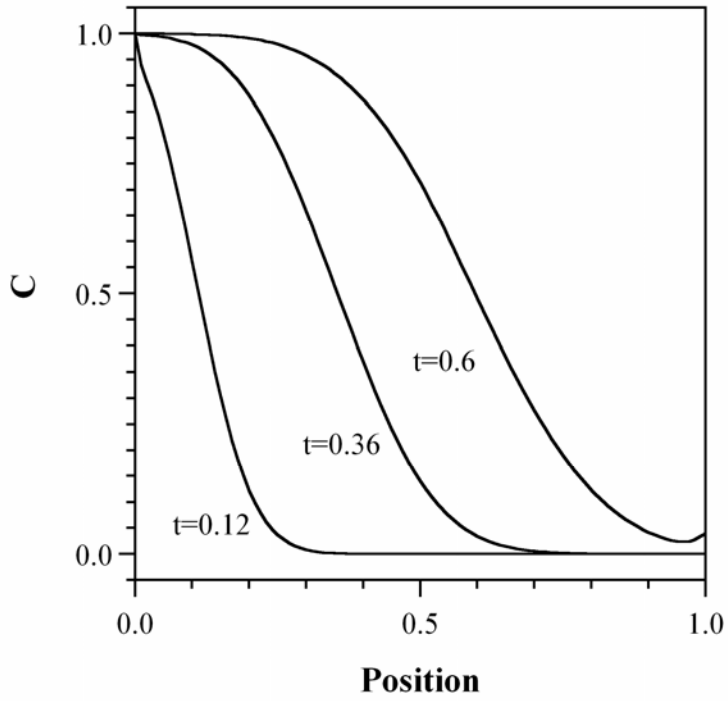

Figure SM 33. Ion concentration profiles when hole mobility is the same as the ion mobility.

1.2.2.7 Effect of Concentration at the Polymer/Electrolyte Interface (5.3.1.2.2, Boundary and Initial Conditions)

In the base case, a maximum ion concentration is set for the polymer/electrolyte concentration. The section shows how this boundary condition affects the simulation results. Three different concentrations (0.03, 1, and 2) are tested. These values represent bulk electrolyte concentration (0.03), concentration in the electrolyte (2), and maximum ion concentration in the polymer (1). The results are shown in Figure SM 34 and Figure SM 35.

The ion concentration profiles in the polymer have the same shape with all concentrations. No matter which value is used, the reduced area always has the maximum ion concentration, and no ions in the oxidized area. Using lower

concentrations such as 0.03 will create a slower phase front. The lower concentration also makes the phase front move linearly with time, similar with using lower electrolyte concentration in the full model.

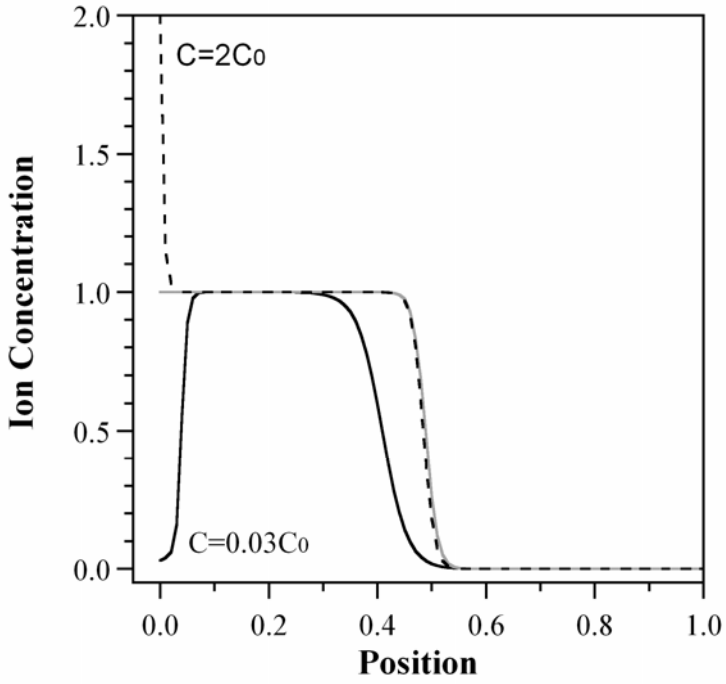

Figure SM 34. Ion concentration profiles with different boundary conditions.

Figure SM 35 shows phase front propagations when different values are used for the ion concentration at the polymer/electrolyte interface. Phase fronts move linearly with square root of t with boundary ion concentration of 1 and 2. The phase front with ion boundary concentration of 0.03 propagates linearly with t. It also has much smaller effective velocities than the other two.

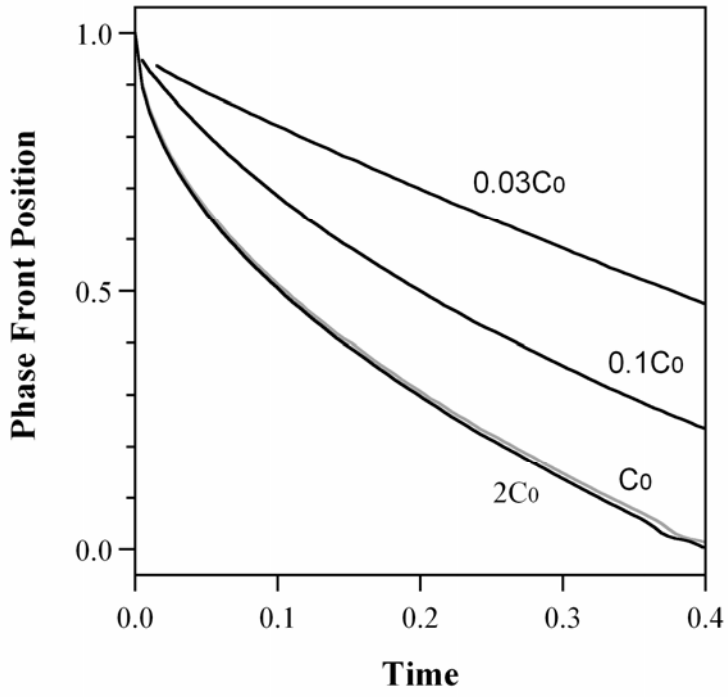

Figure SM 35. Phase front propagations when different values are used for the ion concentration at the polymer/electrolyte interface.

1.2.2.8 Base Case Simulation with only Diffusion (5.5.3.1, Voltage)

Figure SM 36 shows ion and hole concentrations at different time snapshots when they are both driven by diffusion only. In this simulation, the hole boundary condition at the electrode is set to zero in stead of the flux boundary condition that causes the simulation to crash. The zero hole concentration at the right boundary is proved to be valid before ions reach the electrode by all the simulation results.

While the ion profiles resemble those in Figure 57c, the hole profiles bear no relation to what they should because if ions and holes are driven by diffusion only, their movement becomes uncoupled. They move through the polymer independently

because charge neutrality cannot be enforced. As a result, this case leads to unphysical results, as is also illustrated in the potential profile (Figure SM 37).

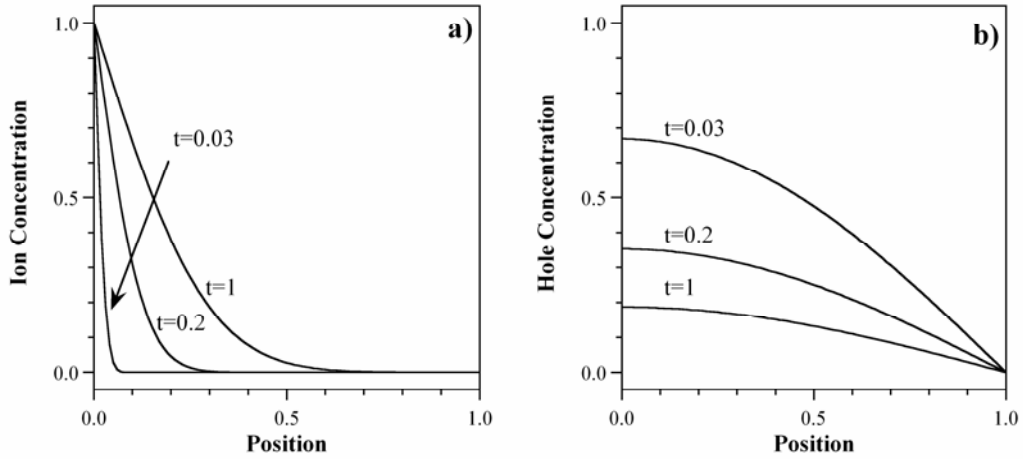

Figure SM 36. a) Ion concentration profiles at t = 0.01, 0.2, and 1. b) Hole concentration at t=0.01. 0.02, and 0.03. Since holes have 1000 times higher mobility, they move out very quick.

The ions diffuse into the polymer as in Figure SM 36a, because at the electrolyte/polymer boundary C = 1. If this were set to another value, then these curves would simply be multiplied in height accordingly, with the final equilibrium value in the polymer equal to the concentration set at the boundary.

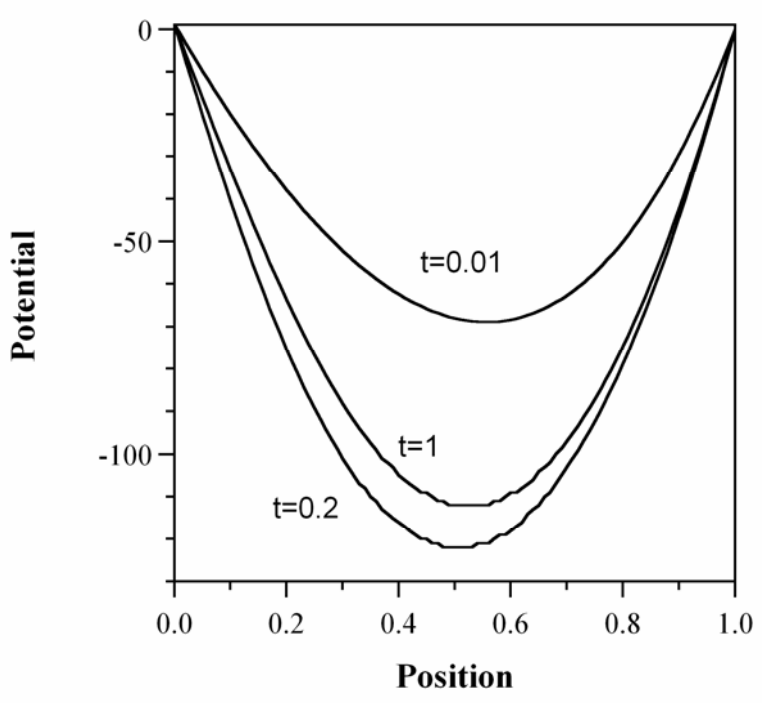

Figure SM 37. Potential profiles when t = 0.01, 0.2, and 1.

1.2.2.9 Base Simulation Results with Enforced Charge Neutrality (5.5.3.4, Charge Neutrality Strictly Enforced)

Ion concentration profiles from the charge neutrality case are shown in Figure SM 38a. As in the base case, the ions travel into the film at a front, and this front broadens over time. In addition (not shown), the speed of the front was proportional to V.

A potential profile at t = 0.25 is presented in Figure SM 38b. Although the potential drops mainly in the reduced area, since the hole mobility was only 5 times higher than that of the ions, a portion of the potential also drops in the oxidized area. If it were possible to use a higher hole mobility in the simulation, the results would have resembled the base case more closely.

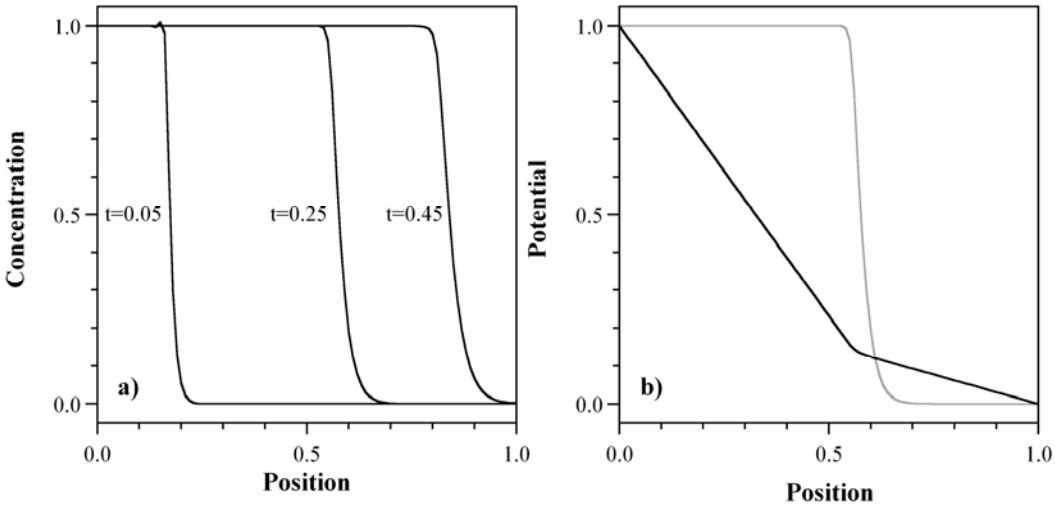

Figure SM 38. a) Ion concentration profile when charge neutrality is enforced in the polymer. Due to simulation difficulties, hole mobility is only 5 times that of ions. b) Potential profile when t=0.25.

The front position vs. time with charge neutrality strictly enforced is shown in Figure SM 39. Again because $\mu_H/\mu_C = 5$, this front moves more slowly (there is a smaller voltage drop across the reduced region) and the velocity is more constant. These results arise from the small hole mobility, not from enforcing charge neutrality.

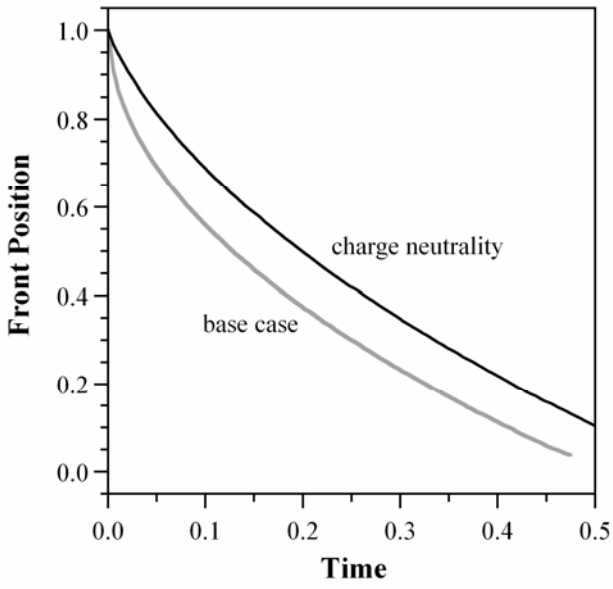

Figure SM 39. Front position vs. time.

1.2.2.10 Effect of Varying D/μ (5.5.3.2Relationship between D and μ)

The ratio between diffusivity and mobility is varied 6 orders of magnitude from 0.000026 to 0.026 and 26. Ion concentration profiles are shown in Figure SM 40. The simulation results show that ion concentration profiles with *D/M* ratio of 0.026 (Einstein relation) and 0.000026 are very similar. The ion concentration profile with 26 *D/M* ratio is bell shaped indicating a diffusion dominant case.

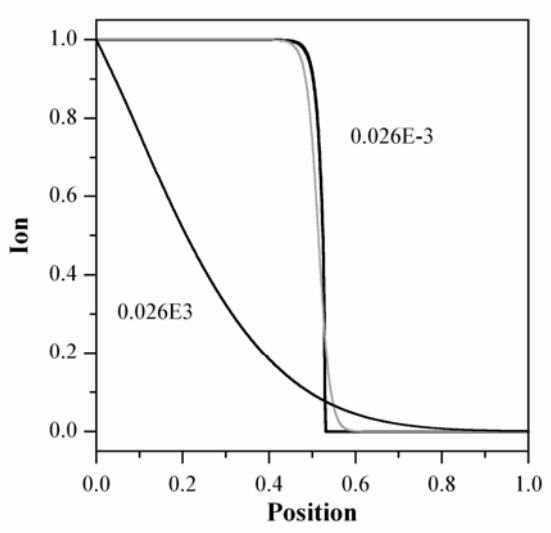

Figure SM 40. Ion concentration profiles at different D/μ ratio. Gray is the base case. The ratio was set 3 orders of magnitude higher (0.026E3) or lower (0.026E-3) than the Einstein relation (0.026).

These results showed that by varying the relationship between diffusivity and mobility, ion concentration profiles may show either diffusion process features or migration process features. *Increasing the ratio between diffusivity and mobility has similar effects of using lower reduction potential.* However, whether the Einstein relationship is valid or not for ions in conjugated polymers has not been proved by experimental data yet.

1.2.3 Reduction of Full Model

1.2.3.1 Ion Flux in the Electrolyte (5.6.4, Addition of the Electrolyte)

The section compares the drift term and diffusive term in the electrolyte to find out the importance of the drift term. The ions in the electrolyte move exclusively by drift between x = -10 and -5, as shown in Figure SM 41a, and increasingly by diffusion closer to the polymer interface where there are concentration gradients. Within 0.03 of the polymer interface, as shown in Figure SM 41b, the migration component

increases to large positive values, and the diffusion component to large negative values: the strong electric field pulls the cations toward the interface, but the high concentration of the cations in the double-layer produces a large flux away from the interface back into the electrolyte. These two components approximately balance, the difference being the flux into the polymer.

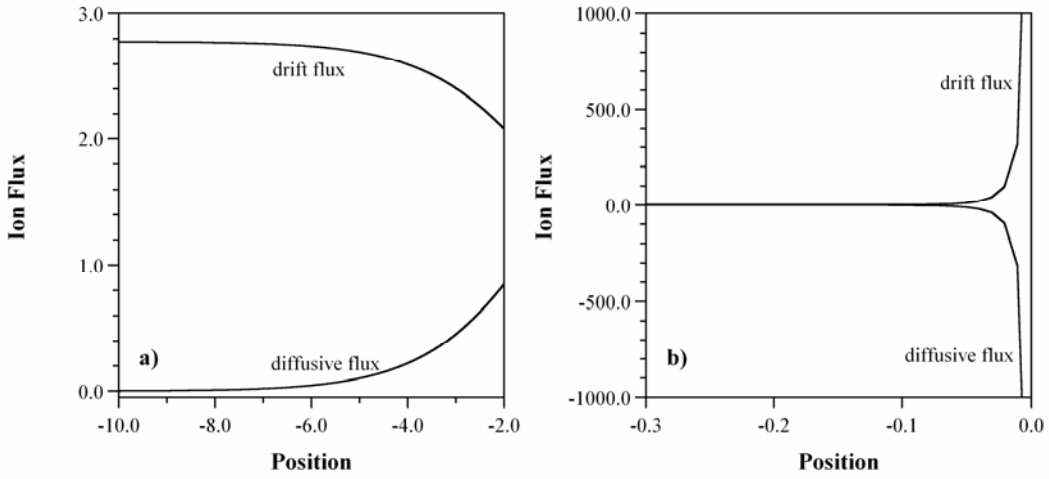

Figure SM 41. a) Diffusive and drift flux of cations in the electrolyte. The graph does not include the data close to the polymer yet. B) Diffusive and drift flux of cations in the double layer. Note the difference in scale from a).

1.2.3.2 Potential Drop over the Polymer (5.6.4.2, Full Model Results)

Figure SM 42 shows the potential drop across the polymer when the electrolyte is added to the model. The potential over the polymer increases rapidly till $t = 0.01$ and then grows very slowly till the film is fully reduced ($t = 0.2$).

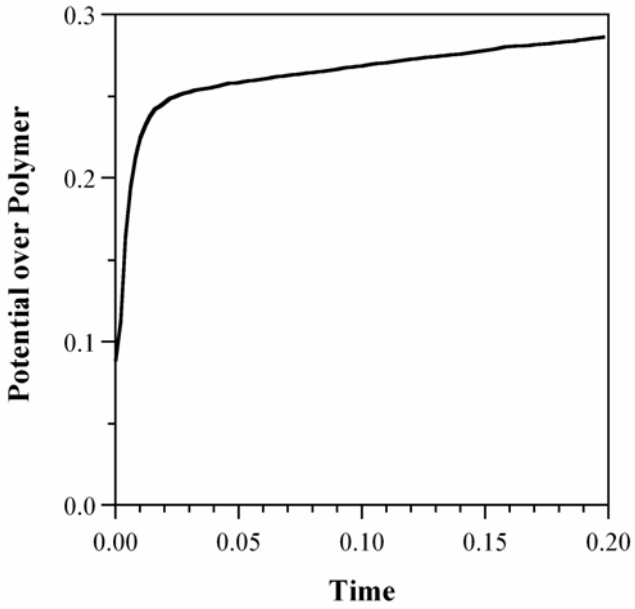

Figure SM 42. Potential drop over the polymer film in the full model. Reduction potential is -1.

1.2.3.3 Comparison between Full Model and Base Case (5.6.4.2, Full Model Results)

Figure SM 43 shows the ion concentration profiles predicted by the full model and the base model at the same (t = 0.08). The ion concentration profile predicted by the base case is slightly ahead of that predicted by the full model. This is because ion concentration at the polymer/electrolyte interface is smaller than the maximum ion concentration, which decreases the overpotential across the polymer. The results suggest that film will behave identically as long as the overpotential is the same.

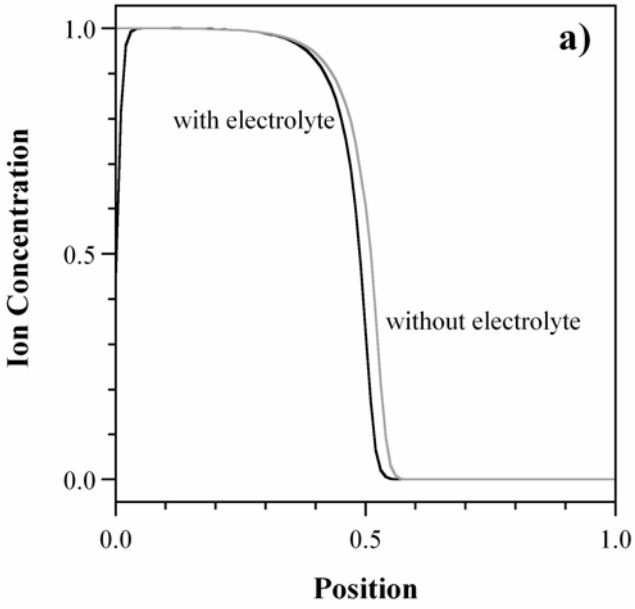

Figure SM 43. Ion concentration predicted with full model (solid line) and that with base case (grey line). Both concentration profiles are taken at the same time (t=0.08). The full model has a potential drop of 1. The potential over the polymer is approximately 0.25 after *t* = 0.01. The base case has a potential of 0.25.

1.2.3.4 Effects of Electrolyte Concentration C_e on the Double Layer (5.8.1, Effect of Electrolyte Concentration)

In this section, effects of the electrolyte concentrations on the double layer are reported. We will show how the double layer changes with electrolyte concentration and whether the double layer affects the ion transport in the polymer. An understanding in literature of ion transport is that the high concentration in the double layer diffuses ion into the polymer. Such an understanding has not been experimentally confirmed yet. The simulation results may help to evaluate such an understanding.

Figure SM 44 shows the ion concentration across the polymer/electrolyte interface. For each figure, ion concentrations at two times were shown. One is right after the

voltage is applied. The other is when the film was approximately halfway reduced. For the electrolyte concentration of 0.033, ion concentrations in the double layer are never higher than the 1. For the electrolyte concentration of 0.5, ions in the double layer piles up to a concentration of 1.3 at the beginning of the reduction but dropped to 1 when the film is halfway reduced. For concentration of 1 and 2, the double layer keeps ion concentration higher than 1 at these two times.

The ion concentrations in the polymer keep the maximum ion concentration of 1, which creates zero concentration gradient in the reduced area, no matter what the ion concentration in the double layer. Knowing this, ion transport in the polymer will not be affected by the double layer if only diffusion drives ions in the polymer.

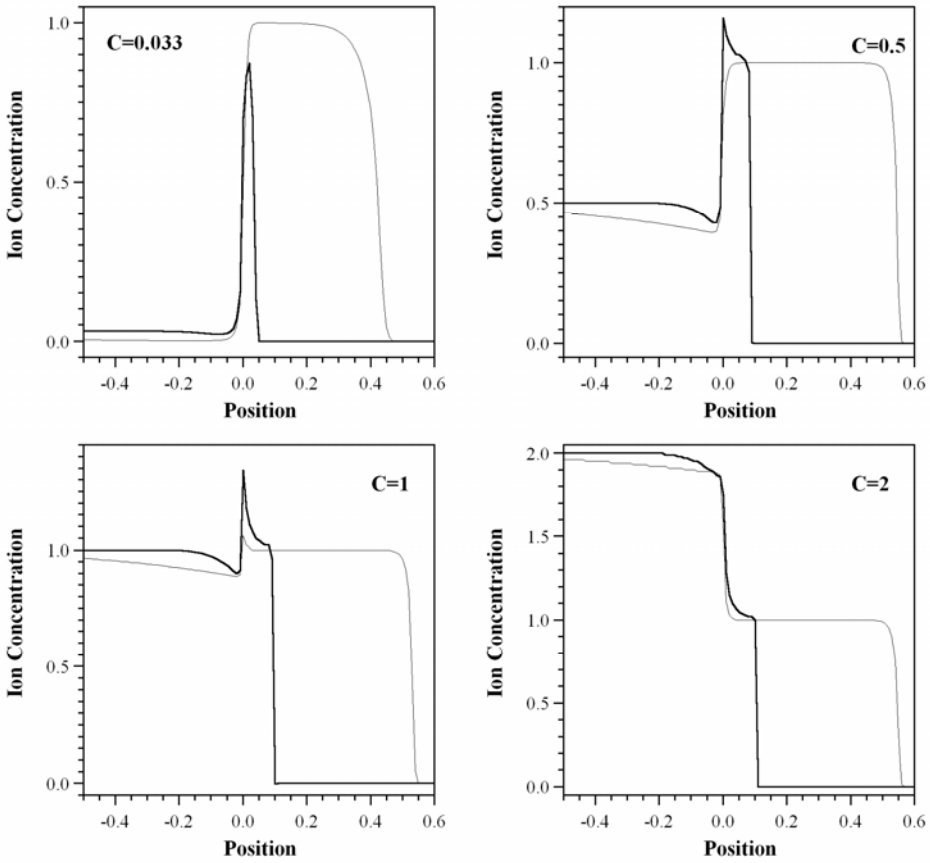

Figure SM 44. Effects of electrolyte concentration on cation concentrations across the polymer/electrolyte interface.

Figure SM 45 shows the flux across the double layer, which is formed due to the imbalanced inward flux and outward flux. As shown in Figure SM 45, at the very beginning, the outward flux of the polymer/electrolyte interface is zero since ion concentration in the polymer is zero. As a result, ions pile up at the interface until the inward flux and outward flux equals.

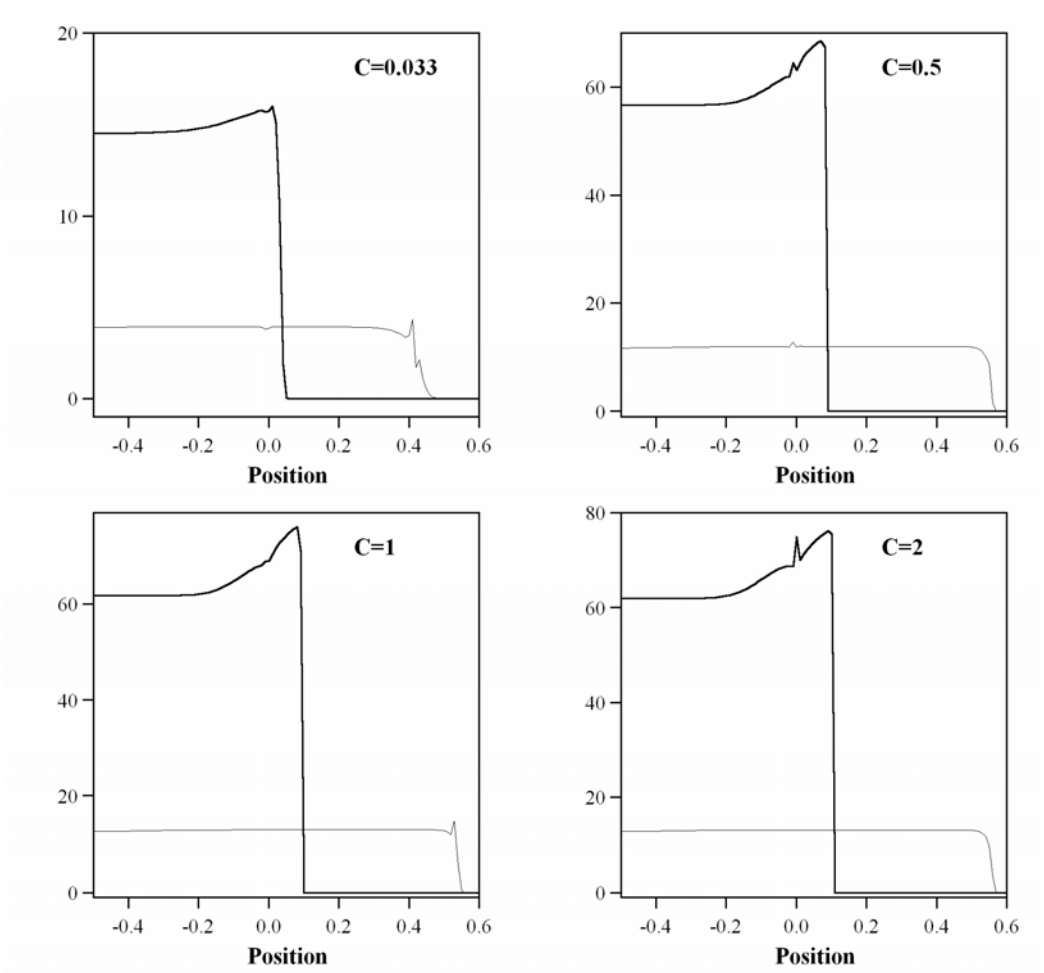

Figure SM 45. Total flux profiles corresponding to the ion profiles in Figure SM 44.

1.2.4 Full Model with only Diffusion

In this section, we present the results if the full model is driven by diffusion only. Three cases are presented. In the first, only the cation mobility in the polymer is set to zero, and the diffusivity is set equal to the experimentally derived exponential dependence on concentration. In the second, both ions and holes in polymer are driven by diffusion only, while both types of ions in the electrolyte are driven by migration. In the last case, all charges in the system are driven by diffusion only.

1.2.4.1 Simulation Results with Capping Function

The capping function of $D_C = D_0(1+ 0.01e^{15(C - 0.8)})$ is used in the simulation when ion migration term is turned off in the polymer. This is to find out whether the capping function can change the predictions. Figure SM 46 compares the ion concentration profiles with the capping function (solid lines) and without the capping function (grey lines). Ion concentration profiles with the capping function are slightly ahead of those without the capping function, but the effect is negligible. This is because ion concentration in the film is not high enough to dramatically increase the diffusion. For example, at t = 0.02, ion concentration at the interface is 1.15. This creates a diffusivity increase of 2.9 times.

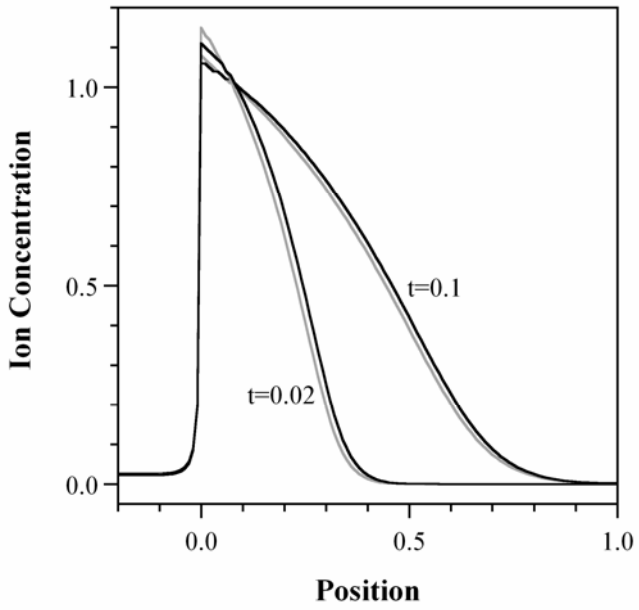

Figure SM 46. Ion concentration profiles (solid line) when capping function is applied. Migration term of ions in the polymer is turn off. The capping function is $D_C = D_0(1+ 0.01e^{15(C - 0.8)})$. Grey line is the ion concentration profiles without using capping function.

1.2.4.2 Diffusivity Proportional to e^{5C}

Phase fronts were formed in the polymer due to the steeper diffusivity, as shown in Figure SM 47a. At lower potential (<1), maximum ion concentration was lower than 1 (Figure SM 47a), while ion concentrations reached maximum concentration ion concentration (Figure SM 47b). Figure SM 47b also shows that ion concentration in the polymer reached a value higher than 1 due to the high ion concentration in the doubly layer. When reduction voltage was increased, the velocity of phase front increased a logarithmic way (Figure SM 47d), which is not consistent with experimental results. The reason why phase front velocity increased is because higher voltage increased the ion concentration in the double layer that drove ions into the polymer.

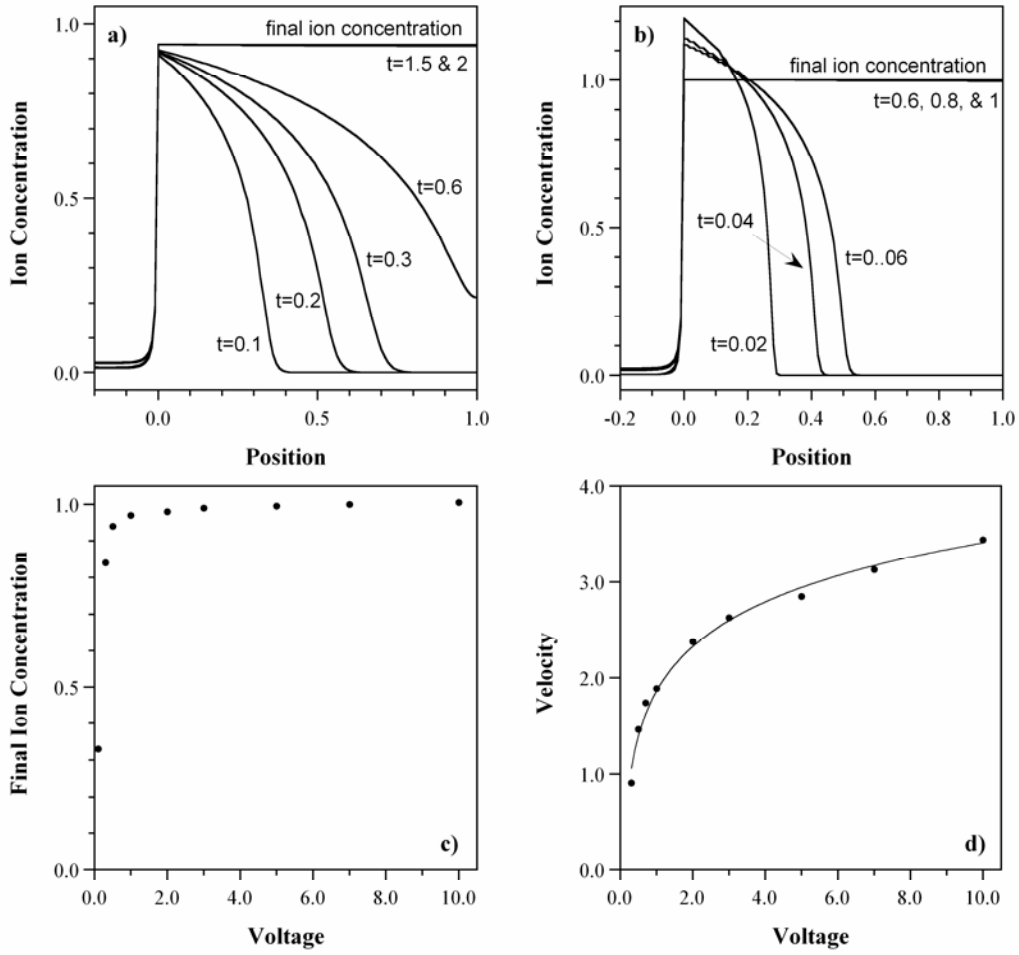

Figure SM 47. Results of the full model during reduction when the migration of ions in the polymer is turned off and $D_C = D_0 e^{5C}$. Ion concentration profiles for a) V = 0.5 and b) V = 7. c) Final ion concentrations in the polymer at the end of the reduction process for different applied potentials. d) The phase front velocity vs. potential. The line shows a log fit.

1.2.4.3 Ion and Holes in Polymer are Driven by Diffusion Only.

When both ions and holes in the polymer are driven by diffusion only, the simulation shows that the major potential drop occurs in the polymer as shown in Figure SM 48. Since the potential drop in the electrolyte is small, no double layer is formed at the interface. Ions enter the polymer with a very low rate and can not reach to the

maximum ion concentration. Even with very long time (50), ions only reach 0.1 concentration, and the film is far from fully reduced, as shown in Figure SM 49.

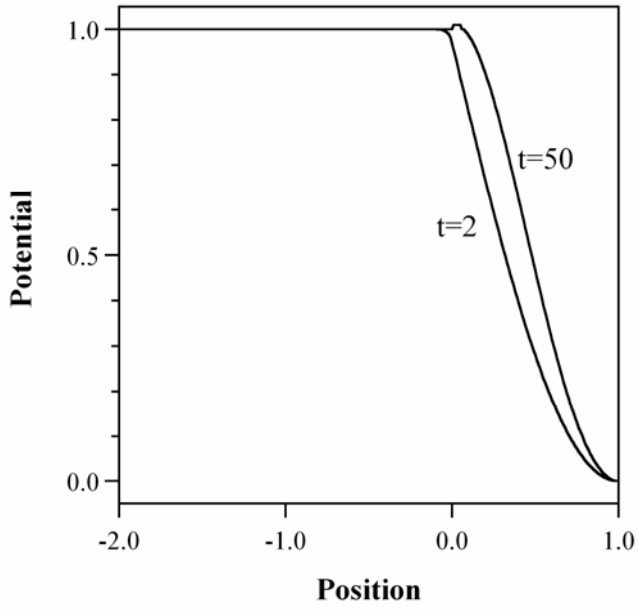

Figure SM 48. Potential profiles when ion and hole in the polymer are driven by diffusion.

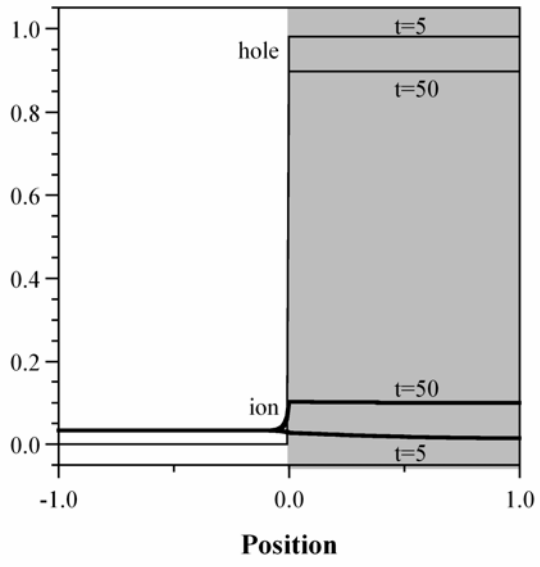

Figure SM 49 Ion and hole concentrations when ion and hole in the polymer are driven only by diffusion.

1.2.4.4 Ions in the Electrolyte are Driven by Diffusion Only.

When ions in the electrolyte were driven by diffusion only, the simulation showed that the ion concentration in the polymer equals to the bulk electrolyte no matter how long the simulation runs, Figure SM 50.

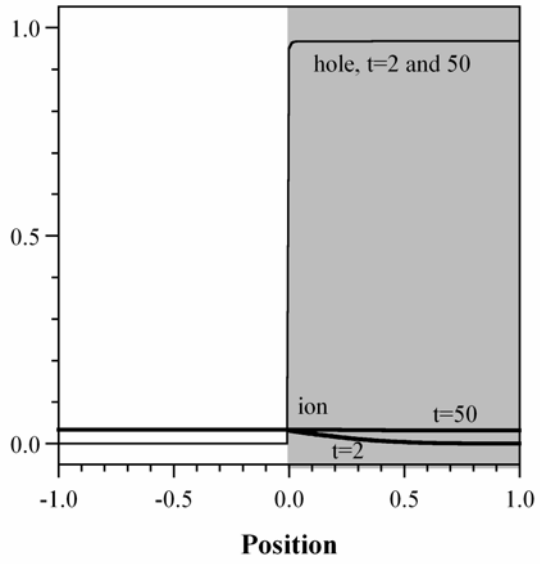

Figure SM 50. When ions in the electrolyte are driven only by diffusion, what the ion and hole concentration profile look like.

1.2.5 Oxidation of Full Model

1.2.5.1 Diffusive and Migration Flux in the Polymer (5.8.2, Oxidation of a Cation-Transporting Material)

The following plot shows the migration flux and diffusivity flux in the polymer during cation oxidation. The drift flux is comparable with diffusive flux during cation oxidation due to the small potential drop in the polymer. At the reduced region, the drift flux is a bit larger than the diffusivity flux. From the reduced area to the oxidized area, the drift flux decreases due to the lowering of ion concentration,

while the diffusive flux increases. At the area close to the polymer/electrolyte interface, the diffusive flux is eventually larger than the drift flux.

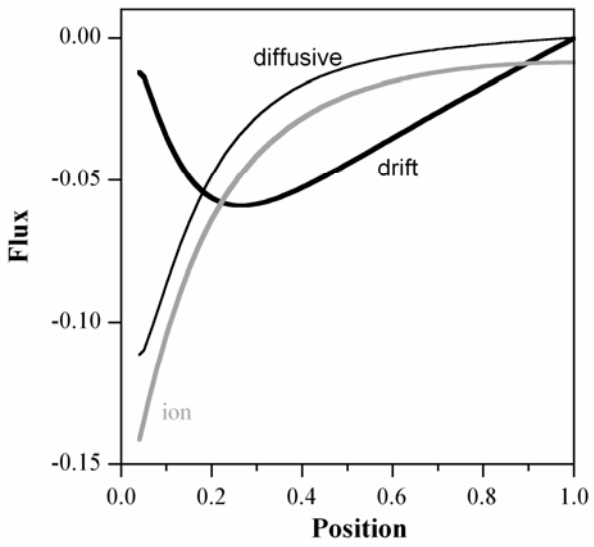

Figure SM 51. Diffusive flux and drift flux of ions during oxidation (*t* = 1). They are comparable. Gray line is the ion concentration profile.

1.2.5.2 Effect of Voltage on Oxidation Speed (5.8.2, Oxidation of a Cation-Transporting Material)

The oxidation voltage is varied to find out how it affects the oxidation process. Two types of curves are presented: ion concentration profiles (Figure SM 52a) at the same time and total ions in the film (Figure SM 52a). The ion concentration profiles keep the same shape when oxidation potential is varied from 0.5 to 2. With higher voltages, ions leave the polymer slightly faster. Since no phase fronts are formed during cation oxidation, the second curve, total ions vs. sqrt(t), is used to reveal effect of oxidation voltage. As shown in Figure SM 52b, when different voltages are applied, they have large effects on ion egress at the beginning of oxidation but have negligible effect once the oxidation occurs certain time (such as 0.7). This is

evidence on the total ion vs. sqrt(t) curve: the difference of total ions in the film is mainly formed at the very beginning. After certain time, the curves are parallel with each other, meaning that ions leave the film with the same rate. The difference in offset is understandable. At the very beginning, polymer has large potential drop due to low conductivity. At the very beginning, ions are kicked out by both migration and diffusion, but later one, ion egress is controlled only by diffusion. Therefore, when oxidation voltage is increased, the ions are kicked out quicker at the beginning and then resume the same rate as controlled by diffusion.

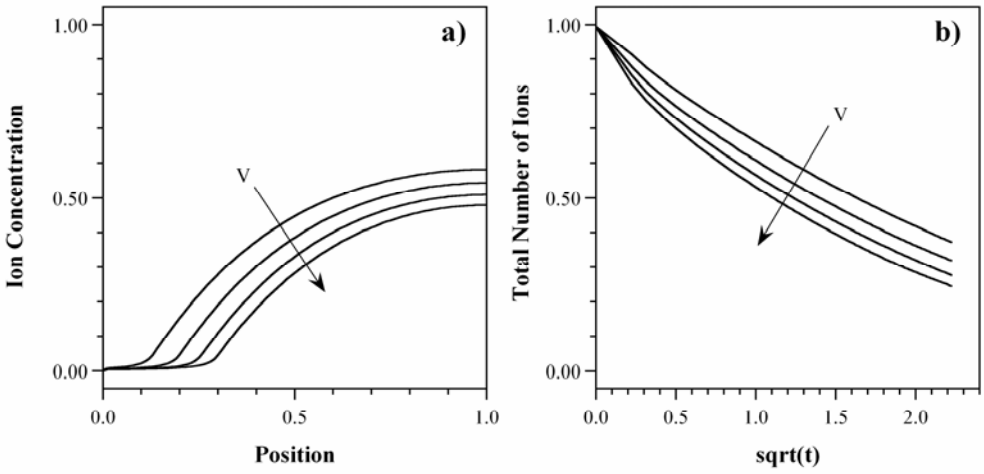

Figure SM 52. Effect of oxidation voltage (*V* = 0.5, 1.0, 1.5, and 2. The arrow shows the voltage increase.) on a) ion concentration profiles (*t* = 5) and b) total number of ions in the film.

1.2.5.3 Ion Concentration Profiles when t = 5 with Different Capping Functions (5.8.2.3, Role of the Capping Technique)

In 5.8.2.3, Role of the Capping Technique, we have shown that ion concentrations profiles (t = 0.5) with these methods are similar. Figure SM 53 shows the ion concentration profiles at t = 5. The same as shown in the paper, ion concentration

profiles of the charge neutrality case and the no aping case follow each other, while the high diffusion and no migration cases are similar. Overall, ion concentration profiles are close to each other no matter which capping function is used.

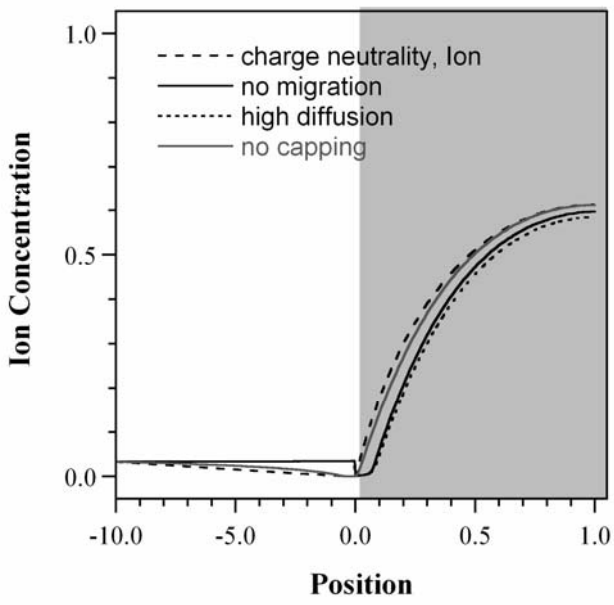

Figure SM 53. Ion concentration profiles at t = 5 with different capping functions.

1.2.6 Predictions

1.2.6.1 Reduction of Uncovered Films (5.8.3.2, Uncovered Films with Isotropic Transport Coefficients)

For uncovered film, we also obtained the results along the electrical filed line, which is perpendicular to the bottom electrode. As shown in Figure SM 54, ion and hole concentration have similar shape with the 1D model. The film width (1) instead of film thickness (0.2) is used for the X axis in order to properly compare the shape and front width with the 1D model. While the net charge region appears to be wider than in the base case, it is not: it appears that way only because we visually magnify the

film thickness by using an aspect ratio of 1:5 (and compensate for this by scaling the variables) rather than the actual aspect ratio of 1:1000.

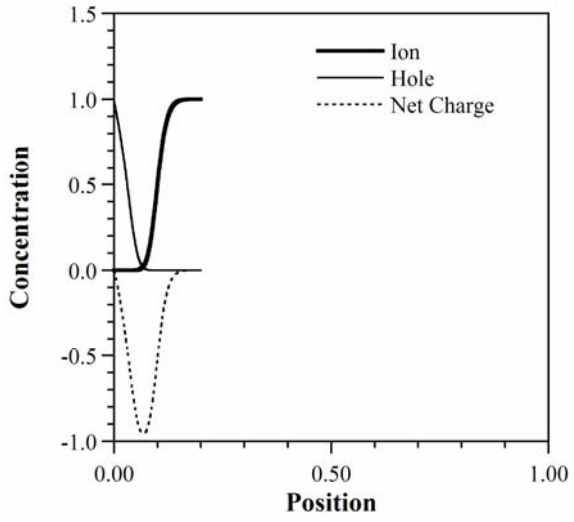

Figure SM 54. Ion, hole, and net charge along an electrical field streamline (x = 0.5, t = 1e-5). The x axis is set to 1 so that the front width looks similar with 1D model or along the film width direction.

The phase front position in ion concentration profiles is showed in Figure SM 55a and Figure SM 55b. Clearly, the front does not propagate linearly with time. The plot shows that the propagation is better to be describe to have a linearly relationship with square root time, but it also does not have a perfect linear relationship with $\sqrt{t}$ shown in Figure SM 55b. The explanation lies in the potential profile as shown in Figure SM 56. First of all, the potential profile changes with time. Therefore, no linear relationship with time is expected. Second, the film does not have a clear boundary between the oxidized and reduced area. Since the film thickness is small compared with the front width, everywhere in the film is partially or fully reduced right after the voltage is applied. Since the front width quickly covers the film thickness, the

potential profile does not change as much as those in the base case whose phase fronts propagate linearly with time.

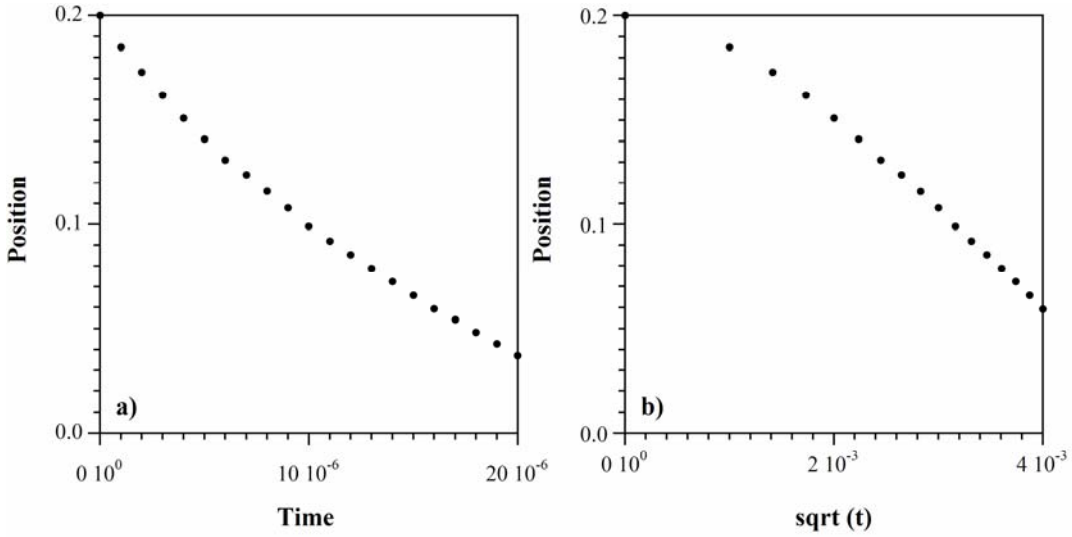

Figure SM 55. a) Phase front position vs. time along the electrical field streamline.

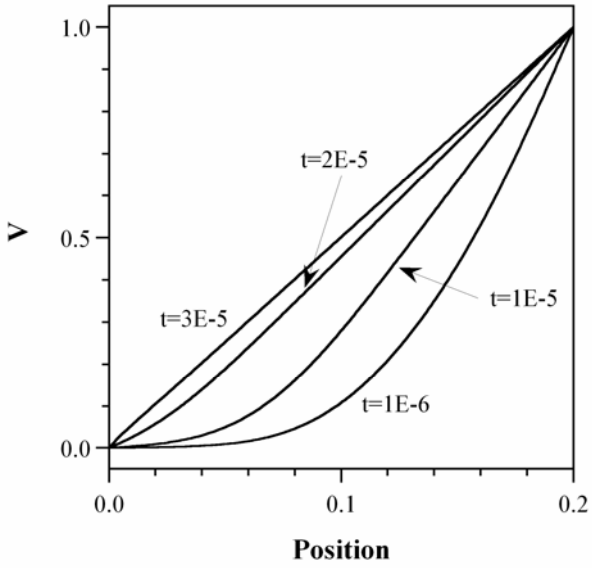

Figure SM 56. Potential along the electrical field lines.

1.2.6.2 Anion Reduction (5.8.4.2, Anion Reduction)

Anion concentration profiles in the polymer when different reduction voltage is applied. The voltage has negligible effects on the ion transport.

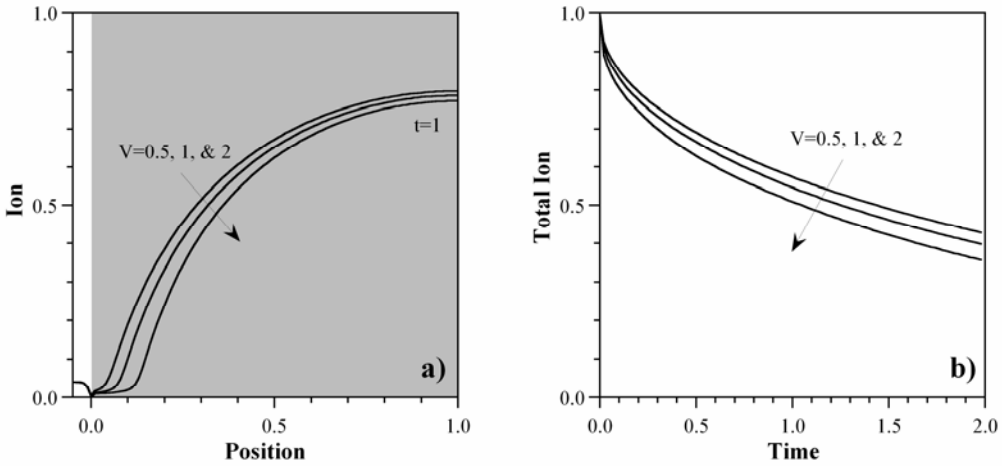

Figure SM 57. a) Ion concentration when t = 1. b) Total ions in the film.

Bibliography

Chapter 1

[1] C. speed, http://www.factmonster.com/ipka/A0004737.html.

[2] Spittlebugs, http://www.newscientist.com/article.ns?id=dn4008.

[3] Hummingbirds, http://hypertextbook.com/facts/2000/MarkLevin.shtml.

[4] Red_Kangaroo, http://en.wikipedia.org/wiki/Red_Kangaroo.

[5] Octopuse, http://nationalzoo.si.edu/support/adoptspecies/animalinfo/giantoctopus/default.cfm.

[6] R. Baughman, "Conducting polymer artificial muscles," *Synth. Met.*, vol. 78 (3), pp. 339-353, 1996.

[7] Q. B. Pei and O. Inganas, "Electrochemical Muscles - Bending Strips Built from Conjugated Polymers," *Synth. Met.*, vol. 57 (1), pp. 3718-3723, 1993.

[8] T. F. Otero and J. M. Sansinena, "Artificial Muscles Based on Conducting Polymers," *Bioelectrochem. Bioenerg.* , vol. 38 (2), pp. 411-414, 1995.

[9] C. Immerstrand, K. Holmgren-Peterson, K. E. Magnusson, E. Jager, M. Krogh, M. Skoglund, A. Selbing, and O. Inganas, "Conjugated-polymer micro- and milliactuators for biological applications," *MRS Bulletin*, vol. 27 (6), pp. 461-464, 2002.

[10] L. Bay, K. West, P. Sommer-Larsen, S. Skaarup, and M. Benslimane, "A conducting polymer artificial muscle with 12% linear strain," *Adv. Mat.*, vol. 15 (4), pp. 310-313, 2003.

[11] L. Hunter, "A comparison of muscle with artificial actuators," Proc. IEEE Solid-State Sensor and Actuator Workshop, Hilton Head Island, SC, USA, 1992, pp. 178-185.

[12] L. Bay, N. Mogensen, S. Skaarup, P. Sommer-Larsen, M. Jorgensen, and K. West, "Polypyrrole doped with alkyl benzenesulfonates," *Macromol.*, vol. 35 (25), pp. 9345-9351, 2002.

[13] P. Murray, G. M. Spinks, G. G. Wallace, and R. P. Burford, "In-situ mechanical properties of tosylate doped (pTS) polypyrrole," *Synth. Met.*, vol. 84 (1-3), pp. 847-848, 1997.

[14] G. M. Spinks, L. Liu, G. G. Wallace, and D. Z. Zhou, "Strain response from polypyrrole actuators under load," *Adv. Funct. Mater.* , vol. 12 (6-7), pp. 437-440, 2002.

[15] P. Chiarelli, D. Derossi, A. Della Santa, and A. Mazzoldi, "Doping-Induced Volume Change in a Pi-Conjugated Conducting Polymer," *Polym. Gels Networks* vol. 2 (3-4), pp. 289-297, 1994.

[16] E. Jager, "On-chip microelectrodes for electrochemistry with moveable PPy bilayer actuators as working electrodes," *Sensors and Actuators B*, vol. 56 (1-2), pp. 73-78, 1999.

[17] E. Jager, "Microfabricating conjugated polymer actuators," *Science*, vol. 290 (24), pp. No1540-1545., 2000.

[18] E. W. H. Jager, O. Inganas, and I. Lundstrom, "Microrobots for micrometer-size objects in aqueous media: Potential tools for single-cell manipulation," *Science*, vol. 288 (5475), pp. 2335-2338, 2000.

[19] E. W. H. Jager, E. Smela, O. Inganas, and I. Lundstrom, "Polypyrrole microactuators," *Synth. Met.*, vol. 102 (1-3), pp. 1309-1310, 1999.

[20] E. Smela, "Microfabrication of ppy microactuators and other conjugated polymer devices," *J. Micromech. Microeng.*, vol. 9, pp. 1-18, 1999.

[21] E. Smela, "controlled folding of micrometer-sized structures," *Science*, vol. 268 (5218), pp. 1735-1738, 1995.

[22] E. Smela, M. Kallenbach, and J. Holdenried, "Electrochemically driven polypyrrole bilayers for moving and positioning bulk micromachined silicon plates," *J. Microelectromech. Syst.*, vol. 8 (4), pp. 373-383, 1999.

[23] E. Smela, "Conjugated polymer actuators for biomedical applications," *Adv. Mat.*, vol. 15 (6), pp. 481, 2003.

[24] J. M. Pernaut and J. R. Reynolds, "Use of conducting electroactive polymers for drug delivery and sensing of bioactive molecules. A redox chemistry approach," *J. Phys. Chem. B*, vol. 104 (17), pp. 4080-4090, 2000.

[25] S. Skaarup, N. Mogensen, L. Bay, and K. West, "Polypyrrole actuators for tremor suppression," Proc. SPIE 11th Annual International Symposium: Smart Structures and Materials, vol. 5051, San Diego, CA, USA, 2003, pp. 423-428.

[26] H. Xu, C. Wang, C. L. Wang, J. Zoval, and M. Madou, "Polymer actuator valves toward controlled drug delivery application," *Biosens. Bioelectron.* , vol. 21 (11), pp. 2094-2099, 2006.

[27] J. D. W. Madden, B. Schmid, M. Hechinger, S. R. Lafontaine, P. G. A. Madden, F. S. Hover, R. Kimball, and I. W. Hunter, "Application of polypyrrole actuators: Feasibility of variable camber foils," *IEEE Journal of Oceanic Engineering*, vol. 29 (3), pp. 738-749, 2004.

[28] M. K. Andrews, M. L. Jansen, G. Spinks, D. Zhou, and G. G. Wallace, "An integrated electrochemical sensor-actuator system," *Sensors and Actuators a-Physical*, vol. 114 (1), pp. 65-72, 2004.

[29] I. W. Hunter, http://bioinstrumentation.mit.edu/Projects/CP/AUV.aspx.

[30] Rajesh, S. S. Pandey, D. Kumar, W. Takashima, and K. Kaneto, "Electrochemomechanical deformation studies of [Fe(CN)6]3- ion doped conducting polypyrrole film," *Thin Solid Films*, vol. 467 (1-2), pp. 227-230, 2004.

[31] G. M. Spinks, D. Z. Zhou, L. Liu, and G. G. Wallace, "The amounts per cycle of polypyrrole electromechanical actuators," *Smart Mater. Struct.*, vol. 12 (3), pp. 468-472, 2003.

[32] A. Mazzoldi, "Actuative properties of polyaniline fibers under electrochemical stimulation," *Materials Science and Engineering C*, vol. 6 (1), pp. 65-72, 1998.

[33] B. H. Qi, W. Lu, and B. R. Mattes, "Strain and energy efficiency of polyaniline fiber electrochemical actuators in aqueous electrolytes," *J. Phys. Chem. B*, vol. 108 (20), pp. 6222-6227, 2004.

[34] Q. B. Pei and O. Inganas, "Conjugated Polymers and the Bending Cantilever Method - Electrical Muscles and Smart Devices," *Adv. Mat.*, vol. 4 (4), pp. 277-278, 1992.

[35] T. Otero, "Characterization of triple layers," Proc. Smart Structures and Materials, 2001, vol. 4329, San Diego, California USA, 2001, pp. 93-100.

[36] G. Alici, B. Mui, and C. Cook, "Bending modeling and its experimental verification for conducting polymer actuators dedicated to manipulation applications," *Sensors and Actuators a-Physical*, vol. 126 (2), pp. 396-404, 2006.

[37] G. Han and G. Shi, "High-response tri-layer electrochemical actuators based on conducting polymer films," *J. Electroanal. Chem.*, vol. 569 (2), pp. 169-174, 2004.

[38] A. Della Santa, A. Mazzoldi, C. Tonci, and D. De Rossi, "Passive mechanical properties of polypyrrole films: a continuum, poroelastic model," *Materials Science & Engineering C-Biomimetic Materials Sensors and Systems*, vol. 5 (2), pp. 101-109, 1997.

[39] M. Christophersen, B. Shapiro, and E. Smela, "Characterization and modeling of PPy bilayer microactuators - Part 1. Curvature," *Sens. Actuators, B*, vol. 115 (2), pp. 596-609, 2006.

[40] J. Madden, P. G. A. Madden, and I. W. Hunter, "Polypyrrole actuators: modeling and performance," Proc. Smart Mater. Struct. , vol. 4329, San Diego, CA, 2001, pp. 72-83.

[41] A. Della Santa, "Characterization and modeling of a conducting polymer muscle-like linear actuator," *Smart Mater. Struct.* , vol. 6 (1), pp. 23-34, 1997.

[42] J. L. Bredas and R. Silbey, *Conjugated Polymers*, MA, USA, Kluwer Academic Publishers, 1991.

[43] P. Y. Bruice, *Organic Chemistry*, New Jersey, USA, Prentice-Hall Inc., 1998.
[44] R. Kaner, "Plastics that conduct electricity," *Sci. Amer.*, Feb, pp. 60-65, 1988.

[45] A. J. Heeger, "Semiconducting and metallic polymers: The fourth generation of polymeric materials," *J. Phys. Chem. B*, vol. 105 (36), pp. 8475-8491, 2001.

[46] W. Barford, *The International Series of Monographs on Physics*, New York, USA, Oxford University Press Inc., 2005.

[47] A. Pron, "Processible conjugated polymers: from organic semiconductors to organic metals and superconductors," *Prog. Polm. Sci.*, vol. 27 (1), pp. 135-190, 2002.

[48] W. P. Su, J. R. Schrieffer, and A. J. Heeger, "Soliton Excitations in Polyacetylene," *Phys. Rev. B*, vol. 22 (4), pp. 2099-2111, 1980.

[49] A. J. Heeger, S. Kivelson, J. R. Schrieffer, and W. P. Su, "Solitons in Conducting Polymers," *Reviews of Modern Physics*, vol. 60 (3), pp. 781-850, 1988.
[50] B. G. Streetman and S. Banerjee, *Solid State Electronic Devices*, 5th ed, Upper Saddle River, Prentice-Hall, 2000.

[51] D. Blackwood and M. Josowicz, "Work Function and Spectroscopic Studies of Interactions between Conducting Polymers and Organic Vapors," *J. Phys. Chem.* , vol. 95 (1), pp. 493-502, 1991.

[52] R. Yang, W. H. Smyrl, D. F. Evans, and W. A. Hendrickson, "Evolution of Polypyrrole Band-Structure - a Scanning Tunneling Spectroscopy Study," *J. Phys. Chem.* , vol. 96 (3), pp. 1428-1430, 1992.

[53] W. P. Su, J. R. Schrieffer, and A. J. Heeger, "Solitons in Polyacetylene," *Phys. Rev. Lett.*, vol. 42 (25), pp. 1698-1701, 1979.

[54] R. G. Davidson and T. G. Turner, "An Ir Spectroscopic Study of the Electrochemical Reduction of Polypyrrole Doped with Dodecyl-Sulfate Anion," *Synth. Met.*, vol. 72 (2), pp. 121-128, 1995.

[55] J. C. Scott, P. Pfluger, M. Krounbi, and G. B. Street, "Electron-spin-resonance studies of pyrrole polymers: Evidence for bipolarons," *Phys. Rev. Lett.*, vol. 28 (4), pp. 2140-2145, 1983.

[56] G. Zotti and G. Schiavon, "Spin and Spinless Conductivity in Polypyrrole. Evidence for Mixed-Valence Conduction," *Chem. Mater.*, vol. 3 (1), pp. 62-65, 1991.

[57] J. L. Bredas, J. C. Scott, K. Yakushi, and G. B. Street, "Polarons and bipolarons in polypyrrole: Evolution of the band structure and optical spectrum upon doping," *Phys. Rev. B*, vol. 30 (2), pp. 1023-1025, 1984.

[58] J. F. Kaufman and N. Colaneri, "Evolution of polaron states into bipolarons in polypyrrole," *Phys. Rev. Lett.*, vol. 53 (10), pp. 1005-1008, 1984.

[59] T. A. Skotheim, *Handbook of Conducting Polymers*, vol. 2, New York, USA, Marcel Dekker Inc., 1986.

[60] E. Smela and N. Gadegaard, "Volume changes in polypyrrole studied by atomic force microscopy," *J. Phys. Chem. B*, vol. 105 (39), pp. 9395-9405, 2001.

[61] E. Smela, "Surprising volume change in PPy(DBS): an atomic force microscopy study," *Adv. Mat.*, vol. 11 (11), pp. 953-957, 1999.

[62] Q. B. Pei and O. Inganas, "Conjugated Polymers as Smart Materials, Gas Sensors and Actuators Using Bending Beams," *Synth. Met.*, vol. 57 (1), pp. 3730-3735, 1993.

[63] L. Bay, T. Jacobsen, S. Skaarup, and K. West, "Mechanism of actuation in conducting polymers: Osmotic expansion," *J. Phys. Chem. B*, vol. 105 (36), pp. 8492-8497, 2001.

[64] X. W. Chen and O. Inganas, "Doping-Induced Volume Changes in Poly(3-Octylthiophene) Solids and Gels," *Synth. Met.*, vol. 74 (2), pp. 159-164, 1995.

[65] M. R. Gandhi, P. Murray, G. M. Spinks, and G. G. Wallace, "Mechanism of Electromechanical Actuation in Polypyrrole," *Synth. Met.*, vol. 73 (3), pp. 247-256, 1995.

[66] L. Lizarraga, E. M. Andrade, and F. V. Molina, "Swelling and volume changes of polyaniline upon redox switching," *J. Electroanal. Chem.*, vol. 561 (1-2), pp. 127-135, 2004.

[67] M. Pyo and C. H. Kwak, "In situ scanning tunneling microscopy study on volume change of polypyrrole/poly (styrene sulfonate)," *Synth. Met.*, vol. 150 (2), pp. 133-137, 2005.

[68] K. Kaneto, "Soft actuators based on conducting polymers," *Electrochemistry*, vol. 71 (9), pp. 804-808, 2003.

[69] K. Kaneto, "Artificial muscle: electromechanical actuators using polyaniline films," *Synth. Met.*, vol. 71 (1-3), pp. 2211-2212, 1995.

[70] Y. Velmurugu and S. Skaarup, "Ion and solvent transport in polypyrrole: Experimental test of osmotic model," *Ionics*, vol. 11 (5-6), pp. 370-374, 2005.

[71] T. Otero, H. Grande, and J. Rodriguez, "A new model for electrochemical oxidation of polypyrrole under conformation relaxation control," *J. Electroanal. Chem.*, vol. 394 (pp. 211-216, 1995.

[72] T. Otero, H. Grande, and J. Rodriguez, "Reinterpretation of polypyrrole electrochemistry after consideration of conformational relaxation processes," *J. Phys. Chem. B*, vol. 101 (19), pp. 3688-3697, 1997.

[73] K. West, L. Bay, M. M. Nielsen, Y. Velmurugu, and S. Skaarup, "Electronic Conductivity of Polypyrrole-Dodecyl Benzene Sulfonate Complexes," *J. Phys. Chem.* , vol. 108 (39), pp. 15001-15008, 2004.

[74] K. Crowley and J. Cassidy, "In situ resonance Raman spectroelectrochemistry of polypyrrole doped with dodecylbenzenesulfonate," *J. Electroanal. Chem.*, vol. 547 (1), pp. 75-82, 2003.

[75] Q. Pei and O. Inganas, "Electrochemical applications of the bending beam method: a novel way to study ion transport in electroactive polymers," *Solid State Ionics*, vol. 60 (1-3), pp. 161-166, 1993.

[76] Y. J. Qiu and J. R. Reynolds, "Dopant Anion Controlled Ion-Transport Behavior of Polypyrrole," *Polym. Eng. Sci.*, vol. 31 (6), pp. 417-421, 1991.

[77] C. Baker, Y. J. Qiu, and J. Reynolds, "Electrochemically induced charge and mass transport in polypyrrole/poly(styrenesulfonate) molecular composites," *J. Phys. Chem.*, vol. 95, pp. 4446-4452, 1991.

[78] Q. B. Pei and O. Inganas, "Electrochemical Applications of the Bending Beam Method .2. Electroshrinking and Slow Relaxation in Polypyrrole," *J. Phys. Chem.* , vol. 97 (22), pp. 6034-6041, 1993.

[79] S. Skaarup, L. Bay, K. Vidanapathirana, S. Thybo, P. Tofte, and K. West, "Simultaneous anion and cation mobility in polypyrrole," *Solid State Ionics*, vol. 159 (1-2), pp. 143-147, 2003.

[80] H. Ge and G. G. Wallace, "Ion-Exchange Properties of Polypyrrole," *Reactive Polymers*, vol. 18 (2), pp. 133-140, 1992.

[81] X. M. Ren and P. G. Pickup, "Ion-Transport in Polypyrrole and a Polypyrrole Polyanion Composite," *J. Phys. Chem.* , vol. 97 (20), pp. 5356-5362, 1993.

[82] R. A. Khalkhali, W. E. Price, and G. G. Wallace, "Quartz crystal microbalance studies of the effect of solution temperature on the ion-exchange properties of polypyrrole conducting electroactive polymers," *React. Funct. Polym.* , vol. 56 (3), pp. 141-146, 2003.

[83] Q. J. Xie, S. Kuwabata, and H. Yoneyama, "EQCM studies on polypyrrole in aqueous solutions," *J. Electroanal. Chem.*, vol. 420 (1-2), pp. 219-225, 1997.

[84] K. M. Mangold, C. Weidlich, J. Schuster, and K. Juttner, "Ion exchange properties and selectivity of PSS in an electrochemically switchable PPy matrix," *J. Appl. Electrochem.* , vol. 35 (12), pp. 1293-1301, 2005.

[85] T. Otero, C. Santamaria, and R. K. Bunting, "Kinetic studies of polypyrrole electrogeneration in three solvents," *J. Electroanal. Chem.*, vol. 380 (1-2), pp. 291-294, 1995.

[86] X. W. Chen and O. Inganas, "Three-step redox in polythiophenes: Evidence from electrochemistry at an ultramicroelectrode," *J. Phys. Chem.* , vol. 100 (37), pp. 15202-15206, 1996.

[87] Y. Tezuka and K. Aoki, "Concentration profiles of conducting species in polypyrrole films in cyclic voltammetry by means of a diode array detector," *J. Electroanal. Chem.*, vol. 425 (1-2), pp. 167-172, 1997.

[88] H. Yang and J. Kwak, "Mass transport investigated with the electrochemical and electrogravimetric impedance techniques .1. Water transport in PPy/CuPTS films," *J. Phys. Chem. B*, vol. 101 (5), pp. 774-781, 1997.

[89] H. Yang and J. Kwak, "Mass transport investigated with the electrochemical and electrogravimetric impedance techniques .2. Anion and water transport in PMPy and PPy films," *J. Phys. Chem. B*, vol. 101 (23), pp. 4656-4661, 1997.

[90] J. J. L. Cascales and T. F. Otero, "Molecular dynamics simulations of the orientation and reorientational dynamics of water and polypyrrole rings as a function of the oxidation state of the polymer," *Macromol. Theory Simul.* , vol. 14 (1), pp. 40-48, 2005.

[91] W. T. Yap, R. A. Durst, E. A. Blubaugh, and D. D. Blubaugh, "Chronoamperometry of polymer-modified electrodes charge transport by diffusion and migration," *J. Electroanal. Chem.*, vol. 144 (1-2), pp. 69-75, 1983.

[92] R. Lange and K. Doblhofer, "The transient response of electrodes coated with membrane-type polymer films under conditions of diffusion and migration of the redox ions," *J. Electroanal. Chem.*, vol. 237 (1-2), pp. 13-26, 1987.

[93] C. D. Paulse and P. G. Pickup, "Chronoamperometry of polypyrrole: migration of counterions and effect of uncompensated solution resistance," *J. Phys. Chem.*, vol. 92 (1), pp. 7002-7006, 1988.

[94] P. G. Pickup and R. A. Osteryoung, "Charging and discharging rate studies of polypyrrole films in AlCl3: 1-methyl-(3-ethyl)-imidazolium chloride molten salts and in CH3CN," *J. Electroanal. Chem.*, vol. 195 (2), pp. 271-88, 1985.

[95] F. Miomandre, M. N. Bussac, E. Vieil, and L. Zuppiroli, "Monte-Carlo simulation of linear sweep voltammograms during redox switching of conducting polymers," *Electrochim. Acta*, vol. 44 (12), pp. 2019-2024, 1999.

[96] J. C. Lacroix, K. Fraoua, and P. C. Lacaze, "Moving front phenomena in the switching of conductive polymers," *J. Electroanal. Chem.*, vol. 444 (1), pp. 83-93, 1998.

[97] P. G. A. Madden, J. D. W. Madden, P. A. Anquetil, N. A. Vandesteeg, and I. W. Hunter, "The relation of conducting polymer actuator material properties to performance," *IEEE Journal of Oceanic Engineering*, vol. 29 (3), pp. 696-705, 2004.

[98] Y. Osada and D. De Rossi, *Polymer Sensors and Actuators*, New York, Springer, 2000.

[99] X. Z. Wang, E. Smela, and B. Shapiro, "Visualizing ion currents in conjugated polymers," *Adv. Mat.*, vol. 16 (18), pp. 1605-1609, 2004.

[100] Q. B. Pei and O. Inganas, "Electrochemical Applications of the Bending Beam Method .1. Mass-Transport and Volume Changes in Polypyrrole During Redox," *J. Phys. Chem.* , vol. 96 (25), pp. 10507-10514, 1992.

[101] T. Otero, H. Grande, and J. Rodriguez, "Role of conformational relaxation on the voltammetric behavior of polypyrrole. Experiments and mathematical model," *J. Phys. Chem. B*, vol. 101 (42), pp. 8525-8533, 1997.

[102] P. J. S. Foot, F. Mohammed, P. D. Calvert, and N. C. Billingham, "Diffusion in conducting polymers," *J. Phys. D: Appl. Phys.*, vol. 20 (11), pp. 1354-1360, 1987.

[103] D. A. Edwards, "Non-Fickian diffusion in thin polymer films," *Journal of Polymer Science Part B-Polymer Physics*, vol. 34 (5), pp. 981-997, 1996.

[104] N. E. Schlotter and P. Y. Furlan, "A Review of Small Molecule Diffusion in Polyolefins," *Polymer*, vol. 33 (16), pp. 3323-3342, 1992.

[105] N. L. Thomas, "A theory of case II diffusion," *Polymer*, vol. 23 (4), pp. 529-542, 1982.

[106] M. Ilg, B. Pfleiderer, K. Albert, W. Rapp, and E. Bayer, "Investigation of the Diffusion Process in Cross-Linked Polystyrenes by Means of NMR Imaging and Solid-State NMR-Spectroscopy," *Macromol.*, vol. 27 (10), pp. 2778-2783, 1994.

[107] M. Kalaji, L. Nyholm, and L. M. Peter, "A microelectrode study of the influence of pH and solution composition on the electrochemical behavior of polyaniline films," *J. Electroanal. Chem.*, vol. 313 (1-2), pp. 271-289, 1991.

[108] X. Wang, E. Smela, and B. Shapiro, "Understanding Ion Transport in Conjugated Polymers," Proc. SPIE 12th Annual International Symposium: Smart Structures and Materials, San Diego, California USA, 2005.

[109] C. Odin and M. Nechtschein, "Slow relaxation in conducting polymers," *Phys. Rev. Lett.*, vol. 67 (9), pp. 1114-1117, 1991.

[110] H. Mao and P. G. Pickup, "In situ measurement of the conductivity of polypyrrole and poly(1-methyl-3-(pyrrole-1-ylmethyl)pyridinium)+ as a function of potential by mediated voltammetry. Redox conduction or electronic conduction," *Journal of American Chemical Society*, vol. 112 (5), pp. 1776-1782, 1990.

[111] K. P. Vidanapathirana, M. A. Careem, S. Skaarup, and K. West, "Ion movement in polypyrrole/dodecylbenzenesulphonate films in aqueous and non-aqueous electrolytes," *Solid State Ionics*, vol. 154 (Sp. Iss), pp. 331-335, 2002.

[112] S. Shimoda and E. Smela, "The effect of ph on polymerization and volume change in ppy(DBS)," *Electrochim. Acta*, vol. 44 (2-3), pp. 219-238, 1998.

[113] H. Mao and P. G. Pickup, "Ion-Transport in a Polypyrrole-Based Ion-Exchange Polymer," *J. Phys. Chem.* , vol. 93 (17), pp. 6480-6485, 1989.

[114] S. Maw, E. Smela, K. Yoshida, P. Sommer-Larsen, and R. B. Stein, "The effects of varying deposition current density on bending behavior in PPy(DBS)-

actuated bending beams," *Sensors and Actuators A-Physical*, vol. 89 (3), pp. 175-184, 2001.

[115] M. Christophersen and E. Smela, "Polypyrrole/gold bilayer microactuators: response time and temperature effects," Proc. SPIE 13th Annual Int'l. Symposium on Smart Structures and Materials, EAPAD, vol. 6168, San Diego, CA, 2006.

[116] K. Neoh, "Structure and degradation behavior of polypyrrole doped with sulfonate anions of different sizes subjected to undoping -redoping cycles," *Chem. Mat.*, vol. 8 (1), pp. 167-172, 1996.

[117] S. Skaarup, K. West, L. Gunaratne, K. P. Vidanapathirana, and M. A. Careem, "Determination of ionic carriers in polypyrrole," *Solid State Ionics*, vol. 136 (Sp. Iss), pp. 577-582, 2000.

[118] W. Lu, "Use of ionic liquids for pi-conjugated polymer electrochemical devices," *Science*, vol. 297 (5583), pp. 983-987, 2002.

[119] A. Della Santa, D. DeRossi, and A. Mazzoldi, "Characterization and modeling of a conducting polymer muscle-like linear actuator," *Smart Materials & Structures*, vol. 6 (1), pp. 23-34, 1997.

[120] X. Lin, J. Li, E. Smela, and S. Yip, "Polaron-induced conformation change in single polypyrrole chain: an intrinsic actuation mechanism," *Int. J. Quant. Chem.*, vol. 102 (5), pp. 980-985, 2005.

[121] T. F. Otero and I. Boyano, "Comparative study of conducting polymers by the ESCR model," *J. Phys. Chem. B*, vol. 107 (28), pp. 6730-6738, 2003.

[122] T. F. Otero, H. Grande, and J. Rodriguez, "A conformational relaxation approach to polypyrrole voltammetry," *Synth. Met.*, vol. 85 (1-3), pp. 1077-1078, 1997.

[123] K. Naoi, Y. Oura, M. Maeda, and S. Nakamura, "Electrochemistry of surfactant-doped polypyrrole film (I): formation of columnar structure by electropolymerization," *J. Electrochem. Soc.* , vol. 142 (2), pp. 417-22, 1995.

[124] E. W. H. Jager, E. Smela, and O. Inganas, "Microfabricating conjugated polymer actuators," *Science*, vol. 290 (5496), pp. 1540-1545, 2000.

[125] H. Xu, V. V. Konovalov, C. I. Contescu, S. A. Jaffe, and M. Madou, "Water trans port in a non-aqueous, polypyrrole electrochemical cell," *Sens. Actuators, B*, vol. 114 (1), pp. 248-253, 2006.

[126] V. Syritski, K. Idla, and A. Opik, "Synthesis and redox behavior of PEDOT/PSS and PPy/DBS structures," *Synth. Met.*, vol. 144 (3), pp. 235-239, 2004.

[127] W. Wernet, M. Monkenbusch, and G. Wegner, "A new series of conducting polymers with layered structure: Polypyrrole n-alkylsulfates and n-alkylsulfonates," *Makromol. Chem., Rapid Commun.*, vol. 5 (1), pp. 157, 1984.

[128] D. M. Collard and M. S. Stoakes, "Lamellar Conjugated Polymers by Electrochemical Polymerization of Heteroarene-Containing Surfactants - Potassium 3-(3-Alkylpyrrol-1-Yl)Propanesulfonates," *Chem. Mat.*, vol. 6 (6), pp. 850-857, 1994.

[129] K. Oldham and J. C. Myland, *Fundamentals of electrochemical science*, Academic Press, 1994.

[130] D. R. Lide, *CRC Handbook of Chemistry and Physics*, 85th ed, CRC press, 2004.

[131] Z. H. Cai and C. R. Martin, "Electrochemical investigations of electronically conductive polymers .6. Mechanism of the redox reactions for the electronically conductive form of polypyrrole," *J. Electroanal. Chem.*, vol. 300 (1-2), pp. 35-50, 1991.

[132] S. Govindjee and J. C. Simo, "Coupled Stress Diffusion - Case-II," *Journal of the Mechanics and Physics of Solids*, vol. 41 (5), pp. 863-887, 1993.

[133] A. S. Argon, R. E. Cohen, and A. C. Patel, "A mechanistic model of case II diffusion of a diluent into a glassy polymer," *Polymer*, vol. 40 (25), pp. 6991-7012, 1999.

[134] N. L. Thomas and A. H. Windle, "A Deformation Model for Case-II Diffusion," *Polymer*, vol. 21 (6), pp. 613-619, 1980.

Chapter 2

None

Chapter 3

[1] P. Yam, *Sci. Amer.*, **1995**, (July), 74.

[2] E. Smela, *Adv. Mat.*, **2003**, *15 (6)*, 481.

[3] Q. Pei, O. Inganäs, *Sol. State Ion.*, **1993**, *60*, 161.

[4] M. R. Gandhi, P. Murray, G. M. Spinks, G. G. Wallace, *Synth. Met.*, **1995**, *73*, 247.

[5] P. Chiarelli, A. Della Santa, D. De Rossi, A. Mazzoldi, *J. Intell. Mater. Syst. Struct.*, **1995**, *6*, 32.

[6] T. F. Otero, H. Grande, J. Rodriguez, *J. Phys. Org. Chem.*, **1996**, *9*, 381.

[7] J.-M. Sansiñena, V. Olazábal, in *Electroactive Polymer (EAP) Actuators as Artificial Muscles: Reality, Potential, and Challenges* (Ed: Y. Bar-Cohen) SPIE Press, Bellingham, **2001**, p. 193.

[8] R. H. Baughman, *Synth. Met.*, **1996**, *78*, 339.

[9] E. Smela, N. Gadegaard, *Adv. Mat.*, **1999**, *11 (11)*, 953.

[10] T. F. Otero, I. Boyano, *J. Phys. Chem. B*, **2003**, *107 (28)*, 6730

[11] P. J. S. Foot, F. Mohammed, P. D. Calvert, N. C. Billingham, *J. Phys. D: Appl. Phys.*, **1987**, *20 (11)*, 1354.

[12] T. J. Alfrey, E. F. Gurnee, W. G. Lloyd, *J. Polym. Sci.*, **1966**, *C12*, 249–61.

[13] A. J. Bard, L. R. Faulkner, *Electrochemical Methods: Fundamentals and Applications*, 2nd ed., John Wiley & Sons, Inc., New York, **2001**.

[14] B. G. Streetman, S. Banerjee, *Solid State Electronic Devices*, 5th ed., (Ed: N. J. Holonyak) Prentice-Hall, Upper Saddle River, **2000**.

[15] R. P. Feynman, R. B. Leighton, M. Sands, *The Feynman Lectures on Physics*, Addison-Wesley Publishing Company, **1964**.

[16] Y. Tezuka, S. Ohyama, T. Ishii, K. Aoki, *Bull. Chem. Soc. Jpn.*, **1991**, *64***,** 2045.

[17] Y. Tezuka, K. Aoki, H. Yajima, T. Ishii, *Journal of Electroanalytical Chemistry*, **1997**, *425***,** 167.

[18] J. C. Lacroix, K. Fraoua, P. C. Lacaze, *J. Electroanal. Chem.*, **1998**, *444 (1)***,** 83.

[19] M. A. De Paoli, R. C. D. Peres, S. Panero, B. Scrosati, *Electrochim. Acta*, **1992**, *37 (7)***,** 1173.

[20] T. Matencio, M.-A. De Paoli, R. C. D. Peres, R. M. Torresi, S. I. Cordoba de Torresi, *Synth. Met.*, **1995**, *72***,** 59.

[21] E. Smela, N. Gadegaard, *J. Phys. Chem. B*, **2001**, *105 (39)***,** 9395.

[22] E. Smela, *J. Micromech. Microeng.*, **1999**, *9***,** 1.

Chapter 4

[1] B. Francois, N. Mermilliod, and L. Zuppiroli, "Swelling of polyacetylene when doped by iodine or sodium," *Synth. Met.*, vol. 4, pp. 131-8, 1981.

[2] Q. Pei and O. Inganäs, "Conjugated polymers and the bending cantilever method: electrical muscles and smart devices," *Adv. Mat.*, vol. 4 (4), pp. 277-278, 1992.

[3] T. F. Otero, E. Angulo, J. Rodriguez, and C. Santamaria, "Electrochemomechanical properties from a bilayer: polypyrrole/non-conducting and flexible material -- artificial muscle," *J. Electroanal. Chem.*, vol. 341, pp. 369, 1992.

[4] R. H. Baughman, L. W. Shacklette, R. L. Elsenbaumer, E. Plichta, and C. Becht, "Conducting polymer electromechanical actuators," in *Conjugated Polymeric Materials: Opportunities in Electronics, Optoelectronics, and Molecular Electronics*, vol. 182, *NATO ASI Ser., Ser. E*, J. L. Brédas and R. R. Chance, Eds. Dordrecht: Kluwer Academic Publishers, 1990, pp. 559-82.

[5] R. H. Baughman, "Conducting polymer artificial muscles," *Synth. Met.*, vol. 78, pp. 339-353, 1996.

[6] T. F. Otero, "Artificial muscles, electrodissolution and redox processes in conducting polymers," in *Conductive Polymers: Transport, Photophysics, and Applications*, vol. 4, *Organic Conductive Molecules and Polymers*, H. S. Nalwa, Ed. New York: John Wiley & Sons, 1997, pp. 517-594.

[7] J.-M. Sansiñena and V. Olazábal, "Conductive polymers," in *Electroactive Polymer (EAP) Actuators as Artificial Muscles: Reality, Potential, and Challenges*, Y. Bar-Cohen, Ed. Bellingham: SPIE Press, 2001, pp. 193-222.

[8] M. T. Cortés and J. C. Moreno, "Artificial muscles based on conducting polymers," *e-Polymers*, vol.041, pp. 1-42, 2003.

[9] E. Smela, "Conjugated polymer actuators for biomedical applications," *Adv. Mat.*, vol. 15 (6), pp. 481-94, 2003.

[10] D. Leo, E. Smela, J. Madden, K. Kim, Z. Ounaies, and D. F. Infante, "Standard testing methods for extensional and bending electroactive polymer actuators," Proc. ASME 2005, International Mechanical Engineering Congress and Exposition (IMECE), Orlando, FL, 2005, pp. 2005-82440.

[11] Q. Pei and O. Inganäs, "Electrochemical applications of the bending beam method; a novel way to study ion transport in electroactive polymers," *Sol. State Ion.*, vol. 60, pp. 161-166, 1993.

[12] X. Wang, B. Shapiro, and E. Smela, "Visualizing ion transport in conjugated polymers," *Adv. Mat.*, vol. 16 (18), pp. 1605-1609, 2004.

[13] T. F. Otero and E. Angulo, "Oxidation-reduction of polypyrrole films -- kinetics, structural model and applications," *Solid State Ionics*, vol. 63-5, pp. 803-809, 1993.

[14] T. F. Otero, H. Grande, and J. Rodriguez, "A new model for elecrochemical oxidation of polypyrrole under conformational relaxation control," *J. Electroanal. Chem.*, vol. 394, pp. 211, 1995.

[15] T. F. Otero, H. Grande, and J. Rodriguez, "Conformational relaxation during polypyrrole oxidation: from experiment to theory," *Electrochim. Acta*, vol. 41 (11/12), pp. 1863-1869, 1996.

[16] T. F. Otero, H. Grande, and J. Rodriguez, "An electromechanical model for the electrochemical oxidation of conducting polymers," *Synth. Met.*, vol. 76, pp. 293, 1996.

[17] T. F. Otero, H. Grande, and J. Rodriguez, "Electrochemical oxidation of polypyrrole under conformational relaxation control. Electrochemical relaxation model," *Synth. Met.*, vol. 76, pp. 285, 1996.

[18] T. F. Otero and H. Grande, "Thermally enhanced conformational relaxation during electrochemical oxidation of polypyrrole," *Electroanal. Chem.*, vol. 414, pp. 171, 1996.

[19] T. F. Otero, H.-J. Grande, and J. Rodriguez, "Reinterpretation of polypyrrole electrochemistry after consideration of conformational relaxation processes," *J. Phys. Chem. B*, vol. 101, pp. 3688-3697, 1997.

[20] T. F. Otero, H. Grande, and J. Rodriguez, "A conformational relaxation approach to polypyrrole voltammetry," *Synth. Met.*, vol. 85, pp. 1077, 1997.

[21] T. F. Otero, H. Grande, and J. Rodríguez, "Role of conformational relaxation on the voltammetric behavior of polypyrrole. Experiments and mathematical model," *J. Phys. Chem. B*, vol. 101, pp. 8525-33, 1997.

[22] T. F. Otero and M. Bengoechea, "UV-visible spectroelectrochemistry of conducting polymers. Energy linked to conformational changes," *Langmuir*, vol. 15, pp. 1323-1327, 1999.

[23] T. F. Otero and I. Boyano, "Comparative study of conducting polymers by the ESCR model," *J. Phys. Chem. B*, vol. 107 (28), pp. 6730 -6738, 2003.

[24] T. F. Otero and I. Boyano, "Potentiostatic oxidation of polyaniline under conformational relaxation control: experimental and theoretical study," *J. Phys. Chem. B*, vol. 107 (18), pp. 4269-4276, 2003.

[25] T. F. Otero and J. Padilla, "Anodic shrinking and compaction of polypyrrole blend: electrochemical reduction under conformational relaxation kinetic control," *J. Electroanal. Chem.*, vol. 561 (1), pp. 167-71, 2004.

[26] L. Bay, T. Jacobsen, S. Skaarup, and K. West, "Mechanism of actuation in conducting polymers: osmotic expansion," *J. Phys. Chem. B*, vol. 105 (36), pp. 8492-8497, 2001.

[27] X. Wang, E. Smela, and B. Shapiro, "Understanding ion transport in conjugated polymers," Proc. SPIE 11th Annual Int'l. Symposium on Smart Structures and Materials, EAPAD, vol. 5385, San Diego, CA, 2004, pp. 146-154.

[28] X. Wang, E. Smela, and B. Shapiro, "Understanding ion transport in conjugated polymers," Proc. SPIE 12th Annual Int'l. Symposium on Smart Structures and Materials, EAPAD, San Diego, CA, 2005.

[29] J. H. Kaufman, N. Colaneri, J. C. Scott, and G. B. Street, "Evolution of polaron states into bipolarons in polypyrrole," *Phys. Rev. Lett.*, vol. 53 (10), pp. 1005-8, 1984.

[30] J. L. Brédas, J. C. Scott, K. Yakushi, and G. B. Street, "Polarons and bipolarons in polypyrrole - evolution of the band structure and optical spectrum upon doping," *Phys. Rev. B*, vol. 30 (2), pp. 1023-1025, 1984.

[31] Y. Tezuka, S. Ohyama, T. Ishii, and K. Aoki, "Observation of propagation speed of conductive front in electrochemical doping process of polypyrrole films," *Bull. Chem. Soc. Jpn.*, vol. 64, pp. 2045-51, 1991.

[32] Y. Tezuka, T. Kimura, T. Ishii, and K. Aoki, "Concentration distribution of conducting species with time resolution in electrochemical undoping process at the polypyrrole-film-coated electrode in the light of electric percolation," *J. Electroanal. Chem.*, vol. 395, pp. 51-55, 1995.

[33] J. C. Carlberg and O. Inganas, "Fast optical spectroscopy of the electrochemical doping of poly(3,4-ethylenedioxythiophene)," *J. Electrochem. Soc.*, vol. 145 (11), pp. 3810-3814, 1998.

[34] T. Johansson, N. K. Persson, and O. Inganas, "Moving redox fronts in conjugated polymers studies from lateral electrochemistry in polythiophenes," *J. Electrochem. Soc.*, vol. 151 (4), pp. E119-E124, 2004.

[35] S. Shimoda and E. Smela, "The effect of pH on polymerization and volume change in PPy(DBS)," *Electrochim. Acta*, vol. 44 (2-3), pp. 219-238, 1998.

[36] S. Skaarup, L. Bay, K. Vidanapathirana, S. Thybo, P. Tofte, and K. West, "Simultaneous anion and cation mobility in polypyrrole," *Sol. State Ion.*, vol. 159 (1-2), pp. 143-147, 2003.

[37] H. Mao and P. G. Pickup, "Ion transport in a polypyrrole-based ion-exchange polymer," *J. Phys. Chem.*, vol. 93 (17), pp. 6480-6485, 1989.

[38] E. Smela and N. Gadegaard, "Volume change in polypyrrole studied by atomic force microscopy," *J. Phys. Chem. B*, vol. 105 (39), pp. 9395-9405, 2001.

[39] H. Yang and J. Kwak, "Mass transport investigated with the electrochemical and electrogravimetric impedance techniques 1. Water transport in PPy/CuPTS films," *J. Phys. Chem. B*, vol. 101 (5), pp. 774-781, 1997.

[40] C. K. Baker, Y.-J. Qiu, and J. R. Reynolds, "Electrochemically induced charge and mass transport in polypyrrole/poly(styrenesulfonate) molecular composites," *J. Phys. Chem.*, vol. 95, pp. 4446-4452, 1991.

[41] J. C. Lacroix, K. Fraoua, and P. C. Lacaze, "Moving front phenomena in the switching of conductive polymers," *J. Electroanal. Chem.*, vol. 444 (1), pp. 83-93, 1998.

[42] M. R. Gandhi, P. Murray, G. M. Spinks, and G. G. Wallace, "Mechanism of electromechanical actuation in polypyrrole," *Synth. Met.*, vol. 73 (3), pp. 247-256, 1995.

[43] G. L. Duffitt and P. G. Pickup, "Enhanced ionic conductivity of polypyrrole due to incorporation of excess electrolyte during potential cycling," *J. Chem. Soc. Faraday Trans.*, vol. 88 (10), pp. 1417-1423, 1992.

[44] Y. Li, "On the large overpotential of the first reduction of polypyrrole perchlorate films in organic solutions," *Electrochim. Acta*, vol. 42 (2), pp. 203-210, 1997.

[45] L. Lizarraga, E. M. Andrade, and F. V. Molina, "Swelling and volume changes of polyaniline upon redox switching," *J. Electroanal. Chem.*, vol. 561 (1), pp. 127-35, 2004.

[46] K. West, T. Jacobsen, B. Zachau-Christiansen, M. A. Careem, and S. Skaarup, "Electrochemical synthesis of polypyrrole: influence of current density on structure," *Synth. Met.*, vol. 55-57 (2-3), pp. 1412-1417, 1993.

[47] P. Murray, G. M. Spinks, G. G. Wallace, and R. P. Burford, "In-situ mechanical properties of tosylate doped (pTS) polypyrrole," *Synth. Met.*, vol. 84 (1-3), pp. 847-848, 1997.

[48] E. Smela, W. Lu, and B. R. Mattes, "Polyaniline Actuators,Part 1: PANI(AMPS) in HCl," *Synth. Met.*, vol. 151 (1), pp. 25–42, 2005.

[49] E. Smela and N. Gadegaard, "Surprising volume change in PPy(DBS): an atomic force microscopy study," *Adv. Mat.*, vol. 11 (11), pp. 953-7, 1999.

[50] M. Christophersen, Y. Liu, B. Shapiro, and E. Smela, "Characterization and modeling of PPy bilayer microactuators. Part 1: Curvature," *Sens. Act. B*, vol. 115 (2), pp. 596-809, 2006.

[51] B. Shapiro and E. Smela, "Bending actuators with maximum curvature and force and zero interfacial stress," *J. Intell. Mater. Syst. Struct.*, in press, 2005.

[52] Y. Berdichevsky and Y.-H. Lo, "Polymer microvalve based on anisotropic expansion of polypyrrole," Proc. Mat. Res. Soc. Symp. Fall 2003 Meeting, vol. 782, Boston, 2003, pp. A4.4.1.

[53] A. Della Santa, D. De Rossi, and A. Mazzoldi, "Performances and work capacity of a polypyrrole conducting polymer linear actuator," *Synth. Met.*, vol. 90 (2), pp. 93-100, 1997.

[54] S. W. Feldberg, "Reinterpretation of polypyrrole electrochemistry. Consideration of capacitive currents in redox switching of conducting polymers," *J. Am. Chem. Soc.*, vol. 106, pp. 4671-4674, 1984.

[55] S. Maw and E. Smela, "Effects of monomer and electrolyte concentrations on actuation of PPy(DBS) bilayers," *Synth. Met*., vol.155 (1), pp. 18-26, 2005.

[56] B. G. Streetman and S. Banerjee, *Solid State Electronic Devices*, 5th ed, Upper Saddle River, Prentice-Hall, 2000.

[57] X. Lin, J. Li, E. Smela, and S. Yip, "Polaron-induced conformation change in single polypyrrole chain: an intrinsic actuation mechanism," *Int. J. Quant. Chem.*, vol. 102, pp. 980-5, 2005.

[58] J. P. Aime, F. Bargain, M. Schott, H. Eckhardt, G. G. Miller, and R. L. Elsenbaumer, "Structural study of doped and undoped polythiophene in solution by small-angle neutron scattering," *Phys. Rev. Lett,*, vol. 65 (1), pp. 55-58, 1989.

[59] J. D. Madden, P. G. Madden, P. A. Anquetil, and I. W. Hunter, "Load and time dependence of displacement in a conducting polymer actuator," Proc. MRS Symposium Proceedings, vol. 698, Electroactive Polymers and Rapid Prototyping, Boston, Massachusetts, 2001, pp. 137-144.

Chapter 5

[1] W. J. Albery and A. R. Mount, "Transmission-line model for conducting polymers including cations and Donnan exclusion," *J. Chem. Soc. Faraday Trans.*, vol. 89 (14), pp. 2487-2497, 1993.

[2] S. Fletcher, "Contribution to the theory of conducting-polymer electrodes in electrolyte solutions," *J. Chem. Soc. Faraday Trans.*, vol. 89 (2), pp. 311-320, 1993.

[3] J. C. Lacroix, K. Fraoua, and P. C. Lacaze, "Moving front phenomena in the switching of conductive polymers," *J. Electroanal. Chem.*, vol. 444 (1), pp. 83-93, 1998.

[4] F. Berthier, J.-P. Diard, and C. Montella, "Numerical solution of coupled systems of ordinary and partial differential equations. Application to the study of electrochemical insertion reactions by linear sweep voltammetry," *J. Electroanal. Chem.*, vol. 502, pp. 126-31, 2001.

[5] E. Deiss, O. Haas, and J. B. Schlenoff, "Numerical-simulation of the cyclic voltammogram of polyacetylene," *J. Electrochem. Soc.*, vol. 142 (10), pp. 3256-3262, 1995.

[6] J. Bisquert and V. S. Vikhrenko, "Analysis of the kinetics of ion intercalation. Two state model describing the coupling of solid state ion diffusion and ion binding processes," *Electrochim. Acta*, vol. 47 (24), pp. 3977-3988, 2002.

[7] X. Wang, B. Shapiro, and E. Smela, "Visualizing ion transport in conjugated polymers," *Adv. Mat.*, vol. 16 (18), pp. 1605-1609, 2004.

[8] X. Wang, E. Smela, and B. Shapiro, "Understanding ion transport in conjugated polymers," Proc. SPIE 12th Annual Int'l. Symposium on Smart Structures and Materials, EAPAD, San Diego, CA, 2005.

[9] L. Bay, T. Jacobsen, S. Skaarup, and K. West, "Mechanism of actuation in conducting polymers: osmotic expansion," *J. Phys. Chem. B*, vol. 105 (36), pp. 8492-8497, 2001.

[10] B. G. Streetman and S. Banerjee, *Solid State Electronic Devices*, 5th ed, Upper Saddle River, Prentice-Hall, 2000.

[11] H. M. Schey, *Div, Grad, Curl, and All That: An Informal Text on Vector Calculus*, New York, W. W. Norton & Company, 1973.

[12] A. J. Bard and L. R. Faulkner, *Electrochemical Methods: Fundamentals and Applications*, 2nd ed, New York, John Wiley & Sons, Inc., 2001.

[13] N. W. Ashcroft and N. D. Mermin, *Solid State Physics*, Philadelphia, Saunders College, 1976.

[14] S. E. Guidoni and C. M. Aldao, "On diffusion, drift and the Einstein relation," *Eur. J. Phys.*, vol. 23, pp. 395–402, 2002.

[15] R. P. Feynman, R. B. Leighton, and M. Sands, *The Feynman Lectures on Physics*, Addison-Wesley Publishing Company, 1964.

[16] Y. Roichman and N. Tessler, "Generalized Einstein relation for disordered semiconductors—implications for device performance," *Appl. Phys. Lett.*, vol. 80 (11), pp. 1948-50, 2002.

[17] R. L. Panton, *Incompressible Flow*, 2 ed, New York, NY, John Wiley & Sons, Inc., 1996.

[18] T. F. Otero and I. Boyano, "Comparative study of conducting polymers by the ESCR model," *J. Phys. Chem. B*, vol. 107 (28), pp. 6730 -6738, 2003.

[19] D. Comoretto, G. Dellepiane, F. Marabelli, P. Tognini, A. Stella, J. Cornil, D. A. dos Santos, J. L. Bredas, and D. Moses, "Experimental and theoretical studies of the anisotropical complex dielectric constant of highly stretch-oriented poly(p-phenylene-vinylene)," *Synthetic Metals*, vol. 116 (1-3), pp. 107-110, 2001.

[20] A. J. Epstein, A. P. Lee, and V. N. Prigodin, "Low-dimensional Variable Range Hopping in Conducting Polymers," *Synth. Met.*, vol. 117, pp. 9-13, 2001.

[21] A. Kaynak, J. Unsworth, G. E. Beard, and R. Clout, "Study of Conducting Polypyrrole Films in the Microwave Region," *Mat. Res. Bull.*, vol. 28 (11), pp. 1109-1125, 1993.

[22] C. Y. Lee, H. M. Kim, J. W. Park, Y. S. Gal, J. I. Jin, and J. Joo, "AC electrical properties of conjugated polymers and theoretical high-frequency behavior of multilayer films," *Synthetic Metals*, vol. 117 (1-3), pp. 109-113, 2001.

[23] G. Phillips, R. Suresh, J. Waldman, J. Kumar, J. Ichen, S. Tripathy, and J. C. Huang, "Dielectric-Properties of Polypyrrole Doped with Tosylate Anion in the Far Infrared and Microwave," *Journal of Applied Physics*, vol. 69 (2), pp. 899-905, 1991.

[24] C. D. Paulse and P. G. Pickup, "Chronoamperometry of polypyrrole: migration of counterions and effect of uncompensated solution resistance," *J . Phys. Chem.*, vol. 92 (24), pp. 7002-7006, 1988.

[25] T. J. R. Hughes, L. P. Franca, and M. Balestra, "A New Finite-Element Formulation for Computational Fluid-Dynamics .5. Circumventing the Babuska-Brezzi Condition - a Stable Petrov-Galerkin Formulation of the Stokes Problem Accommodating Equal-Order Interpolations," *Computer Methods in Applied Mechanics and Engineering*, vol. 59 (1), pp. 85-99, 1986.

[26] J.-C. Lacroix and A. F. Diaz, "Electrolyte effects on the switching reaction of polyaniline," *J. Electrochem. Soc.*, vol. 135 (6), pp. 1457-63, 1988.

[27] R. John and G. G. Wallace, "Doping-dedoping of polypyrrole: a study using current-measuring and resistance-measuring techniques," *J. Electroanal. Chem.*, vol. 354, pp. 145-61, 1993.

[28] E. M. Genies, G. Bidan, and A. Diaz, "Spectroelectrochemical study of polypyrrole films," *J. Electroanal. Chem.*, vol. 149, pp. 101-113, 1983.

[29] T. Osaka, K. Naoi, S. Ogano, and S. Nakamura, "Dependence of film thickness on electrochemical kinetics of polypyrrole and on properties of lithium/polypyrrole battery," *J. Electrochem. Soc.*, vol. 134 (9), pp. 2096-2102, 1987.

[30] Y. Tezuka and K. Aoki, "Concentration profiles of conducting species in polypyrrole films in cyclic voltammetry by means of a diode array detector," *Journal of Electroanalytical Chemistry*, vol. 425, pp. 167-172, 1997.

[31] Y. Tezuka and K. Aoki, "Direct demonstration of the propagation theory of a conductive zone in a polypyrrole film by observing temporal and spatial variations of potentials at addressable microband array electrodes," *J. Electroanal. Chem.*, vol. 273, pp. 161-168, 1989.

[32] Y. Tezuka and T. Kimura, "Concentration distribution of conducting species with time resolution in electrochemical undoping process at the polypyrrole film coated electrode in the light of electric percolation," *Journal of Electroanalytical Chemistry*, vol. 395, pp. 51-55, 1995.

[33] X. Wang and E. Smela, "Ion transport in conjugated polymers: Part 1. Experimental studies on PPy(DBS)," in preparation, 2006.

[34] N. E. Schlotter and P. Y. Furlan, "A Review of Small Molecule Diffusion in Polyolefins," *Polymer*, vol. 33 (16), pp. 3323-3342, 1992.

[35] D. A. Edwards, "Non-Fickian diffusion in thin polymer films," *Journal of Polymer Science Part B-Polymer Physics*, vol. 34 (5), pp. 981-997, 1996.

[36] M. Ilg, B. Pfleiderer, K. Albert, W. Rapp, and E. Bayer, "Investigation of the Diffusion Process in Cross-Linked Polystyrenes by Means of Nmr Imaging and Solid-State Nmr-Spectroscopy," *Macromolecules*, vol. 27 (10), pp. 2778-2783, 1994.

[37] N. L. Thomas, "A theory of case II diffusion," *Polymer*, vol. 23 (pp. 529-542, 1982.

[38] P. G. A. Madden, J. D. W. Madden, P. A. Anquetil, N. A. Vandesteeg, and I. W. Hunter, "The relation of conducting polymer actuator material properties to performance," *IEEE J. Ocean Eng.*, vol. 29 (3), pp. 696-705, 2004.

[39] P. Burgmayer and R. W. Murray, "Ion gate electrodes. Polypyrrole as a switchable ion conductor membrane," *J. Phys. Chem.*, vol. 88, pp. 2515-21, 1984.

[40] M. J. Ariza and T. F. Otero, "Ionic diffusion across oxidized polypyrrole membranes and during oxidation of the free-standing film," *Colloids and Surfaces a-Physicochemical and Engineering Aspects*, vol. 270, pp. 226-231, 2005.

[41] E. Smela and N. Gadegaard, "Surprising volume change in PPy(DBS): an atomic force microscopy study," *Adv. Mat.*, vol. 11 (11), pp. 953-7, 1999.

[42] W. Wernet, M. Monkenbusch, and G. Wegner, "A new series of conducting polymers with layered structure: Polypyrrole n-alkylsulfates and n-alkylsulfonates," *Macromolecular Rapid Communications*, vol. 26 (6), pp. 430-437, 2005.

[43] K. Naoi, "Electrochemistry of surfactant-doped polypyrrole film: formation of columnar structure by elelctropolymerization," *J. of Elelctrochemical Society*, vol. 142 (2), pp. 417-421, 1995.

[44] X. Wang, B. Shapiro, and E. Smela, "Modeling charge transport in conjugated polymers," Proc. SPIE 13th Annual Int'l. Symposium on Smart Structures and Materials, EAPAD, vol. 6168, San Diego, CA, 2006.

Chapter 6

None

Chapter 7

None